DISSERTATION

NO$_x$ FORMATION IN METHYL ESTER, ALCOHOL, AND ALKANE DROPLET

AUTOIGNITION AND COMBUSTION: PLIF MEASUREMENTS AND DETAILED KINETIC

MODELING

Submitted by

Torben Grumstrup

Department of Mechanical Engineering

In partial fulfillment of the requirements

For the Degree of Doctor of Philosophy

Colorado State University

Fort Collins, Colorado

Summer 2014

Doctoral Committee:

    Advisor: Anthony J. Marchese
    Co-Advisor: Azer Yalin

    Sonia Kreidenweis
    Daniel B. Olsen

ABSTRACT

NO$_x$ FORMATION IN METHYL ESTER, ALCOHOL, AND ALKANE DROPLET
AUTOIGNITION AND COMBUSTION: PLIF MEASUREMENTS AND DETAILED KINETIC
MODELING

Numerous studies have shown that diesel engines fueled by fatty-acid methyl ester biodiesel often exhibit slightly increased production of oxides of nitrogen (NOx) in comparison to petroleum diesel. A number of explanations for this increase have been proposed. One theory, which has been supported by optical engine test results, suggests that the presence of oxygen atoms in the methyl ester fuel molecule results in a leaner premixed autoignition zone, thereby increasing in-cylinder temperatures and promoting Zel'dovich NOx production. Other experiments have suggested that the unsaturated methyl esters in biodiesel cause an increase in CH radical production (and/or other potential precursors such as C2O) which in turn increases Fenimore NOx formation. In this work, these hypotheses are explored experimentally and computationally by considering autoignition and combustion of single, isolated methyl ester, alcohol and alkane droplets.

Experiments were conducted in which the planar laser-induced fluorescence (PLIF) spectroscopy technique was applied to burning liquid fuel droplets in free-fall. A monodisperse stream of droplets was generated by a piezoelectric device and passed through a resistively heated ignition coil. A pulsed laser beam from a Nd:YAG-pumped dye laser (10 Hz, 10 ns width) was formed into a sheet and passed through the droplet flame. The dye laser was tuned to excite hydroxyl (OH) at 282.9 nm and nitric oxide (NO) at 226.0 nm. The resulting fluorescence was imaged by a Cooke Corporation DiCam Pro ICCD digital camera. Band pass filters were utilized to reject laser light scattering while admitting fluorescence

wavelengths. Due to the small fluorescence signal, many fluorescence images were averaged together to create a useful average image; approximately 250 and 1000 images were averaged for OH and NO spectroscopy, respectively. Finally, pixel intensity of the averaged fluorescence image was integrated about the droplet center to create qualitative radial profiles of OH and NO concentration. Profiles were generated for a number of oxygenated fuels and one pure hydrocarbon: methanol, ethanol, 1-propanol, methyl butanoate, methyl decanoate, and n-heptane.

To quantitatively interpret the contribution of Zel'dovich and Fenimore NOx mechanisms on NOx formation in the vicinity of igniting liquid droplets, detailed numerical droplet combustion simulations were conducted. The transient, spherically symmetric droplet combustion modeling featured detailed gas-phase kinetics, spectrally resolved radiant heat transfer, and multicomponent gas transport. New chemical kinetic mechanisms were created by appending NOx chemical kinetics to existing detailed methanol, methyl butanoate, and n-heptane mechanisms. In the computations, non-oxygenated (heptane) and oxygenated (methyl butanoate, methanol) fuel droplets are introduced into a hot (1150 K) air ambient whereupon the liquid vaporizes, thus producing a stratified fuel/air mixture that thermally autoignites after an ignition delay period. The computational results suggest that NOx formation in stratified fuel/air mixture in the vicinity of a cold liquid droplet is influenced greatly by the detailed full NOx chemistry (Fenimore, Zel'dovich and N2O) and cannot be fully explained by considering only the Zel'dovich NOx route.

The computations also suggest, however, that the stoichiometry of the premixed autoignition zone in the laminar gas phase surrounding a spherical droplet differs from that observed in turbulent diesel spray ignition. In single droplets, irrespective of the fuel used,

autoignition always initiates in the relatively hot lean region far from the droplet. In diesel sprays, depending on the thermodynamic conditions and fuel reactivity, ignition can occur in lean or rich regions by virtue of turbulent transport of heat and mass. In large molecular weight fuels like n-heptane or petroleum diesel fuel, this is often in mixtures which are quite rich ($\phi \approx 3$). To underscore the difference between turbulent spray ignition and ignition of a single droplet, the most reactive mixture fraction and critical scalar dissipation rate were derived for the case of turbulent ignition The results show that for a turbulent non-premixed flame to ignite, two requirements must be met: (1) the fuel/air mixture fraction must be equal or similar to the most reactive mixture fraction, (2) the local scalar dissipation rate must be less than the critical scalar dissipation rate. Due to the effect of scalar dissipation rate on transport and mixing in turbulent, non-premixed flames, it is concluded that, at least as far as autoignition is concerned, autoignition of spherically-symmetric isolated fuel droplets has limitations as physical model for ignition of diesel sprays in compression ignition engines. However, the computations clearly show that transient NOx formation in presence of thermal and concentration gradients cannot be adequately described by the Zel'dovich NOx mechanism, which has consequences with regards to capability of computational engine simulations to accurately predict NOx formation.

TABLE OF CONTENTS

LIST OF FIGURES

CHAPTER 1

INTRODUCTION

Common liquid transportation fuels such as gasoline, diesel, and jet fuel are tremendously energy dense. A single liter of any of these fuels contains roughly 35 million joules of chemical energy. This amount of chemical energy is the equivalent to approximately 10 kWh, which is equal to the electrical energy consumed by a typical American single-family home in seven hours [1]. Granted, it is physically impossible to extract all of that energy as useful work or electricity, but it nonetheless illustrates the remarkable energy storage capability of liquid fuels, in contrast to batteries which typically contain approximately 2 million joules of electrical energy per liter of battery volume (more than an order of magnitude less than liquid transportation fuels).

To extract useful work, liquid transportation fuels are nearly always burned and the resulting release of thermal energy is converted to mechanical motion like the spinning driveshaft of a truck or thrust from a jet aircraft engine. Combustion has been the principal source of mechanical energy for the past three centuries and the role of combustion is likely to continue for centuries to come. As such, the study of combustion, and in particular combustion emissions, remains a relevant area of study.

The vast majority of liquid transportation fuels produced in the United States are derived from petroleum products [2] that are extracted from subterranean reservoirs. When the fuel is burned in an engine, carbon dioxide CO_2 is released as one of the principle products of combustion. Approximately 2.4 kilograms of carbon dioxide are emitted per liter of petroleum-derived fuel burned [3]. The consensus among climate experts [4] is that such

emissions increase the concentration of carbon dioxide in Earth's atmosphere which has and will continue to change the climate by enhancing the greenhouse effect.

Biologically-derived fuels like corn-grain ethanol and biodiesel have the potential to mitigate emissions of carbon dioxide and associated climate change effects. Combusting such fuels still results in formation of carbon dioxide. However, the emissions are offset by the atmospheric carbon dioxide that was consumed by the feedstock plants or microorganisms when they engaged in life processes like photosynthesis. For example, soybean plants use sunlight and carbon dioxide to produce energy that enables them to grow bean pods. The beans are harvested and processed to produce soybean oil which is chemically altered to make biodiesel. A truck fueled by the biodiesel still emits carbon dioxide from the tail pipe, but a fraction of the CO_2 emitted is balanced by that consumed by the soybean plants to produce the feedstock oil contained in the beans[1]. This is in contrast to petroleum-derived fuels whose feedstocks are hydrocarbons (crude oil) extracted from subterranean geological formations and surface oil sands. Carbon dioxide emitted from combustion of these fuels is not offset by any process because the carbon released to the atmosphere was previously sequestered.

Biodiesel and ethanol are both biologically-derived fuels that contain oxygen in the fuel molecules and are termed *oxygenated fuels*. These fuels are chemically different from petroleum-derived fuels like diesel, gasoline, and aviation fuel which are pure hydrocarbons– containing only hydrogen and carbon atoms. One benefit of oxygenated fuels is that they reduce emissions of carbon monoxide and soot when mixed with petroleum-derived fuels or

---

[1]Extraction of oil from the plant matter and subsequent conversion to biodiesel requires energy which is usually produced from fossil fuels.
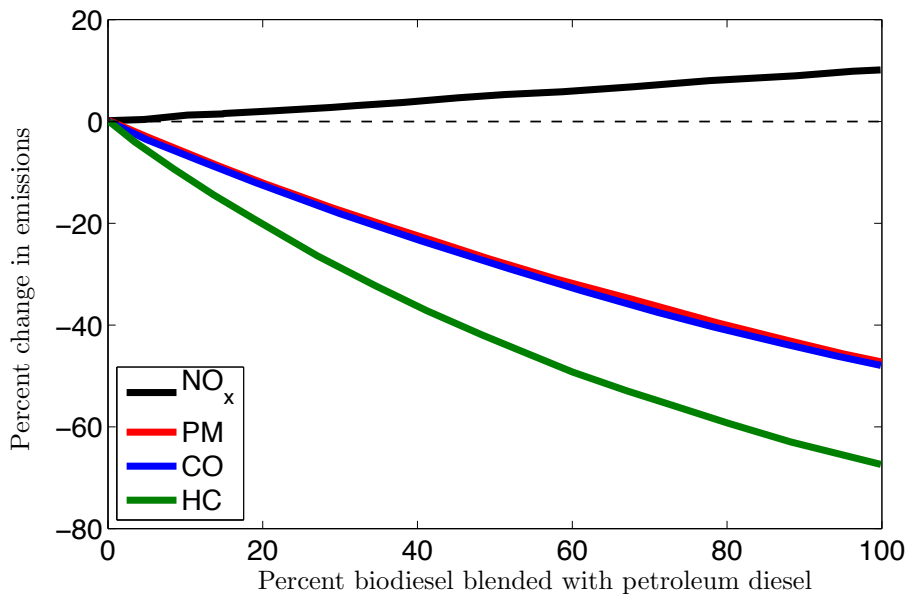
FIGURE 1.1. Percent change in NO_x, particulate matter, carbon monoxide, and unburned hydrocarbon emissions for engines fueled by a range of biodiesel-petroleum-diesel blend rates compared to emissions from engines fueled by pure petroleum diesel. Adapted from EPA, 2002.

used in neat form. However, the presence of oxygen in the fuel molecule also means oxygenated fuels have slightly (in the case of biodiesel) or significantly (in the case of ethanol) lower heat content per unit volume compared to pure hydrocarbons. Some biologically-derived fuels produced higher emissions of pollutants. For example, diesel engines fueled with biodiesel appear to produce slightly more NO_x emissions than when fueled with petroleum diesel [5].

Oxides of nitrogen (NO_x) are a group of combustion emissions that are known to contribute to photochemical smog, formation of acid rain precursors, stratospheric ozone consumption, and formation of ground level ozone [6, 7, 8]. Due to these harmful effects, NO_x emissions regulations have been steadily tightened by the United State Environmental Protection Agency, beginning with the Clean Air Act in 1970 [9]. For example, since 1985, the permitted rate of NO_x emissions for on-road heavy-duty diesel vehicles has decreased

by more than a factor of 50: from 10.6 to 0.2 $g/(BHP \cdot hr)^2$. Despite increased regulation, on-road vehicles like cars and trucks remain the principle source of NO_x emissions by mass in the United States [10]. Simply from the standpoint of human health and air quality, it is important that NO_x emissions be understood. However, there is an economic factor as well, since meeting ever-stricter NO_x emissions standards requires investment on the part of engine manufacturers, electrical utilities, and other industrial sectors.

Numerous studies have been conducted in the past several decades in which production of oxides of nitrogen and other emissions were monitored in the exhaust of diesel engines fueled by biodiesel. A 2002 report by the United States Environmental Protection Agency (EPA) compiled results from such studies to attempt to find trends in the data [5]. The plot in Figure 1.1, adapted from the EPA report, shows how criteria pollutant emissions change with a variation of the fraction of biodiesel blended with petroleum diesel. Emission reductions of particulate matter (PM), carbon monoxide (CO), and unburned hydrocarbons (HC) are observed with increasing biodiesel fraction. On the other hand, increased NO_x emissions are seen as the fraction of biodiesel is increased. When running neat (pure) biodiesel, a 10% increase in NO_x emissions is typically observed in comparison to that produced by pure petroleum diesel [5]. This result is well known and has been the subject of dedicated research in the combustion community for nearly two decades because the apparent increase in NO_x formation by biodiesel represents an obstacle to widespread implementation as a replacement for petroleum fuel[3].

Hypotheses explaining increased NO_x formation in biodiesel-fueled engines can be grouped into six principle categories [11] and are summarized here:

---

[2]Units are grams per brake-specific horsepower per hour.

[3]The widespread adoption by manufacturers of selective catalyst reduction (SCR) in new diesel vehicles diminishes concern over the 10% NO_x increase due to biodiesel.

A. *Injection Timing:* Biodiesel has a higher bulk modulus compared to petroleum diesel and therefore has a correspondingly higher sonic velocity. This causes the pressure wave in the fuel line feeding the injector to travel faster, thereby initiating injection slightly earlier. With earlier injection comes earlier ignition meaning that reactants in the cylinder experience a longer residence time at high temperatures which favors NO formation by the Zel'dovich NO chemical pathway [6]. The advanced injection timing effect is dramatic in older low-pressure pump injectors, but less so in modern high-pressure common rail injector technology.

B. *Combustion Phasing:* Biodiesel tends to have a higher cetane number than petroleum diesel, causing earlier ignition and combustion of the fuel spray. And, like the above explanation, this means reactants have a longer residence time in a high temperature environment which favors NO formation by Zel'dovich NO chemistry.

C. *Premixed-burn Fraction Stoichiometry:* Biodiesel is (usually) comprised of methyl esters which contain oxygen atoms in their molecular structure. During fuel injection, but prior to ignition, the fuel evaporates and mixes with air to create a rich mixture. The presence of oxygen atoms in the fuel makes the fuel-air mixture slightly less rich which causes the subsequent premixed combustion phase to be slightly hotter and therefore enhances Zel'dovich NO formation. (A detailed discussion of this topic is found in Section 1.2.)

D. *Fuel Molecular Structure:* Biodiesel, having a different molecular structure from petroleum diesel, exhibits different chemical pathways to formation of NO_x . For example, the higher percentage of C=C double bonds may result in increased CH

production [12] and/or the presence of oxygen in the methyl ester may lead to the formation of C_2O which may enhance Fenimore NO_x formation [13, 14, 15, 16, 17].

E. *Radiative Heat Transfer:* Being an oxygenated fuel, biodiesel generates less soot than petroleum diesel. Radiant heat transfer between soot and the cylinder wall of an engine is an important means of heat loss from the flame. As such, biodiesel flames exhibit lower heat transfer to the cylinder wall, causing higher flame temperatures. The result is higher temperature of the gas phase species in the cylinder which favors Zel'dovich NO formation.

The most comprehensive optical engine study conducted to date was produced by Mueller, et al. [11]. In the Mueller study, an instrumented single-cylinder compression-ignition research engine was operated with various fuels to ascertain the relative importance of hypotheses B and E for increased NO_x production in biodiesel-fueled engines. The result reported by Mueller, et al. was that at least for the operating conditions used in the experiment, hypothesis C was the main reason for increased NO_x formation by the engine [11]. Specifically, that the presence of fuel-bound oxygen caused the premixed burn fraction to be less rich, causing an increase in in-cylinder temperature. Moreover, the standing premixed autoignition zone that occurs after the transition to non-premixed combustion will be less rich as well, with the same consequences. The concepts of premixed burn fraction and standing premixed autoignition zone are described in detail in Section 1.2.

The Mueller, et al. [11] study provides a logical explanation for increased NO_x formation in biodiesel-fueled engines, but three key points are worth pointing out. First, Mueller, et al. used soy biodiesel that was comprised of long chain methyl esters with the attendant fuel-bound oxygen. If the oxygen contained in the ester group of the methyl esters was responsible

for making the premixed burn fraction and standing premixed autoignition zone less rich, then any oxygenated fuel should exhibit the same effect. For example, an engine fueled by a mixture of 5% methanol and 95% petroleum diesel should produce more NO_x emission than when the same engine is fueled by pure petroleum diesel because the fuel-bound oxygen in the methanol would make the premixed burn fraction and standing premixed autoignition zone less rich. Second, Mueller states explicitly that it is possible that some of the increased NO_x formed by biodiesel-fueled engines is due to Fenimore and N_2O mechanisms, but that they focus only on Zel'dovich NO production because the role of Fenimore and the N_2O mechanisms in diesel spray ignition and combustion [11], "is not well understood." Mueller, et al. states [11] and others confirm [18, 19] the premixed burn fraction and standing premixed autoignition zone are rich, which is precisely the condition that favors the Fenimore NO_x mechanism. Therefore, it stands to reason that Fenimore NO_x should be expected to be an important contributor to overall NO_x formation. Third, attempts by Mueller [20] or others to detect NO_x species using in-cylinder planar laser diagnostics during the premixed burn fraction phase of combustion have thus far been unsuccessful (due to in-cylinder conditions being extremely unfavorable to such measurements). Without knowing the relative amount of NO produced during the premixed burn fraction compared to overall production, it is difficult to speculate about the corresponding relative importance of Zel'dovich NO formation with respect to Fenimore or N_2O path.

The research conducted on spherically-symmetric isolated droplet autoignition and combustion for this dissertation is meant to build on the work of Mueller, et al. described above with a geometry more amenable to experiments and modeling. The droplet geometry shares a number of physical traits with diesel spray autoignition and combustion: a cold liquid-state

fuel exposed to a hot ambient, evaporation and mixing of fuel vapor with ambient oxidizer, thermal and stoichiometric stratification, autoignition and consumption of premixed fuel and air, transition to a non-premixed flame, and a quasi-steady state non-premixed flame. These similarities (as well as limitations) will be expanded upon later, but the point being emphasized here is that the same physics that influence the combustion and therefore NO_x formation in diesel sprays is present in droplets as well. This means that autoignition and combustion of isolated droplets has potential for acting as a physical model for diesel spray. Since experiments and computations with single droplets are less challenging than those on an operating diesel engine, a droplet physical model for diesel combustion would allow one to relatively easily implement sophisticated measurement techniques (i.e., planar laser-induced fluorescence spectroscopy) that have proven challenging for in-cylinder application [20]. Moreover, because only a single spatial dimension is required to describe a spherically-symmetric domain, computational simulations could use detailed chemical kinetics and species-specific transport properties–a level of complexity that is beyond the capability of modern spray combustion modeling.

The potential for a droplet ignition physical model of diesel spray autoignition is easily stated, but the implications are significant. Measurements from droplet experiments could be used to validate detailed kinetic mechanisms which include chemistry required to capture NO_x formation. This process could be employed not just for small surrogates like methyl butanoate, but real practical fuels with large molecular masses like methyl oleate ($C_{19}H_{36}O_2$, 297 g/mol). This process would be an advance in combustion research because it would comprise an additional geometry against which to validate chemical mechanisms that predict

NO$_x$ formation in practical fuels with large molecular masses (another being, e.g., one-dimensional opposed flow [21]). Given the potential, one of the purposes of this research was to assess the viability of a droplet physical model for diesel combustion from a theoretical standpoint.

1.1. Oxides of Nitrogen

Urban photochemical smog is formed through a series of reactions in which nitric oxide (NO) is among the reactants. Most NO in urban areas is formed in internal combustion engines in cars, trucks, and other modes of transport. Due to the detrimental effect of smog on air quality, government agencies have regulated NO emissions since the 1970's. Not coincidentally, that time period was also the beginning of a significant increase in research activity on NO formation in combustion systems. [22]

Nitric oxide is a member of a group of nitrogen-and-oxygen-containing molecules termed "oxides of nitrogen." There are several distinct oxides of nitrogen molecules with varying numbers of oxygen and nitrogen atoms. However, those that are of greatest interest to combustion researchers are NO, NO$_2$, and N$_2$O, and are referred to as a group[4] as NO$_x$. NO and NO$_2$ molecules emitted at ground level will readily react with constituents of the atmosphere there. This is in contrast to N$_2$O which is quite stable at ground level and can be convected into the stratosphere. At such altitudes, N$_2$O participates in reactions that cause ozone-depletion and, because it readily absorbs infrared radiation, acts as a robust greenhouse gas [6].

The majority of NO$_x$ produced by combustion is NO [6] and is largely the focus of the research reported on by this thesis. In combustion systems in which air is the oxidizer, NO

---

[4]Sometimes only NO and NO$_2$ are grouped together as NO$_x$ at the exclusion of N$_2$O. Here, NO$_x$ is intended to mean all three species for the sake of brevity and clarity.

TABLE 1.1. Summary of NO_x formation mechanisms.

Mechanism	Additional Species	Additional Reactions	Favorable Conditions
Zel'dovich NO	2	3	$T > 1800$ K, lean
Fenimore NO_x	34	432	cool, rich
N_2O-Path	2	2	high pressure, lean

is formed by reactions with atmospheric molecular nitrogen (N_2) through three chemical pathways: Zel'dovich NO, Fenimore NO_x, and the N_2O-path mechanism [6, 23]. These three mechanisms are discussed in the remainder of this section. It should be noted that a further significant source of NO is that formed from combustion of fuels which contain bound nitrogen [6, 23]. This NO production path is, however, beyond the scope of this dissertation since all fuels considered are devoid of fuel-bound nitrogen[5].

A note on nomenclature is in order. Although it often appears as "Zel'dovich NO_x" in the literature, the mechanism can produce only NO and not the other oxides of nitrogen. Therefore, whether the mechanism appears as Zel'dovich NO_x or Zel'dovich NO, it should be understood that NO is sole oxide of nitrogen formed by this mechanism. On the other hand, the Fenimore NO_x mechanism can produce NO, N_2O, and/or NO_2. The N_2O-path chemical kinetic mechanism for formation of NO is sometimes grouped with Fenimore NO_x, but following Law [24], the N_2O-path is treated separately here.

Table 1.1 contains a summary of the three NO_x formation mechanisms considered in this work. The table shows the number of additional species and reactions that are required to capture the chemistry of the respective paths. The right-most column indicates in what conditions the mechanism is favored. Each of the three NO_x mechanisms are described in the subsections that follow.

---

[5]Nor do gasoline, diesel, and aviation fuel contain fuel-bound nitrogen

1.1.1. ZEL'DOVICH NO MECHANISM. The Zel'dovich NO mechanism, also referred to as the thermal mechanism [25], is comprised of three reactions:

$$O + N_2 \longrightarrow NO + N \tag{R1}$$

$$N + O_2 \longrightarrow NO + O \tag{R2}$$

$$N + OH \longrightarrow NO + H. \tag{R3}$$

The rate-limiting step is Reaction (R1) in which the particularly strong molecular nitrogen bond is broken.

The reactions that occur during oxidation of fuel are normally much faster than production of NO by the Zel'dovich mechanism. As such, the Zel'dovich NO reactions can be approximated as being decoupled from fuel oxidation [6]. A relatively simple derivation can be made to estimate the rate of production from the Zel'dovich mechanism by assuming equilibrium concentration for atomic oxygen such that $\frac{1}{2}O_2 \longleftrightarrow O$ with atomic nitrogen assumed to exist in quasi-steady-state:

$$\frac{d}{dt}[N] = k_1[O][N_2] - k_2[N][O_2] - k_3[N][OH] \approx 0. \tag{1}$$

Having made use of these assumptions, the rate of production of NO can be written as [26]:

$$\frac{d}{dt}[NO] = 1.70e17 \cdot T^{-1/2} \, e^{\hat{}} \left[\frac{-69750}{T(K)}\right] \cdot [O_2]_{eq}^{1/2} \, [N_2]_{eq} \, . \tag{2}$$

The assumptions required to arrive at the above equation are not necessarily realistic, resulting in important consequences that will be discussed in the next section on Fenimore NO formation. Nevertheless, Equation (2) is useful for the purpose of discussion because it

shows that the rate of formation of NO by the Zel'dovich NO mechanism is strongly (and non-linearly) dependent on temperature, T. Namely, unless the temperature is very high, the $e^{\hat{}}(-69460/T)$ factor is vanishingly small, resulting in a correspondingly small NO production rate. This result makes physical sense because a significant amount of energy is required to break the strong molecular nitrogen bond. As a consequence, Zel'dovich NO is important only when combustion temperatures exceed roughly 1800 Kelvin [27]. A further fact can be gleaned from Equation (2): there is also a somewhat weaker dependance of NO production on the availability of molecular oxygen in product gases. As such, Zel'dovich NO formation is maximal for hot, slightly lean flames [24].

1.1.2. FENIMORE NO MECHANISM. The Fenimore NO mechanism, in which hydrocarbon fuel fragments react with molecular nitrogen, was postulated by Fenimore in 1971 [28]. This mechanism contains many more reactions than the Zel'dovich NO and is not strictly limited to high temperature conditions. At present, it is widely agreed that the initiating reactions are these [22, 6, 29]:

$$N_2 + CH \longrightarrow NCN + H \tag{R4}$$

$$N_2 + CH_2 \longrightarrow HCN + NH. \tag{R5}$$

The NCN produced by Reaction (R4) is oxidized by O, OH, and O_2 leading to the formation of NO [24]. The products of Reaction (R5) participate in a number of reactions which ultimately form atomic nitrogen. The major reactions of the sequence are shown here:

$$HCN + O \longrightarrow NCO + H \tag{R6}$$

$$\text{HCN} + \text{H} \longrightarrow \text{CN} + \text{H}_2 \tag{R7}$$

$$\text{HCN} + \text{OH} \longrightarrow \text{CN} + \text{H}_2\text{O} \tag{R8}$$

$$\text{NCO} + \text{H} \longrightarrow \text{NH} + \text{CO} \tag{R9}$$

$$\text{NH} + \text{H} \longrightarrow \text{N} + \text{H}_2 \tag{R10}$$

$$\text{NH} + \text{OH} \longrightarrow \text{N} + \text{H}_2\text{O} \tag{R11}$$

$$\text{CN} + \text{O} \longrightarrow \text{N} + \text{CO} \cdot \tag{R12}$$
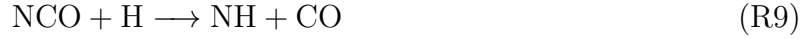
The atomic nitrogen produced in the latter three reactions then react with O_2 and OH in Reactions (R2) and (R3) to form NO.

Another principle component of the Fenimore NO_x mechanism is the NO_2 path [6] which is comprised of the following primary formation and consumption reactions:

$$\text{NO} + \text{HO}_2 \longrightarrow \text{NO}_2 + \text{OH} \tag{R13}$$

$$\text{NO}_2 + \text{H} \longrightarrow \text{NO} + \text{OH} \cdot \tag{R14}$$

The formation of NO_2 tends to occur in relatively low temperature (<1500 K) parts of a flame by Reaction (R13) with NO which has diffused from high-temperature regions. At high temperatures (>1500 K), Reaction (R14) rapidly consumes NO_2, making it short-lived in hot flames.

1.1.3. N_2O PATH TO NO. Another source of NO is that in which N_2O is an intermediate species. There is no formal name for this path, but is often referred to as the N_2O path, or N_2O mechanism. Molecular nitrogen reacts with atomic oxygen in the presence of a third

body to form N_2O which in turn also reacts with atomic oxygen to form NO.

$$N_2 + O + M \longrightarrow N_2O + M \tag{R15}$$

$$N_2O + O \longrightarrow NO + NO \tag{R16}$$

Above, species "M" represents any collision partner. Notice both reactions of the sequence require atomic oxygen. Moreover, the initiating reactions is a three-body recombination reaction. Given these two facts, the N_2O mechanism is favored in lean flames at high pressure [24].

The fact that the reaction rate of Reaction (R15) exhibits a pressure dependence most likely has an effect on the importance of the N_2O-path to overall NO_x formation in droplet autoignition relative to diesel spray ignition. The droplet experiments and simulations reported herein were both conducted at approximately atmospheric pressure. However, the autoignition and combustion of a diesel spray in an engine takes place at significantly higher pressures. The disparity in pressure between the experiments and simulations, and an operating engine suggest that the N_2O-path mechanism to NO_x formation is more important in engines because the pressures are much higher.

1.2. Diesel Spray Autoignition and Combustion

One of the purposes of the research reported in this thesis is to determine if isolated droplet ignition and combustion comprises a legitimate physical model for the those same processes occurring in a diesel spray. In support of that discussion, a description of diesel spray ignition and combustion is found here. The explanation contained herein is based on

laser sheet and chemiluminescence imaging conducted by John Dec on a research engine and reported on in his 1997 SAE paper [30].

A number of diagrams depicting ignition and combustion of a diesel spray were created by Dec [30] and are reproduced in Figures 1.2 and 1.3. The images are not averages of repeated observations, but rather characteristic depictions of results Dec obtained from imaging diagnostics for the indicated crank angle. It should be understood that these illustrations are based on examinations of one particular research engine and some variation should be expected for practical engines with various operating parameters (fuel chemistry, engine timing, boost pressure, load, injection technology, etc.). Nonetheless, Dec's illustrations are entirely adequate for the purpose here of explaining the process of diesel ignition and combustion.

Figure 1.2 contains ten illustrations [30] of the diesel jet for the the indicated crank angle degrees after the start of fuel injection (ASI). The small gray circles from which the jet emanates represent the location of the injector nozzle orifice. The various colors correspond to the jet components as they are indicated in the legend at the bottom of the page.

At 1.0° ASI the brown elongated teardrop structure represents liquid fuel entering the cylinder. Although not depicted in the diagrams, the jet is comprised of a purely liquid core surrounded by droplets and ligaments of liquid fuel.

A tan region is shown surrounding the liquid jet at 2.0° ASI and represents a rich fuel vapor and air mixture with equivalence ratio $\phi = 2$ to 4. A combination of means are responsible for the mixing of fuel vapor and air: entrainment of ambient air by the fuel jet, diffusion, and turbulent convection. In comparing the length of the liquid jet between 1.0 and 2.0° ASI, it is apparent the length has approximately doubled during that interval. Also
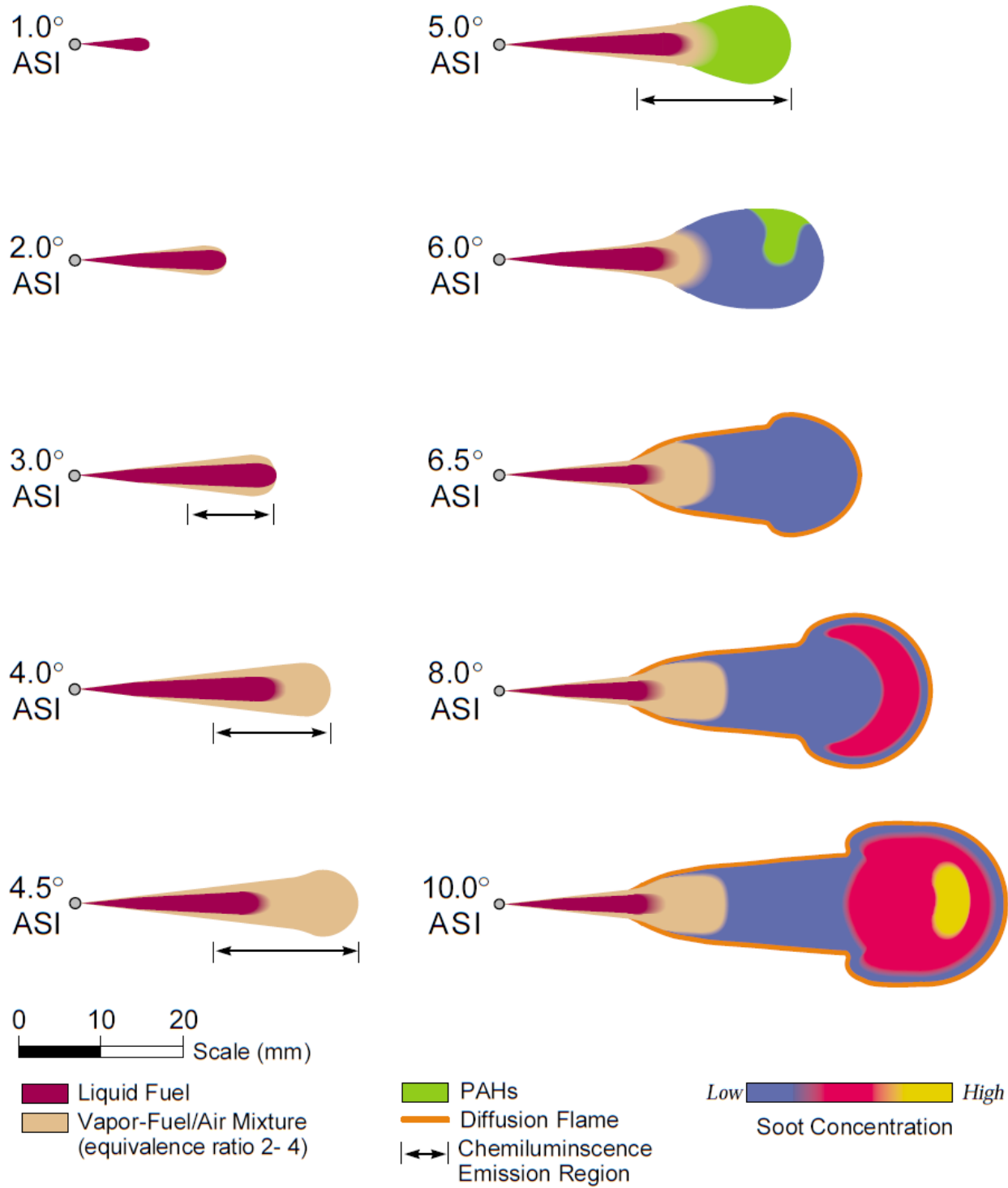
FIGURE 1.2. Diagrams reproduced from Dec, 1997 which depict the ignition and combustion of a diesel spray. Reproduced with permission.

notable is that there is no fuel-air mixture depicted as being present at the leading edge of the liquid jet, nor along the left-most 1/3 of the liquid jet.

By 3.0° ASI, the liquid jet has reached its maximum extent of about 20mm. The liquid jet will more or less maintain the same size and shape until the end of injection. The fuel-air mixture region (tan) continues to grow in size. Over the past crank angle degree, the radial thickness of the fuel-air mixture region between the edge of the liquid jet and white image background (ambient) has approximately doubled. However, just as with the prior crank angle step, the fuel-air mixture does not extend beyond the leading edge of the liquid jet. The bracketed arrow indicates the region of rich premixed fuel and air in which OH chemiluminescence was first observed to occur by Dec. The bracket includes nearly the entire width of the fuel-air mixture, meaning that OH chemiluminescence was observed nearly everywhere in the fuel-air mixture. The presence of OH is evidence of the initiation of ignition since the radical is an important combustion intermediate.

At 4.0° ASI, the liquid jet remains the same length while the fuel-air mixture extends further into the cylinder. By 4.5° ASI, OH chemiluminescence is seen throughout the fuel-air mixture beyond the liquid jet. This, along with evidence from Raleigh scattering experiments, indicates that combustion is occurring volumetrically in this rich fuel-air mixture region. The fuel-air mixture is rolling up into a toroidal vortex as shown by the widening of the leading tan region. The lime-green region seen at 5.0° ASI symbolizes the presence of polycyclicaromatic hydrocarbons (PAHs) which are thought to be a precursor to soot particles. At 6.0° ASI, some of the PAHs have been transformed into soot particles which are indicated to be present in low concentrations by the purple color. By 6.5° ASI, the rich fuel-air mixture is largely exhausted and combustion has transitioned to a state in which a
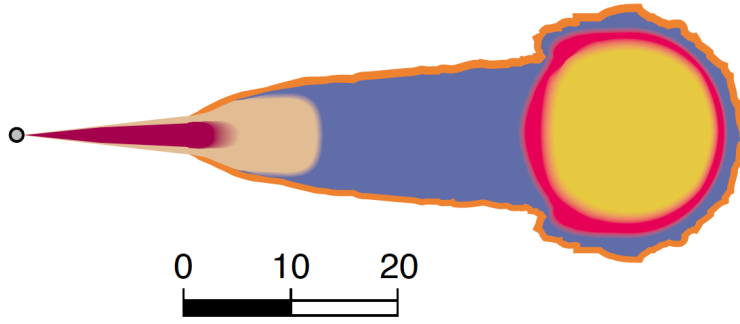
FIGURE 1.3. Diagram reproduced from Dec, 1997 that shows diesel spray combustion in pseudo steady-state prior to the end of injection. Reproduced with permission.

transport-limited non-premixed flame generates the majority of the heat release. The non-premixed flame is indicated by the orange outline of the gaseous part of the diesel spray. A rich fuel-air mixture region (tan) is present just beyond the end of the liquid jet. This is formed by fuel vapor mixing with air entrained by the fuel jet between the orifice and non-premixed flame. Partial oxidation of the fuel-air mixture forms soot particles (purple) which are contained within the perimeter of the non-premixed flame. In the remaining diagrams, 8.0° and 10° ASI, the gaseous part of the jet continues to extend further into the cylinder as the toroidal vortex grows larger. Higher soot concentrations are also seen within the vortex region as indicated by the red and yellow regions. Up to this point (10° ASI) the jet depicted is that which occurs with ongoing fuel injection. The gaseous part of the jet will continue to elongate and the region of high soot concentration will grow before achieving quasi-steady state condition illustrated in Figure 1.3. This arrangement will continue as long as injection of fuel is ongoing. When fuel stops flowing at the end of injection (EOI), the remaining fuel is consumed and combustion ceases.

Some details of diesel spray ignition and combustion relevant to the research reported herein are worth pointing out. Dec concluded that ignition in the diesel spray occurred at

approximately 3.0° ASI [30]. This was accomplished by imaging chemiluminescence emissions of the hydroxyl radical (OH) which is an important combustion intermediate. Since such a technique is integrative in nature, Dec was unable to be more specific about the location of ignition apart from that it occurred somewhere in the fuel vapor and air mixture.

Dec [30] having observed ignition starting in the rich fuel-air mixture is supported by other experimental work and numerical simulation. Vogel, et al. [19] conducted experiments in which a diesel fuel surrogate (n-decane) was injected into a hot (720 K), high-pressure (73 bar) chamber. Planar laser Rayleigh scattering was used to image concentration of fuel vapor prior to, during, and following autoignition. The resulting images (see Figure 8 in [19]) show a relatively homogenous rich mixture of n-decane vapor and air igniting near the jet centerline, then exhibiting a combustion wave that propagates from the ignition location, outward toward the ambient [19]. Gopalakrishnan and Abraham [31] conducted transient constant-volume axisymmetric simulations of an n-heptane spray into a high-pressure chamber containing hot air and compared the results to experimental work. Ignition was observed to start in a rich mixture with mixture fraction $\phi \approx 3$.

1.3. Isolated Droplet Ignition and Combustion

This section contains a number of topics important to the study of isolated droplet ignition and combustion. First, a phenomenological description of isolated droplet ignition and combustion is presented with the purpose of familiarizing the reader with the relevant concepts. Second, a review of classical droplet combustion theory follows which yields the widely-known d^2-law, and analytical expressions for rate of fuel consumption, flame location, and flame temperature during quasi-steady droplet combustion. Third, in order to predict
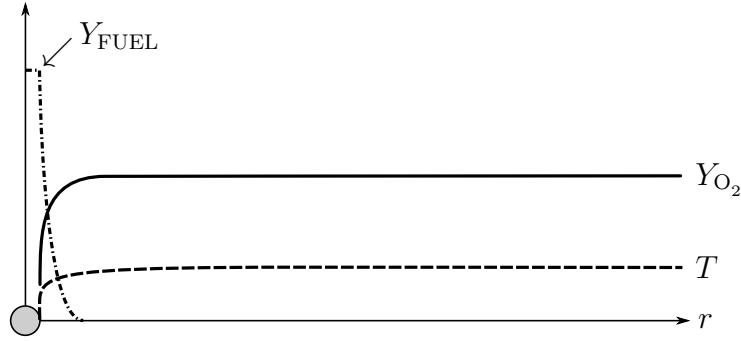
FIGURE 1.4. Plot showing radial profiles of fuel, oxygen, and temperature for a droplet in a hot ambient at initial time.

the onset of ignition, it is necessary to leave classical theory behind and apply asymptotic analysis to droplet combustion.

1.3.1. PHENOMENOLOGICAL DESCRIPTION OF SPHERICALLY-SYMMETRIC ISOLATED DROPLET AUTOIGNITION AND COMBUSTION. For the purpose of explaining the important stages of isolated droplet ignition and combustion, imagine a relatively cold ($\sim$300 K) fuel droplet suddenly appearing in a large volume of relatively hot ($\sim$1000 K) air. The diameter of the droplet is approximately 300 microns and we assume the absence of a gravitational field so buoyancy effects are neglected. As such, all mass and energy transport is purely radial; there are no circumferential or azimuthal components for any quantity or derivative. In other words, the domain is spherically symmetric with the origin at the center of the droplet. This means only a single (radial) spatial variable and time is required to describe some quantity

Figure 1.4 shows a drawing of a plot containing profiles of fuel mass fraction, oxygen mass fraction, and temperature shortly after the appearance of the droplet in the hot ambience. The gray circle represents the physical extent of the droplet, and the horizontal axis of the plot is radial distance. The vertical axis is magnitude of mass fraction or temperature. The profile for mass fraction of fuel Y_{FUEL} shows that a small amount of liquid fuel has evaporated

and the resultant vapor diffused away from the droplet surface. This is apparent because the Y_{FUEL} curve does not fall to zero until a short distance away from the droplet surface. (The mass fraction of fuel at the droplet surface is determined by the assumption of vapor-liquid equilibrium.) Correspondingly, the profile for mass fraction of molecular oxygen Y_{O_2} declines as it approaches the surface of the droplet. The temperature profile T is uniform until it approaches the cold droplet. This indicates that heat is being transported from the hot ambient to the droplet. We will arbitrarily declare the state depicted in Figure 1.4 as initial time ($t = 0$). Figure 1.5 contains a drawing of a sequence of plots which show the evolution of fuel, oxygen, and temperature profiles for the droplet with increasing time ($t > 0$).

Figure 1.5A shows the droplet just at the onset of ignition, which occurs at approximately $t = 10$ to 20 ms for reactive fuels such as n-heptane. Starting at initial time and prior to this state in Figure 1.5A, thermal energy diffuses from the hot ambient and is absorbed by the cold liquid droplet. Most of the transported thermal energy goes into evaporating the liquid fuel, with the remainder diffusing into and heating the interior of the liquid droplet. One can discern the thermal diffusion of heat into the liquid droplet because the ambient is slightly cooler in Figure 1.5A as shown by the T curve. Fuel vapor created by evaporation at the droplet surface diffuses radially outward into the ambient, and in doing so, becomes mixed with oxidizer (typically air). The diffusion of fuel vapor away from the droplet is reflected by the Y_{FUEL} curve extending further from the droplet surface in Figure 1.5A as compared to that at initial time in Figure 1.4. The most notable feature of Figure 1.5A is the dip in oxygen and bump in temperature seen right of center. The small, localized increase in temperature is caused by exothermic chemical reactions. Although the Y_{FUEL} curve appears to show that the fuel concentration at this location is apparently zero, there

21
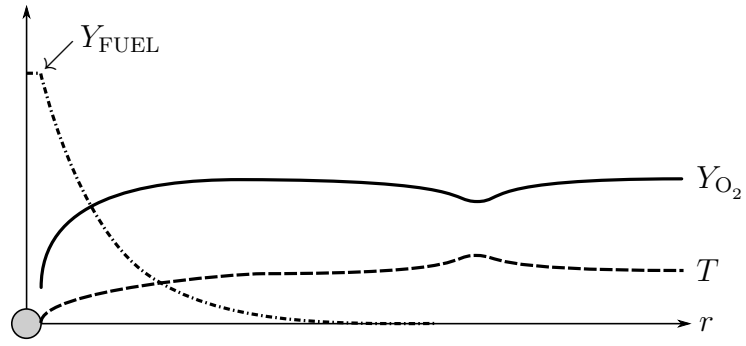
(A) Thermal runaway begins far from droplet surface.
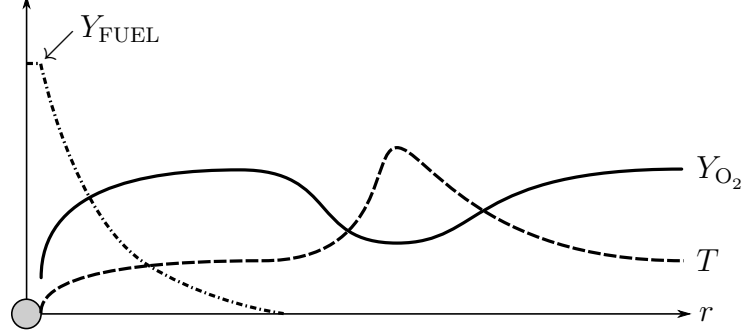
(B) The reaction wave propagates inward toward the droplet surface.
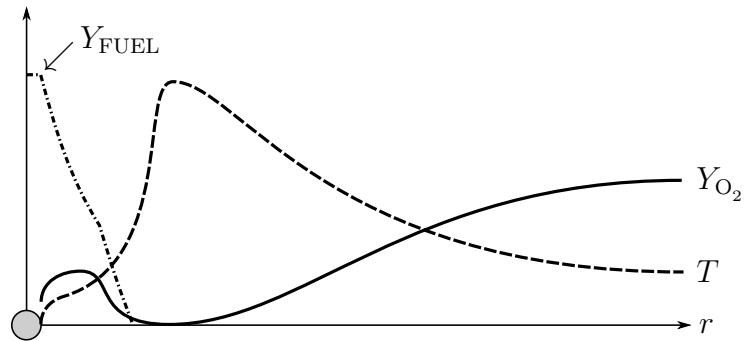
(C) The premixed fuel and air are nearly exhausted.
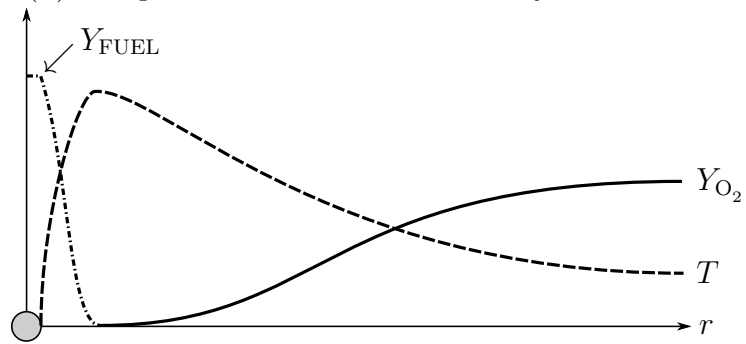
(D) Non-premixed phase of combustion.

FIGURE 1.5. A series of plots show generic profiles of fuel, oxygen, and temperature at key stages of spherically-symmetric droplet autoignition and combustion.

is nonetheless a minuscule amount of fuel that has reached this region via mass diffusion. This fuel, having traveled so far, has spent sufficient time in the hot, oxygen-rich region away from the droplet for a series of temperature-sensitive reactions to begin. The first of these reactions are endothermic and possible only once a certain energy threshold is met. Once the energy requirement is overcome by enthalpy from the hot ambient, a chemical chain reaction is initiated in which exothermic reactions start to dominate the endothermic ones. In the early stages of the chain reaction, these exothermic reactions create a localized heating as shown in Figure 1.5A. This local increase in temperature increases the rate of the exothermic reactions so that thermal energy is released even faster. This in turn increases reaction rates even more. The self-perpetuating cycle of chemical reactions and heat release is termed 'thermal runaway' and is the basis of spontaneous thermal ignition (autoignition).

The state shown in Figure 1.5B occurs very soon after that of Figure 1.5A: perhaps several hundred microseconds later. During this stage, thermal runaway is creating higher and higher temperatures which results in faster and faster chemical reactions. The temperature peak is well above ambient and can be assumed to correspond to the location of the flame. Also notice the region of peak temperature has moved inward toward the droplet surface. As fuel is depleted, the wave of chemical reactions propagates toward increasing fuel concentration. A point worth reinforcing is that the flame is propagating through premixed fuel and air. This is apparent because the Y_{FUEL} and Y_{O_2} curves are nonzero between the droplet and flame. Moreover, judging by the fact that the Y_{FUEL} curve is very small at the point of maximum temperature, the mixture is very lean.

The speed of flame propagation is such that the state depicted in Figure 1.5C occurs only a few hundred microseconds after the preceding state in Figure 1.5B. Only a small amount

of premixed fuel and air remains as shown by the presence of molecular oxygen between the droplet surface and the flame. For the first time, the Y_{O_2} curve has reached a nominal value of zero, which suggests the rate of reactions in the flame have reached or are very near the maximum possible. The peak temperature in the flame has achieved its maximum value as shown by the T curve. Furthermore, recall the flame is spherical in shape meaning that the area of the flame is decreasing with the square of the flame radius.

In Figure 1.5D, the premixed fuel and air has been exhausted and combustion has transitioned to a non-premixed, transport-limited flame. The flame is supported by fuel vapor diffusing from the droplet surface to the flame and by fresh oxidizer diffusing inward from the ambient. The temperature of the flame is slightly lower than the previous state because the freshly-evaporated fuel leaving the droplet surface is colder than the pre-heated fuel available during the premixed combustion phase. Although not depicted here, the products of combustion such as water, CO_2, and oxides of nitrogen diffuse away from the flame into the ambient. This non-premixed configuration will remain until the fuel is exhausted or the flame extinguished.

Notice that in all of the states shown in Figure 1.5 the values for Y_{O_2} and T at the far end of the radius axis remained unchanged. This is a trait of all spherically-symmetric domains. Despite the presence of radial heat and mass fluxes caused by the chemical reactions in the flame, in the far field all quantities asymptote to the values they held at initial time. This feature simplifies defining boundary conditions for computer simulations of droplet ignition and combustion.

1.3.2. CLASSICAL DROPLET COMBUSTION THEORY: REACTION-SHEET LIMIT. After the initial transient autoignition, combustion of the gas-phase surrounding the droplet proceeds in a quasi-steady manner during which the fuel evaporated from the surface is balanced by that consumed in the flame ($m_v = m_c$) and the radial profiles of temperature T, fuel mass fraction Y_F, and oxygen mass fraction Y_O remain roughly constant when the radial coordinate is normalized by the time-dependent droplet radius, $r/r_s(t)$. The reason combustion following transient autoignition is termed quasi-steady is that the recession of the droplet surface due to evaporation is sufficiently slow compared to the flux of gas-phase species, that gas-phase transport can be assumed to be steady.

Consider the schematic drawing of quasi-steady liquid fuel droplet combustion found in Figure 1.6. The liquid fuel in the droplet evaporates and diffuses radially outward to the flame (dashed circle). The mass fraction of the fuel is indicated by the heavy dark contour. Oxidizer from the ambient diffuses inward to the flame from the far field and reacts (combusts) with the fuel. The mass fraction of oxygen is indicated by the heavy dashed contour. There is chemical heat release which raises the temperature as shown by the thin solid line. Products of combustion like carbon dioxide, water, and oxides of nitrogen diffuse radially outward into the ambient. Some useful results can be obtained if one assumes the activation energy is a large quantity. This assumption is called the reaction sheet limit and is the foundation upon which classical droplet combustion theory is built. When the activation energy is very high, the region over which the chemical reactions take place becomes a very thin planar structure, like a sheet.

The following derives the bulk parameters mass consumption rate, radius of the flame, and flame temperature for quasi-steady droplet combustion in the reaction sheet limit. Then,
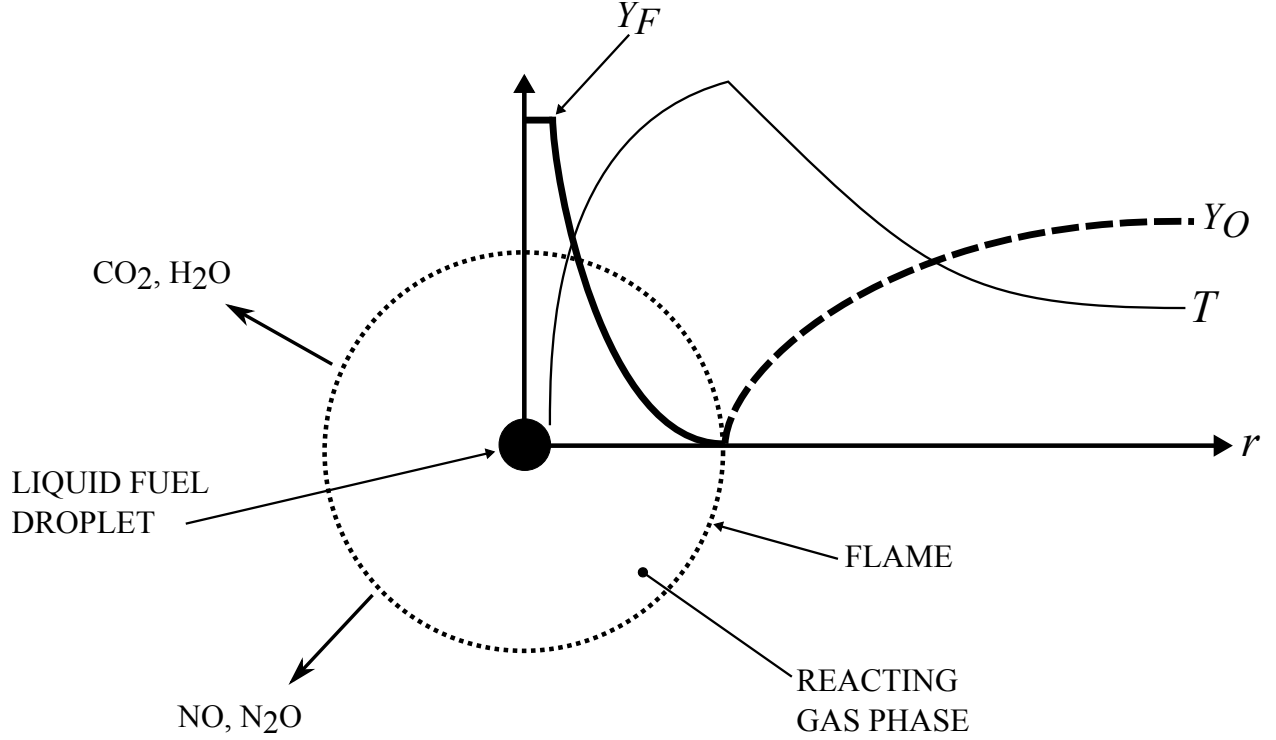
FIGURE 1.6. A schematic drawing of quasi-steady droplet combustion in the reaction sheet limit with temperature profile, reactant mass fraction profiles, and product fluxes.

using the bulk parameters, profiles for temperature and reactant mass fraction are obtained. Finally, the classic d-squared law of quasi-steady droplet combustion is derived. The remainder of this section follows Law and others [24, 32, 33, 34, 35, 36, 37, 38].

The rate at which fuel is consumed by combustion in a droplet is obtained by integration of the continuity equation:

$$m_c = 4\pi r^2 \rho u \tag{3}$$

where ρ and u are density and radial flow velocity, respectively. Normalized mass combustion rate is given by

$$\tilde{m}_c \equiv \frac{m_c}{4\pi(\lambda/c_p)r_s}, \tag{4}$$

26

where λ is thermal conductivity and c_p the specific heat at constant pressure. The quotient (λ/c_p) is assumed to be constant in this analysis. The radial spatial variable is normalized by the radius of the droplet:

$$\tilde{r} \equiv \frac{r}{r_s}, \tag{5}$$

so that at the droplet surface $\tilde{r} = 1$ and at the flame location, $\tilde{r}_f = r_f/r_s$. The mass fraction of oxidizer is normalized by the stoichiometric mass ratio of oxidizer to fuel:

$$\tilde{Y}_O \equiv \frac{Y_O}{\sigma_O}. \tag{6}$$

Extending the same logic to the fuel mass fraction simply results in:

$$\tilde{Y}_F \equiv Y_F. \tag{7}$$

Heat released by combustion is normalized by the latent heat of vaporization of the fuel:

$$\tilde{q}_c \equiv \frac{q_c}{q_v}. \tag{8}$$

Finally, normalized temperature is given by

$$\tilde{T} \equiv \frac{c_p\, T}{Y_{F,s}\, q_c}, \tag{9}$$

where the quantity $Y_{F,s}\, q_c/c_p$ is the temperature rise resulting from the combustion of a homogenous fuel-air mixture with fuel mass fraction $Y_F = Y_{F,s}$. Subscripts s (as in eqn. 9) and ∞ respectively indicate a quantity at the droplet surface and far field ambience.

27

The coupling function or Shvab-Zel'dovich formulation of conservation equations is an important tool in mathematical combustion analysis. The principle lies in the fact that, for equivalent thermal diffusivity and mass diffusivity (unity Lewis number), the sum of temperature and mass fraction is a conserved scalar. Therefore, conservation equations for coupling functions of temperature and species, $\beta_i = T + Y_i$, can be formulated and solved, yielding useful results.

Steady spherically-symmetric conservation equations for coupling functions for oxidizer and fuel in a convective-diffusive environment are given by:

$$\frac{d}{d\tilde{r}}\left(\tilde{m}_c\beta_i - \tilde{r}^2\frac{d\beta_i}{d\tilde{r}}\right) = 0, \quad i = O, F, \tag{10}$$

and have the following boundary conditions:

$$\tilde{r} \to \infty: \qquad \tilde{Y}_O = \tilde{Y}_{O,\infty}, \quad \tilde{Y}_F = 0, \quad \tilde{T} = \tilde{T}_\infty \tag{11}$$

$$\tilde{r} = 1: \qquad \tilde{m}_c\tilde{Y}_{O,s} - \left(\frac{d\tilde{Y}_O}{d\tilde{r}}\right)_1 = 0, \quad \tilde{m}_c\tilde{Y}_{F,s} - \left(\frac{d\tilde{Y}_F}{d\tilde{r}}\right)_1 = \tilde{m}_c$$

$$\left(\frac{d\tilde{T}}{d\tilde{r}}\right)_1 = \tilde{m}_c\tilde{q}_v, \quad \tilde{T} = \tilde{T}_s. \tag{12}$$

Equations (10) through (12) comprise a second order linear boundary value problem for the coupling functions β_i whose solutions are the coupling functions for oxidizer and fuel, respectively:

$$\beta_O = \tilde{T} + \tilde{Y}_O = (\tilde{T}_s - \tilde{q}_v) + \left\{[\tilde{T}_\infty - (\tilde{T}_s - \tilde{q}_v)] + \tilde{Y}_{O,\infty}\right\}e^{-\tilde{m}_c/\tilde{r}}, \tag{13}$$

$$\beta_F = \tilde{T} + \tilde{Y}_F = [1 + (\tilde{T}_s - \tilde{q}_v)] + \left\{\tilde{T}_\infty - [1 + (\tilde{T}_s - \tilde{q}_v)]\right\}e^{-\tilde{m}_c/\tilde{r}}. \tag{14}$$

These coupling functions are used to obtain bulk parameters of the spherical flame: mass burning rate m_c, flame location r_f, and flame temperature T_f.

Here, it is assumed the activation energy is relatively large, causing chemical reactions to be confined to a narrow sheet (i.e., a thin flame). Furthermore, it is assumed that the chemical reactions which occur at the sheet completely consume fuel and oxidizer. Formally, this means that the mass fraction of fuel and oxidizer are both zero at the flame:

$$\tilde{Y}_F(\tilde{r}_f) = 0, \quad \tilde{Y}_O(\tilde{r}_f) = 0. \tag{15}$$

The absence of oxygen at the droplet surface is also implied:

$$\tilde{Y}_O(1) = 0. \tag{16}$$

This is reasonable since it was just established above that oxygen is completely consumed in the flame. Substituting equations (15) and (16) into (13) and (14) results in the following equations from which mass burning rate, flame sheet location, and flame temperature can be determined:

$$\tilde{m}_c = \ln\left(1 + \frac{c_p(T_\infty - T_s) + (Y_{O,\infty}/\sigma_O)q_c}{q_v}\right), \tag{17}$$

$$\tilde{r}_f = \frac{\tilde{m}_c}{\ln(1 + \tilde{Y}_{O,\infty})} = 1 + \frac{\ln[1 + (\tilde{T}_f - \tilde{T}_s)/\tilde{q}_v]}{\ln(1 + \tilde{Y}_{O,\infty})}, \tag{18}$$

$$T_f = \frac{T_s + AT_\infty + (q_c - q_v)/c_p}{1 + A}, \tag{19}$$

where,

$$A = \sigma_O\left(1 + \frac{1 - Y_{O,\infty}}{Y_{O,\infty}}\right). \tag{20}$$

Consider Equation (18) which describes the normalized radial location of the flame for quasi-steady spherically symmetric droplet combustion in the reaction sheet limit. The fact that the normalized radial flame location is defined in a quasi-steady system means that $\tilde{r}_f$ is constant.

Having obtained the bulk parameters above, profiles for temperature and species over the spherically-symmetric combustion domain can now be obtained. As discussed above, the reaction sheet assumption means no leakage of reactants through the flame, this implies two concepts. First, there is no oxygen between the droplet surface and the flame. Second, there is no fuel vapor between the flame and the far field. Formally, these can be written as:

$$\tilde{Y}_O = 0, \quad 1 \leq \tilde{r} \leq \tilde{r}_f \tag{21}$$

$$\tilde{Y}_F = 0, \quad \tilde{r}_f \leq \tilde{r} \leq \infty. \tag{22}$$

Applying equation (21) to equation (13) yields the temperature profile between the droplet surface and flame. Similarly, the temperature profile for the region outside of the flame is obtained by applying equation (22) to (14). Thus, the temperature profile over the whole domain is:

$$\tilde{T}^- = (\tilde{T}_b - \tilde{q}_v) + \left(\tilde{T}_\infty - \tilde{T}_b + \tilde{q}_v + \tilde{Y}_{O,\infty}\right) e^{-\tilde{m}_c/\tilde{r}}, \qquad 1 \leq \tilde{r} \leq \tilde{r}_f, \tag{23}$$

$$\tilde{T}^+ = (\tilde{T}_b - \tilde{q}_v + 1) + \left(\tilde{T}_\infty - \tilde{T}_b + \tilde{q}_v - 1\right) e^{-\tilde{m}_c/\tilde{r}}, \qquad \tilde{r}_f \leq \tilde{r} \leq \infty, \tag{24}$$

where it has been assumed the droplet surface temperature is equivalent to the boiling temperature of the liquid fuel, $T_s = T_b$. Although T_s can be determined by way of the

Clausius-Clapeyron relation, it is often unnecessary since chemical heat release typically overwhelms any enthalpy contribution by T_s.

With the temperature field known, profiles of mass fraction can be determined. Substituting Equation (24) into (13), and (23) into (14) yields equations for mass fractions for fuel and oxidizer, respectively:

$$\tilde{Y}_F = 1 - \left(1 + \tilde{Y}_{O,\infty}\right) e^{-\tilde{m}_c/\tilde{r}}, \qquad\qquad 1 \leq \tilde{r} \leq \tilde{r}_f \qquad (25)$$

$$\tilde{Y}_O = -1 + \left(1 + \tilde{Y}_{O,\infty}\right) e^{-\tilde{m}_c/\tilde{r}}, \qquad\qquad \tilde{r}_f \leq \tilde{r} \leq \infty. \qquad (26)$$

The bulk parameters of droplet combustion have been determined. Now an expression to relate mass consumption to droplet surface regression can be obtained. We begin by equating Equations (4) and (17) and solving for m_c to obtain:

$$m_c = 4\pi(\lambda/c_p)r_s \cdot \ln\left(1 + \frac{c_p(T_\infty - T_s) + (Y_{O,\infty}/\sigma_O)q_c}{q_v}\right). \qquad (27)$$

The rate of fuel vaporization m_v is, by definition, the time rate of change of droplet mass:

$$m_v \equiv -\frac{d}{dt}\left(\frac{4}{3}\pi r_s^3\right). \qquad (28)$$

Since we have established that the chemical reactions in the flame are sufficiently vigorous to consume all of the reactants, all vaporized fuel must be consumed by combustion, meaning $m_c = m_v$. Using this fact, we can equilibrate Equations (27) and (28) resulting in the following:

$$-\frac{d}{dt}\left(\frac{4}{3}\pi r_s^3\right) = 4\pi(\lambda/c_p)r_s \cdot \ln\left(1 + \frac{c_p(T_\infty - T_s) + (Y_{O,\infty}/\sigma_O)q_c}{q_v}\right). \qquad (29)$$

Equation (29) can be simplified and manipulated to achieve this form:

$$\frac{dr_s^2}{dt} = -K_c \tag{30}$$

where K_c is the burning rate constant for a droplet:

$$K_c = 2\frac{(\lambda/c_p)}{\rho_\ell} \cdot \ln\left(1 + \frac{c_p(T_\infty - T_s) + (Y_{O,\infty}/\sigma_O)q_c}{q_v}\right). \tag{31}$$

Equation (30) is integrated and, using the initial condition $r_s(t=0) = r_{s,\circ}$, one obtains:

$$r_s^2 = r_{s,\circ}^2 - K_c t, \tag{32}$$

which is in terms of the droplet radius. An equation in terms of the droplet diameter is obtained simply by making the substitution $r^2 = d^2/4$ to yield:

$$d^2 = d_\circ^2 - 4K_c t. \tag{33}$$

Equation (33) is the d^2-law for combustion of a fuel droplet. It is interpreted as meaning that the square of the diameter of a burning droplet will decrease linearly with time.

1.3.3. ASYMPTOTIC ANALYSIS OF DROPLET COMBUSTION: IGNITION. The treatment above, which resulted in determination of $\tilde{m}_c$, $\tilde{r}_f$, T_f, and profiles for $\tilde{Y}_F$ and $\tilde{Y}_O$, used the flame-sheet limit in which chemical reactions are assumed to occur infinitely fast in comparison to transport of reactants and heat. In order to understand and predict ignition and extinction phenomena, it is necessary to discard the reaction sheet limit and examine the reaction zone with finite rate chemistry. Such an analysis utilizes the structure equations

of nonpremixed flames which are obtained using perturbation methods. The discussion in this section follows Law [24, 39]

Consider the energy conservation equation for a spherically-symmetric domain in which it is assumed the chemistry is described as being one-step overall and the reaction second-order:

$$\frac{\tilde{m}}{\tilde{r}^2}\frac{d\tilde{T}}{d\tilde{r}} - \frac{1}{\tilde{r}^2}\frac{d}{d\tilde{r}}\left(\tilde{r}^2\frac{d\tilde{T}}{d\tilde{r}}\right) = Da_c\,\tilde{Y}_O\tilde{Y}_F\,e^{-\tilde{T}_a/\tilde{T}}. \tag{34}$$

The convection term can be eliminated by a change of spatial variable:

$$\xi \equiv 1 - e^{-\tilde{m}/\tilde{r}}, \tag{35}$$

so the domain $\tilde{r} = (1, \infty)$ is mapped to $\xi = (\xi_s, 0)$ and equation (34) becomes

$$\frac{d^2\tilde{T}}{d\xi^2} = -Da_c\left[\frac{\tilde{m}^2}{(1-\xi)^2[\ln(1-\xi)]^4}\right]\tilde{Y}_O\tilde{Y}_F\,e^{-\tilde{T}_a/\tilde{T}}, \tag{36}$$

with the following boundary conditions:

$$\tilde{T}(0) = \tilde{T}_\infty \tag{37}$$

$$\tilde{T}(\xi_s) = \tilde{T}_s. \tag{38}$$

Equation (36) with boundary conditions (37) and (38) comprise a linear second order boundary value problem in $\tilde{T}$. The mapping of Equation (34) to (36) is involved but ingenious; the procedure is presented in Appendix A.

Consider a cold liquid fuel droplet which suddenly appears in a hot (say, 1000°C) oxidizer ambience. Vaporized fuel will diffuse and convect away from the droplet surface and mix with the oxidizer. Ignition is expected to occur spontaneously out in the furthest reaches

of the fuel vapor cloud where temperature is highest, thereby inducing the most active chemistry between fuel and oxidizer. The temperature of this chemically-active region, called the reaction zone, is described by perturbing the energy Equation (36). This leads to an equation for the $\mathcal{O}(1)$ perturbation function θ given by

$$\frac{d^2\theta}{d\chi^2} = -\Delta\frac{(\chi - \theta)}{\chi^4}e^{(\theta - \beta_v\chi)}, \tag{39}$$

$$\theta(0) = 0, \tag{40}$$

$$\left(\frac{d\theta}{d\chi}\right)_\infty = 0, \tag{41}$$

where

$$\Delta = \left(\frac{\tilde{m}_{v,0}}{\tilde{T}_\infty^2/\tilde{T}_a}\right)^2 Da_c\,\tilde{Y}_{O,\infty}\,e^{-\tilde{T}_a/\tilde{T}_\infty}, \tag{42}$$

is the reduced Damköhler number with $m_{v,0}$ the rate of fuel vaporization in the frozen (chemistry-free) limit. The beta variable in the exponent of (39) is defined as

$$\beta_v = (\tilde{T}_\infty - \tilde{T}_s) + \tilde{q}_v \tag{43}$$

and can be thought of as the enthalpy driving potential, with the bracketed term the ambience contribution and the $\tilde{q}_v$ term that of the heat of vaporization of the liquid fuel. The derivation of Equation (39) from (36) is lengthy and is found in Appendix B.

Equation (39) is a second order differential equation and nonlinear in θ; it is not known to have an analytic solution. The solution, which can be determined numerically, provides the ignition turning point from which the ignition Damköhler number $\Delta_I(\beta_v)$ is determined. However, a numerical solution is not necessary to assess ignitability since a quite good

approximation to $\Delta_I(\beta_v)$ was derived by Makino [40] and is shown here:

$$\Delta_I(\beta_v) = 0.5 \left[\frac{4}{e(1 - \beta_v)} \right]^4 - 0.6 \left[\frac{4}{e(1 - \beta_v)} \right]^2 . \tag{44}$$

Thus, a droplet will ignite when Δ exceeds $\Delta_I(\beta_v)$. Physically, this means the droplet will ignite if the transport of fuel vapor is such that there is sufficient residence time for chemical reactions of a certain rate to proceed. In the case of droplet ignition, it will be seen in the computational results that the condition $\Delta > \Delta_I(\beta_v)$ is met by fuel vapor that diffuses from the droplet surface to far out into the ambient where the mixture is very lean and nearly as hot as the far-field ambient. The criteria for ignition are met because: (1) the fuel vapor has experienced along residence time in an oxidizer while traveling, (2) the relatively high temperature of the mixture makes the reactions sufficiently fast that the fuel vapor has time to react with the oxidizer. Therefore, autoignition in droplets will occur in the relatively hot, lean region far from the droplet surface.

1.4. Liquid Fuel Combustion

The names, formulae, and skeletal diagrams of the six liquid fuels examined in the research conducted for this thesis appear in Figure 1.7. They were selected as being representative of three principal classes of fuels: methyl esters, alcohols, and pure hydrocarbons. Methyl butanoate and methyl decanoate are methyl esters, and are surrogate fuels for biodiesel. They are characterized by an oxygen-containing ester group which appears on the right end of the skeletal diagrams in Figure 1.7 (A) and (B). Biodiesel fuels are typically comprised of methyl esters that are larger than methyl butanoate and methyl decanoate,

TABLE 1.2. Physical properties for the fuels examined in the experiments and simulations. Unless otherwise indicated, values were taken from the *CRC Handbook of Chemistry and Physics*, 94th edition., 2013-2014.

Property	Methyl Butanoate $C_5H_{10}O_2$	Methyl Decanoate $C_{11}H_{22}O_2$	n-Heptane C_7H_{16}	Methanol CH_3OH	Ethanol C_2H_5OH	1-Propanol C_3H_7OH
Molecular Mass, [g/mol]	102.1	186.3	100.2	32.0	46.1	60.1
Boiling Temperature, [K]	376	506	372	338	352	370
Density (298K), [kg/m^3]	898.4[a]	873.0	676.7[a]	784.6[a]	789.3	799.7
Specific Heat (liq. @ 298K), $C_{p,\ell}$ [kJ/(kg·K)]	1.94[a]	2.06[a]	2.25[a]	2.56[a]	2.43	2.40
Thermal Conductivity, [W/(m·K)]	0.140	0.115[b]	0.131[a]	0.202	0.167	0.154
Heat of Vaporization, [kJ/kg]	385[a]	359[a]	365[a]	1156[a]	837	689
Heat of Combustion, [MJ/kg]	28.9	36.7	48.1	22.7	29.7	33.6
Stoichiometric Coefficient	6.5	15.5	11	1.5	3	4.5
Adiabatic Flame Temp, [K] $\phi = 1.05$	2259[c]	2283[c]	2294[c]	2234[c]	2251[c]	2268[c]
Cetane Number, CN	6[d]	48[e]	58[e]	3[e]	11[e]	12[e]

a: From Reference [41].

b: Estimated using method found in Section 10.44 of Reference [42].

c: Determined by conducting a gas-phase, homogenous, constant-pressure, autoigniting mixture simulation in CHEMKIN.

d: From Reference [13].

e: From Reference [43].

36

(A) Methyl butanoate: $C_5H_{10}O_2$

(B) Methyl decanoate: $C_{11}H_{22}O_2$

(C) Methanol: CH_3OH

(D) Ethanol: C_2H_5OH

(E) 1-Propanol: C_3H_7OH

(F) n-Heptane: C_7H_{16}
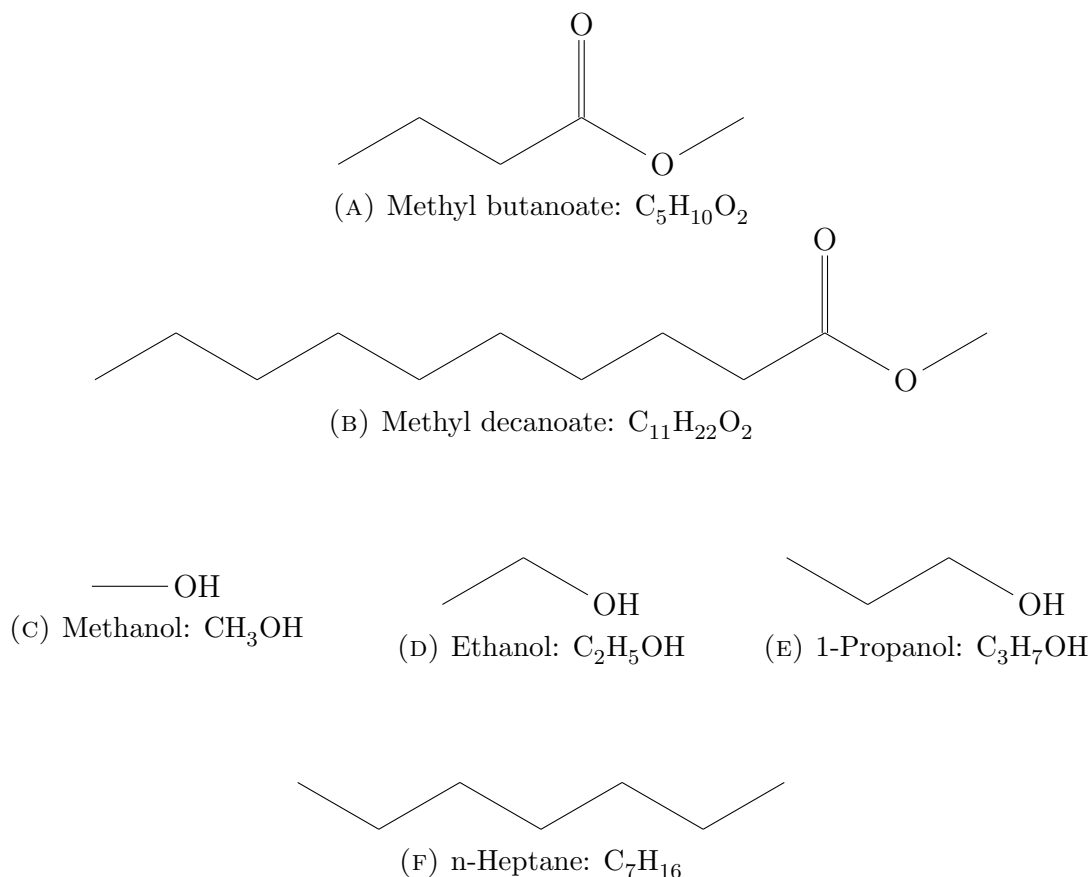
FIGURE 1.7. Skeletal diagrams of the fuels used in the experiments and computer simulations of isolated droplet ignition and combustion.

such as methyl oleate: $C_{19}H_{36}O_2$. However, such a compound is more computationally expensive to simulate because its chemical kinetic mechanism is correspondingly larger. For example, a detailed mechanism for methyl oleate has 3500 species and 17,000 reactions [44], making computations (apart from transient, zero-dimensional domains) beyond the capability of most accessible computer technology. On the other hand, chemical mechanisms for methyl butanoate and methyl decanoate, with a few hundred species and several hundred reactions, are accessible to modern high-performance desktop PC's or modest LINUX servers. Regardless, both methyl butanoate and methyl decanoate contain an ester group just as methyl oleate does, so presumably they should, at the very least, exhibit chemistry that is specific to ester-containing fuels.

Three alcohols were selected for this study: methanol, ethanol, and 1-propanol. Methanol was selected because it is the smallest oxygenated hydrocarbon fuel and has been relatively well studied: e.g., [45, 46, 47, 48, 49, 32]. Ethanol accounts for a substantial fraction of the transportation fuel consumption in the United States in the form of "E10" and "E85" fuel. It is especially prevalent in the plains states where corn production (the grain of which is the primary feedstock) is significant. Ethanol is a mediocre transportation fuel because it is hydrophilic and has a substantially lower heating value per unit volume compared to gasoline ($\sim$30% lower [50]). On the other hand, ethanol has a relatively high octane number which makes it well suited for high-compression, turbocharged, or supercharged engines. Normal propanol was selected as an example of a longer-chain alcohol.

Normal heptane (n-heptane) was selected for simulation because it is a pure hydrocarbon and the chemical mechanism for it has been well developed and vetted by experts in the combustion research community [18, 31, 47, 51, 52, 53, 54, 55, 56, 57, 58, 59]. Normal heptane also happens to have a number of physical properties which are remarkably similar to those of methyl butanoate, thereby facilitating comparison of combustion behavior between the two fuels.

A summary of physical properties of the fuels studied are found in Table 1.2. Only three of the fuels were simulated: methyl butanoate, n-heptane, and methanol. However, all six were included in the laser spectroscopy experiments. As noted in the previous paragraph, n-heptane and methyl butanoate share some similar physical properties: compare molecular mass, boiling temperature, heat of vaporization, and adiabatic flame temperature in Table 1.2.

1.5. Research Questions and Hypotheses

The work presented herein was born out of a desire to better understand increased NO_x emissions from diesel engines fueled by biodiesel. The work of Mueller, et al. [11] lead to the formulation of research questions that are summarized here:

(1) If the Mueller explanation for increased NO_x in biodiesel-fuled engines is correct, would not all oxygenated fuels produce greater NO_x emissions in diesel engines?

(2) Mueller's theory only considers Zel'dovich NO_x chemistry. What is the relative importance of Fenimore and N_2O path chemistry to overall NO_x formation?

(3) Is there something unique to methyl ester combustion chemistry during the premixed burn phase that promotes the formation of Fenimore NO_x precursors?

(4) Since ignition of a single liquid fuel droplet shares much of the relevant physics with ignition of a diesel spray, would experiments and modeling of single droplet ignition be effective for evaluating the role of Zel'dovich and Fenimore NO_x chemistry on NO_x formation during the premixed burn phase of oxygenated diesel fuel combustion?

In order to address the above research questions, an experimental, numerical, and theoretical investigation was conceived in which the subject of research was not diesel sprays, but rather ignition of isolated spherically-symmetric fuel droplets. By examining droplet ignition instead of diesel sprays, the significant challenges of implementing experiments on and conducting numerical modeling of diesel sprays was avoided. Thinking of droplet ignition as being analogous to diesel spray ignition is not unreasonable because the two systems share important physical processes. The objective of the investigation was to address the following three hypotheses:

HYPOTHESIS (1):

Autoignition of spherically-symmetric isolated droplets can be used as a physical model for a diesel spray to investigate NO_x formation in the premixed autoignition zone of a diesel spray.

HYPOTHESIS (2):

If the increased NO_x formation in biodiesel is a consequence of a leaner (but still rich) premixed autoignition zone, all oxygenated droplets should exhibit increased NO_x during their premixed burn phase.

HYPOTHESIS (3):

If the increased NO_x observed in biodesel is a consequence of unique chemical kinetics for methyl esters (e.g., enhanced Fenimore NO_x) during the premixed burn phase, only methyl ester droplets will exhibit increased NO_x during the premixed burn phase.

The first hypothesis speaks to a decades-old assumption among researchers who focus on droplets that igniting droplets are a good physical analogy to ignition phenomena in a diesel spray. The assumption is not unreasonable because many physical processes that are important to ignition phenomena and emissions formation are shared by the two physical systems. In this work, droplet ignition and diesel spray ignition are examined from a theoretical perspective to assess the viability of the analogy.

The second hypothesis grows out of the explanation proposed by Mueller, et al. [11] for increased NO_x formation in biodiesel-fueled engines compared to that formed when fueled by petroleum diesel. Mueller suggested fuel-bound oxygen in biodiesel caused the premixed autoignition zone (premixed burn fraction) to be slightly less rich, which leads to a higher

flame temperature, therefore enhancing Zel'dovich NO_x formation. Biodiesel is comprised of methyl esters which contains two fuel-bound oxygen atoms in the ester group of each molecule. However, there is no reason that any oxygenated fuel would cause the same result, even if the fuel were not methyl esters. For example, a mixture of 5% methanol and 95% petroleum diesel should produce more NO_x just like any biodiesel would. A comparison of overall NO_x formation among numerical simulations of droplets comprised of a pure alkane, methyl ester, and alcohol with Zel'dovich NO_x chemistry would test Hypothesis 2.

The third hypothesis is based on the premise that increased NO_x emissions from biodiesel-fueled engines is rooted in the molecular structure of fatty acid methyl ester (FAME) biodiesel. For example, the presence of double bonds among carbon atoms in a FAME molecule may increase formation of CH which could lead to enhanced Fenimore NO_x because CH is an important precursor to that NO_x mechanism [60]. A further possibility is enhanced Fenimore NO_x by way of the C_2O radical [13, 14, 15, 16, 17] whose production may be linked to ester group chemistry of the FAME molecule [61, 62]. The presence of double bonds and ester groups are unique to methyl esters like methyl butanoate and methyl decanoate, so it is expected that if one or both of these enhanced Fenimore NO_x theories are correct, that only the methyl esters will exhibit increased NO_x and not other oxygenated fuels like alcohols, nor pure alkanes like n-heptane.

1.6. Organization of Dissertation

This dissertation presents results of an effort to investigate the autoignition and combustion of isolated liquid fuel droplets in a hot ambient. The research was motivated by the need to better understand the formation of oxides of nitrogen (NO_x) emissions in compression-ignition (diesel) engines, specifically when such engines are fueled by oxygenated fuels such

as biodiesel. The foundational premise of the work was that autoignition and combustion of isolated liquid fuel droplets is a reasonable a physical model for autoignition and combustion in diesel engines. Were this a viable concept, it would obviate the need for difficult and expensive in-cylinder measurements and simulations to study autoignition, combustion, and NO_x formation in diesel sprays. Instead, experiments and simulations could be conducted on droplets with much greater ease and affordability. The research effort was threefold. First, simulations using a previously-developed spherically symmetric droplet autoignition and combustion code were conducted. Second, laser diagnostics were used to measure profiles of hydroxyl (OH) and nitric oxide (NO) species in freely-falling droplet flames. Third, the viability of the droplet physical model for diesel spray was evaluated from a theoretical standpoint.

In Chapter 2, the technique used to perform computer simulations of spherically-symmetric autoignition and combustion of isolated liquid fuel droplets is described. A code was utilized that was developed previously by the Dryer group of Princeton University. The kinetic mechanisms which comprised the chemical reaction input data for the code were created as part of the dissertation research by combining established fuel mechanisms with NO_x chemistry taken from a gaseous fuel mechanism. The fuels simulated were methyl butanoate, n-heptane, and methanol. Mechanisms with two levels of NO_x chemistry detail were created for each fuel (full NO_x chemistry and Zel'dovich chemistry only). The six simulations for the three fuels and two levels of NO_x chemistry detail conducted by a collaborator, but the data were analyzed and interpreted by the author of this dissertation. The simulations were solved on a transient, spherically symmetric combustion code with detailed chemical kinetics, and species-specific diffusivity.

Chapter 3 contains an explanation of how the experimental apparatus was constructed and how data was processed. A piezoelectric droplet generator was used to create a monodisperse stream of liquid fuel droplets at a rate of 10 Hz. The fuels tested were methyl decanoate, methyl butanoate, n-heptane, methanol, ethanol, and 1-propanol. The droplets, of diameter 200 - 400 μm fell under the influence of gravity and passed through a electrical resistance-heated coil causing them to ignite. The droplet flames were then subjected to a laser sheet to create fluorescence images of OH and NO. The planar laser-induced fluorescence spectroscopy techniques was used in which an ultraviolet laser beam was tuned to a wavelength readily absorbed by the species of interest (OH and NO) and formed into a sheet. The laser sheet was passed through a droplet flame causing OH and NO to fluoresce. An intensified CCD camera imaged the fluorescence emitted from the droplet flames. Hundreds of the resulting single-shot fluorescence images were averaged together to obtain an averaged image. Profiles of OH/NO were obtained from the average fluorescence image which corresponded to the concentration of those species in the flame.

Chapter 4 contains results from the simulation of autoignition and combustion of isolated liquid droplets of methyl butanoate, n-heptane, and methanol. The results appear in the form of a series of plots at times selected to convey the important phenomena such as auto-ignition, combustion of premixed fuel and air, transition to non-premixed combustion, and arrival at a quasi-steady state non-premixed flame. A discussion is presented that points out and explains various combustion phenomena observed in the simulations results. The ignition delay varied among the three fuels with methyl butanoate being the longest, followed by methanol and n-heptane. The maximum temperature reached in the simulations correlated with the adiabatic flame temperature of the respective fuels. The n-heptane

simulation produced more nitric oxide (NO) than methyl butanoate by a factor of five, and ten times more than methanol. Simulations with full NO_x chemistry consistently produced drastically more NO than simulations with only Zel'dovich NO chemistry irrespective of fuel, thereby demonstrating the importance of Fenimore and N_2O-path chemistry in overall NO_x formation.

In Chapter 5, results of planar laser-induced fluorescence spectroscopy of droplet flames are presented. The results showed profiles of OH and NO species for the six fuels tested at approximately 16 ms after ignition. Additionally, profiles of OH and NO were also shown for n-heptane 19 and 22 ms after ignition. A plot shows how NO is correlated with adiabatic flame temperature of the respective fuels.

In Chapter 6, the concepts of most reactive mixture fraction and critical scalar dissipation rate are introduced to examine the viability of autoignition and combustion of isolated liquid fuel droplets as a physical model for autoignition and combustion of diesel sprays. Mixture fraction is a non-dimensional number that represents the concentration of fuel in non-premixed flames. Scalar dissipation rate is a parameter that comes from the flamelet equations for turbulent non-premixed flames. It is a measure of the rate of dissipation of heat and mass in mixture fraction space. A combination of these parameters was used to explain how and why a non-premixed flame may ignite in a lean or rich region. In this context, it is shown that droplet autoignition has limitations as a physical model for autoignition in diesel sprays.

Finally, Chapter 7 presents suggested avenues of research stemming from this work and an overall conclusion.

CHAPTER 2

Numerical Simulation Methods

2.1. Introduction

Computer simulations of spherically-symmetric droplet ignition and combustion were conducted as part of the research reported by this thesis. The simulations were performed with methyl butanoate, n-heptane, and methanol fuels. The setup and running of the simulations was carried out by collaborator Prof. Tanvir Farouk of the University of South Carolina. The chemical mechanisms for the four fuels were created by Professor Farouk and modified by the author of this thesis to include chemistry for formation of oxides of nitrogen. Details of the modifications follow in Section 2.2.

Due to the computational savings afforded by a spherically-symmetry domain, it is possible to simulate the transient ignition and combustion of single and multicomponent liquid droplets with detailed gas-phase chemical kinetics, multicomponent molecular transport, radiative heat transfer, non-ideal vapor-liquid equilibrium, and liquid phase transport. Cho, et al. [63] performed the first such time-dependent calculations for the combustion of a pure methanol droplet. Marchese and Dryer [49] continued this work by examining in detail the effect of water absorption in methanol droplet combustion. The same authors also studied multicomponent alkane droplet combustion [51] and have examined the effects of non-luminous thermal radiation in droplet combustion [64]. More recently, Marchese, et al. [61], performed the first transient methyl ester droplet ignition and combustion computations using a reduced methyl decanoate mechanism. The computations compared favorably against ignition delay experiments conducted by Vaughn and coworkers [65].

The numerical simulation of spherically-symmetric ignition and combustion of isolated droplets used the latest version of this code that was written and validated by Kenneth Kroenlein for his PhD research [47]. The code was, in large part, mathematically identical to that developed by the researchers cited above (i.e., [51, 63, 49, 64, 61]) but with improvements in implementation, speed, and the ability to accept CHEMKIN-format chemical kinetic mechanism files.

Since Kroenlein's graduation in 2007, the code has been used for further research on droplet combustion. Farouk and Dryer added capability to account for the effects of the wire on combustion of a wire-tethered droplet [66] which the same authors used to investigate methanol droplet combustion in CO_2-enriched environments [45]. Farouk, et al. conducted experiments and simulations of methyl butanoate droplet combustion [67]. Detailed numerical modeling of methyl decanoate droplets was done by Liu, et al. [68]. And, most recently, Farouk and Dryer investigated two-stage combustion behavior in n-heptane droplet flames [53].

2.2. Creation of Fuel Mechanisms with NO_x Chemistry

Existing chemical mechanisms for each of the four fuels were modified for use in simulations of ignition and combustion of isolated droplets. The modifications comprised of appending chemical reactions and species necessary for the formation of oxides of nitrogen. The fuel mechanisms used were those reported on by the references indicated here: methyl butanoate [67], methanol [69], and n-heptane [53]. The methanol mechanism is a full, detailed mechanism with 21 species and 93 reactions. The methyl butanoate mechanism is a reduced mechanism and has 98 species and 626 reactions. The n-heptane mechanism is also a reduced mechanism with 130 species and 568 reactions.

The chemistry for formation of oxides of nitrogen was taken from the Konnov v0.6 mechanism for small hydrocarbon (methane, ethane) combustion mechanism with NO_x chemistry [14]. During the process of verifying the new combined mechanism, a numerical instability in the Konnov mechanism was discovered. A discussion of the measures taken to mitigate the instability are discussed in the next subsection. The details of appending the nitrogen chemistry to the existing fuel mechanisms is in Section 2.2.2.

2.2.1. NUMERICAL INSTABILITY OF KONNOV MECHANISM. The process of appending nitrogen chemistry to the fuel mechanisms was facilitated by performing steady burner-stabilized premixed flame calculations using CHEMKIN software program [70]. This effort used to check for errors and verify functionality. During the course of this work, it was discovered the Konnov mechanism [14] contains an inherent numerical instability that caused the burner-stabilized flat flame model to fail. Specifically, there are four chemical reactions whose reverse reaction rates are unrealistically high ($k_r = $ 1e30 to 1e40) for temperatures around 300K. The reactions in question are these:

$$C_2N_2 + M \longleftrightarrow 2\,CN + M$$

$$C_3H_3 + H \longleftrightarrow C_3H_2 + H_2$$

$$CH_3 + M \longleftrightarrow CH + H_2 + M$$

$$HNCN + M \longleftrightarrow H + NCN + M.$$
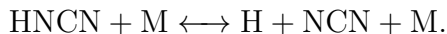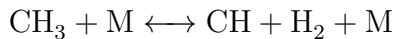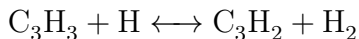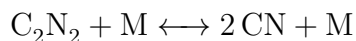
TABLE 2.1. Results of burner-stabilized flat flame simulations using CHEMKIN with various versions of Konnov mechanism to test various solutions to the numerical instability.

Modifications to Konnov v0.6	Max X_{NO}, [ppm]	Computation time
Umodified v0.6	21.7	4 min, 20 sec
Forward only	18.8	3 min, 31 sec
$k_r = k_r(2200K)$	19.5	15 min, 35 sec
$k_r \propto 1/T$	19.1	10 min, 29 sec

The reverse reaction rates are not explicit inputs from the mechanism but are calculated by the CHEMKIN code using equilibrium constants via the following [71]:

$$k_{ri} = \frac{k_{fi}}{K_{ci}},$$

(45)

where k_{ri} is the reverse reaction rate for species i, k_{fi} is the forward reaction rate for species i, and K_{ci} is the equilibrium constant for species i. A series of simulations were conducted to determine the importance of these reactions for production of NO_x and how to best mitigate the numerical instability.

The CHEMKIN model used to investigate the instability was the burner-stabilized flat flame (BSFF). The BSFF model simulates a laminar flame similar to the flames generated by the McKenna flat flame burner used for dye laser tuning as described in Section 3.3. Premixed gaseous fuel and air flow through a permeable disk of sintered metal and combusts in a laminar flat flame which is stabilized by heat loss to the water-cooled sintered disk. The numerical instability was avoided by specifying fresh fuel-air mixture have a temperature of 500 °C. Four simulations were conducted with different versions of the Konnov mechanism, but were otherwise identical in setup with a stoichiometric methane-air flame.

Table 2.1 summarizes the four BSFF simulation cases with the resulting maximum NO mole fraction and computation time. The first case represents the control case in which the

Konnov v0.6 mechanism is unmodified. In the second case, the four problem reactions shown above are forced to be forward only so that the non-physical reverse reaction rates are never computed. Third, the reverse reaction rates for the four problem reactions are fixed at the values calculated for 2200 K. In the forth, an arbitrary, but not unreasonable, relationship between k_r and inverse temperature is specified.

Notice that the unmodified case resulted in a final mole fraction of NO of 21.7 ppm. This is higher than any of the other three modified cases. This means that in the unmodified Konnov v0.6 mechanism, the reverse rates of the four problem reactions were somewhat important for the formation of NO. On the other hand, the reverse reaction rates for these reactions is so high at low temperatures as to be absurd. Such high reaction rates at low temperature ($\sim$300 K) is non-physical as chemistry should be frozen, so any contribution they might provide to formation of NO is likewise non-physical. A further reason to be unconcerned about the difference in NO formation between the unmodified and modified Konnov mechanisms is that the nitrogen chemistry in question was applied to combustion of fuel molecules larger than methane, and, in the case of n-heptane and methyl decanoate, *much* larger. Using the nitrogen chemistry on such large fuels adds a level of complexity for which it was not originally intended. The application to which the nitrogen chemistry was applied, namely predicting NO formation in droplet flames of the selected liquid fuels, was merely an initial attempt and the results have much uncertainty. As such, the nitrogen chemistry which was added to the liquid fuel mechanism was based on the second case in which the problem reactions were forced to be forward-only. This scheme was selected because it was the simplest modification and appeared to be the least computationally expensive as indicated by the shortest computation time in Table 2.1.

2.2.2. APPENDING NO$_x$ CHEMISTRY TO FUEL MECHANISMS. Appending nitrogen chemistry to the fuel mechanisms was, unfortunately, not as easy as simply combining the corresponding files and running the simulations. The source of the difficulties lie largely with the fact that there are not universally agreed upon abbreviations for some compounds, or even standards for capitalization. In a trivial example, "CH4" and "ch4" clearly both represent methane, but CHEMKIN treats them as distinct species because the interpreter is case-sensitive. As long as a mechanism is self-consistent in the syntax of the species names, there is no trouble. However, when combining mechanisms, such duplicates must be sought out and rectified.

None of the original fuel mechanisms for methyl butanoate, n-heptane, or methanol contained any nitrogen-containing species[1], so the nitrogen reactions obtained from Konnov and appended to the fuel mechanisms did not create duplicate species. However, some species which were present in the Konnov nitrogen chemistry were not present in the fuel mechanisms. For example, consider the chemistry file of the chemical kinetic mechanism for methyl butanoate with full NO$_x$ chemistry found in Appendix H. Notice the very last chemical reaction listed is the following:

$$C_2 + N_2 \longleftrightarrow CN + CN \tag{R17}$$

in which C$_2$ reacts with molecular nitrogen to create two cyanide molecules. The C$_2$ molecule was not already part of the methyl butanoate fuel mechanism, so it was necessary to add it. A script was written to seek out all the reaction in the complete Konnov mechanism which

---

[1]With the exception of N$_2$ which was included because it comprises ∼79 percent of air and therefore acts as a diluent and can participate as a third body in three-body recombination reactions such as Reaction (R15).

contained C_2. The result of the search was Reaction (R17) plus three others:

$$C_2H + OH \longleftrightarrow C_2 + H_2O \qquad\qquad (R18)$$

$$C_2 + H_2 \longleftrightarrow C_2H + H \qquad\qquad (R19)$$

$$C_2 + O_2 \longleftrightarrow CO + CO. \qquad\qquad (R20)$$

These four reactions, (R17) through (R20), were appended to the original fuel mechanism and Konnov nitrogen chemistry and appear at the very end of Appendix H. The same was true for C_2O and C whose reactions appear in Appendix H prior to those of C_2 described above, and all the reactions containing C_2O and C were sought out in the unmodified Konnov mechanism to be included in the methyl butanoate with full NO_x chemical mechanism in Appendix H. The process of adding chemistry for C, C_2, and C_2O was necessary for all three fuels simulated for this dissertation: methyl butanoate, n-heptane, and methanol.

Examining Reactions (R4) and (R5) show that the fuel fragments CH and CH_2 are important because they participate in the initiating reactions for Fenimore NO_x formation. In the case of methanol and n-heptane, those species were eliminated during the course of chemical mechanism reduction. As such, the reactions containing CH and CH_2 were restored because of the important role they play. In the methyl butanoate mechanism, CH and CH_2 were already present, so no change was necessary.

Sometimes when combining the nitrogen chemistry from the Konnov mechanism and the fuel mechanism, duplicate species occurred which were not always easy to detect because the same species may have different names in the respective mechanisms. MATLAB scripts were written to seek out possible duplicates based on number of atoms present in the molecule

which are specified as an input in the thermodynamics file of a chemical mechanism. The script sifted through the thermodynamics file of the combined fuel and NO_x mechanisms and identified pairs of species which contained identical numbers of atoms. A list was then generated of possible duplicates and checked by hand to determine if an actual duplicate was identified or simply an isomer. If a duplicate was found, the molecule name was changed to the NIST preferred name[2]. For example, when singlet CH_2 was found to be written CH_2s, it was changed to the NIST preferred symbol: $CH_2(S)$.

2.3. Computer Code for Simulation of Isolated Droplet Ignition and Combustion

The computer code used for the simulation of isolated droplet ignition and combustion was the latest version of a series of codes developed since 1990 by the Dryer group at Princeton University. A summary of the computer code's major features are contained herein. Details of the development, function, and implementation of the computer code are found in the following references: [45, 47, 51, 72, 61, 66].

The code used in the simulations was a transient and spherically-symmetric combustion model meaning the dependent variables were time and radius. The detailed gas-phase kinetics included reactions for fuel combustion and formation of oxides of nitrogen species. Gas transport was species-specific. The species and energy equations for a spherically symmetric

---

[2]See http://kinetics.nist.gov/kinetics/index.jsp.

domain are:

$$\int_{r_-}^{r_+} \frac{\partial}{\partial t}(\rho Y_i)r^2 dr + \frac{r^2\dot{r}\ |_{r_-}^{r_+}}{\frac{1}{3}r^3\ |_{r_-}^{r_+}} \int_{r_-}^{r_+} \rho Y_i r^2 dr + \rho Y_i(u-\dot{r})r^2\ |_{r_-}^{r_+} =$$

$$- \rho Y_i V_i r^2\ |_{r_-}^{r_+} + \int_{r_-}^{r_+} w_i r^2 dr \quad (46)$$

$$\int_{r_-}^{r_+} \frac{\partial}{\partial t}(\rho h)r^2 dr + \frac{r^2\dot{r}\ |_{r_-}^{r_+}}{\frac{1}{3}r^3\ |_{r_-}^{r_+}} \int_{r_-}^{r_+} \rho h r^2 dr + \rho h(u-\dot{r})r^2\ |_{r_-}^{r_+} = -qr^2\ |_{r_-}^{r_+} \quad (47)$$

where Y_i is mass fraction, ρ is density, r is the radial coordinate, u is the bulk fluid velocity, $\dot{r}$ is the velocity of the control volume boundary, V_i is diffusion velocity of the ith species through the gas mixture, w_i is rate of production of species i by chemical reaction(s), h is mass-normalized enthalpy, and q is a combined heat flux term.

As an example of representative results from the droplet code, consider Figure 2.1 which is reproduced with permission from Reference [61]. The droplet was methyl decanoate ($C_{11}H_{22}O_2$) with initial diameter of 1.0 mm. At initial time, the droplet was inserted into ambient air of temperature 1200 K. The plots show mass fraction profiles of fuel, oxygen, and major combustion products as a function of normalized radius for the indicated time steps. Temperature is indicated by the heavy solid line and corresponds to the vertical scale on the right side of the plots. The first plot at $t = 0.070$ s shows the fuel vapor diffusing into the ambient from the droplet surface and mixing with ambient air. In the second plot at $t = 0.081$ s depicts a reaction zone locally depleting fuel and oxygen, and producing heat. At $t = 0.100$ s, vigorous non-premixed combustion is ongoing with a flame temperature of nearly 2400 K. The new simulation results presented in Section 4.2 exhibit similar behavior to that seen in Figure 2.1. However, unlike the results in Figure 2.1, the new results incorporate chemical kinetics for formation of oxides of nitrogen like NO, N_2O, and NO_2.

53
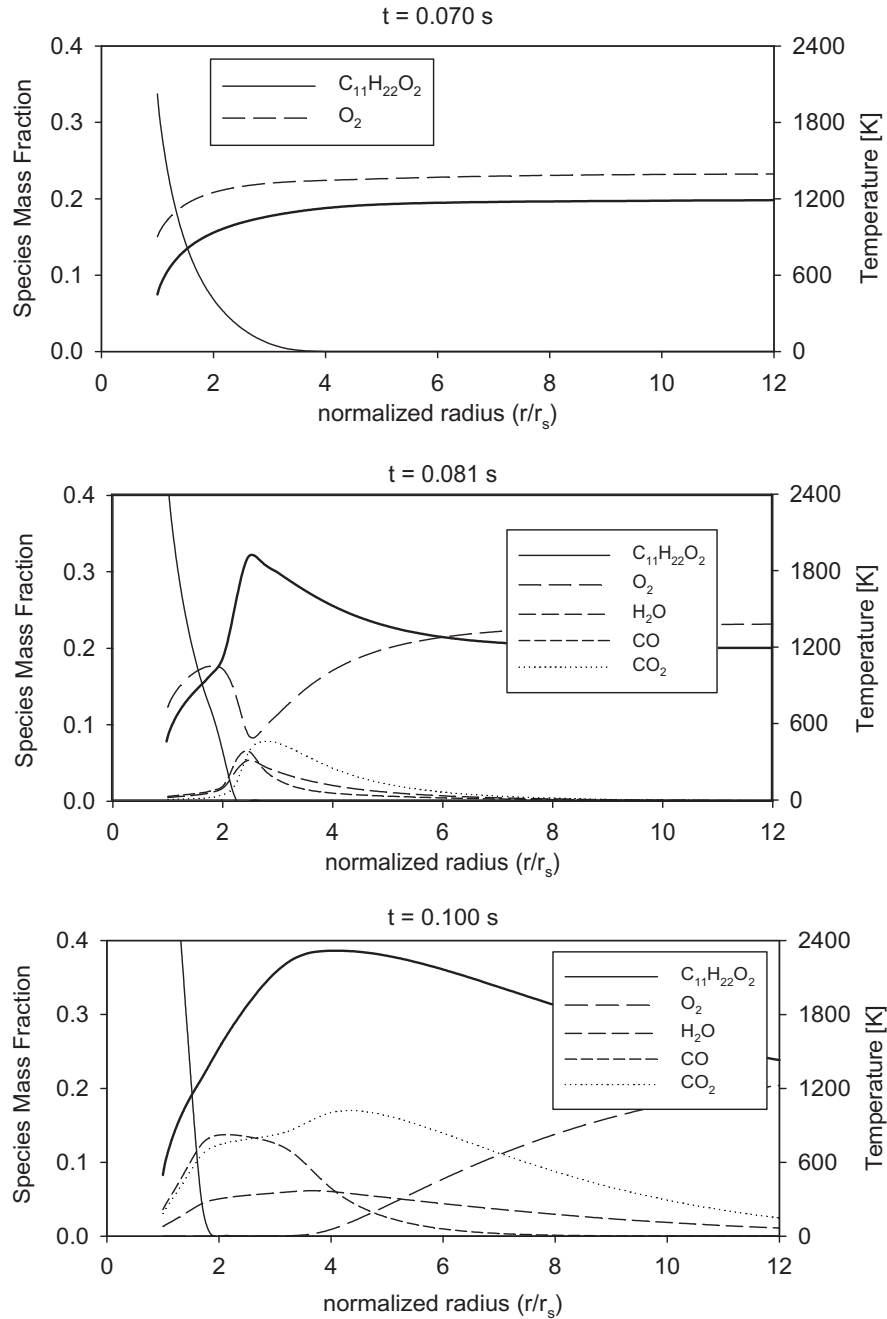
FIGURE 2.1. Results of a spherically-symmetric isolated autoignition and combustion simulation of methyl decanoate. Reproduced with permission from Marchese, et al., 2011.

In the simulations that were conducted for the research for this dissertation, the spatial domain was defined as having a spatial extent 200 times the initial droplet radius. Since all droplet had an initial radius of 200 μm, the spatial domain had a maximum radius 20 mm.

The spatial domain was comprised of 140 nodes whose density was varied by the code from time step to time step. The extent of the time domain was such that the droplet was able to burn to extinction; less than 100 ms for all fuels simulated. Dirichlet (fixed) boundary conditions were defined for the outer boundary: ambient air composition of 79% nitrogen and 21% oxygen, and temperature 1150 Kelvin.

The results of the numerical modeling are presented in Chapter 4. The mass of NO_x species as a function of time are an important quantity for interpretation and analysis of the results and are calculated using the following equation. The the total mass of any species i in a spherically-symmetric domain is given by:

$$m_i = \int_{r_s}^{\infty} 4\pi r^2 \rho Y_i dr, \tag{48}$$

where r is the radial coordinate, ρ is density of the gas-phase mixture, Y_i is the mass fraction of species i, and r_s is the radius of the liquid fuel droplet. Both ρ and Y_i are a function of radius and location: $\rho = \rho(r, t)$ and $Y_i = Y_i(r, t)$. The radius of the droplet decreases as fuel vaporizes, therefore it is a function of time: $r_s = r_s(t)$.

CHAPTER 3

EXPERIMENTAL TECHNIQUES

3.1. INTRODUCTION

The purpose of the experimental component of the research presented in this thesis was to create fluorescence images and profiles of hydroxyl (OH) and nitric oxide (NO) produced in droplet flames. This chapter contains a description of the equipment and methods used to achieve this result. First, a brief review of the theory of the spectroscopic technique is presented followed by a detailed description of the associated laser spectroscopy experimental setup. Then, the droplet generation and ignition system is presented. This is followed by an explanation of how the timing of the various components was managed. Finally, a discussion appears on the method developed to process the fluorescence images produced.

3.2. LASER-INDUCED FLUORESCENCE SPECTROSCOPY

The experimental component of this work was conducted using a type of spectroscopy called laser-induced fluorescence wherein a laser beam is passed through a flame, causing certain species within the flame to emit light. The magnitude of the emitted light provides information about the concentration and location of that species. Laser-induced fluorescence is a common technique in the combustion research community for measurement of species and temperature in flames. It is considered a nonintrusive technique because the interaction of the laser light with combustion species (typically) has negligible effect on the combustion physics. This section contains a basic explanation of the physics of laser-induced fluorescence as it was implemented in the experiments. A deeper discussion of molecular spectroscopy theory is found in Appendix C.

Speaking in general terms, an atom or molecule can be raised to an excited state by a collision with photons, electrons, or even other molecules. After some finite time, the exited atom or molecule may emit radiation which is termed *fluorescence*. Thus, laser-induced fluorescence (LIF) is radiation emitted from atoms or molecules that have been excited by collision with a photon from a laser beam. [73]

In the experiments described herein, the species on which laser-induced fluorescence was conducted were hydroxyl (OH) and nitric oxide (NO) molecules. It is possible to selectively excite OH or NO (and many other species [73, 74, 75]) by tuning the laser to a wavelength that is readily absorbed by the desired species. For example, setting the laser to 282.93 nm caused OH species in the flame to become electronically excited and emit fluorescence light. On the other hand, NO molecules were induced to emit fluorescence when the laser was tuned to 226.03 nm.

A laser beam can be focused down to a miniscule diameter by passing it through a lens with a positive focal length. The focal point can be located anywhere in a flame and fluorescence will be emitted only by those species located in the beam. In this way, it is possible to make measurements with a spatial resolution that is limited only by the minimum diameter to which a laser beam can be focused (a few hundred microns). Such measurements are termed *point* or *zero-dimensional laser induced fluorescence* spectroscopy, often abbreviated simply as LIF. On the other hand, the laser beam can be formed into a thin sheet using a series of lenses as described in Section 3.3. Passing a laser sheet through a flame will cause a two-dimensional planar region of the flame to emit fluorescence. This fluorescence can be imaged by an intensified camera to create images of the fluorescence.
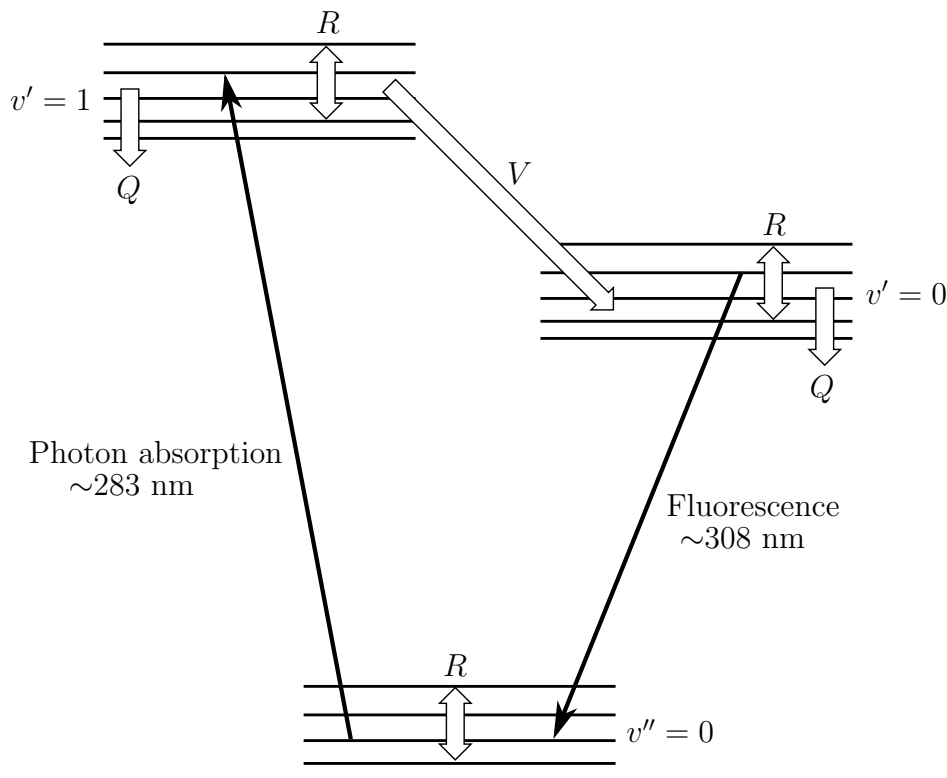
FIGURE 3.1. A diagram of $A^2\Sigma^+$ and $X^2\Pi$ electronic energy levels of OH. Photon absorption and fluorescence is indicated by dark line arrows. The open box arrows indicate rotational energy transfer, vibrational energy transfer, and quenching. Adapted from Smyth and Crosley, 2002.

This technique is referred to as *planar laser-induced fluorescence* spectroscopy or PLIF. Both point LIF and PLIF are used in the experiments described here.

Figure 3.1 contains a simplified diagram showing energy transfer processes among the energy levels of the $A^2\Sigma^+ - X^2\Pi$ electronic band system of OH and was adapted from Reference [76]. Laser light is tuned to a transition in the (1,0) vibrational band of OH with a wavelength of near 283 nm. Photons are absorbed, raising a population of OH molecules to an excited state in the $v' = 1$ level as shown by the heavy upward arrow. Certain energy states within the $v' = 1$ level are populated through a process called *rotational energy transfer* (RET) at a rate dependent on the population of that level and the rate constant R. Some

of the excited population is lost through a collision processed called *quenching*, the rate of which is, like RET, dependent on the population and rate constant Q. [76]

A third process called *vibrational energy transfer* (VET) is responsible for populating the $v' = 0$ vibrational level, which is depicted as a diagonal arrow in Figure 3.1. The rate of VET is dependent on the population in the $v' = 1$ level and the rate coefficient V. Both RET and quenching play a factor in the population distribution in the $v' = 0$ level just like in the next higher level. Some OH molecules that are members of the $v' = 0$ population will return to the lower state by undergoing fluorescence which is indicated by the heavy downward arrow. The wavelength of the fluorescence will be in the vicinity of 308 nm. [76]

Notice that the wavelength of the fluorescence emission is about 25 nm longer than the laser wavelength. This is a useful outcome because it means that optical filters can be used to block scattered laser light while passing fluorescence emissions [75]. A similar scheme is used for NO fluorescence, where the laser is tuned to near 226 nm and fluorescence is collected around 250 nm.

The laser wavelength for OH PLIF was 282.93 nm and was selected to maximize absorption of laser light. The absorption line in question was a combined transition: $Q_1(6) + Q_2(1)$ in the $A^2\Sigma^+ \leftarrow X^2\Pi$ (1,0) band. Fluorescence was imaged over a range of 306 to 322 nm, which were emitted from the (0,0) and (1,1) bands.

Guidance on selection of a pump wavelength for NO PLIF was provided by Refs. [77, 78]. The pump line resides in the $A \leftarrow X$ (0,0) band of NO and is comprised of multiple transitions: $P_1(23.5), Q_1 + P_{21}(14.5), Q_2 + R_{12}(20.5)$. The absorption peak near 226.03 nm was recommended in Refs. [77, 78] because it minimized interference from molecular oxygen (O_2) while still providing good signal strength. Although, since all of these experiments

TABLE 3.1. Quantities used to find the laser spectral irradiance for the OH and NO PLIF laser.

Species	E_p [J]	A [cm^2]	t_p [s]	ℓ [cm^{-1}]	I^ν [W/(cm$^2 \cdot$ cm^{-1})]
OH	5×10^{-3}	0.1	10×10^9	0.5	10×10^6
NO	0.8×10^{-3}	0.1	10×10^9	0.5	1.6×10^6

were at atmospheric pressure, molecular oxygen would not be expected to provide much interference. Fluorescence was detected from the (0,2) and (0,3) bands over the range of 240 to 260 nm. Fluorescence from the (0,1) band, while more intense, was too close to the laser line to be of use.

Saturated LIF occurs when the laser irradiance is sufficient to cause absorption and emission to dominate collisional quenching rate [73]. Saturated LIF produces maximum fluorescence signal [73] which is desirable for PLIF. While it is often trivial to achieve saturation in point measurements with modern dye lasers such as the Sirah Cobra Stretch used in this study, planar measurements tend to require higher intensity beams to saturate because the laser light is spread out over the height of the sheet. In the following, the OH PLIF and NO PLIF spectroscopy setups used for this work are examined to determine if saturation was achieved.

The laser spectral irradiance is the power of a laser pulse per unit area per unit frequency interval [73]:

$$I^\nu \approx \frac{E_p}{A\, t_p\, \ell}. \tag{49}$$

In Equation (49), E_p is the laser pulse energy in joules, A the area of the laser spot or sheet in square centimeters, t_p the duration of the pulse in seconds, and ℓ the value of the line overlap integral in inverse centimeters. The latter is a measure of how well the spectral line shape of the laser matches that of the absorbing transition. The values for the above variables

TABLE 3.2. Calculated laser spectral irradiance for OH and NO PLIF. Rotationally frozen and relaxed limits for saturated laser spectral irradiance. All quantities in units of $[\text{MW}/(\text{cm}^2 \cdot \text{cm}^{-1})]$.

Species	I^ν	Frozen I^ν_{SAT}	Relaxed I^ν_{SAT}
OH	10	0.1	1.1
NO	1.6	0.094	2.9

and the resulting laser spectral irradiance for OH and NO PLIF configurations are presented in Table 3.1. E_p was determined by measurement, A was based on the laser sheet having dimensions two centimeters high and 0.5 cm wide, t_p was determined by measurement, ℓ was a conservative estimate (it is probably close to unity). The right hand column of Table 3.1 shows the resulting laser spectral irradiance for the two PLIF configurations.

The laser spectral irradiance required for saturation of fluorescence species I^ν_{SAT} is dependent on the degree of RET in a given vibrational level. The upper and lower bounds are for the rotationally relaxed and frozen limits, respectively. In a practical experiment, the rotational state is somewhere in the middle [73]. Table 3.2 shows the laser spectral irradiance I^ν for the laser sheet used for OH and NO PLIF that was calculated above in the second column. The saturated laser spectral irradiance in the rotationally frozen and relaxed limit [73] are shown in the latter two columns.

In Table 3.2, the calculated laser spectral irradiance for OH is well above that required even for a rotationally relaxed vibrational level by nearly an order of magnitude. This result implies that OH fluorescence was thoroughly saturated spatially and temporally. However, were this the case, normalization of the fluorescence images by the laser sheet profile (see Section 3.5) would not be necessary. Since normalization *was* required, some fluorescence was produced from non-saturated energy levels. It is likely that this result can be explained by variation in the power of the laser pulse in time. Ideally, the power of a laser pulse would

appear as a square wave as a function of time. Instead, when the dye laser is pumped by an Nd:YAG, the shape is often a smooth double peak. As such, the vibrational states were probably saturated only part of the time while the laser pulse passed through the droplet flame.

In the case of NO, the facts are more straight-forward. The calculated laser spectral irradiance in Table 3.2 falls squarely between the upper and lower limits suggesting that the upper vibrational state of the fluorescing transitions of NO were probably only partially saturated, if at all. This is consistent with visual observations that showed the intensity of NO fluorescence varied strongly with the position of the droplet flame relative to the laser sheet.

3.3. Setup of Planar Laser-Induced Fluorescence Spectroscopy System

Figure 3.2 contains a diagram of the layout of optical components for conducting planar laser-induced fluorescence spectroscopy. The setup was actually comprised of two separate spectroscopy systems. The first system was a zero-dimensional laser-induced fluorescence (LIF) spectroscopy system for fine-tuning the wavelength of the dye laser (the daily checking of which was necessary due to drift). The second system was two-dimensional planar laser-induced fluorescence (PLIF) spectroscopy system for capturing fluorescence images of burning droplets.

Laser light for both beamlines was produced with an Nd-YAG and dye laser combination (Figure 3.2, items (a) and (b), respectively). The Nd-YAG was a flashlamp-pumped Spectra-Physics LAB150[1] laser with internal second and third harmonic generator. The pulse rate was 10 Hz and pulse width about 10 ns. When conducting OH spectroscopy, the Nd-YAG

---

[1]Spectra-Physics, http://www.spectra-physics.com/
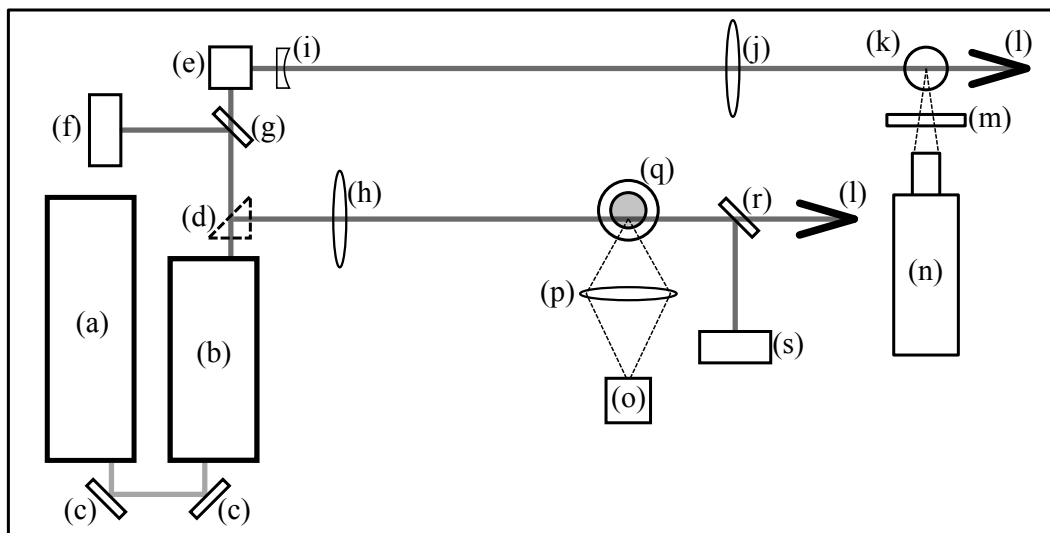
FIGURE 3.2. Diagram of the plan view of the experimental layout. (a) 10 Hz Nd-YAG laser, (b) dye laser, (c) laser line mirrors, (d) movable prism, (e) periscope, (f) photodiode, (g) window, (h) spherical mirror, (i) cylindrical lens, (j) spherical mirror, (k) droplet generator, (l) beam dump, (m) optical filter, (n) intensified CCD camera, (o) photomultiplier tube, (p) spherical mirror, (q) flat flame burner, (r) window, (s) photodiode.

fundamental of 1064 nm was frequency doubled to 532 nm and adjusted to obtain a pulse energy of about 200 mJ. For NO spectroscopy, the fundamental was doubled and mixed to obtain a 355 nm beam with a pulse energy of about 100 mJ. The output beam of the Nd-YAG was routed into the dye laser with high-power laser line mirrors (Figure 3.2, items (c)). The dye laser was a Sirah Cobra Stretch[2] (Figure 3.2, item (b)) which contained oscillator, pre-amplifier, and amplifier stages. A 566 nm fundamental beam was required for OH spectroscopy and was obtained using Rhodamine 590 dye. The 566 nm beam was frequency doubled to 282.93 nm with a pulse energy of approximately 5 mJ. Spectroscopy of NO required a 452 nm fundamental, which was provided by Coumarin 450 dye. (Both dyes were purchased from Exiton, Inc[3].) The 452 nm fundamental was frequency doubled to 226.03 nm; the pulse energy was about 0.8 mJ.

---

[2]Sirah Lasertechnik GmbH, http://www.sirah.com/
[3]Exiton, Inc., http://www.exciton.com/

Laser light exiting the dye laser could be routed to one of two beam lines using a prism attached to a precision flip-mount (Figure 3.2, item (d)). With the prism inserted into the beamline, laser light was directed to the right where it was focused by a spherical lens with focal length 200 mm (Figure 3.2, item (h)). The lens was positioned so that the beam waist was located approximately 5mm above the flame of a McKenna flat flame burner[4] (Figure 3.2, item (q)). The burner had a water-cooled sintered bronze plug through which premixed municipal natural gas and air was passed. Fluorescence from OH and NO species produced by the premixed flame was imaged by a spherical lens (Figure 3.2, item (p)) of focal length 60 mm onto a Hamamatsu[5] R3896 photomultiplier tube (PMT). Signals from the PMT (Figure 3.2, item (o)) were acquired by a 4 GHz Agilent Infiniium oscilloscope controlled by a LabView virtual instrument program via a GPIB interface. Laser light that passed through the burner flame was in large part transmitted through a window (Figure 3.2, item (r)) and absorbed by a beam dump (Figure 3.2, item (l)). The small fraction of light that was reflected by the window was routed to a Thorlabs DET25K photodiode[6] (Figure 3.2, item (s)), which monitored shot-to-shot variation of the laser energy. The LIF data acquired from the combustion products of the flat fame were used to fine tune the wavelength setting of the dye laser. A narrow wavelength scan was conducted over the width of the spectroscopic line to identify the wavelength of peak absorption. The dye laser was then set to that wavelength. It was found that the wavelength indicated by the dye laser control software of the absorption peak drifted on the order of 0.001 nm from day to day. This could very well be explained by temperature variation in the room, or gear lash in the grating translation mechanism of

---

[4]Holthuis and Associates, http://www.flatflame.com/
[5]Hamamatsu, http://www.hamamatsu.com
[6]Thorlabs, Inc., http://www.thorlabs.us/

the dye laser. Regardless, it is good practice to frequently verify the dye laser wavelength to make sure one is obtaining maximum possible fluorescence signal.

During PLIF operations, the flip-mounted prism was positioned outside the beamline and the beam passed to the periscope depicted as item (e) in Figure 3.2. The periscope was comprised of two prisms whose purpose was to route the beam to a greater height above the surface of the optical table. Upon exiting the periscope, the beam passed through the two elements of the sheet forming optics: first, a cylindrical lens of focal length -200 mm (Figure 3.2, item (i)); second, a spherical lens of focal length 1000 mm and diameter 50 mm (Figure 3.2, item (j)). The distance between the cylindrical lens and the spherical lens was about 800 mm. The scheme described here produced a laser sheet with a height[7] of approximately 20 mm and thickness 0.5 mm. The sheet waist, where the thickness is smallest, was about 1000 mm past the spherical lens.

The droplet generator (Figure 3.2, item (k)) was positioned above the laser sheet waist so the droplet flames passed through the narrowest part of the sheet. Just past the droplet generator, a beam dump absorbed the laser sheet. Details of the droplet generator and ignition follow in Section 3.4. Fluorescence produced by OH and NO species in the droplet flames was gathered by a f/3.5 Hamamatsu ultra-violet imaging lens of focal length 50 mm and imaged onto the sensor of a Cooke Corporation[8] DiCam Pro intensified charge-coupled device (ICCD) camera (Figure 3.2, item (n)). Optical filters (Figure 3.2, item (m)) were used to reject scattered laser light while passing the desired fluorescence bands. Spectroscopy of OH used two "Schott glass" filters: UG-11 bandpass and WG-305 longpass.

---

[7]This particular scheme of sheet forming optics will produce a sheet with a height of approximately five times the diameter of the initial beam spot. The method is not as tune-able as using three cylindrical lenses, but the cost savings are not insignificant.

[8]Cooke Corporation is now PCO-TECH Inc., http://www.pco-tech.com/

A single bandpass filter was used for NO specotroscopy: 248 ± 5 nm. All three filters were stock items purchased from Andover Corporation[9]. A further discussion of optical filters is worthwhile for the benefit of those setting up LIF and PLIF systems in the future and is found in Appendix E.

The ICCD camera was linked to a Microsoft Windows XP desktop computer via a fiberoptic link. Control of the camera was accomplished with the manufacturer's proprietary software. The intensifier of the camera was gated at 40 ns to accommodate temporal jitter of the 10 ns laser pulse from the dye laser. The camera's sensor was binned 2×2 to improve signal sensitivity. Triggering of the camera is discussed in Section 3.6.

3.4. Droplet Generation and Ignition

The diagram in Figure 3.3 shows the arrangement of the droplet generation and ignition apparatus. The location of the apparatus relative to the optical components is indicated by item (k) in Figure 3.2. There it is labeled simply as "droplet generator" but the other components evident in Figure 3.3 are at that location as well. Figure 3.3 is an elevation (or side) view so that droplets created by the droplet generator at the top fall through the heat shield and pass through the center of the ignition coil where they ignite spontaneously. Directly under the ignition coil is the laser sheet which causes the OH and NO species in the droplet flame to fluoresce. The droplet continues to fall into the flow tube where it burns to extinction. The dashed box containing the droplet flame diagram and part of the laser sheet shows the approximate field of view of the ICCD camera. In the following, each component will be described in detail.

_____

[9]Andover Corporation, http://www.andovercorp.com/
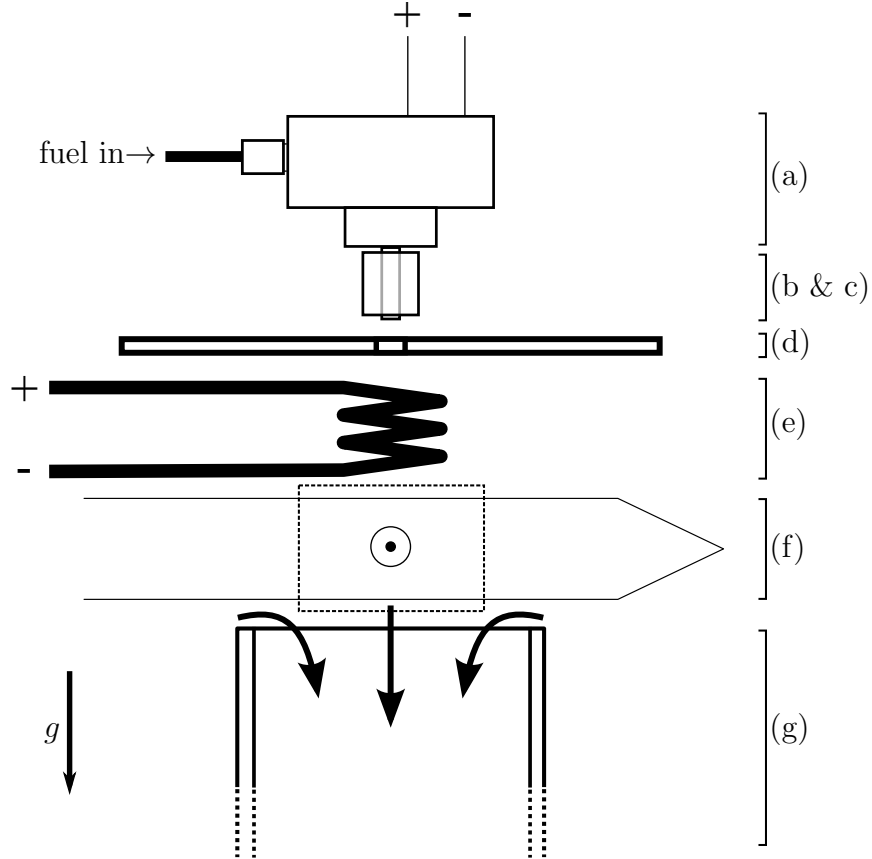
FIGURE 3.3. A schematic of the elevation view of: (a) droplet generator, (b) glass nozzle, (c) insulator, (d) heat shield, (e) ignition coil, (f) laser sheet, (g) flow tube. The dashed box shows the approximate field of view of the ICCD camera. The arrow with label g indicates the direction of gravitational acceleration.

A piezoelectric droplet generator (Figure 3.3, item (a)) was used to create a monodisperse stream of fuel droplets. It was operated at a frequency of 10 Hz to match the pulse rate of the Nd-YAG laser. The device was manufactured in-house by a member of the research group, Timothy Vaughn, for a previous unrelated study [79]. The design of the droplet generator was based on that found in Reference [80].

The droplet generator is comprised of a stainless steel disc body with a thin chamber machined out of one end. A piezoelectric disc covers the open end of the chamber and is held in place by a ring and four machine screws. Electrical pulses from a Hewlett-Packard

214B Pulse Generator are transmitted to the piezoelectric disc by leads soldered to the exposed surface (see top of Figure 3.3). Practical aspects of droplet generation are found in Appendix F.

On the opposite end of the body, a glass nozzle is fixed in place by inserting it in a teflon bushing, then covered with a collar, which is held by four machine screws. A hole drilled through the centerline of the droplet generator body permits flow of fuel from the chamber to the nozzle. Liquid fuel is supplied to the chamber from a reservoir (not shown) by a length of flexible teflon tubing entering from the side of the device as indicated at the upper left of Figure 3.3.

The glass nozzles were manufactured in-house by heating the end of a 3.2 mm diameter glass tube with a torch. This caused the inner diameter to collapse to a tiny orifice of approximately 100 microns in diameter. Once cooled, the collapsed end was ground flat with progressively finer diamond abrasive. The nozzles were cut to a ∼15 mm length. Several nozzles were manufactured and characterized by visiting undergraduate scholar, Patrick Hock. The most consistent nozzle was selected and used for all of the experiments reported herein.

It was discovered during the course of experimentation that heat transfer from the ignition coil would cause the fuel in the glass nozzle to boil, thereby causing the droplet generator to stop functioning. Heating of the nozzle was reduced by installing an insulator that fit snugly over the nozzle. The nozzle and insulator are depicted as items (b) and (c) in Figure 3.3. The insulator was made by drilling a hole through a rubber cylinder of length 15 mm and diameter 12 mm. As shown in Figure 3.3, the insulator was position so the nozzle protruded

slightly from the bottom. This was done to prevent the insulator from interfering with the formation of droplets at the nozzle exit.

A heat shield (Figure 3.3, item (d)) was used to further reduce heat transfer from the ignition coil to the glass nozzle and droplet generator body. It was comprised of a stainless steel disc of thickness 3 mm and diameter 100 mm. A 4 mm diameter hole was drilled through the center to permit the passage of falling droplets.

The ignition coil provided heat to initiate spontaneous ignition of falling droplets. The 12 gauge Kanthal A-1 wire was purchased as a ten-foot coil from Krueger Pottery Supply[10]. A short ($\sim$ 30 cm) length was cut off and wound around a 3/8-inch diameter rod three to four times to create a coil with long leads. The leads were formed and trimmed to permit attachment to a solid mount. Alternating electrical current was supplied by a VARIAC power supply.

During an experiment, droplets passed through the center of the hot coil, ignited, then fell burning through the laser sheet as shown by item (f) in Figure 3.3. Since the ambient air was nominally quiescent, the burning droplets experienced a net convective flow. From the perspective of the droplet, there was a breeze passing around it from below. This caused distortion of the flame surrounding the droplet and even at times caused localized extinction at the leading edge. This was unacceptable since the focus of the research was on spherically symmetric flames. Ideally, one would arrange a downward flow in some manner of chamber so that the droplet would experience net-zero convective flow as it fell under gravity. Better yet, the experiment would be conducted in earth orbit where the lack of gravitational acceleration would permit the experiment to proceed with a stationary droplet and flame, free from the

[10]Krueger Pottery Supply, http://kruegerpottery.com/
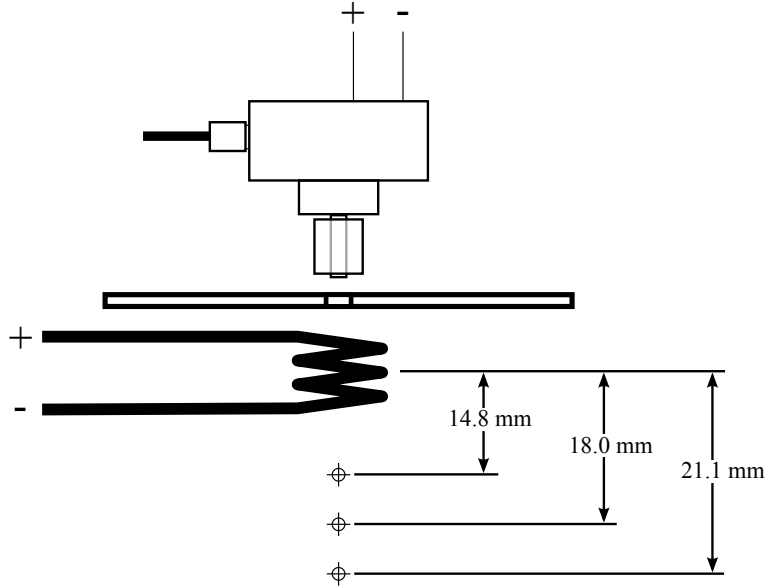
FIGURE 3.4. Heights to which the coil, heat shield, and droplet generator were elevated relative to the laser sheet and ICCD camera.

effects of bouyancy. Since these two options were beyond the scope and resources of the project, an alternative solution was conceived.

A 50 mm diameter pipe was position beneath the laser sheet (Figure 3.3, item (g)) and connected to an intake of the laboratory exhaust system. A gate valve was adjusted to produce a gentle flow into the pipe. The flow created by what is referred to in this thesis as the 'flow pipe' served to draw air downward at a velocity roughly matching that of the droplet flame as it fell through the laser sheet. This had the effect of negating the convective flow experienced by the droplet flame, thereby reducing the distortion of the flame.

Fluorescence images of OH and NO were captured for all fuels approximately 16 ms after ignition. This time period was based on the assumption that ignition occurred when the droplet had passed through half of the height of the coil. It was not possible to actually determine where the droplet ignited because the coil obstructed the laser sheet and fluorescence. However, by visual examination, it was perceived that the droplets were igniting while they passed through the coil. Thus, the above assumption.

The droplet velocity was determined by taking a photograph of a falling droplet which was scattering light produced by a strobe light. The strobe frequency was set so that several flashes occurred during a single exposure so that the strobe-illuminated droplet appeared multiple times on a single photograph. The location of the droplet images were measured on the photograph and, using the strobe period as the time increment, a plot of droplet height with respect to time was produced. A second order polynomial was fitted to the resulting curve with the restriction that it pass through the origin (meaning the nozzle exit was deemed to be zero height). The equation of the fitted curve was used to determine the time-of-flight from the assumed ignition point to the field of view of the camera. Fluorescence images for all fuels were obtained 14.8 mm below the center of the coil which corresponded to time interval from ignition to imaging of about 16 ms. In addition, fluorescence images were also acquired for 19 and 22 ms after ignition for n-heptane. This was accomplished by raising the droplet generator, coil, and heat shield to various heights above the laser sheet and camera, both of which remained fixed. A diagram depicting the three heights is found in Figure 3.4, where 14.8, 18.0, and 21.1 mm corresponded to 16.0, 19, and 22 ms after ignition, respectively.

The diameter of the droplets produced by the droplet generator were determined by acquiring backlit video images of them with a digital camera fitted with a microscope lens. A 500 Watt halogen work light was set up to point toward the droplet stream. A Pixelink[11] PL-B741U monochrome digital USB camera was set up opposite of the droplet stream from the work light. A microscope lens magnified the image of the droplets so that images with adequate pixel resolution were obtained. The timing of the exposure of the camera was dictated by the timing device (see Section 3.6) so that a silhouette of the droplet appeared

---

[11]http://www.pixelink.com/

on each frame of the video. A MATLAB script was written to determine the size of the droplet using typical image processing techniques. It was found that the diameter of the droplet varied less than 1% for a sample size of approximately 100 droplets for all six fuels.

3.5. Laser Sheet Profiling

The intensity of any laser sheet will vary over its height from top to bottom. Since the fluorescence intensity of OH and NO in droplet flames was related to the intensity of the laser sheet in thec PLIF system, it was necessary to normalize by its intensity profile. A system was designed and manufactured in-house to acquire the profile of the laser sheet, a diagram for which appears in Figure 3.5.

The principle of the system was to pass the laser sheet through an optical quartz cell containing inert gas that had been saturated with acetone vapor. Acetone is a broadband ultraviolet light absorber that fluoresces in the visible blue [81]. Fluorescence caused by the laser sheet was imaged with the ICCD camera and an intensity profile produced from the resulting video. Any inert gas can be used for this purpose, with the most obvious choice being nitrogen. Argon was used here because the gas was left over from an unrelated experiment. The acetone tank was manufactured from a 183 cm long stainless steel pipe of diameter 15.2 cm with caps welded to either end. The acetone tank was mounted vertically and filled with about eight liters of HPLC-grade acetone. Argon flowed continuously ($\sim$0.5 LPM) into the bottom of the tank through a porous sintered stainless steel solvent filter[12], which created very small bubbles to enhance contact. Acetone-saturated argon passed out of the top of the tank and into a condensate trap to remove residual liquid acetone from the argon-acetone vapor stream. The gas then flowed through an optical quality quartz cell[13] of

---

[12]IDEX Health & Science, http://www.idex-hs.com/
[13]Starna Cells, http://www.starnacells.com/
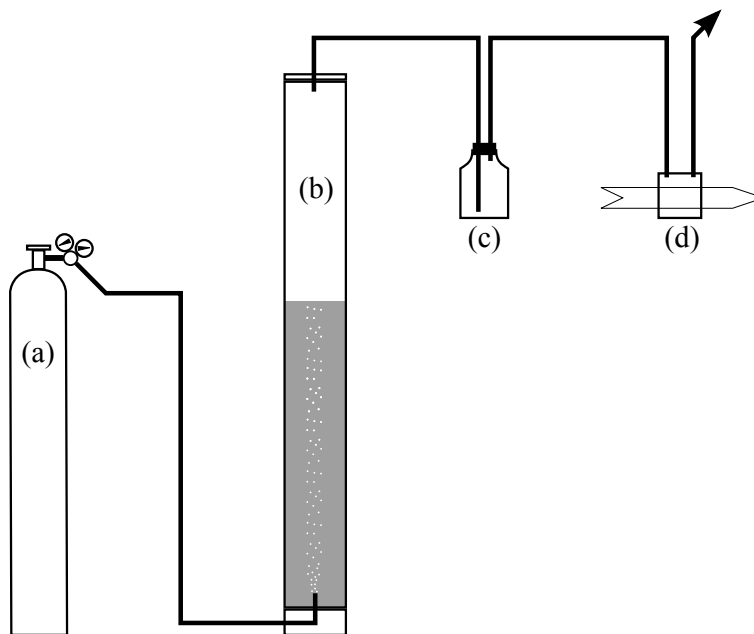
FIGURE 3.5. Diagram of the system used to obtain the intensity profile of the laser sheet: (a) argon gas bottle, (b) liquid acetone tank, (c) condensate trap, and (d) laser sheet passing through optical quartz cell.

dimensions: $40 \times 40 \times 12$ mm. Gas exiting the cell was released into the exhaust system of the lab.

When imaging the acetone fluorescence created by the laser sheet, two 290-frame videos were generated by the ICCD camera. First, with the laser on, a video was acquired which captured the acetone-fluorescence caused by the laser sheet. A second video was subsequently acquired with the laser shuttered to obtain the background. The frames of this latter video were averaged together to create an averaged background image which is shown in false color in Figure 3.6A. Next, the average background image was subtracted from each of the frames of the fluorescence video, then averaged all together to create an averaged fluorescence image as found Figure 3.6A. Notice the intensity of the fluorescence declines from left to right. This result is due to a corresponding decline in intensity of the laser sheet caused by absorption of laser light by acetone. Next, each horizontal row of pixels in the average fluorescence

(A) ICCD camera background image

(B) Averaged laser sheet image

(C) Laser sheet intensity profile

(D) Horizontally-averaged laser sheet image
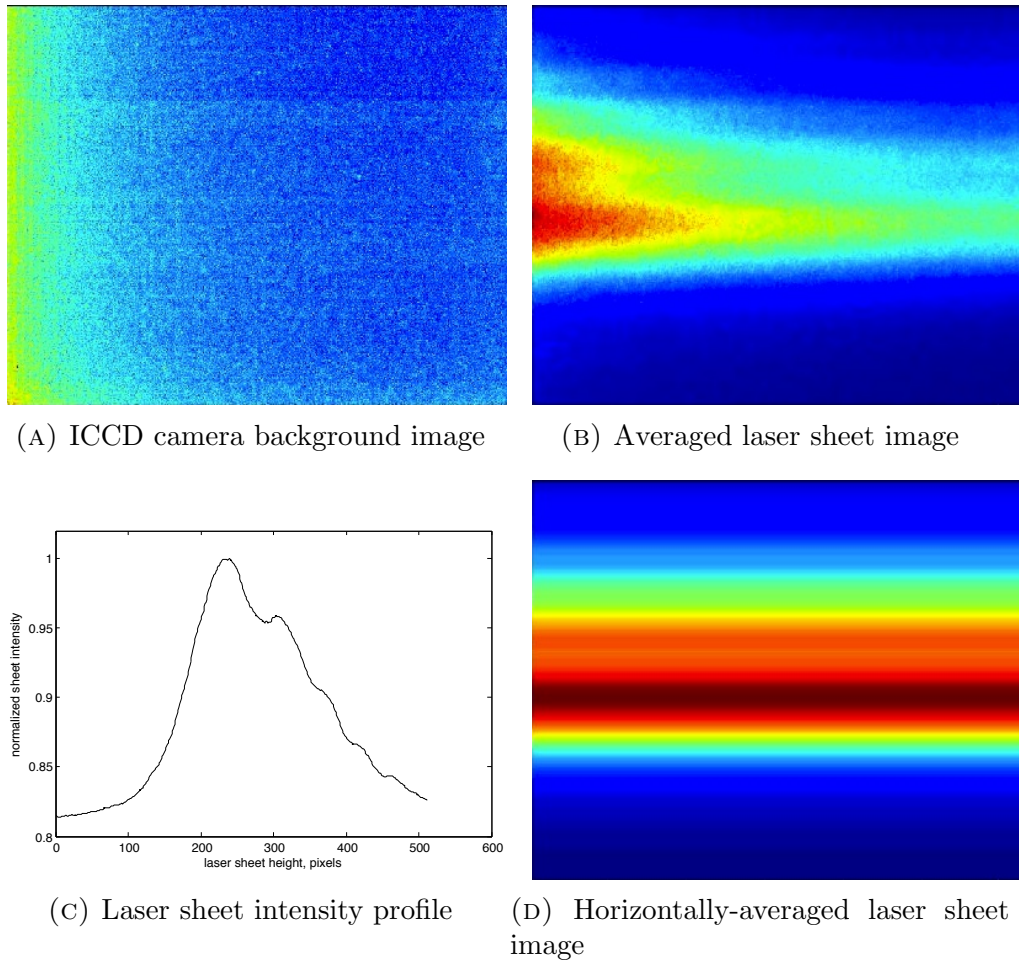
FIGURE 3.6. Intermediate results of the procedure for obtaining an average laser sheet image.

image was averaged to obtain a one-dimensional profile of the intensity of the laser sheet which can be seen in Figure 3.6C. A new image was then created in which this profile was repeatedly inserted into all of the vertical columns of pixels until it had the same dimensions as the ICCD camera video frames. This image, which is shown in Figure 3.6d, was used to normalize droplet flame fluorescence videos.

The ideal laser sheet would have a profile in the shape of a top hat. Such a laser sheet would create even fluorescence images without the need for normalization. It is clear from Figure 3.6C that the laser sheet used here did not exhibit a top hat profile, but rather a

broad, double peaked curve. This was caused by asymmetries in the laser spot prior to being formed into a sheet.

The same result could have been accomplished simply by imaging Rayleigh scattering of the laser sheet in ambient room air. However, a system like that described above would be required if one was acquiring single-shot fluorescence images of a flame and wished to normalize with the profile of the corresponding single-shot laser pulse. The reason is that the light produced by the acetone fluorescence is greater than that of Rayleigh scattering of air.

3.6. Timing

Devising a timing scheme for the electronic components of the experiment proved challenging because two vastly different time scales were present. On one hand, it was necessary to delay the ICCD camera relative to the Nd-YAG with nanosecond precision because the laser pulse was ~ 10 ns in duration. On the other hand, droplets fell at a relatively languid rate so that the travel time from the nozzle exit to the camera field of view was approximately 15 to 20 ms, a difference in time scale of six orders of magnitude.

Timing was managed by a Berkeley Nucleonics BNC-555 Pulse/Delay Generator[14]. The BNC-555 coordinated the Nd-YAG pump laser, droplet generator, ICCD camera, and beam power data acquisition. Figure 3.7 contains a diagram depicting the equipment that received timing pulses from the BNC-555.

The 10 Hz timing pulse sent to the Nd-YAG was considered to be the master clock because it had zero delay. As mentioned above, the ICCD camera was delayed so that the intensifier was activated for 40 ns as the laser sheet passed through the field of view. Since

---

[14]Berkeley Nucleonics Corporation, http://www.berkeleynucleonics.com/
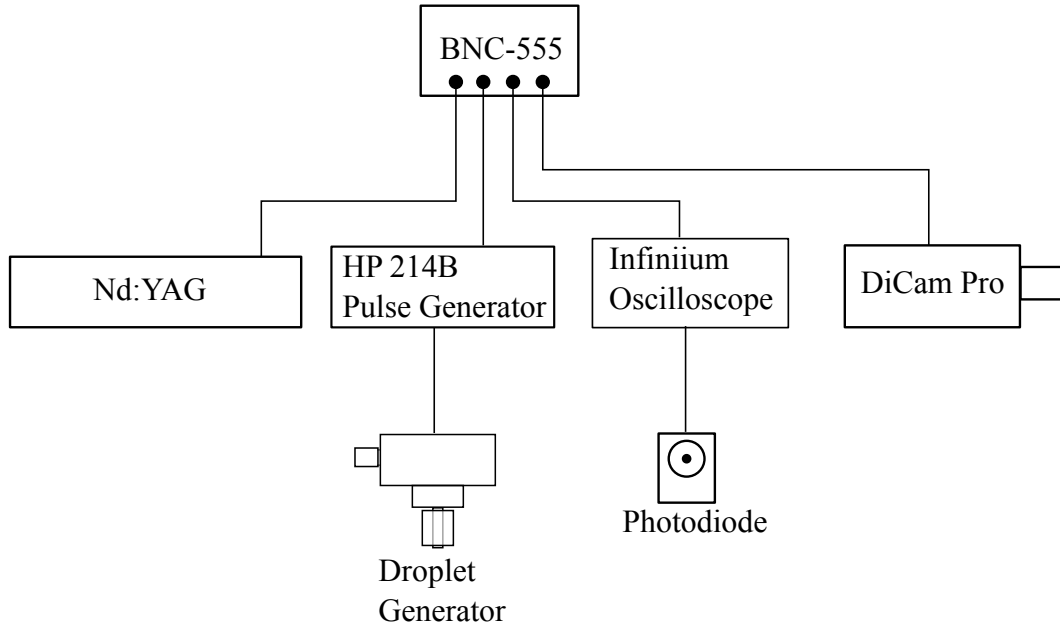
FIGURE 3.7. A diagram shows the paths by which the BNC-555 controlled timing of the major components of the experiment.

the laser pulse was approximately 10 ns long, this allowed for a 15 ns buffer ahead of and behind the arrival of the laser sheet in the field of view. This technique was necessary because there was some temporal jitter in the arrival time of the laser sheet. Specifically, for a fixed interval between pulses, the arrival time of the sheet varied by a few nanoseconds from pulse to pulse. It was somewhat time-consuming to set the timing for a gate as narrow as 40 ns. Having a much longer gate would have made timing trivial, but there would be a greater risk of the camera imaging other light unrelated to fluorescence. With a narrow, 40 ns gate, no special effort was required to control stray light, such as operating the system with room lights off.

A photodiode was installed to monitor average power of the laser beam. The signal from the photodiode was acquired by the 4 GHz Agilent Oscilloscope, which was triggered by a signal from the BNC-555. This quantity was important for NO PLIF because the required Coumarin 450 laser dye had a short lifetime. The average power of the beam declined over

the course of a few hours, so it was necessary to normalize fluorescence images with respect to it. This was in contrast to OH PLIF which uses Rhodamine 590, a dye with a lifetime on the order of several weeks.

Establishing the timing of the ICCD camera was accomplished in the following manner[15]. A business card or other heavy paper was placed in the path of the laser sheet so that light was scattered *away* from the camera lens. A small fraction of laser light managed to penetrate the paper and was imaged by the camera. The iris of the imaging lens on the camera was opened a minute amount to further reduce the amount of light falling on the cathode. The ICCD camera output a square wave that corresponded to when the intensifier gate was open. This signal, along with the beam power monitoring photodiode was imaged on an oscilloscope. The position of the camera gate could then be made coincident in time with the beam power photodiode signal by varying the camera delay on the BNC-555. This caused the image of the laser sheet passing through the paper to be visible. It was then a simple matter to center the laser pulse in time relative to the 40 ns gate by adjusting the delay of the camera triggering signal.

The HP 214B pulse generator was also triggered by the BNC-555 which caused a droplet to be expelled from the nozzle of the droplet generator (ten times per second). The droplets were backlit with a halogen work light illuminating a translucent plastic sheet. The ICCD camera was set to a 30 microsecond gate so droplets appeared as dark spots on an even grey background. The pulse generator delay was adjusted until the drop appeared in the center of the field of view.

---

[15]It should be noted that this procedure should be undertaken with extreme care, it being entirely possible to permanently damage the cathode of an ICCD camera if too much light is imaged onto it.
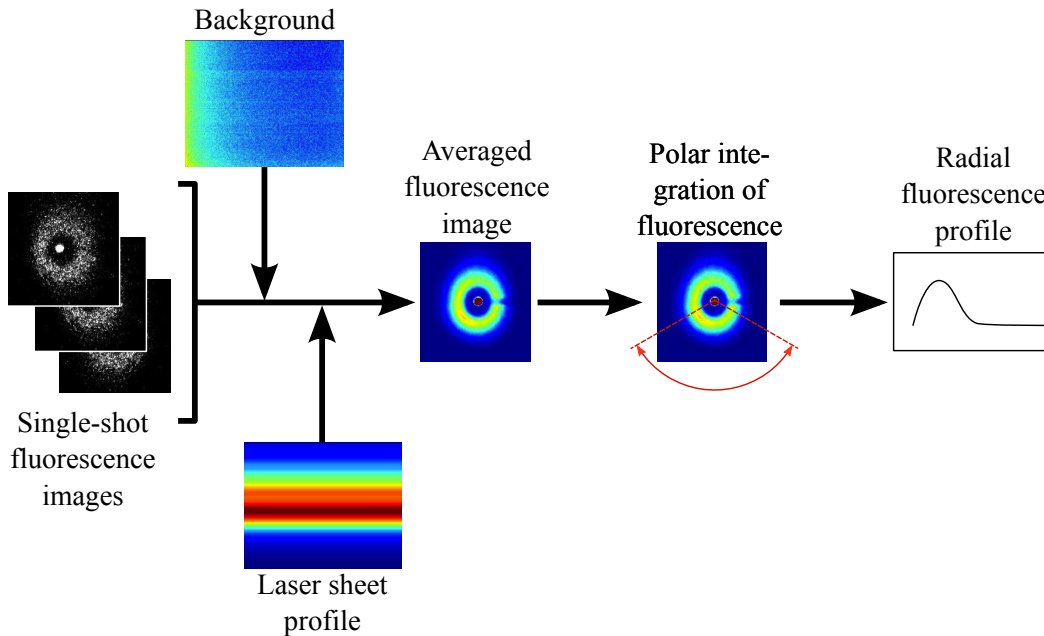
FIGURE 3.8. A flow diagram illustrates the sequence of image manipulation required to produce profiles of OH and NO from fluorescence images.

3.7. FLUORESCENCE IMAGE PROCESSING

Due to the low signal level of the fluorescence, single-shot images were inadequate for obtaining profiles of OH and NO species in the droplet flames. Instead, it was necessary to acquire hundreds of frames and average them together. This section describes the process used to produce radial profiles of NO and OH from large collections of single-shot fluorescence images.

The difference in fluorescence signal intensity between OH and NO PLIF corresponded to a difference in the number of single-shot fluorescence images acquired for each fuel. For all OH PLIF cases, because of the relatively high signal intensity, about 250 images were acquired. In the other extreme, methanol flames produce very little NO, so more than 1400 frames were required when conducting NO PLIF on that fuel.

An overview of the image processing conducted is illustrated by the flow diagram in Figure 3.8. Each frame in a group of single-shot fluorescence images had the background

subtracted off, then was normalized by the laser sheet profile image. After this manipulation, all of the single-shot fluorescence images were then averaged together to create an averaged fluorescence image. A fluorescence profile was created by applying polar coordinates with the origin at the droplet center in the average fluorescence image and averaging the pixel intensity azimuthally about the origin. Image processing of the fluorescence images was conducted using scripts written by the author in MATLAB, which are included in Appendix G. A detailed explanation of the image processing procedure follows below.

Fluorescence videos of droplet flames captured by the ICCD camera were saved in a proprietary format. Each of the 290 frames of the video were then exported as individual "tif" format images using the camera control software. The resolution of the images was 512×640 pixels[16]. The horizontal and vertical position of droplets varied from one to the next. As such, the droplet[17] and the surrounding fluorescence appeared at different spatial locations in sequential frames. This being the case, it was necessary to locate the droplet and fluorescence in each single-shot fluorescence image and store the associated coordinates. The MATLAB script `xcorr_drop_center_AC.m` accomplished this task by loading one of the single-shot fluorescence images and taking the two-dimensional cross correlation of it with a previously-stored canonical droplet image. The result of the cross-correlation was a two-dimensional surface in which the surface height corresponded to the location in the single-shot fluorescence image at which the droplet image appeared most similar to the stored

---

[16]The resolution of the ICCD camera sensor was 1024×1280, but the pixels were binned 2×2 to improve sensitivity to fluorescence. Hence, the reduced image resolution.

[17]Laser light was scattered by the droplet, the wavelength of which was largely blocked by the optical filter mounted on the camera. Ideally, the filter would transmit exactly zero photons of the laser wavelength. In practice, the transmissivity of the laser wavelength by the filter is very small, but not zero. For example, the filter used for NO PLIF had a bandpass of 248 ± 5 nm and transmitted light at the laser wavelength of 226.03 nm at a rate of less than 6 parts per million. However, because the laser light scattered by the droplet was so intense, some laser light managed to pass through the filter and was imaged by the ICCD, making the the droplet visible. See Appendix E for a further discussion of optical filters for PLIF.

(A) Single-shot OH PLIF image   (B) Averaged OH PLIF image
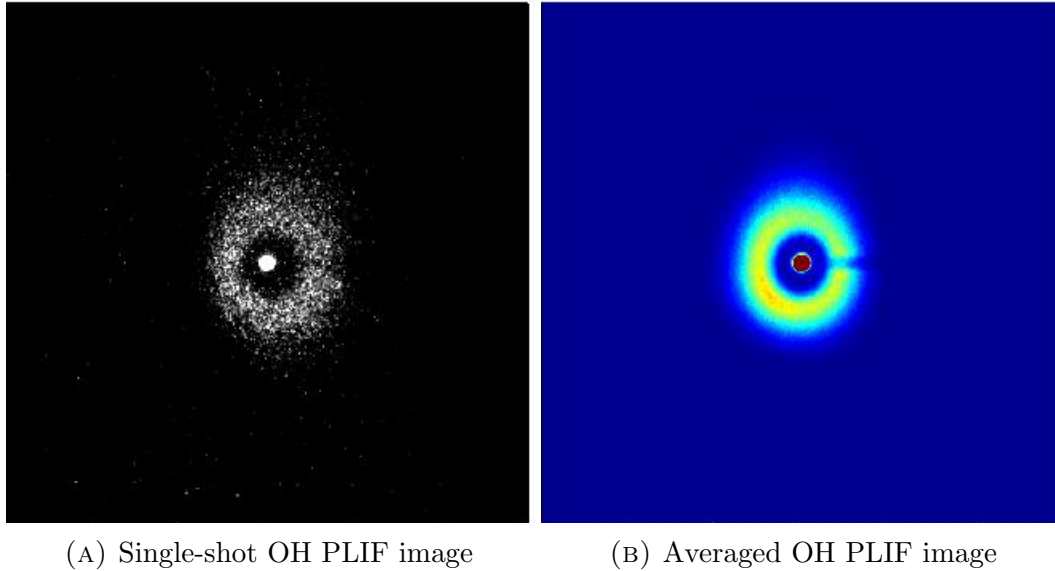
FIGURE 3.9. Example images produced during image processing of OH PLIF image data of 1-propanol droplet flames.

canonical droplet image. Thus, the location of the peak of this surface can be manipulated to obtain the coordinates of the droplet in the single-shot fluorescence image. This process was repeated on all single-shot fluorescence images in a group to obtain a list of coordinate pairs for the location of the droplet in every frame. A crude filter was implemented where if the peak of the cross correlation did not exceed a pre-determined threshold, the frame was discarded. This caused those frames to be discarded wherein the droplet happened to fall outside of the laser sheet and therefore were not properly centered. Approximately 1% of frames were discarded by this mechanism.

The coordinate pairs for the location of the droplet were passed to the next MATLAB script: `avg_fluor_image_AU.m` where the majority of image manipulation occurred. In this script, each single-shot fluorescence image was sequentially processed then the entire group averaged together. A description of the procedure follows. First, the image was loaded and the average background image was subtracted. This subtraction procedure caused a small number of pixels to acquire negative values; these were set to zero. The resulting image was

then normalized by the laser sheet. Next, the image was normalized by average laser power. This step was especially important for NO PLIF images since the laser power declined due to deteriorating laser dye over the course of repeated fluorescence video acquisitions. The coordinate of the droplet determined by the previous script was used to crop out a 600×600 pixel image with the droplet at the center. A typical example of such an image appears in Figure 3.9A which contains a single-shot OH fluorescence image of a 1-propanol droplet flame. All such images were averaged together to created an averaged fluorescence image like the one in Figure 3.9B. The averaged fluorescence image is saved as a binary data file for use by the next script.

The bright white circle at the center of Figure 3.9 is the droplet and the diffuse ring of white pixels around it is OH fluorescence. The flame and associated OH field is, of course, nearly spherical in shape. However, since the laser sheet is thin compared to the diameter of the flame, the fluorescence visible in the image is a slice of the sphere, hence a ring shape. Since OH is an important combustion intermediate, the flame can be assumed to reside roughly in the middle of the fluorescence. The dark region between the droplet and the fluorescence contains mostly fuel vapor and products of combustion (i.e., no intermediates like OH). Therefore, it is reasonable that the region is dark since fluorescence species are absent there.

Notice the droplet is off center relative to the ring of fluorescence. This is caused by convective flow features (e.g., turbulent eddies) of the surrounding ambient deforming the flame relative to the droplet. Ideally, there would be no distortion because the ambient would be quiescent relative to the droplet and flame. The experiments here only approximates such conditions, so some distortion is inevitable. By acquiring a sufficiently large number of
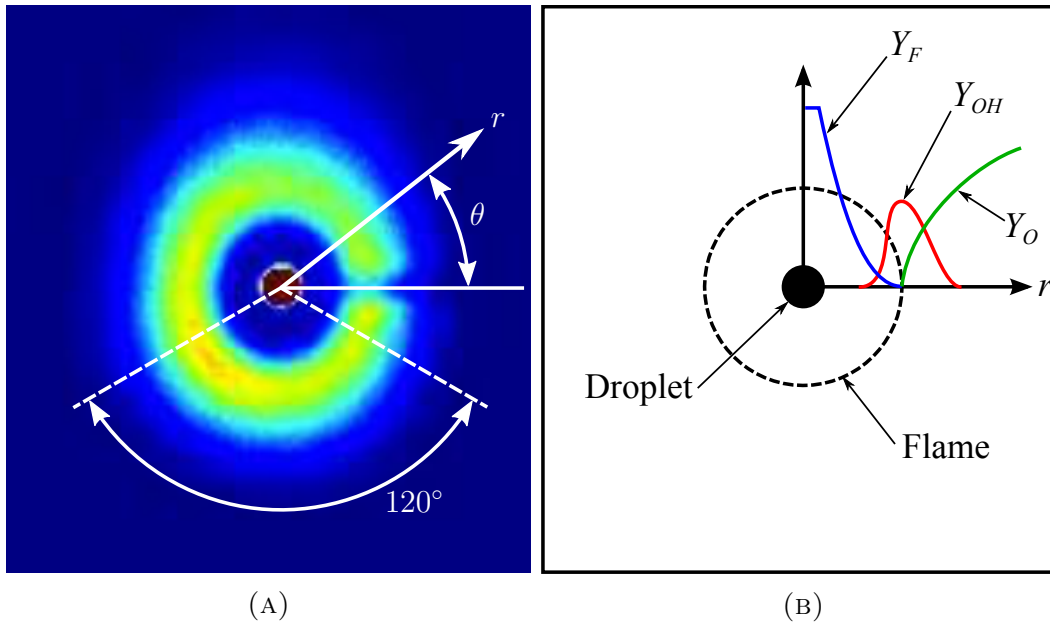
FIGURE 3.10. (A) Diagram overlaying an averaged fluorescence image for OH PLIF shows the angle over which the fluorescence intensity is averaged. (B) Schematic drawing of a burning droplet showing radial mass fraction contours for fuel, oxidizer, and OH.

single-shot fluorescence images, the statistically-random distortions become smoothed when the images are averaged.

The third and last image processing script is `fluor_profile_NO_AE.m`. It loads the averaged fluorescence image and finds an average fluorescence profile. It does so by applying a polar coordinate system with the origin at the droplet center and averaging pixel intensity in the angular direction from $210°$ to $330°$, a sector of $120°$ as shown in Figure 3.10A. The fluorescence was not averaged about $360°$ because the laser sheet intensity had poor uniformity from top to bottom, causing the fluorescence to be likewise non-uniform. If laser-induced fluorescence were a purely linear process, then normalizing the fluorescence image by the laser sheet intensity profile would ameliorate the non-uniformity. Unfortunately, it is only linear for laser intensities much lower than those used in these experiments. It is apparent in Figure 3.10A that the fluorescence intensity is non-uniform around the droplet. There is
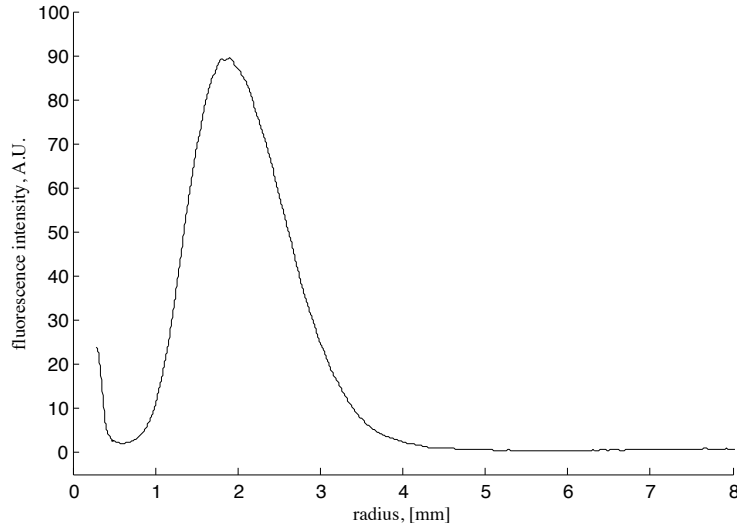
FIGURE 3.11. Example of a fluorescence profile obtained by averaging the pixel intensity from an averaged fluorescence image.

a bright region on the left side of the sector and a relatively dim region from about 45° to 90° degrees. (The dark bight at zero degrees is caused by the droplet obstructing laser light coming from the left.) This variation is not caused by differences in OH concentration, but rather that of laser sheet intensity from top to bottom. For these experiments, the timing was set so that the fluorescence image was created when the brightest part of the laser sheet was passing through the bottom part of the droplet flame. Furthermore, as explained above, the fluorescence was averaged over a narrow angular sector to minimize effects of the laser sheet intensity variation. Figure 3.10B contains a drawing which shows an idealized flame and droplet with representative profiles of fuel, oxidizer, and OH.

When the pixel intensity is averaged as described above, a profile of the fluorescence like the one in Figure 3.11 is produced. The peak in intensity from 1 to 4 mm is due to fluorescence. The local minima at approximately $r = 0.6$ mm is the region between the droplet surface and the flame that does not contain any fluorescing species. The increase in intensity between zero and 0.6 is due to the image of the droplet and is not fluorescence.

The data is truncated at radii smaller than the local minima then the radial coordinate is normalized by droplet radii.

Fluorescence images from the six fuels examined were treated identically so that the fluorescence intensity for the respective species could be compared. For example, by comparing the NO fluorescence from methanol and n-heptane, it is apparent that n-heptane flames produce more NO. Likewise, OH fluorescence profiles can be compared among fuels. On the other hand, it is not meaningful to compare fluorescence profiles of OH and NO, even if the fuel is the same. This is so because the optical setups that captured fluorescence from OH and NO were disparate systems, with different losses and fluorescence efficiencies. For example, the optical filter used for OH fluorescence had a much higher transmissivity for the OH fluorescence bands than the NO filter had for NO fluorescence bands. All else being equal, OH may then appear to be present in much higher concentrations than NO. This may or may not be true[18] but it cannot be determined solely by examining the relative fluorescence intensities of the two species produced by these experiments. In order to be able to compare profiles, it would be necessary to produce fully quantitative fluorescence images, a technique that is particularly challenging and beyond the scope of the research reported herein.

3.8. Some Practical Matters of Experiment Implementation

During the course of setting up, debugging, and executing the experiments, a number of lessons were learned, some of which were subtle and some less so. This section will a include brief explanation of these lessons to help future experimentalists and those seeking an especially thorough understanding of the work reported herein.

---

[18]It *is* true for the fuels and conditions studied here based on modeling results.

Further discussion of the droplet generator is warranted here because these devices often prove difficult to operate consistently. If a single general observation could be distilled from months of experience with the droplet generator, it would be that nearly all problems with droplet formation could be attributed to bubbles in the device. As noted in Lee's PhD thesis [82], the importance of ensuring that no bubbles are present in the droplet generator cannot be over-emphasized. Some tips on how to eliminate bubbles are discussed here.

In the experiments described herein, both the droplet generator and fuel reservoir were mounted on optical rods so their respective positions could be easily adjusted. When filling with a new fuel, the droplet generator was flipped upside-down and reservoir was raised approximately 30 mm above the nozzle exit as depicted in Figure 3.12A. Fuel was added to the reservoir (with a large syringe) until it was seen issuing from the nozzle exit. The reservoir was then quickly lowered until fuel no longer flowed from the nozzle, but not so low that fuel withdrew from the tip of the nozzle (See Figure 3.12B). Then, a small syringe (~ 20 ml) with a short length of flexible tubing was attached to the glass nozzle, and fuel and bubbles were drawn out of the chamber of the droplet generator. This procedure was done repeatedly (2-3 times) until no bubbles were seen to leave the chamber. Tapping on the body of the droplet generator with the plastic handle of a screw driver helped dislodge bubbles so they could be drawn out of the chamber with the syringe. Following this procedure, the droplet generator was carefully turned right-side up and the reservoir was lowered slightly so the level of the fuel was at the level of the nozzle exit as shown in Figure 3.12C.

The Hewlett-Packard 214B Pulse Generator produced a square wave pulse to actuate the piezoelectric disk. The pulse width was set to 1.687 ms for all experiments and the amplitude varied from 40 to 60 volts depending on the fuel. It was discovered that the
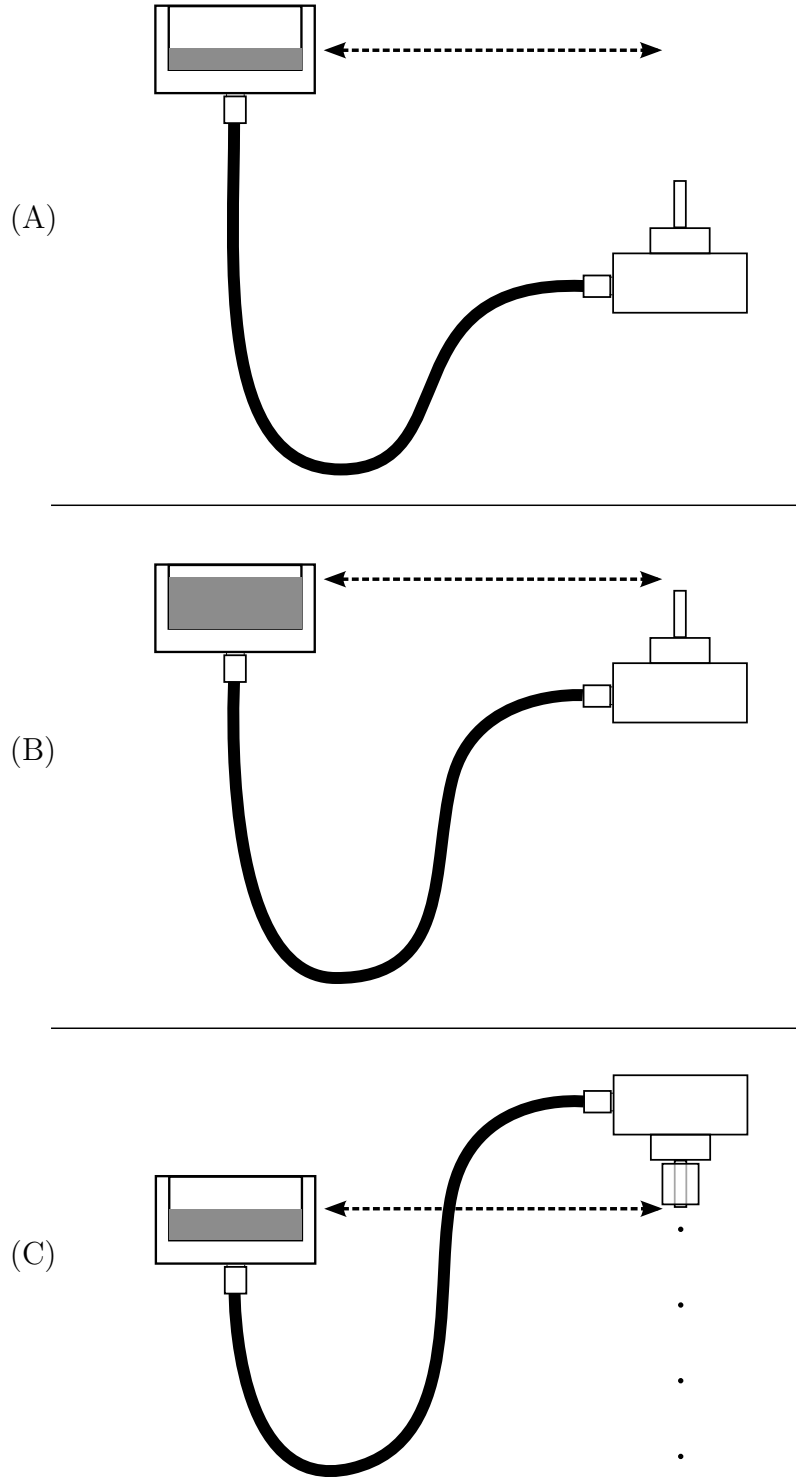
FIGURE 3.12. Diagrams depicting relative elevations of reservoir contents and droplet generator nozzle during (A) filling with fuel, (B) extracting bubbles, and (C) droplet generation.

degree to which the screws holding the piezoelectric disk were tightened affected the voltage required to produce droplets, and presumably the droplet diameter as well. In the future, a new design should be conceived in which the disk is held with a consistent repeatable pressure so that pulse voltage would be the only parameter dictating droplet diameter for a given fuel[19]. Regardless, for any given fuel, it was determined that there was a small range of voltage over which a stream of single droplets was created. Voltage above or below this range created multiple droplets[20], or no droplets at all. Appendix F contains further discussion of droplet generation and solutions to problems which might be encountered in future work.

The droplet generator was mounted on a micrometer-actuated linear stage so that its position orthogonal to the laser sheet could be adjusted. Once the timing delay of the both the droplet generator and the ICCD camera were set (see below), the linear stage was used to position the droplet generator so that the droplets fell through the laser sheet. The alignment of the laser sheet with droplet trajectory was verified by observing the image of the laser sheet on a business card. If the droplet generator was well aligned, the shadow of the droplet was apparent.

As noted earlier in this chapter, it was determined that it was important to minimize heat transfer from the ignition coil to the droplet generator. In addition to mitigation measures like the heat shield and nozzle insulator, the coil was mounted on a spring-loaded linear stage. While preparations for experimentation were under way, or the coil was heating up, it was positioned away from the droplet generator by a locking pin. Once all was ready, the pin was released and the droplet generator slid into position so that droplets fell through

---

[19]On the other hand, such a feature might be exploited as a method to vary the diameter of droplets produced without changing out nozzles of various diameters. In other words, varying the holding pressure on the piezoelectric disk may correspondingly vary the droplet diameter.

[20]Under certain conditions, it was possible to generate two droplets side-by-side. The investigation of combustion in this configuration could be an interesting avenue of future work.

the coil and were ignited. As soon as the camera had filled its buffer, the coil was pulled away from the droplet generator and the pin inserted. In this way, the hot coil was located directly beneath the droplet generator only when the experiment was ongoing. Minimizing the time the hot coil was near the droplet generator by using the linear stage significantly reduced problems with fuel boiling compared to an earlier iteration in which the coil was fixed under the droplet generator at all times.

The DiCam Pro ICCD camera used for fluorescence imaging had a bit depth of 12. Therefore, each pixel of the CCD sensor was capable of discerning $2^{12} - 1 = 4095$ shades of gray with a pixel count of 0 being absolutely black and 4095 being bright white. Since the fluorescence signals were so weak, even the brightest pixel managed a count of only about 270 out of 4095. Moreover, dark current and other unavoidable phenomena cause the darkest pixel count to be around 65. Therefore, all of the fluorescence information captured by the camera resided in a band of pixel counts from 65 to 270. This being the case, the typical image processing technique of contrast stretching was applied to every fluorescence image so that pixel counts of 65 were identified as being absolutely black, and pixel counts of 270, bright white.

3.9. Experimental Sequence

This section contains the sequence of steps that were required to conduct each experiment. Detailed discussion of the technically challenging steps are found elsewhere in this chapter and in the appendix.

(1) The reservoir and droplet generator are filled with fuel.

(2) Bubbles are extracted from the body of the droplet generator.

(3) The HP 214B pulse generator is activated to start droplet production.

(4) Droplets are inspected with a strobe light and adjustments are made as necessary, then the pulse generator is stopped.

(5) Timing delay of the camera is set using a business card.

(6) Droplet generator is resumed and backlight for droplets is installed.

(7) Camera is set to 30 microsecond gate to image the drops against the backlight.

(8) Adjustments are made to the timing delay of the pulse generator so the droplets appear in the center of the field of view of the camera.

(9) The laser is turned on and the position of the droplet generator is adjusted until the shadow of the droplet is visible in the image of the laser sheet on a business card.

(10) The laser is shuttered and the position of the heat shield and ignition coil are checked to ensure the droplets fall straight through the center.

(11) The camera is set for acquisition with a gate of 40 ns.

(12) The coil is positioned away from the droplet generator and the variac is turned on to heat the coil.

(13) Once the coil has reached a steady state (about a minute), the laser shutter is opened.

(14) The ignition coil is moved under the droplet generator and a quick visual ispection is made to ensure drops are igniting.

(15) The camera is activated and it begins to acquire fluorescence images.

(16) While the camera is acquiring, the timing of the pulse generator is adjusted in real time to keep the droplet in the center of the field of view. It is also necessary at times to adjust the position of the droplet generator with the linear stage to ensure the drops fell through the laser sheet.

(17) When the camera buffer is full (290 frames), the coil is moved away from the droplet generator and pinned in place.

(18) The laser is shuttered.

(19) If more frames are to be acquired, the droplet generator and coil are left activated.

(20) The frames just captured by the camera are saved on the PC as a raw recorder sequence.

(21) The camera is reset to obtain a further batch of frames.

(22) The steps are repeated until an adequate number of frames are acquired.

3.10. Sources of Error in Experiments

The configuration of the experiments conducted for this dissertation were not optimal for obtaining the highest quality PLIF data. Specifically, ignition of the droplets by a coil and mitigating buoyancy with a suction pipe could be improved. Rather, these experiments were considered to be an intermediate step so that the best practices could be formulated and the path forward made clear by lessons learned. A scheme that is thought to be optimal and is heavily influenced by the experience from conducting the experiments reported herein is described in Section 7.1.1. Meanwhile, the purpose of this section is to discuss the sources of error in the experiments as implemented.

Droplets formed by the droplet generator fell under the influence of gravity and passed through the center of the coil. When current was supplied to the coil, it heated the air through which the droplet fell, thereby enabling thermal autoignition. For the sake of comparing NO formation among the fuels tested, it would be best if the temperature were identical for every experiment. This attribute is necessary because the temperature of the air will influence the flame temperature, which in turn will dictate the rate of NO formation. Specifically, the

flame temperature increases with increasing air temperature. Therefore, if it is the intent to compare the NO formation among the respective fuels, it would be best to remove air temperature as a variable.

One might imagine that the temperature of the coil has no influence on the flame at the time at which the fluorescence images were acquired because the droplet was well below (at least 14.8 mm; see Figure 3.4) the bottom of the coil. As such, the coil-heated air and whatever influence it had on the flame temperature is far in the past (many milliseconds). This, however, is not consistent with observations. Recall from Section 3.4 that the flow pipe is drawing air downward to mitigate droplet flame distortion by buoyancy. Some of the coil-heated air is drawn downwards as well, and therefore the heat produced by the coil will affect the air temperature in the region in which the fluorescence images are acquired.

The reason it was necessary to vary the temperature (and therefore the heat production) of the coil was that some fuels were more difficult to ignite reliably than others. For example, n-heptane was very easy to ignite in that the coil need not be very hot to reliably ignite every droplet. On the other hand, methyl decanoate was very difficult to ignite consistently[21] and required a very hot coil. In fact the coil had to be so hot that several were destroyed in the course of methyl decanoate experiments. As such, instead of a consistent temperature for all of the experiments, it was necessary to vary the amount of heat output for the respective fuels.

Ultimately, the temperature of the oxidizer being consumed by the droplet when the fluorescence image was taken may vary from fuel to fuel. As such, the Zel'dovich NO formation

---

[21]Which is puzzling because the cetane numbers of methyl decanoate and n-heptane are roughly similar. Therefore, the degree of chemical reactivity should be similarly comparable. Moreover, a discrepancy between the heats of vaporization for the respective fuels cannot provide an explanation either that quantity is similar as well.

path may be enhanced for those fuels (e.g., methyl decanoate) for which a particularly hot coil was necessary. Naturally, this difficulty would be a non-issue if droplet were to fall into a chamber of consistently heated air (or other oxidizer).

As explained in Section 3.2, laser-induced fluorescence (LIF) is a technique wherein light is measured that is produced when combustion species interact with laser light of a particular wavelength. LIF is not, in general, a linear process. For example, if one doubles the intensity of the laser beam, the intensity of the corresponding fluorescence will not necessarily likewise double. In fact, it is possible to achieve a state of saturation in which an arbitrary increase in laser energy will cause no change whatsoever in the fluorescence intensity. Linear behavior is seen in laser-induced fluorescence only when laser power is very low. This is called the "linear fluorescence regime" and is used for quantitative point measurements of species concentration or gas-phase temperature. The linear regime produces much too little fluorescence to be useful for planar imaging purposes with present camera technology. As such, it is necessary to conduct planar laser-induced fluorescence (PLIF) spectroscopy in the non-linear regime to obtain as much fluorescence signal as possible. The non-linear regime resides in the middle between linear and saturated regime in terms of required laser power. For example, suppose doubling the laser energy increased the fluorescence intensity by 20 percent. If the laser energy is doubled again, the fluorescence might increase by only 5 percent.

The nature of non-linear laser-induced fluorescence comes into play as a source of error when normalizing fluorescence images of droplet flames with the laser sheet intensity. The way in which normalizing takes place is that, very simply, the fluorescence images are divided by the laser sheet images (see Section 3.7). Were the images that of linear fluorescence, this would divide out any variation in fluorescence intensity due to corresponding variation in
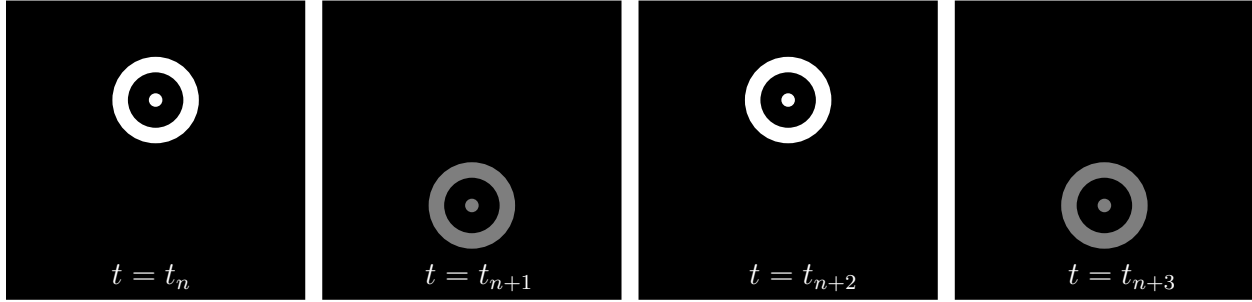
FIGURE 3.13. Sequence of diagrams depicting jitter behavior of the droplet flame.

laser sheet intensity. However, since these experiments were conducted in the non-linear fluorescence regime, some error will be introduced because the intensity of the fluorescence is not linearly related to the laser sheet intensity. Here, the relationship is approximated as being linear. This will introduce some amount of error in the magnitudes of the pixel intensities for the fluorescence images.

This sort of error, introduced when the relationship between laser sheet intensity and emitted fluorescence was treated as being linear, was most apparent in fuels which exhibited an instability referred to here as *jitter*. Consider the diagrams in Figure 3.13 in which the position of the droplet and flame is shown as oscillating from a high to low position in sequential frames ($t = t_n, t_{n+1}, t_{n+2}, t_{n+3}$,). Such behavior was undesirable because the fluorescence intensity was different when it was in the high position compared to the low position because the laser sheet intensity varied over its height. This is depicted in Figure 3.13 by the bright white droplet flame at the top where the laser sheet intensity is high and the dim gray droplet flame at the bottom where the laser sheet intensity is low.

The jitter behavior is caused by some manner of oscillatory instability in the droplet generator and nozzle. Sometimes it can be indicative of the presence of a small bubble in the droplet generator (see Appendix F). However, it was observed that the jitter instability could also be induced by the small amount of liquid fuel heating caused by the proximity

of the ignition coil to the droplet generator nozzle, thereby suggesting it could be linked to liquid fuel viscosity. Regardless, some fuels were more susceptible to jitter than others. Preventing jitter in methyl butanoate and methyl decanoate droplets in particular proved to be challenging. As such, some of the single-shot fluorescence images used to create the averaged fluorescence images for the respective fuels captured this jitter behavior. Therefore, those single-shot fluorescence images that capture the droplet in the low position tend to reduce the intensity of the averaged fluorescence image, making it appear that the concentration of the fluorescing species is lower than it really is. Moreover, jitter would also broaden confidence intervals since the instability would increase the degree of scatter in pixel intensity at any given point in the fluorescence field.

CHAPTER 4

Results: Computer Simulations of Isolated Droplet Autoignition and Combustion

4.1. Introduction

Multiple computer simulations were conducted for the ignition and combustion of an isolated droplet of liquid fuel. The fuels used in the simulation were methyl butanoate (MB), n-heptane (nH), and methanol (MeOH). The chemical mechanisms used in the simulation were created by the author by appending oxides of nitrogen chemistry to existing fuel mechanisms [14, 53, 67, 69], the details of which are found in Section 2.2.2. Simulations for methyl decanoate, ethanol, and 1-propanol were not performed, but are planned for the near future.

The fuel mechanisms used in these simulations have been formulated, reduced, and validated by experts in the field and can be assumed to be as reliable as any chemical kinetic mechanisms [14, 53, 67, 69]. It is worth emphasizing, however, that the production of oxides of nitrogen due to the appended nitrogen chemistry has *not* been validated simply because there are little experimental data by which to do so. Specifically, there are many high-quality experimental studies of NO_x formation in flames of gaseous fuels, but very few of large-molecular mass liquid fuels. As such, the oxides of nitrogen results presented in this chapter should be examined with a critical eye, with the knowledge that these simulations represent a first pass at predicting NO_x formation in practical liquid transportation fuels. That said, useful insights can still be yielded by this initial attempt.

Table 4.1 contains a summary of the figures that contain the simulation gas-phase initial conditions and results with two levels of oxides of nitrogen chemistry. The fuels indicated

TABLE 4.1. Summary of figure numbers containing simulation initial conditions, results with full NO_x chemistry, and results with Zel'dovich NO chemistry for the indicated fuels.

Fuel	ICs	Full NO_x	Zel'dovich NO
Methyl butanoate	4.1	4.2	4.3
n-Heptane	4.1	4.4	4.5
Methanol	4.1	4.6	4.7

as containing "full NO_x" chemistry have Zel'dovich NO, Fenimore NO_x, and N_2O chemical kinetics included in the fuel mechanism. The results under the column labeled with " Zel'dovich NO" contain only Zel'dovich NO chemistry, namely Reactions (R1) through (R3).

The initial conditions for all simulations were the following: initial droplet diameter, $d_o = 200~\mu$m; droplet liquid temperature, 300 K; pressure everywhere fixed at 1 atmosphere; and temperature of ambient air at 1150 K. The plot in Figure 4.1 represents the gas phase initial conditions for the respective fuels for oxygen and fuel mass fraction, and temperature. At initial time ($t = 0$), the mass fraction of the fuel at the droplet surface is specified by vapor-liquid equilibrium and the steep curve is an arbitrary profile specified as an input to the model. The thin thermal boundary layer wherein the temperature rises precipitously from the liquid fuel temperature to the ambient temperature is likewise specified as an input.

In Figures 4.2 through 4.7, the five rows of plots are results from five time steps that were selected for representing important phases of the droplet autoignition and combustion event:

(1) *Induction Period:* Thermal energy is transported from the hot ambient (1150 K) to the cold (300 K) liquid droplet, enabling evaporation. The droplet surface temperature increases, resulting in an increase in fuel mass fraction at the droplet surface ($Y_{F,s}$). Fuel vapor diffuses radially outward into the ambient, creating a mixture of
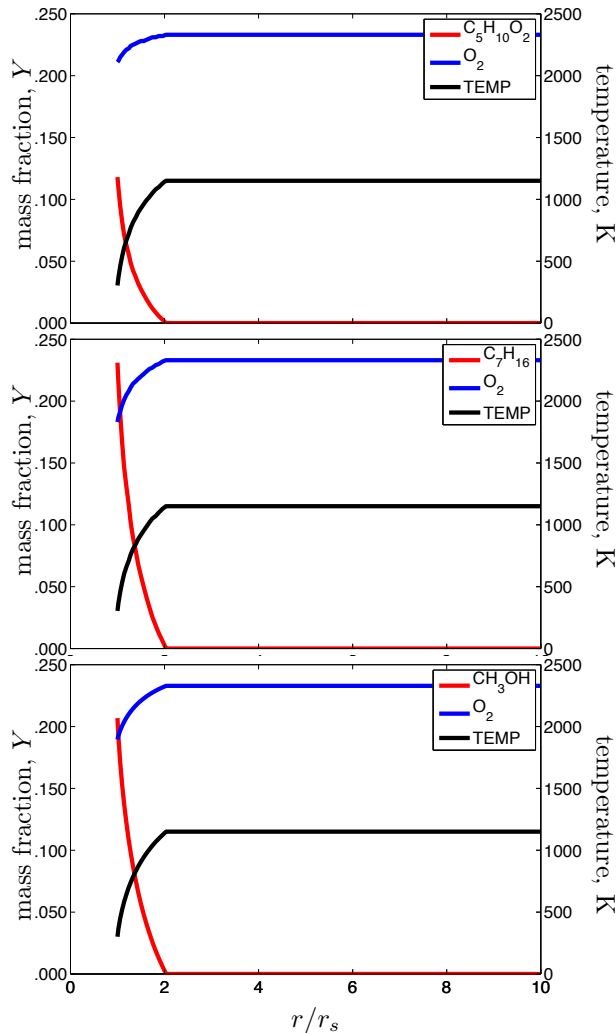
FIGURE 4.1. Gas-phase initial conditions for (top to bottom) methyl butanoate, n-heptane, and methanol.

fuel and air. Induction of chemical reactions take place when fuel vapor from the droplet begins to react with the oxidizer from the ambient.

(2) *Ignition Initiation:* The low-temperature reactions that are the first steps in the autoignition sequence raise the temperature of the gas phase.

(3) *Propagating Reaction Wave:* A chemical reaction wave propagates through the premixed fuel and air toward the droplet. Chemistry is in transition between slow low-temperature activity and that of vigorous combustion.

(4) *Vigorous Premixed Combustion:* Having achieved combustion temperatures ($\sim$2000 K) the reaction wave has become a propagating flame. Chemistry is that of vigorous combustion with high, if not maximum rates, of product formation and heat release.

(5) *Transition to Non-premixed Combustion:* The premixed fuel is exhausted, or nearly so, and the flame must be sustained by oxidizer diffusing from the ambient and fuel diffusing from the droplet surface. Overall chemical reaction rate is at maximum.

(6) *Quasi-steady Non-premixed Combustion:* Non-premixed combustion phase in which the rate of consumption of fuel and oxidizer is limited by the rate at which they are transported to the flame by diffusion. Chemical reaction rates are very high, but slightly reduced from the preceding phase.

As expected, the six phases take place at different times for the respective fuels. However, the time steps between the same fuel with different levels of nitrogen chemistry detail were slightly different as well. This is not surprising because nitrogen chemistry is inherently coupled to fundamental combustion reactions through radicals like OH and O, and fuel fragments like CH and CH_2. As such, the presence (or absence) of nitrogen chemistry reactions will alter the timing and shape of major combustion features to some extent.

Since the three fuels exhibit roughly similar evolution and major combustion features (e.g., the six phases above are evident), only one simulation, methyl butanoate with full NO_x chemistry, is described in great detail below. The remaining simulations, methyl butanoate with Zel'dovich NO; both n-heptane simulations; and both methanol simulations, are addressed briefly with notable differences being identified. In this chapter, the simulation results follow immediately. Section 4.3 contains a discussion of major combustion features of the three simulations. In Section 4.4, NO_x formation in the simulations is explored.

4.2.1. Methyl Butanoate with Full NO$_x$ Chemistry. Plots containing results for methyl butanoate with full NO$_x$ for selected times are shown in in Figure 4.2. Each row of two plots represents data from a single timestep indicated at the top-center of the left-hand plot. The left-hand plots contain curves for fuel mass fraction, molecular oxygen mass fraction, mass fraction of major products of combustion, and temperature. The right hand plots contains mass fraction curves for OH, O, NO, N$_2$O, and NO$_2$. Equivalence ratio is also presented in the right hand plots and, because it is defined with respect to oxygen instead of air, is formulated thus:

$$\phi = \frac{(Y_{\text{oxy}}/Y_{\text{fuel}})_{\text{stoic}}}{Y_{\text{oxy}}/Y_{\text{fuel}}} = \frac{Y_{\text{fuel}}/Y_{\text{oxy}}}{(Y_{\text{fuel}}/Y_{\text{oxy}})_{\text{stoic}}}. \tag{50}$$

Horizontal axis represents radial distance normalized by the time-dependent droplet radius: $r/r_s(t)$. All plots share identical horizontal axis scales that are labeled at the bottom of the figure.

4.2.1.1. *Methyl Butanoate, Full NO$_x$, $t = 27.1$ milliseconds.* The first row of plots in Figure 4.2 shows the state of the simulation at $t = 27.1$ ms. The increase of temperature at the droplet surface $(r/r_s = 1)$ has increased so that $Y_{\text{F,s}}$ is well above 0.25. The elevated $Y_{\text{F,s}}$ is evidence of ongoing evaporation of the liquid fuel enabled by heat absorbed from the hot ambient. The resulting fuel vapor has diffused radially outward as indicated by the Y_{F} curve extending beyond $r/r_s = 25$. The increase in fuel concentration has displaced molecular oxygen near the droplet surface. Heat transfer to the droplet has created a thermal boundary layer so that temperature remains below ambient in the region between the droplet surface $(r/r_s = 1)$ to approximately $r/r_s \approx 10$. Nothing is evident to suggest chemical reactions
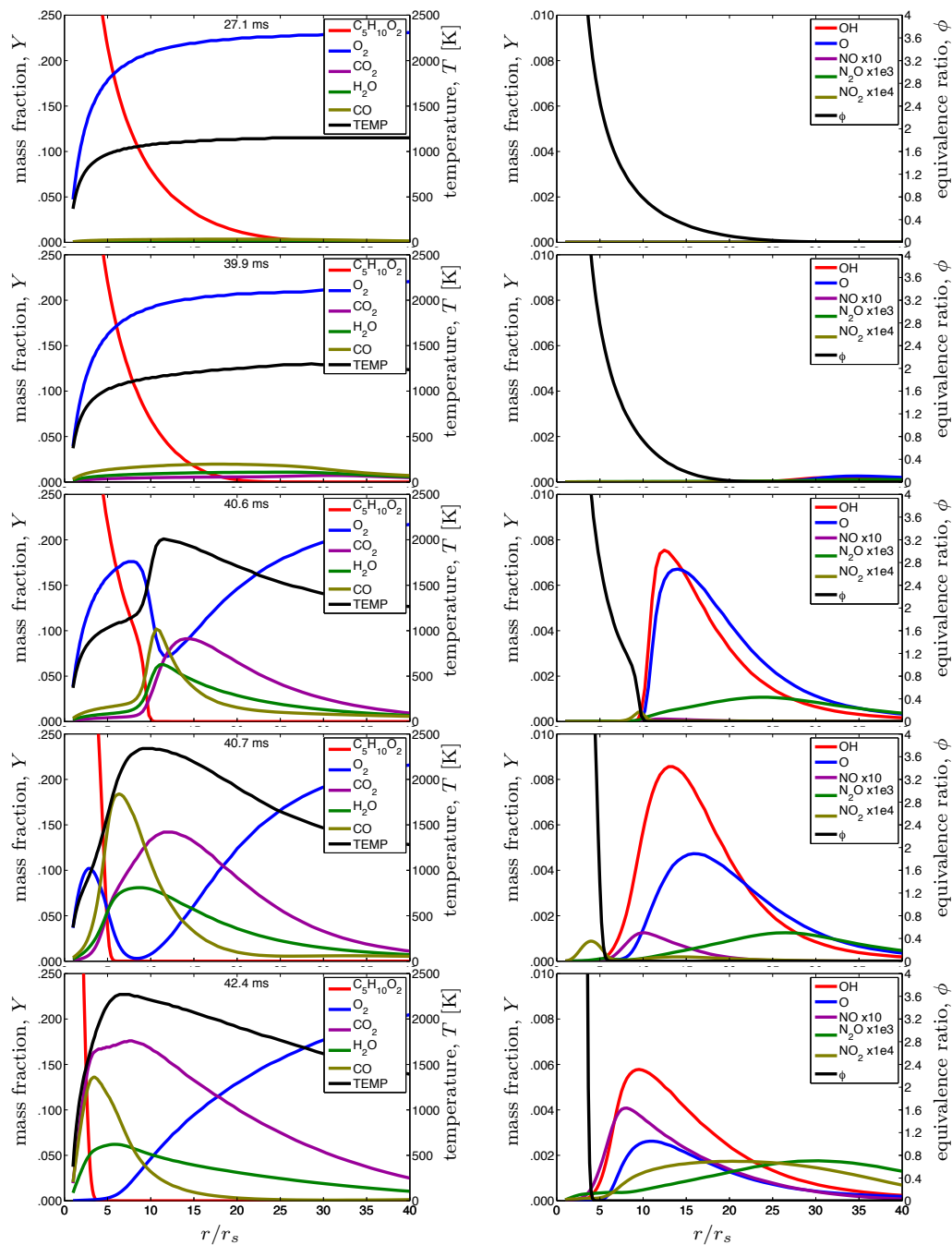
FIGURE 4.2. Calculated species mass fraction and temperature and in the gas-phase surrounding a 200 μm diameter methyl butanoate droplet at the indicated time steps. Calculations were performed with full NO_x chemistry.

are proceeding since the OH and O curves in the right plot appear to be zero everywhere.

However, chemical reactions *are* occurring in the regions in which fuel and oxidizer are mixed.

The equivalence ratio curve in the right hand plot demonstrates the stratified stoichiometry of

the mixture. Near the droplet surface, ϕ is very large, but with increasing normalized radius, the equivalence ratio smoothly asymptotes to zero. At a normalized radius of $r/r_s = 8$, the mixture is stoichiometric, i.e., $\phi = 1$.

4.2.1.2. *Methyl Butanoate, Full* NO_x , $t = 39.9$ *milliseconds.* The second row of plots shows the state of the simulation at $t = 39.9$ ms. Most notable in the left-hand plot is the methyl butanoate curve has become flattened. In the prior time step, the fuel curve was clearly nonzero beyond $r/r_s \approx 25$, now it is close to zero at $r/r_s \approx 20$. The reduction in mass fraction of methyl butanoate is evidence of early, exothermic chemical reactions consuming the fuel and causing the methyl butanoate concentration to be locally reduced. Further evidence is found in a broad rise in temperature with a low peak at around $r/r_s = 28$. Corresponding to the peak in temperature is a shallow dip in oxygen mass fraction. Small quantities of CO_2 and H_2O are now present for $r/r_s > 1$ as well. These features demonstrate the asymptotic nature of ignition. The Y_{MB} curve appears to be nominally zero at the location of the temperature peak ($r/r_s = 28$). Nonetheless, the residence time for fuel vapor diffusing through an oxygen-rich environment at $T \approx 1150$ K increases with radius. Therefore, the initial onset of ignition as indicated by the low peak in temperature is expected to be far from the droplet surface in very lean conditions. In fact, so lean as to make the mass fraction of fuel at $r/r_s = 28$ *appear* to be zero. However, although not shown in the plots, fuel fragments are transported to the region near $r/r_s = 28$ and participate in chemical reactions.

The left plot shows that there is a small amount of OH and O centered about $r/r_s \approx 35$. As these radicals are indicators of chemical reactions, it is interesting that they appear at $r/r_s = 35$ instead of where the temperature peak is located at $r/r_s = 28$. The presence of OH and O near $r/r_s = 35$ can be explained by the increased availability of hot molecular

oxygen at that location, which would enhance the rate of the chain-branching reaction:

$$H + O_2 \longrightarrow OH + O.$$
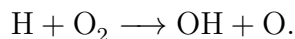
4.2.1.3. *Methyl Butanoate, Full NO$_x$, $t = 40.6$ milliseconds.* At $t = 40.6$ ms, the simulation is in an intermediate state where the rates of chemical reactions and heat release are increasing rapidly, but vigorous combustion has not yet been achieved. The maximum temperature of 2010 K is located at $r/r_s = 13$, which is 15 normalized radii closer compared to the maximum temperature location at the previous time step. The change in location of the maximum temperature means that a chemical reaction wave is propagating from where it started at approximately $r/r_s = 28$, inwards toward the droplet surface. Not only is the reaction wave propagating, but it is increasing in activity as well. This is indicated by the dramatic increase in temperature compared to the last time step and the marked localized decrease in oxygen mass fraction. Moreover, the methyl butanoate curve has developed a knee that is caused by the localized consumption of the fuel by the chemical reaction wave. Also evident are combustion products carbon dioxide, carbon monoxide, and water.

It is worth emphasizing that at this time step ($t = 40.6$ ms), the reaction wave is propagating into premixed fuel and air. It is apparent there is a fuel-air mixture because both the methyl butanoate and molecular oxygen curves are non-zero in the region between the droplet surface and reaction wave ($1 < r/r_s < 13$) in the left-hand plot.

The right plot at $t = 40.6$ ms shows more evidence for rapidly increasing reaction rates given that there are substantially greater quantities of OH an O centered around $r/r_s = 13$, the same location as maximum temperature. Not surprisingly, the equivalence ratio exhibits a knee similar to the one in the methyl butanoate curve, and for the same reason. Also,

oxides of nitrogen are seen at significant quantities for the first time. All three NO_x species are observed to occur at a mass fraction of a few parts per million. It is certain these species are formed via the Fenimore or N_2O-path NO_x mechanisms because Zel'dovich NO chemistry is much too slow to have produced NO_x species so early in the ignition phase. Moreover, Zel'dovich NO chemistry only produces NO, so N_2O and NO_2 can only have come from Fenimore or N_2O-path.

4.2.1.4. *Methyl Butanoate, Full NO_x , $t = 40.7$ milliseconds.* One-tenth of a millisecond later at $t = 40.7$ ms, the peak of the temperature curve has moved still closer to the droplet surface to $r/r_s = 9.6$, which is four normalized radii closer than the last time step. Also, the peak temperature has risen to 2340 K, which is nearly the maximum temperature for the simulation. This being the case, there can be no doubt that vigorous combustion is ongoing at this time step and the flame is located at or very near $r/r_s = 9.6$.

The peak in the molecular oxygen curve at $1 < r/r_s < 9$ with a local maximum at $r/r_s \approx 3$ indicates there remains premixed fuel and air between the droplet surface and the flame. However, the mixture is very rich as can be seen by examining the equivalence ratio curve in the right plot. At $r/r_s = 3$, the equivalence ratio curve is off the plot, but the slope of the ϕ suggests it is a large number (meaning the mixture is very rich). The flame will not propagate through a mixture that is so rich, instead the mixture will be consumed as it diffuses outward toward the flame.

Since vigorous combustion is ongoing, it is no surprise that there are products of combustion CO_2 and H_2O present at the flame. The long tails on the right side of the CO_2 and H_2O mass fraction curves are evidence of diffusive transport of CO_2 and H_2O away from the

flame and into the ambient. In the right plot, the amount of OH continues to increase, but atomic oxygen appears to have decreased somewhat from the last time step.

Examining the NO_x curves in the right plot at $t = 40.7$ ms, shows that significant NO formation is occurring because there is a significant increase in the height and width of the NO mass fraction curve. There is N_2O and NO_2 evident as well, but their concentrations are orders of magnitude smaller than NO. It is not evident from which chemical kinetic mechanism (or mechanisms) the NO originates. However, it will become clear when comparing NO formation with the simulation case in which only Zel'dovich NO chemistry is included that the majority of NO seen here is Fenimore or N_2O-path chemistry.

4.2.1.5. *Methyl Butanoate, Full NO_x , $t = 42.4$ milliseconds.* At $t = 42.4$ ms, the flame has transitioned to a quasai-steady, non-premixed flame as evidenced by methyl butanoate and molecular oxygen mass fractions approaching zero on either side of the flame. The maximum temperature has declined to 2270 K, which is a difference of 90 K compared to the maximum overall simulation temperature of 2360 K. The reason for this reduction in temperature lies in the transient nature of the propagating flame as explained in Section 4.3.3.

Also notable is the location of peak temperature has crept inward to $r/r_s = 6.9$. The reason for this small shift in flame position is explained by the fact that a non-premixed flame will seek out the location in which the fuel and air meeting there will be in stoichiometric proportions. The flame has moved inward, causing the slope of the fuel vapor mass fraction curve to steepen. Since mass diffusion is proportional to the spatial derivative of fuel concentration (or mass fraction) this will cause an increase in the rate of diffusion of fuel

to the flame. Therefore, the flame moved inward to increase the rate of diffusive transport of fuel to the flame.

In the right hand plot, profiles of OH and O continue to diminish compared to the last time step. The reduction in OH and O formation is due to a reduction in the overall rate of combustion reaction. The right-hand plot shows that NO mass fraction continues to increase with a peak value now at 420×10^{-6}. A slow, steady increase of NO is characteristic of the Zel'dovich NO formation path, however it is not yet clear how important this mechanism is to overall NO formation. The other oxides of nitrogen continue to grow as well, but still remain orders of magnitude smaller than NO.

4.2.2. METHYL BUTANOATE WITH ZEL'DOVICH NO CHEMISTRY. The previous subsection described the results of a simulation of an isolated autoigniting methyl butanoate droplet that utilized full NO_x chemistry, which includes the combined contributions from Zel'dovich NO, Fenimore NO_x , and N_2O paths to NO_x formation. In this subsection, results of an identical simulation are presented, except in this case, only the Zel'dovich NO chemical pathway [Reactions (R1-R3)] were included. Having removed the Fenimore NO_x and N_2O paths, the Zel'dovich-only simulation is ultimately less realistic than that with full NO_x chemistry, but the results remain useful because they can be examined in the context of the full NO_x simulation just described above. Specifically, by comparing the results of the simulations with two levels of NO_x chemistry detail, it can be roughly determined what fraction of NO produced in the full NO_x simulation was attributable to the Zel'dovich NO path.

The results of the isolated auto-igniting methyl butanoate droplet simulation with Zel'dovich NO chemistry are found in Figure 4.3. The arrangement of plots is the same as that of the previous subsection in that each row of plots represents results from the time step indicated
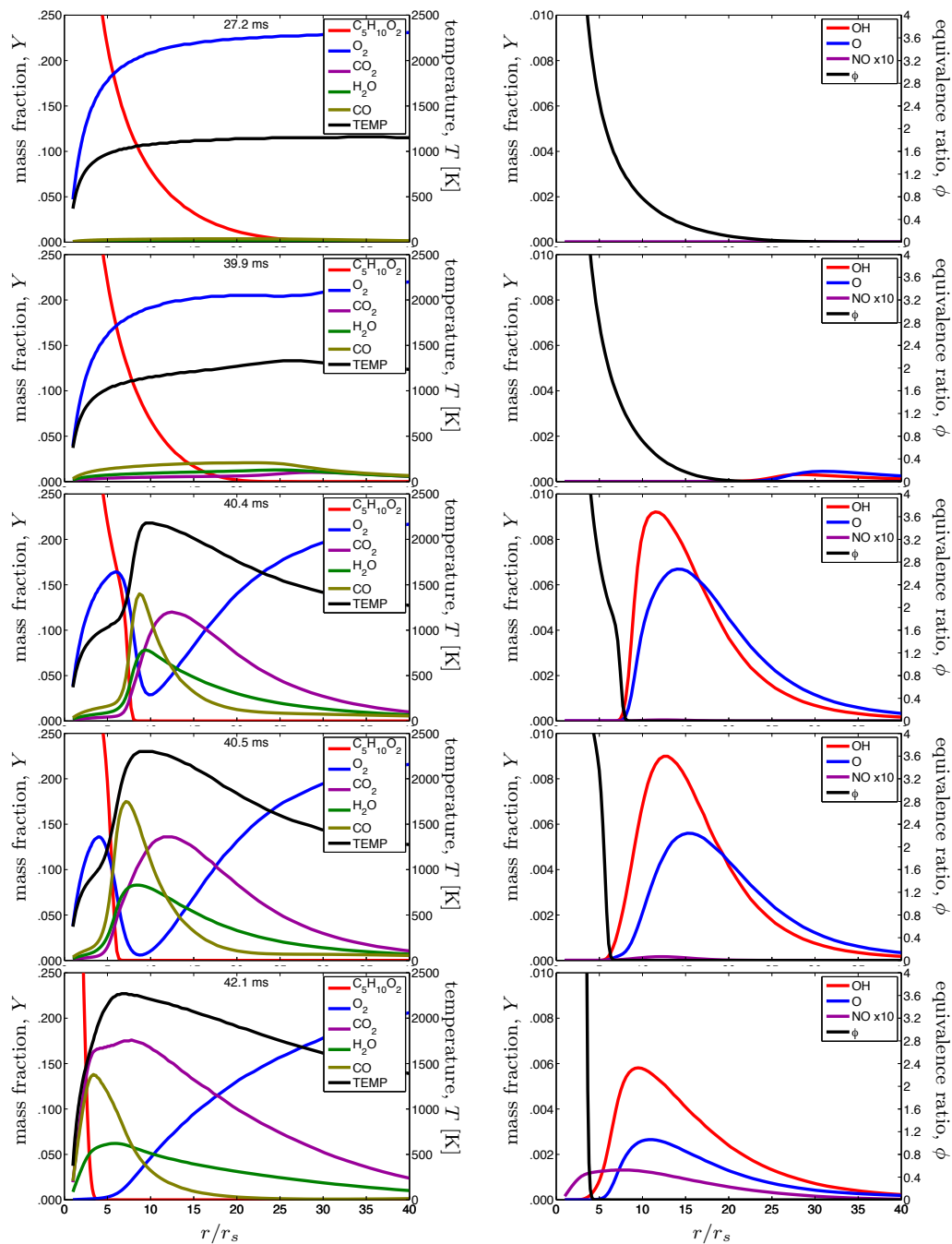
FIGURE 4.3. Calculated species mass fraction and temperature and in the gas-phase surrounding a 200 μm diameter methyl butanoate droplet at the indicated time steps. Calculations were performed with Zel'dovich NO_x chemistry.

in the top center of the left-hand plot. However, since Zel'dovich NO chemistry yields NO and no other oxide of nitrogen, only the NO curve appears in the right-hand plot.

An examination of the plots in the left-hand column of Figure 4.3 shows that major features of the flame structure are still captured with the chemical mechanism containing only Zel'dovich NO chemistry. Specifically, the onset of ignition occurs in the fuel lean region at $r/r_s > 25$ and propagates inward toward the droplet surface. Once the premixed fuel and air is exhausted, the flame transitions to non-premixed combustion. Once again, the maximum gas phase temperature just before the transition to non-premixed combustion is slightly higher than the quasi-steady non-premixed combustion temperature.

Note that the time steps selected for plotting in Figure 4.3 are not identical to those in Figure 4.2. The time steps that do appear in Figure 4.3 were chosen to portray similar features of the premixed autoignition event and transition to non-premixed combustion. While major features of the flame structure were adequately captured with the Zel'dovich NO simulation, the quantity of NO generated was quite different from that predicted by the simulation with full NO_x chemistry. Such comparisons will be examined in the next section. NO first becomes significant at $t = 40.5$ ms with mass fractions on the order of ten parts per million. Then in the next time steps at $t = 40.8$ ms and $t = 42.1$ ms, NO increases gradually and broadly, and even reaches to the droplet surface. The slow, steady formation of NO in high temperature is a characteristic of Zel'dovich NO chemistry.

4.2.3. n-Heptane with Full NO_x Chemistry. Results of an isolated autoigniting droplet simulation for n-heptane with full NO_x chemistry are found in Figure 4.4. The results of this simulation are similar to those of methyl butanoate with full NO_x . Both simulations exhibit the ignition event starting well away from the droplet surface, an inward-propagating reaction wave, transition to non-premixed combustion, then a quasi-steady state non-premixed phase.

The first evidence of the early exothermic reactions that lead to ignition are seen at $t = 13.9$ ms in Figure 4.4. Namely, a broad temperature increase with a low peak is observed, similar to the methyl butanoate temperature curve at $t = 39.9$ ms in Figure 4.2. However, there are two notable differences. First, the peak of the n-heptane temperature curve at $t = 13.9$ is located at a normalized radius of $r/r_s \approx 18$, whereas in the analogous methyl butanoate result, the temperature peak is at $r/r_s \approx 28$. Second, this initial broad temperature rise that is the precursor to full ignition, occurs much earlier for n-heptane ($t = 13.9$) than methyl butanoate ($t = 39.9$). The maximum temperature reached for all time in the respective simulations was different as well: 2460 K for n-heptane and 2360 K for methyl butanoate.

The formation of NO_x species also appears to be different for n-heptane than for methyl butanoate. By comparing the right-hand columns of Figures 4.4 and 4.2[1], it is apparent that approximately three times the NO was produced by n-heptane compared to methyl butanoate. More NO_2 appears to have been formed by n-heptane than methyl butanoate by about a factor of 2. On the other hand, n-heptane seems to have generated about the same amount of N_2O as methyl butanoate.

4.2.4. n-Heptane with Zel'dovich NO Chemistry. Results of the second simulation case for n-heptane, in which only Zel'dovich NO chemistry is included, are found in Figure 4.5. As was the case with methyl butanoate, the Zel'dovich NO version of n-heptane exhibits very similar features to the n-heptane with full NO_x simulation. Also true in comparing the two n-heptane simulations is that less NO was produced by the Zel'dovich-NO case.

---

[1]Note the vertical scales are different for the n-heptane results versus the methyl butanoate results.
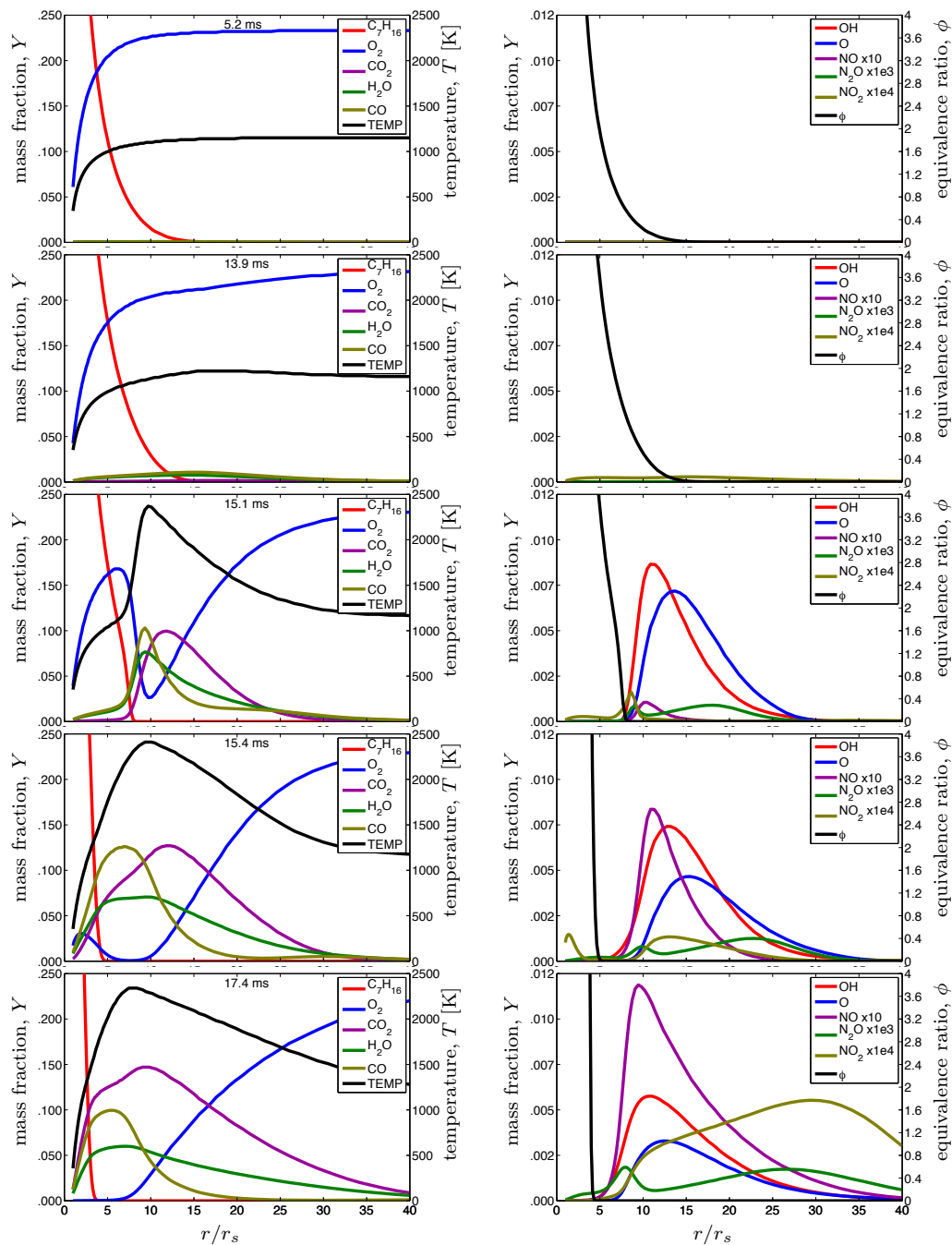
FIGURE 4.4. Calculated species mass fraction and temperature of the gas phase surrounding a 200 μm n-heptane droplet at 1 atmosphere at the indicated time steps. Calculations were performed with full NO_x chemistry.

4.2.5. METHANOL WITH FULL NO_x CHEMISTRY. The results for an isolated, autoigniting methanol droplet simulation are found in Figure 4.6. The major features seen in the methyl butanoate and n-heptane simulations are seen in methanol as well: Low-temperature
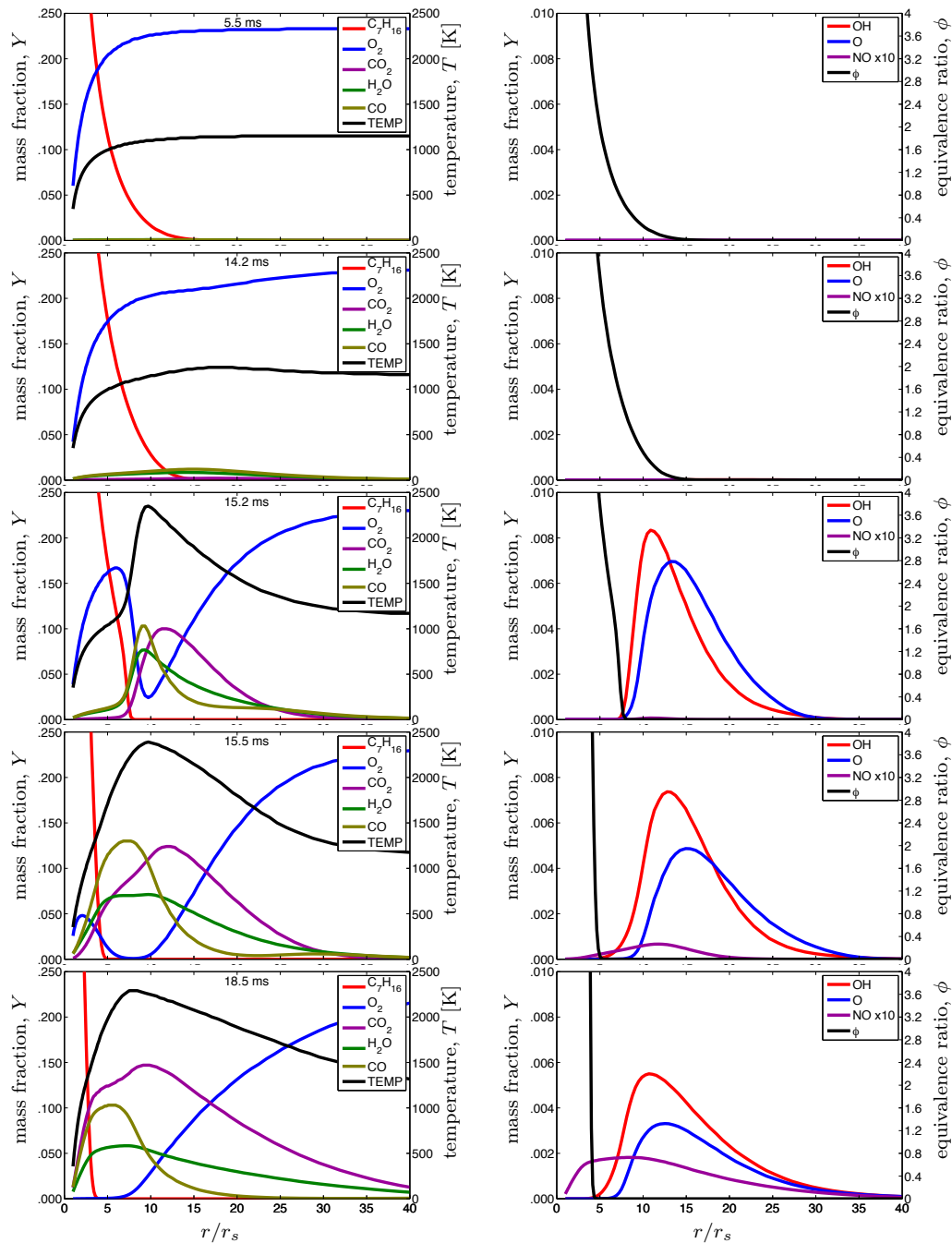
FIGURE 4.5. Calculated species mass fraction and temperature and in the gas-phase surrounding a 200 μm diameter n-heptane droplet at the indicated time steps. Calculations were performed with Zel'dovich NO_x chemistry.

chemistry causes an elevation in temperature of the gas phase mixture. A reaction front propagates inward, consuming the premixed fuel and air. There is a transition to non-premixed combustion followed by a quasi-steady state non-premixed phase. However, in
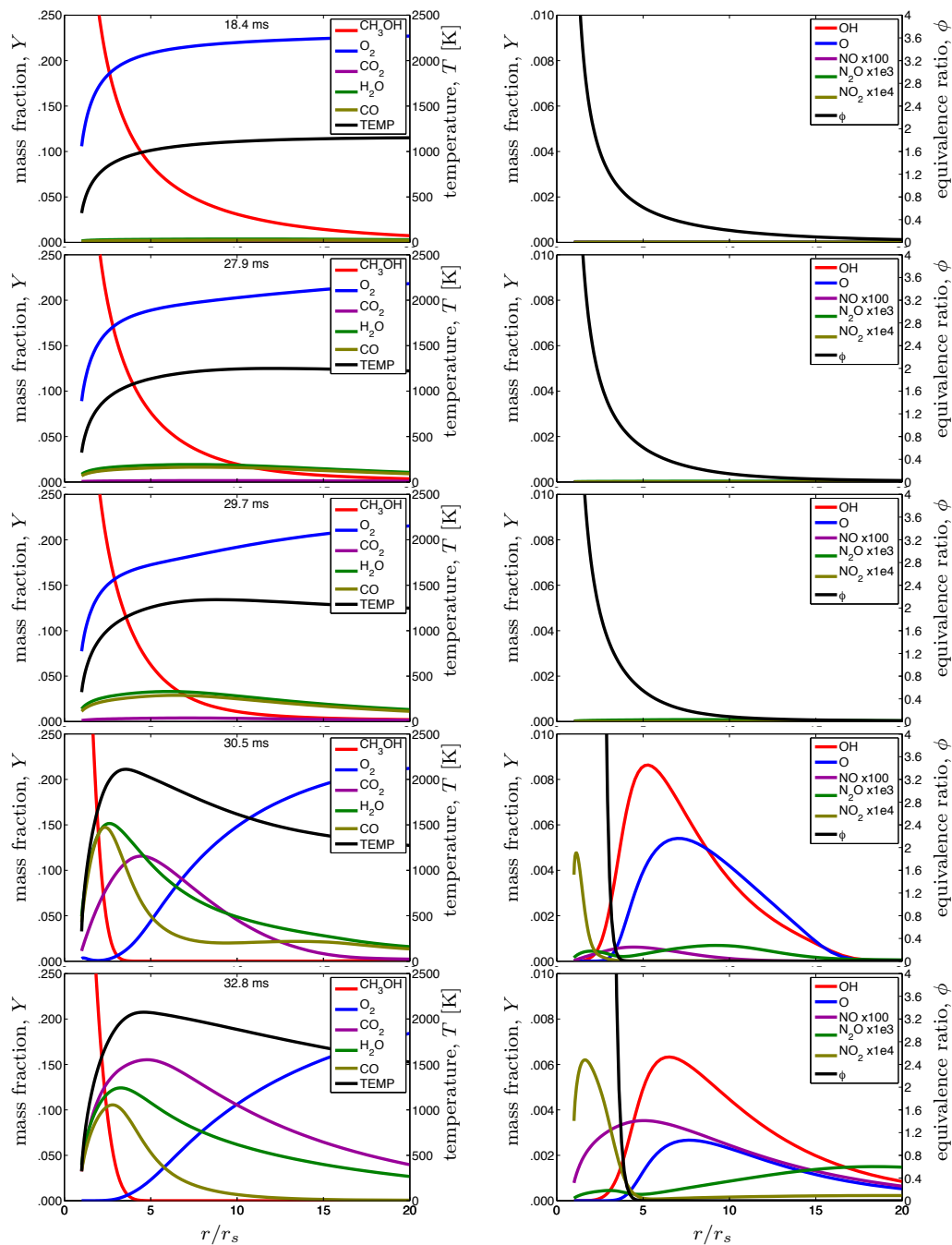
FIGURE 4.6. Calculated species mass fraction and temperature and in the gas-phase surrounding a 200 μm diameter methanol droplet at the indicated time steps. Calculations were performed with full NO_x chemistry.

the case of methanol, the ignition event occurs closer to the droplet surface than that of methyl butanoate or n-heptane. So close, in fact, that there is very little premixed fuel and air through which the reaction wave propagates. Moreover, the reaction wave propagates

much closer to the droplet surface, and the quasi-steady flame (assuming it is indicated by the location of max temperature or OH) resides rather closer to the droplet surface as well. None of these facts are unexpected and will be explained in the next section.

The formation of oxides of nitrogen presented in the plots of the left column of Figure 4.6 are also notable. For example, peak NO is about three orders of magnitude smaller than n-heptane and methyl butanoate. On the other hand, N_2O appears to be comparable. Moreover, apart from a small amount near the flame, NO_2 is all but absent.

4.2.6. METHANOL WITH ZEL'DOVICH NO CHEMISTRY. The simulation results for methanol with Zel'dovich NO chemistry are found in Figure 4.7. Unfortunately, CO_2, O, and OH data were not available. The data that are plotted in the figure are adequate to convey the important facts. Namely, this Zel'dovich NO simulation, like the others exhibits the major features of the simulation with full NO_x chemistry. Moreover, the production of NO appears to be a factor of three smaller here than in the methanol with full NO_x simulation.

4.3. DISCUSSION OF MAJOR COMBUSTION FEATURES

The three fuels for which isolated autoigniting droplet combustion simulations were conducted represent a diversity of physical properties and molecular structure. Therefore, it is no surprise that the results of the simulations exhibited variability. This section contains a discussion of of the differences (and similarities) among the simulations and provides explanation of the fundamental causes.

4.3.1. IGNITION DELAY AND LOCATION. The differences in ignition delay time and location of ignition between n-heptane and methyl butanoate droplets can be explained by the reactivity of the respective fuels. As presented in Table 1.2, n-heptane has cetane number
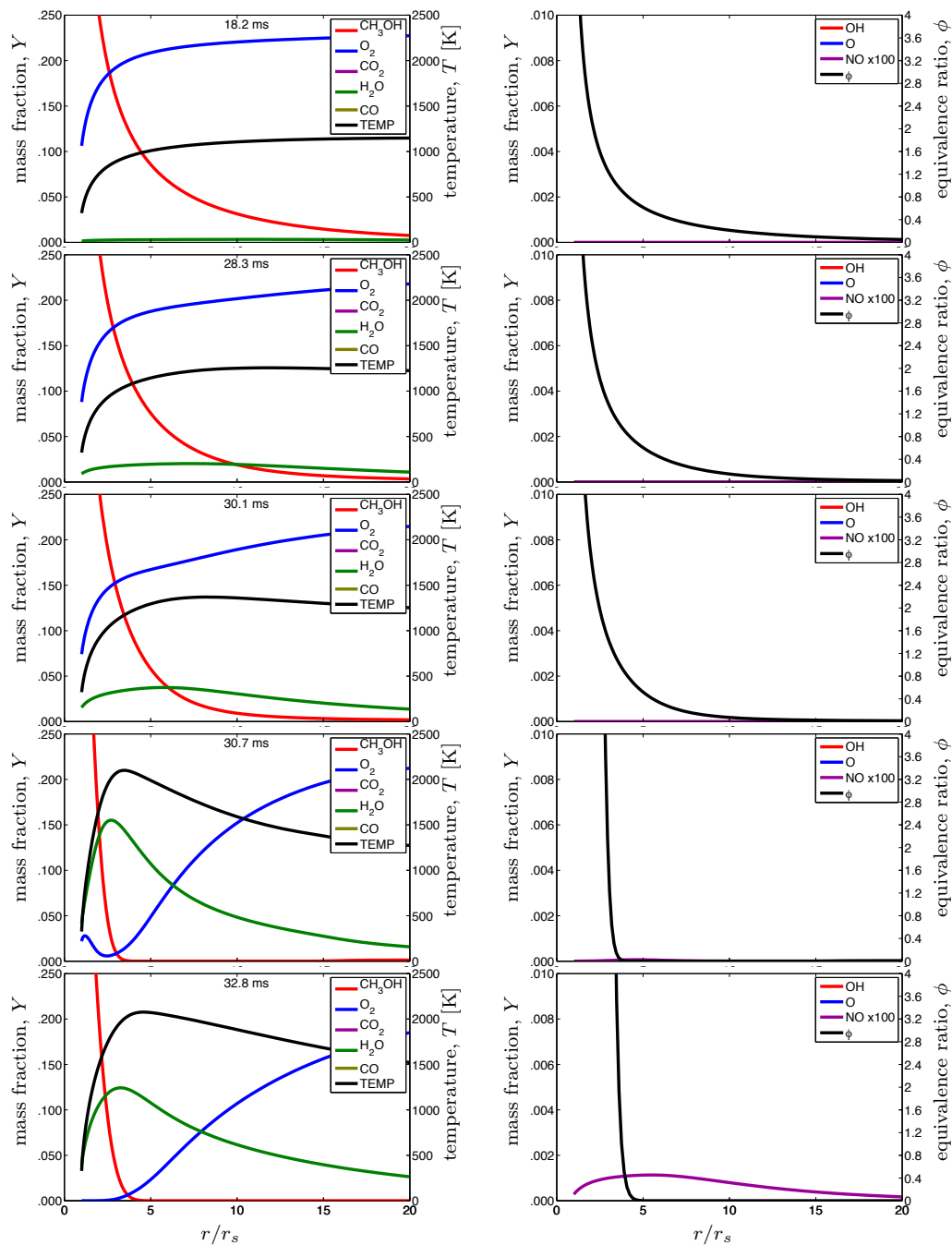
FIGURE 4.7. Calculated species mass fraction and temperature of the gas phase surrounding a 200 μm methanol droplet at the time step indicated. Calculations were performed with Zel'dovich NO_x chemistry.

of CN = 53, which is much higher than that of methyl butanoate: CN = 6. Cetane number is and empirical metric that describes fuel reactivity, with the implication that n-heptane is more reactive than methyl butanoate.

The ignition location of n-heptane being at smaller r/r_s than that of methyl butanoate can be explained in the context of fuel reactivity. Consider the left-hand plot at $t = 5.2$ ms in Figure 4.4 at the radial coordinates $r/r_s = 18$ and $r/r_s = 28$. At $r/r_s = 28$, the location of where ignition initiated for methyl butanoate, the mixture is extremely lean and temperature is high. At $r/r_s = 18$ there is comparatively more fuel available, but the temperature is also lower. A similar scenario is apparent in Figure 4.2 at $t = 27.1$ ms. Why then does the n-heptane ignite at $r/r_s = 18$ and methyl butanoate at $r/r_s = 28$? The answer lies in the reactivity of the two fuels. Since n-heptane is more reactive, it has less time to diffuse outward before ignition occurs. In the case of methyl butanoate, the low reactivity of the fuel permits more time for diffusion of fuel vapor radially outward. Consider that the induction time of methyl butanoate is 39.9 ms and that of n-heptane is 13.9 ms. Methyl butanoate vapor has nearly three times more time to diffuse than n-heptane. Therefore, it makes sense that the ignition of the methyl butanoate droplet is further from the droplet surface than ignition of n-heptane.

A comparison between combustion of methyl butanoate and n-heptane droplets provides an excellent opportunity to discuss the effects of reactivity because many of their other physical properties are similar, as shown in Table 1.2. As such, one can examine the differences in ignition delay and location and be sure that the cause most likely lies in the differences in reactivity. The same, however, cannot be said for methanol.

In the above, the differences in ignition delay and location were explained by differences in reactivity of methyl butanoate and n-heptane. Were the same argument to apply to methanol, then it would be expected that methanol would exhibit an ignition delay and

TABLE 4.2. A summary of some numerical simulation results for the indicated fuels with full NO_x chemistry.

Fuel	t_{ign} [ms]	$\left.\frac{r}{r_s}\right|_{\text{ign}}$	T^* [K]
Methyl Butanoate	39.9	28	2360
n-Heptane	13.9	18	2460
Methanol	28.3	12	2117

location that was similar to methyl butanoate since the cetane numbers are essentially identical. At least in the case of ignition delay, methanol and methyl butanoate are fairly similar. Suppose the time of ignition, t_{ign}, for the purposes of this thesis is assumed to correspond to the second row of plots where a distinct low peak caused by low-temperature reactions is first exhibited by the temperature curve. The time of ignition for the three fuels (with full NO_x chemistry) are summarized in Table 4.2. In a rough sense, the ignition time of methanol is comparable to methyl butanoate as predicted. Now suppose the ignition location, $r/r_s|_{\text{ign}}$, is that location at t_{ign} where temperature is greatest. This corresponds to the where low-temperature reactions are most active and from where thermal runaway will originate. These coordinates are summarized in Table 4.2. When comparing $r/r_s|_{\text{ign}}$ between methanol and methyl butanoate, it is apparent they are quite different. In fact $r/r_s|_{\text{ign}}$ is smaller for methanol than even n-heptane, which is nominally more reactive than both of them. Why would an ostensibly non-reactive fuel like methanol have an ignition location so close to the droplet surface? The answer most likely lies in the combustion chemistry of methanol.

When a liquid droplet is inserted into a hot air ambient, there is no previously produced radical pool present to initiate the chemical reactions that lead to ignition. Instead, the radical pool must often be produced through chemical reactions between oxygen in the ambient and fuel vapor. However, in the case of methanol, the most important initiating

reaction in the absence of a radical pool is [24]:

$$CH_3OH + M \longrightarrow CH_3 + OH + M,$$
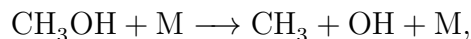
where M is some collision species. This reaction produces the hydroxyl (OH) radical species that can then go on to participate in other reactions leading to ignition. The radical pool required to initiate ignition reactions is provided by the dissociation of the methanol, rather than reactions between molecular oxygen and the fuel. Therefore, it is possible that the reason methanol ignites so close to the droplet surface despite the relatively low fuel reactivity, is that radicals can be produced without reactions with molecular oxygen from the ambient.

4.3.2. VARIATION OF T^* AMONG THE SIMULATED FUELS. Maximum overall temperature calculated in the simulation varied among the three fuels. Suppose the maximum temperature achieved for a given simulation for all time is designated as T^*. In other words:

$$T^* = \max[T(t, r/r_s)]. \tag{51}$$

The values of T^* are summarized in Table 4.2 for the three simulated fuels with full NO_x chemistry. Normal heptane appears to have the highest T^* with 2460 K, with methyl butanoate slightly lower at 2360 K, and methanol significantly cooler at 2117 K. This trend can be explained by the heats of combustion of the three fuels that are found in Table 1.2. It is apparent that n-heptane has more chemical potential energy than methyl butanoate and considerably more than methanol. This explanation is further supported by the adiabatic flame temperatures in Table 1.2, which were obtained by conducting zero-dimensional homogenous mixture autoignition and combustion simulations in CHEMKIN. These results
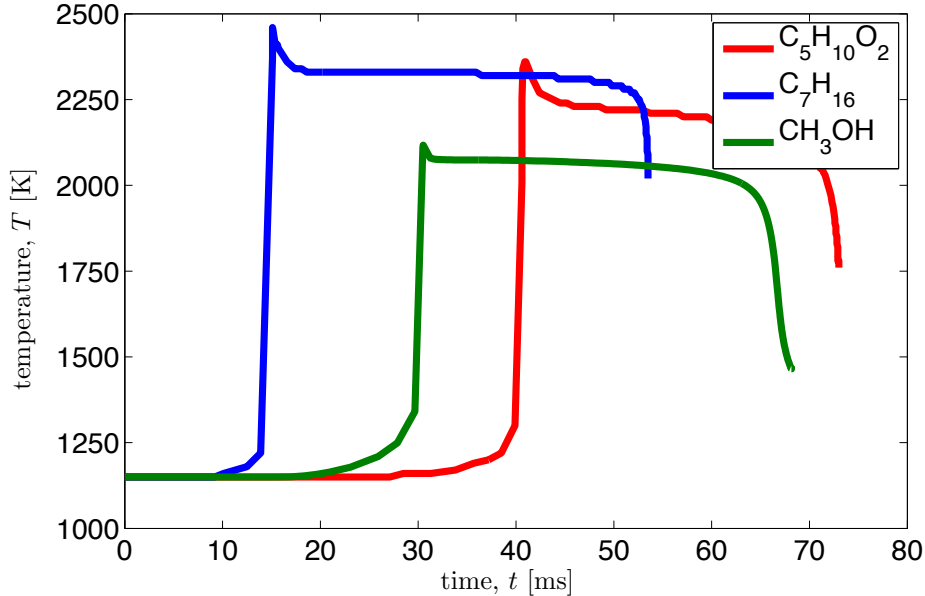
FIGURE 4.8. Maximum temperature as a function of time for methyl butanoate, n-heptane, and methanol with full NO_x chemistry. Results obtained for spherically symmetric isolated droplet autoignition and combustion simulations with initial droplet diameter of 200 μm and ambient temperature 1150 K.

follow a similar trend, with n-heptane having the greatest temperature, methyl butanoate second, and methanol third.

4.3.3. MAXIMUM OVERALL TEMPERATURE. The maximum overall temperature achieved in the simulations, T^*, occured at the end of the combustion of premixed fuel and air. Figure 4.8 contains a plot of the maximum temperature as a function of time for the three simulated fuels with full NO_x chemistry. All three fuels exhibit a similar behavior, so consider the methyl butanoate curve with the solid line for a detailed discussion. Starting at about 27 ms, the temperature begins to rise slowly for the next ten milliseconds. During this period, early exothermic chemical reactions are starting to raise the temperature of the gas-phase fuel-air mixture. At about 40 ms, the temperature rises very rapidly and reaches a maximum value. This rapid temperature increase corresponds to the reaction wave propagating from the ignition location inward toward the droplet. The reaction wave is consuming premixed fuel and

air causing the gas phase temperature to rise quickly. The peak temperature T^* is reached just as the last of the premixed fuel and air are consumed. The temperature is sufficiently high that it is reasonable to assume reaction wave has become a flame. The reaction wave propagation and associated temperature rise occurs very quickly, on the order of hundreds of microseconds. The speed of the temperature rise is evident by the extreme slope of the methyl butanoate temperature curve at 40 ms in Figure 4.8. Once having reached the peak, the temperature then declines somewhat over the course of a few milliseconds and reaches a quasi-steady state. Then, temperature very slowly declines for the next 30 milliseconds before finally falling to extinction. The slow decline is due to increased leakage of reactants through the flame as the droplet diameter decreases.

In all three simulations, the maximum overall temperature, T^*, is momentarily achieved just as the reaction wave consumes the last of the premixed fuel and air and is near its closest approach to the droplet surface. The momentary temperature excursion to T^* is due to the transient nature of the propagating premixed flame. As the flame moves through the premixed fuel and air, it is producing heat from chemical reactions faster than the heat can be transported away by conduction. The maximum overall temperature T^* is reached at the end of premixed combustion, and over the course of approximately three milliseconds, the flame temperature declines as transport of heat by conduction comes into equilibrium with heat release by combustion.

4.3.4. PEAK TEMPERATURES FOR OXYGENATED AND NON-OXYGENATED FUELS. Figure 4.8 shows that maximum flame temperatures are highest for n-heptane, with methyl butanoate a close second, and methanol a distant third. This result seems contrary to what might be expected from the hypothesis of Mueller, et al. [11] that oxygenated fuels should

produced a higher temperature during the premixed autoignition phase because the presence of oxygen atoms in the fuel molecule results in a leaner (but still rich) premixed autoignition zone, thereby increasing in-cylinder temperatures and promoting Zel'dovich NO production. This apparent contradiction is explained by the simple fact that the premixed propagating flame never moves into a rich mixture for any of the fuels simulated, oxygenated or otherwise.

Figure 4.9 shows the flame always resides in a lean fuel-air mixture. in Figure 4.9, the normalized radial location of the flame (red curve) as a function of time is shown for methyl butanoate, n-heptane, and methanol. The plots also show the location of the stoichiometric mixture (blue curve) of fuel and air, in other words: $\phi = 1$. Regions above the dashed curve are further away from the droplet surface, so they are lean. Regions below the dashed curve are closer to the droplet surface, so they are rich. The plots were drawn so that the closest approach of the propagating flame to the droplet surface is centered in the plot. It is apparent that in all three fuel simulations, the flame never moves into a rich mixture because the flame position curve always stays above the $\phi = 1$ curve.

In these simulations, the fact that the propagating flame stays in the lean region for the spherically symmetric autoigniting droplet configuration, means that the premixed autoignition zone will be *further* from stoichiometric for oxygenated fuels. In other words, the fuel-bound oxygen in oxygenated fuels will cause the lean mixture through which the flame propagates to be even more lean. This is the opposite configuration in the theory of Mueller, et al. [11] in which they examine the rich premixed autoignition zone of a diesel spray. Thus, the simulation results presented here neither support nor contradict the theory of Meuller et al. [11].
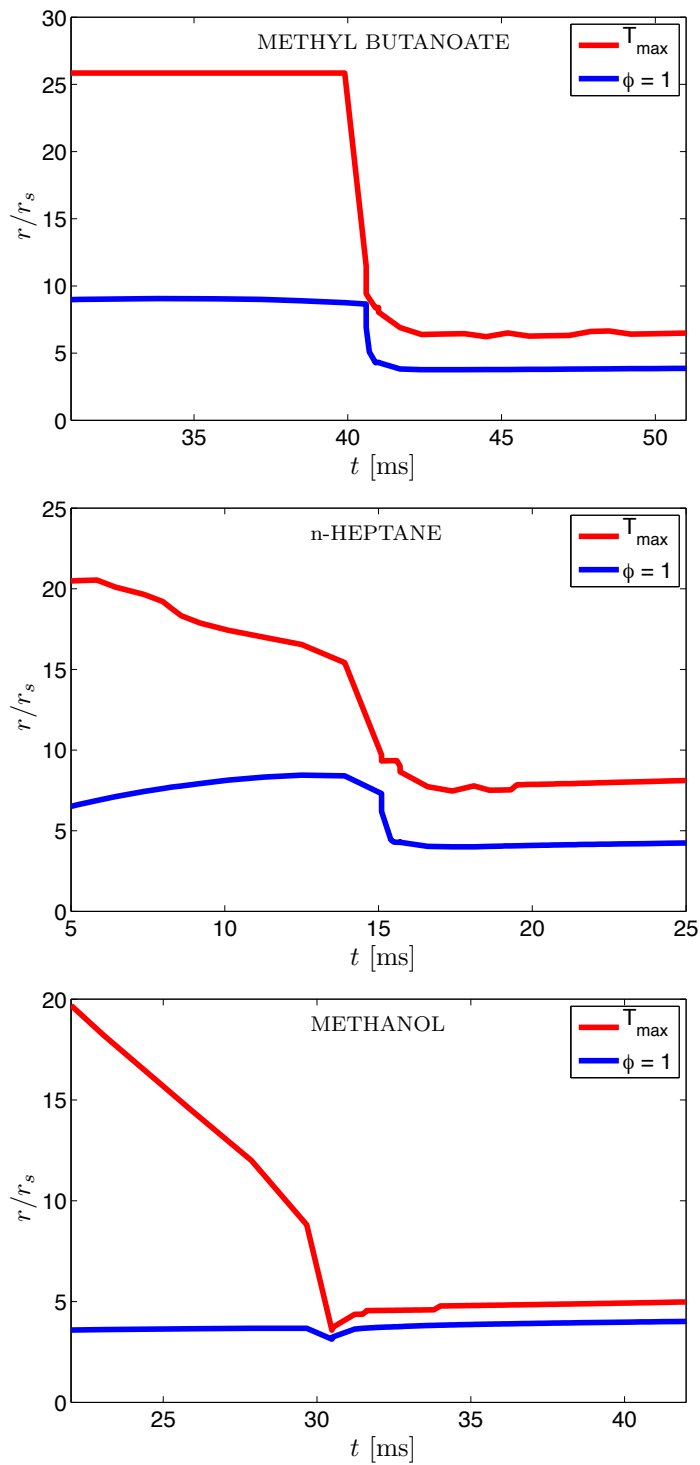
FIGURE 4.9. Normalized radial location of maximum temperature and stoichiometric equivalence ratio as a function of time for methyl butanoate, n-heptane, and methanol detailed numerical simulations of isolated droplet autoignition and combustion.

4.3.5. PREMIXED PROPAGATING REACTION ZONE AND FLAME. The above explanation for flame temperatures is evident from a close examination of Figure 4.2 and Figure 4.8. What is not obvious, however, is why the reaction wave propagates inward from the ignition initiation location toward the droplet surface. Consider Figure 4.9 in which the solid curve shows the normalized radial location of the maximum temperature as a function of time. The dashed curve represents the location of a stoichiometric fuel-air mixture, i.e., unity equivalence ratio: $\phi = 1$.

At early time, the maximum temperature is indicative of the location of the reaction zone in which initial exothermic reactions are occurring in a lean mixture relatively far from the droplet surface. For example, until approximately 39 milliseconds, the maximum temperature in the methyl butanoate droplet is at approximately $r/r_s = 25$. Once sufficient heat is generated, the reaction rate has become sufficiently fast that the reaction zone will begin to propagate, becoming a reaction wave. The propagating reaction wave is particularly clear for the methyl butanoate case in Figure 4.9 where, at $t = 39.9$ ms, the curve drops precipitously, indicating the reaction zone is propagating rapidly toward the droplet.

The reaction zone resides in a gradient of fuel concentration so that toward the droplet, there is a higher concentration of fuel and away from the droplet there is less. Or, to put it another way, toward the droplet is less lean, away from the droplet is more lean. Since fuel is the deficient reactant, the reaction rate will be slightly greater on the droplet side of the reaction zone than the ambient side. As such, the reaction zone shifts in the direction in which more fuel is available, toward the droplet. Having done so, the concentration of fuel toward the droplet is even higher, so the reaction zone shifts again; and so on. This phenomena of the shifting reaction zone is a smooth, continuous process and is called a

propagating reaction wave. The propagation of the reaction wave is apparent by examining the second, third, and fourth rows of the simulation results above (Figures 4.2 - 4.7). It is also evident, as implied above, by the location of the maximum temperature quickly moving toward the droplet in the plots of Figure 4.9.

There are two factors that cause the propagating flame to come to a stop at an equilibrium position. The first is due to evaporation of fuel at the droplet surface causing a net mass flux of fuel vapor in the radial direction that is called Stefan flow [24]. The flow is purely radial due to our assumption of spherical symmetry, therefore the Stefan flow velocity is proportional to inverse square of the radius [24]:

$$u_S \propto \frac{1}{r^2}. \tag{52}$$

Equation (52) suggests the convection of fuel vapor against which the flame must propagate increases very fast as it nears the droplet. The increasing Stefan flow velocity has the effect of balancing the tendency of the flame to propagate closer to the droplet. This is an example of how a diverging flow can stabilize a flame [24].

The second factor that causes the propagating flame to stop at an equilibrium position is heat flux from the flame to the droplet. Return again to the left-hand plot of Figure 4.2 at $t = 40.6$ ms and consider the temperature curve. We know from Fourier's law of conduction that heat flux is proportional to the temperature gradient [83]:

$$q \propto \nabla T. \tag{53}$$

Therefore, the slope of the temperature curve is an indicator of the heat flux from the flame to the droplet by conduction. There is a region in the temperature curve around $r/r_s = 6$

where the slope flattens somewhat. This suggests that the heat flux from the flame to the droplet is relatively low. Compare this to the temperature curve in the left-hand plot at $t = 42.4$ where the slope is quite steep from the flame to the droplet. This means heat flux due to conduction from the flame to the droplet is significant. This causes the flame temperature to decline with a likewise reduction in flame speed. Therefore, as the flame gets closer to the droplet, the heat flux to the droplet increases, causing the flame speed to decline. This, combined with the variation in Stefan flow velocity comprises a stabilizing effect on the flame, causing it to cease propagation and settle into an equilibrium position.

4.4. DISCUSSION OF NO_x FORMATION

In this section, the formation of oxides of nitrogen (NO_x) are discussed in the simulation results presented in Figures 4.2 through 4.7. As explained previously, two levels of NO_x chemistry were simulated for each of the three fuels studied.

The full NO_x case contained the three princeple NO_x formation mechanism: Zel'dovich, Fenimore, and N_2O path. The Zel'dovich case contained only Zel'dovich chemsitry. The two levels of NO_x formation chemistry were implemented in the simulations so that the relative importance of Fenimore and N_2O path mechanisms to overall NO_x species formation could be determined.

Consider the NO curves at the last time step in all simulations. In every case, there is a long tail that extends from the flame location outward to large r/r_s. This is explained by NO forming in the flame and diffusing radially into the ambient. If the plots were extended beyond $r/r_s = 40$, the NO curves would asymptote to zero since the domain is spherically-symmetric. In the simulations with Zel'dovich NO chemistry (Figures 4.3, 4.5, and 4.7) the NO is non-zero at the droplet surface, $r/r_s = 1$. NO is formed in the flame and diffuses

inward toward the droplet surface and, since there are no chemical reactions that consume NO in Zel'dovich NO chemistry, it accumulates in the region between the droplet surface and flame. The full NO_x chemistry does contain reactions that consume NO and so in the methyl butanoate (Figure 4.2) and n-heptane (Figure 4.4) simulations with full NO_x, NO does not reach the droplet surface. Interestingly, in the case of methanol with full NO_x chemistry (Figure 4.6), NO is non-zero at the droplet surface, which is in contrast to the other full NO_x simulations. It seems likely the explanation for this is related to the pool of NO_2 located in the region between the droplet surface and the flame because this is not seen in the other full NO_x simulations.

The plots in Figure 4.10 show mass of three nitrogen oxide species as a function of time for the three simulated fuels. The mass of the NO_x species were calculated using Equation (48). These results are for the case in which full NO_x chemistry was used in the fuel mechanisms. In all three fuels, more NO was produced than the other two oxides of nitrogen as expected [6]. Normal heptane generated the greatest NO at a final mass of nearly 50 ng. This is more than five times greater than methyl butanoate (8.9 ng), and fifty times greater than methanol (0.93 ng). Normal heptane produced about five times more NO_2 than methyl butanoate, but both created about the same mass of N_2O.

The methyl butanoate plot shows a knee in the NO curve at about $t = 41$ ms. This sudden jump in NO production is characteristic of Fenimore NO formation because of the rapidity of the reactions. To a lesser extent this is apparent in the NO curve for n-heptane as well. No knee is seen in the methanol case. The slow, steady rise in NO seen in the three plots is characteristic of Zel'dovich NO formation, although it is not clear from these plots if Zel'dovich NO is the sole pathway responsible; this will be addressed presently.
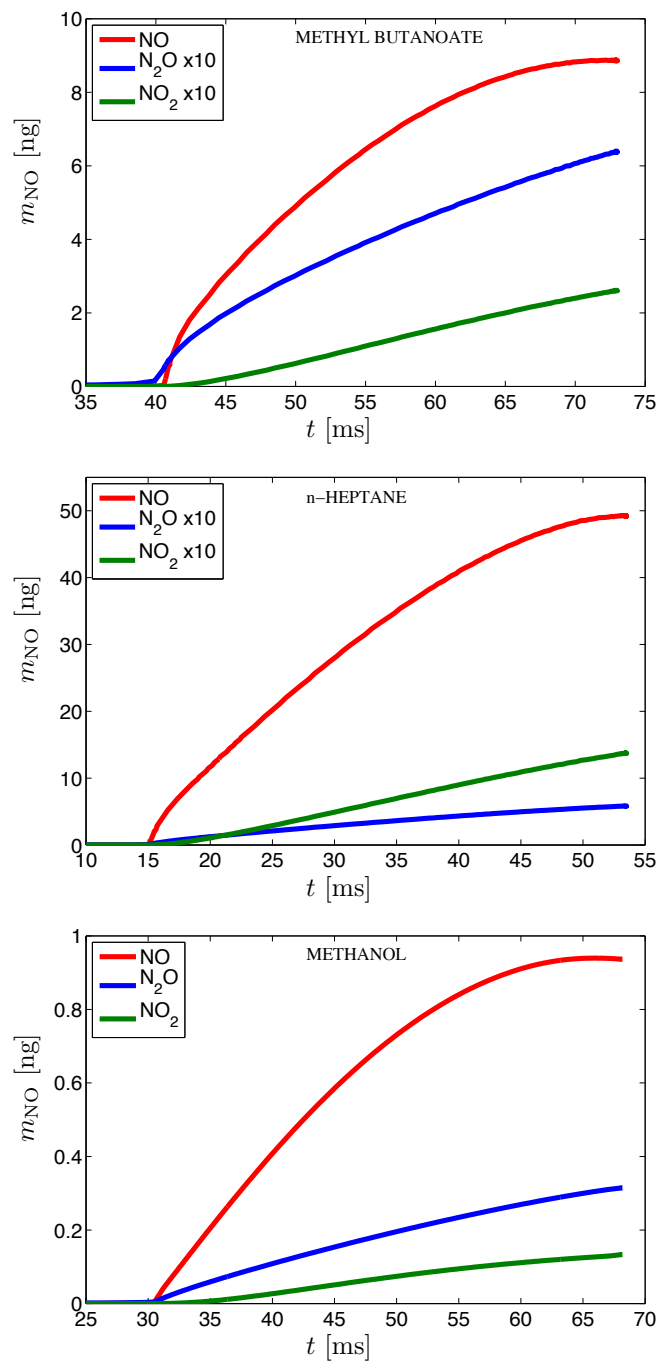
FIGURE 4.10. Total mass of of NO, N_2O, and NO_2 with respect to time for the three fuels simulated with full NO_x chemistry.

In the methyl butanoate and methanol simulations, it is also noted that more N_2O is generated than NO_2, but the opposite is true for n-heptane. Here is a possible explanation: consider that n-heptane formed greater than five times more NO than methyl butanoate

and about fifty times more than methanol. Given the relative abundance of NO in the n-heptane flame, the otherwise vigorous chemical transformation of NO_2 into NO by Reaction (R14) [6] may have been slightly retarded, leading to correspondingly higher amounts of NO_2 observed. The same result would be caused by a relative deficit of hydrogen atoms. Another explanation is that an abundance of HO_2 might be responsible for excessive NO_2 by way of Reaction (R14), but this seems unlikely because HO_2 is stable only at lower temperatures and n-heptane exhibited the highest temperatures of the three fuels simulated.

Figure 4.11 contains plots that show mass of NO_x (in nanograms) as a function of time for the three respective fuels and two levels of nitrogen chemistry. In each plot, the red curve represents mass of NO_x from the simulations in which full NO_x chemistry (combined Zel'dovich NO, Fenimore NO_x , and N_2O-path) was used. The blue curve represents mass of NO generated by the case in which only Zel'dovich NO_x chemistry [Equations (R1) - (R3)] was included. In all three fuels, the simulation with full NO_x chemistry produced significantly more NO_x than that with only Zel'dovich NO_x chemistry.

It is unsurprising that so much more NO_x is produced by those simulations with full NO_x chemistry than those with Zel'dovich if one examines the time evolution of NO formation. Consider n-heptane, which produced the most NO of the three fuels simulated. In Figure 4.11, the n-heptane (middle) plot shows that the full NO_x simulation produced approximately 51 ng of NO by the end of the simulation. This is nearly five times more than the n-heptane simulation with Zel'dovich NO chemistry, which produced about 10 ng of NO. Now examine the right plot of Figure 4.4 at $t = 15.1$ ms. There is a noticeable peak in the NO curve centered at $r/r_s = 11$ with a maximum value of $Y_{NO} \approx 100 \times 10^{-6}$. Contrast this with the analogous plot for n-heptane with Zel'dovich NO chemistry in Figure 4.5 at
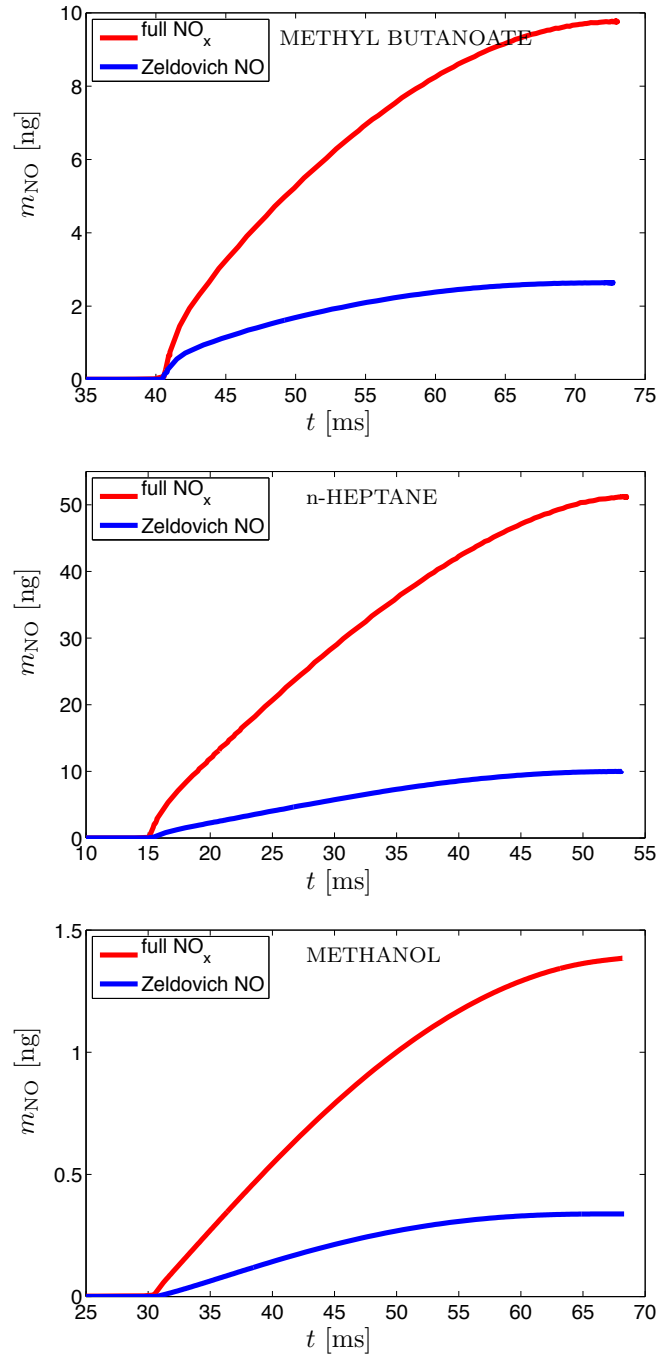
FIGURE 4.11. Calculated total mass of oxides of nitrogen (NO_x) with respect to time for 200 μm diameter methyl butanoate, n-heptane, and methanol droplets in a 1150 K air ambient. Simulations incorporating full NO_x and Zel'dovich chemistry are shown.

$t = 15.2$ ms. In this case, the NO curve is barely visible; perhaps a factor of ten smaller than the simulation with full NO_x chemistry. The presence of significant NO at early time for
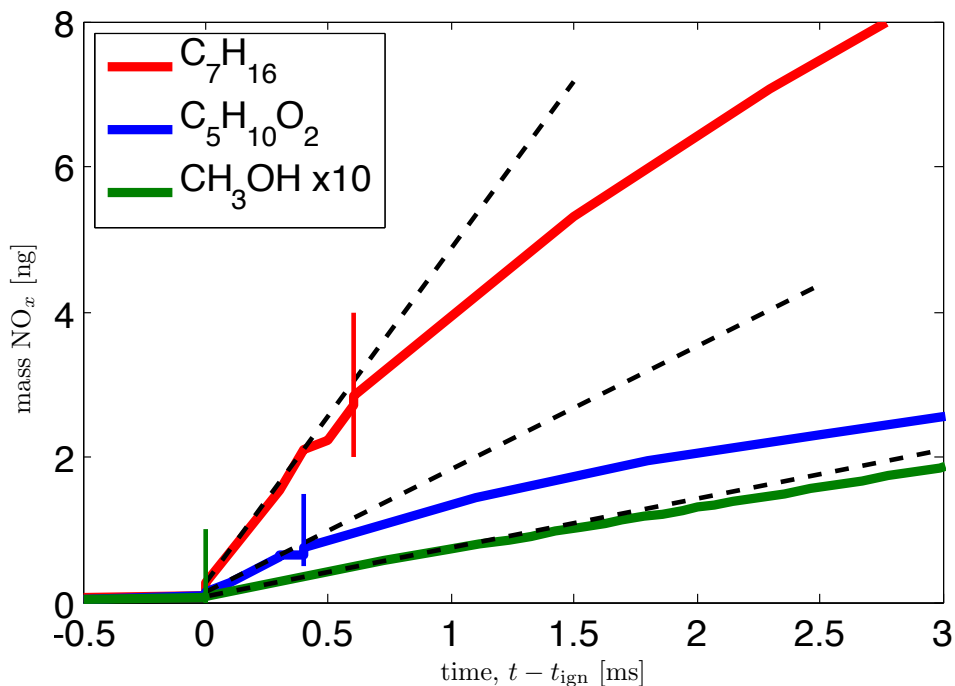
FIGURE 4.12. Calculated mass of NO_x species immediately following autoignition of 200 μm droplets in an air at 1150 K for heptane, methyl butanoate, and methanol fuels. Dashed lines show slope of NO_x curve during premixed burn and solid vertical bars show end of premixed burn.

n-heptane with full NO_x chemistry compared to nearly absent NO for that with Zel'dovich NO chemistry means that Fenimore and N_2O-path NO_x formation are playing an important role in nitrogen oxide formation.

In experiments in which NO_x species are measured in the exhaust stream of an operating engine, the emissions measurements are frequently normalized by shaft work output rate or fuel consumption rate. Analogous plots for droplet combustion are shown in Figure 4.13, where mass of NO_x species are plotted with respect to the mass of fuel vaporized normalized by the initial mass of the fuel droplet. As before, the red contour corresponds to the numerical simulation case in which full NO_x chemistry was used. The blue curve corresponds to that which used Zel'dovich NO_x chemistry. At initial time, a negligible amount of fuel has been vaporized, so $m_v/m_\circ \approx 0$. When the liquid fuel has been exhausted and the droplet
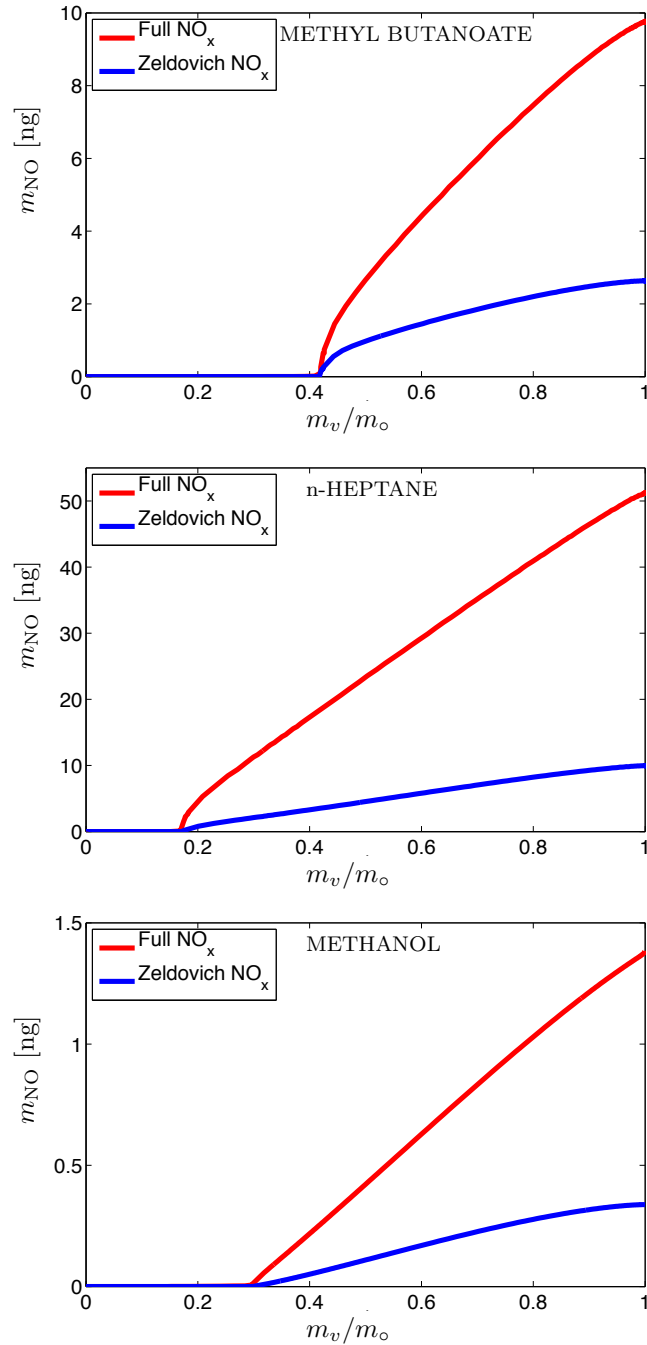
FIGURE 4.13. Calculated total mass of oxides of nitrogen (NO_x) with respect to normalized mass of fuel vaporized for 200 μm diameter methyl butanoate, n-heptane, and methanol droplets in a 1150 K air ambient. Simulations incorporating full NO_x and Zel'dovich chemistry are shown.

extinguishes, all of the fuel has been vaporized, so $m_v/m_\circ = 1$. The red and blue contours become non-zero when ignition has occurred. Just as in the time-dependent plots in Figure

4.11, those in Figure 4.13 also show enhanced NO_x production during the premixed burn phase of combustion for methyl butanoate and n-heptane, but not for methanol.

It is common practice in even the most sophisticated CFD modeling efforts on internal combustion engines to include only Zel'dovich NO chemistry [i.e., Reactions (R1) to (R3)]. As such, even if CFD computations with reduced chemical kinetic mechanisms and reasonably realistic spray models were to accurately predict the onset of autoignition, and model the premixed burn and transition to non-premixed combustion, the results shown in Figure 4.11 strongly suggest that NO formation will be significantly under-predicted if only Zel'dovich NO chemistry is included. That said, it is acknowledged that the addition of some 30 species to the chemical mechanism required for Fenimore NO_x is typically not possible with present technology due to the computational expense incurred. Moreover, if one were to include the full NO_x mechanism with reduced fuel chemistry, it would still not necessarily be accurate since it is critical to adequately capture the formation of Fenimore precursors like CH, CH_2, C_2, and C_2O.

Now consider Figure 4.12 in which mass of NO_x species are plotted as a function of time for n-heptane, methyl butanoate, and methanol[2]. The time axis is expanded so that the NO_x formation activity in the first few milliseconds is visible. Moreover, the ignition time of the respective fuels t_{ign} has been subtracted off so that all three fuels ignite at $t - t_{\text{ign}} = 0$. The vertical bars indicate the time at which all premixed fuel and air has been consumed. In other words, the end of the premixed burn phase. Since the chemical induction time for methanol is relatively short, the premixed burn phase ends very quickly. Therefore, on the time scale of the plot in Figure 4.12, the end of the premixed burn phase for methanol

---

[2]Note that the methanol NO_x mass contour is multiplied by a factor of ten here.

appears to occur instantaneously. In practice, the premixed burn phase for methanol is on the order of tens of microseconds in duration.

The contours for mass of NO_x species in Figure 4.12 for n-heptane and methyl butanoate show a higher rate of NO_x formation during the premixed burn phase of combustion (i.e., between $t - t_{ign} = 0$ and the vertical bars). The higher rate of NO_x formation is apparent because the slope of the curve during the respective premixed burn phase is greater than that during the quasi-steady non-premixed phase that occurs afterwords. The black dashed lines in Figure 4.12 emphasize the difference in slope between the premixed burn phase and the subsequent non-premixed burn phase. Comparing the slopes between n-heptane (red) and methyl butanoate (blue) show that the former forms NO_x species faster than the latter.

If methanol were to exhibit significant NO_x formation during the premixed burn phase of combustion as n-heptane and methyl butanoate do, it would appear in Figure 4.12 in the form of a step increase in the mass of NO_x very near $t - t_{ign} = 0$ since the premixed burn phase is so short. No such step in the methanol curve is seen here. The lack of significant NO_x formation by methanol during the premixed burn phase is a key result. Recall Hypotheses 1, which stated that all oxygenated fuels (not just methyl esters) should exhibit enhanced NO_x formation chemistry during the premixed burn phase of combustion. The results in Figure 4.12 appear to contradict Hypothesis 2 because methanol does not exhibit enhanced NO_x formation during the premixed burn phase despite it being, like methyl esters, an oxygenated fuel.

There is, however, a mitigating factor in the stoichiometry of the premixed autoignition zone in diesel sprays and droplet systems. The hypothesis of Mueller, et al. [11] for increased NO_x formation in biodiesel-fueled compression ignition engines was based on the

well-supported fact that the autoignition zone in a diesel spray is rich. Naturally, an oxygenated fuel would tend to make a rich mixture less rich, and therefore closer to stoichiometric. The numerical modeling results presented herein clearly show the premixed burn phase in a droplet always occurs in lean mixtures. Therefore, the presence of fuel-bound oxygen in the methyl ester and alcohol fuels makes the fuel-air mixture in droplet combustion more lean, or *further* from stoichiometric. Since the stoichiometry of the premixed burn phase of a droplet is the opposite of a diesel spray, the results here neither confirm nor refute the hypothesis of Mueller and Hypothesis 2 of this document.

Now consider Hypothesis 3 which stated that there is combustion chemistry unique to methyl esters which enhances Fenimore NO_x during the premixed burn phase of combustion. Were Hypothesis 3 true, then it would be expected that only methyl butanoate would exhibit an enhanced rate of NO_x formation in Figure 4.12 during the premixed burn phase of combustion. Instead, both methyl butanoate and n-heptane show increased rates of NO_x formation during the premixed burn phase. In fact, n-heptane produces NO_x species at a rate that is greater than both methyl butanoate and methanol. Like before, these results appear to contradict Hypothesis 3, but the stoichiometry of the premixed autoignition zone again weakens the disparity.

Although not mentioned explicitly in the statement of Hypothesis 3, stoichiometry of the premixed autoignition zone is a relevant factor to the viability of the hypothesis because the premixed autoignition zone of a diesel spray is well known to be rich. As such, the chemistry unique to methyl esters could possibly be active only in rich mixtures, and if this were the case, the methyl ester chemistry would not be apparent in the premixed burn phase of a droplet because it is always lean.

4.5. Conclusion

Numerical simulations were conducted of spherically-symmetric isolated droplet autoignition and combustion. The fuels simulated were n-heptane, methyl butanoate, and methanol. Two versions of the chemical kinetic mechanism for each of the three fuels were created: one termed containing chemistry which included the Zel'dovich, Fenimore, and N_2O-path NO_x formation routes and the other having only Zel'dovich chemistry. All droplets were 200 μm in diameter at 300 K and the ambient was air at 1150 K. The pressure was fixed at one atmosphere.

All three fuels exhibited similar overall combustion behavior. First, there was a chemical induction time where the cold droplet absorbed heat from the ambient, thereby raising the temperature of the liquid fuel and enabling evaporation. Early exothermic reactions gradually elevated the temperature of the gas-phase until ignition occurred relatively far from the droplet surface. A premixed flame propagated through the premixed fuel and air as it moved from the periphery of the fuel vapor field, inward toward the droplet surface. The premixed flame always remained in lean regions and never propagated into the rich mixture. Following the consumption of premixed fuel and air, there was a transition to a non-premixed combustion state which remained until extinction of the droplet flame.

The calculated total NO_x formation was compared between the full NO_x and Zel'dovich NO_x cases for the respective fuels. For all three fuels simulated, the full NO_x modeling yielded dramatically more NO_x than the Zel'dovich cases. This result suggests the Fenimore and N_2O-path mechanisms are very important routes for overall NO_x formation in two-phase autoigniting combustion systems like droplets and diesel sprays.

The premixed burn phase of the droplet simulations showed enhanced NO_x formation by n-heptane and methyl butanoate. Methanol did not appear to produce significant NO_x species during its premixed burn phase. These results appeared to contradict Hypotheses 2 and 3, but no conclusion as to the viability of the hypotheses could be made because the premixed burn phase of droplet combustion is always lean whereas that of diesel sprays is well-known to be rich.

Results: PLIF of Isolated Droplet Flames

5.1. Introduction

Planar laser-induced fluorescence (PLIF) spectroscopy was performed on isolated droplet flames for a number of fuels. The resulting fluorescence images were processed to create radial profiles of hydroxyl (OH) and nitric oxide (NO). The experiments were conducted in parallel to the computational effort because spherically-symmetric droplet autoignition and combustion comprise a transient, single-spatial-dimension, chemically reacting flow field that can be solved numerically with detailed chemical kinetics, multicomponent species diffusion, and species-specific physical properties. The flexibility of the experimental apparatus and the requirement for only small volumes of fuel permitted the study of twice the number of fuels examined in the modeling work.

5.2. Experimental results

5.2.1. OH and NO Fluorescence Images of Isolated Droplet Flames. As described previously, hundreds of individual single-shot fluorescence images were averaged together to form averaged fluorescence images. False color images of the averaged fluorescence imges appear in Figures 5.1 and 5.2 for the six fuels, and two fluorescence species. All of the images are labeled first by the chemical formula corresponding to the fuel and second by the fluorescence species. For example, Figure 5.1A is an averaged hydroxyl (OH) fluorescence image of a methyl decanoate droplet flame. The images in Figures 5.1 and 5.2 were acquired approximately 16 ms after droplet ignition. Figure 5.3 contain images that all contain n-heptane flames at the time indicated in their respective captions. Thus, OH and

(A) $C_5H_{10}O_2$, OH

(B) $C_5H_{10}O_2$, NO

(C) $C_{11}H_{22}O_2$, OH

(D) $C_{11}H_{22}O_2$, NO

(E) C_7H_{16}, OH

(F) C_7H_{16}, NO
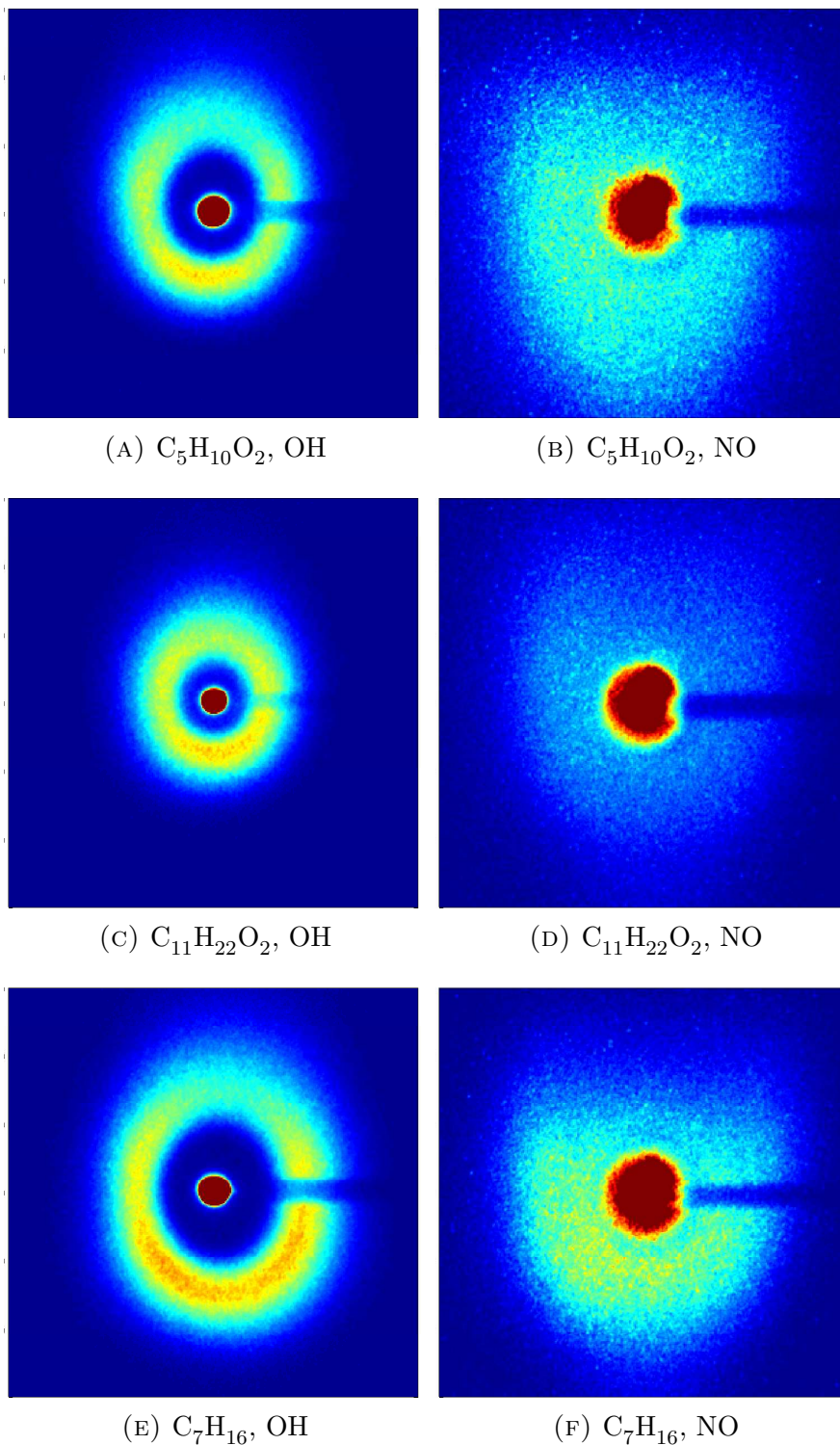
FIGURE 5.1. Averaged OH and NO fluorescence images are shown in a series of false color images for methyl butanoate, methyl decanoate, and n-heptane 16 ms after ignition.

(A) CH$_3$OH, OH   (B) CH$_3$OH, NO

(C) C$_2$H$_5$OH, OH   (D) C$_2$H$_5$OH, NO

(E) C$_3$H$_7$OH, OH   (F) C$_3$H$_7$OH, NO
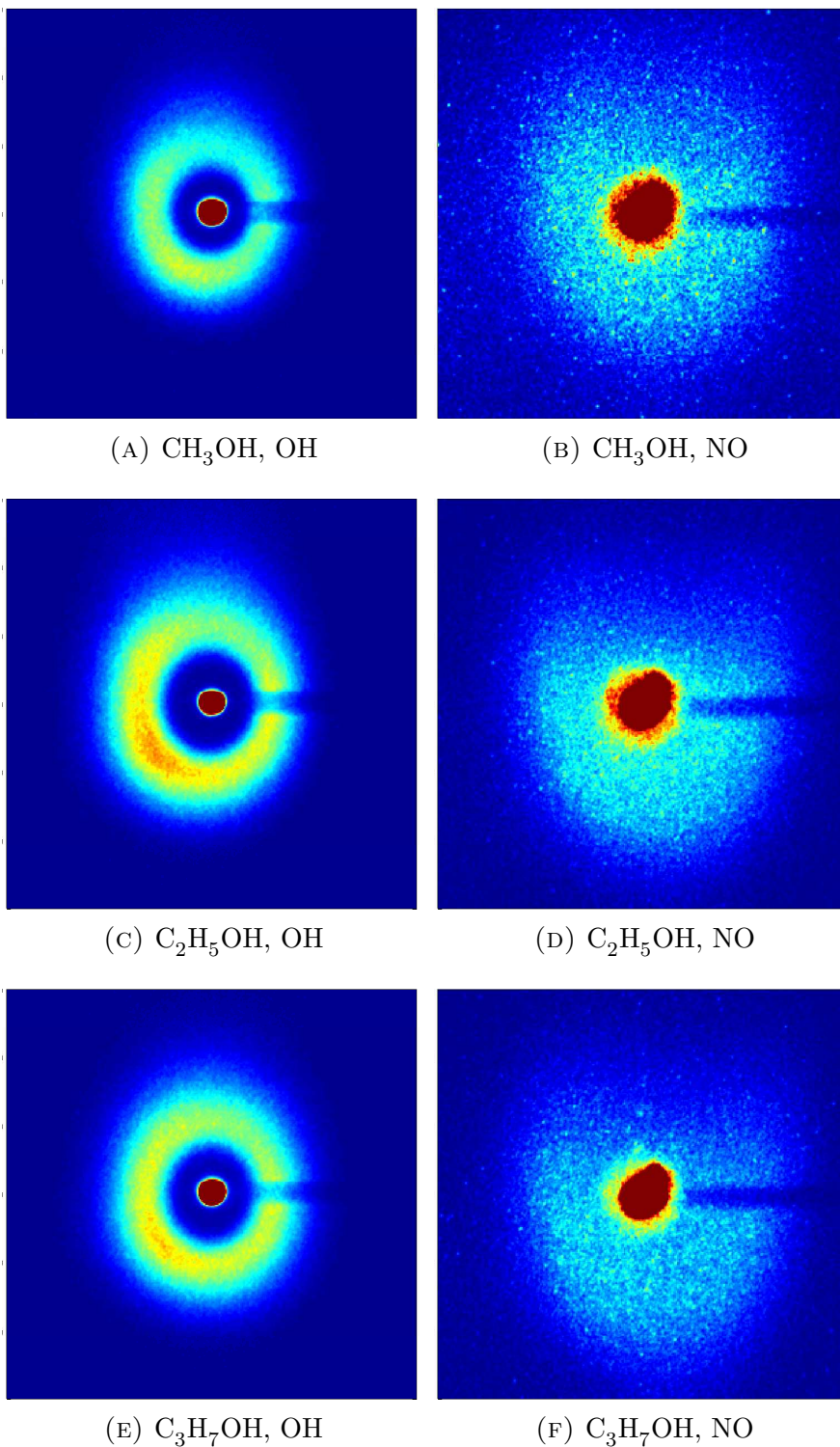
FIGURE 5.2. Averaged OH and NO fluorescence images are shown in a series of false color images for methanol, ethanol, and 1-propanol 16 ms after ignition.
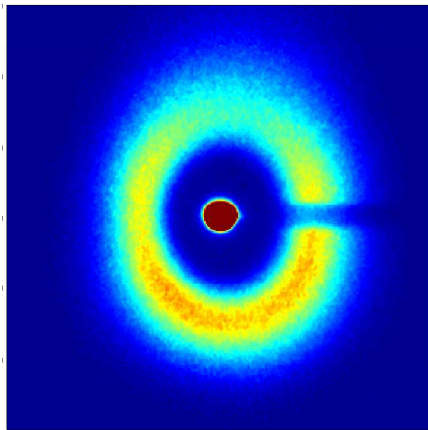
(A) C_7H_{16}, OH, $t = 16$ ms
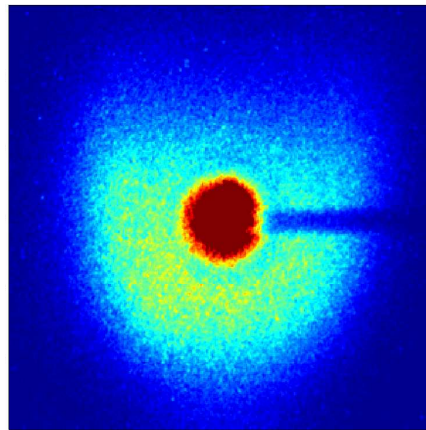
(B) C_7H_{16}, NO, $t = 16$ ms
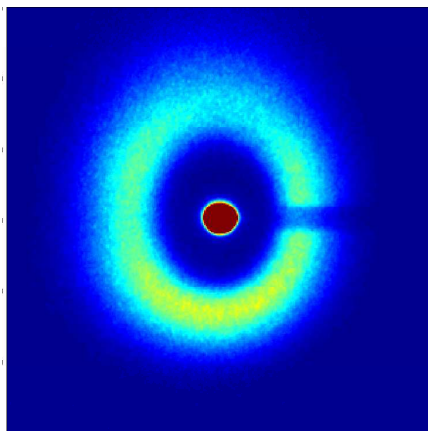
(C) C_7H_{16}, OH, $t = 19$ ms
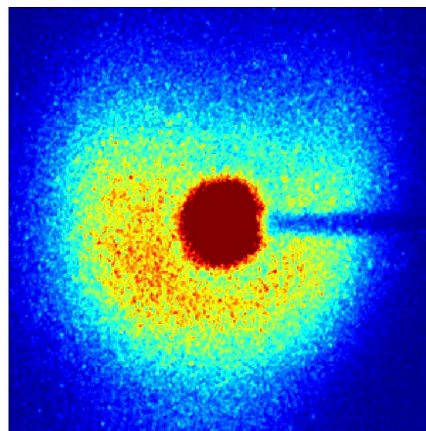
(D) C_7H_{16}, NO, $t = 19$ ms
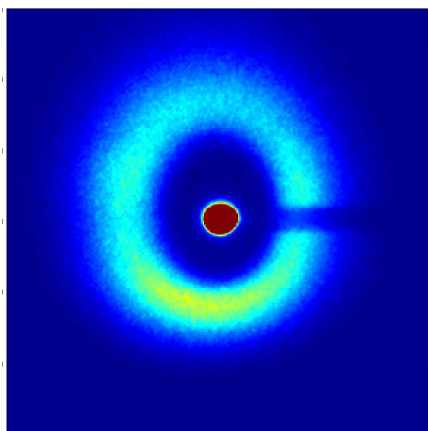
(E) C_7H_{16},OH, $t = 22$ ms
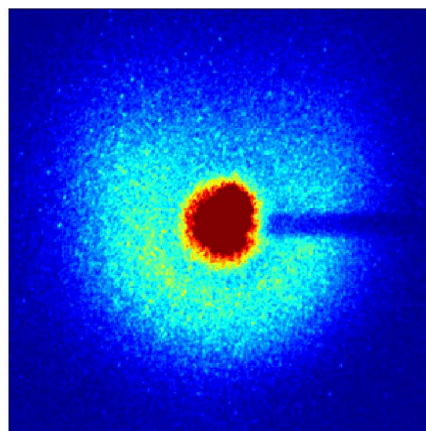
(F) C_7H_{16}, NO, $t = 22$ ms

FIGURE 5.3. Averaged OH and NO fluorescence images are shown in a series of false color images for n-heptane 16, 19, and 22 ms after droplet ignition.

NO fluorescence images of all six fuels were obtained 16 ms after ignition. Additionally, OH and NO fluorescence images were obtained for n-heptane at 19 ms and 22 ms.

All of the averaged fluorescence images in Figures 5.1, 5.2, and 5.3 are presented in false color to better show the variation in pixel intensity: dark red is the maximum value and dark blue is the minimum value. The dark red spots that appear in the very center of every image are the liquid fuel droplets. The rings or clouds surrounding the droplets are the fluorescence caused by the laser light interacting with the respective OH and NO species in the flames. It is less clear in the NO PLIF images but obvious in the OH PLIF images that the fluorescence is in a circular shape. This makes sense because the laser sheet was formed to be thin compared to the diameter of the flame. Therefore, the fluorescence image produced is a slice of the spherical shell of fluorescing species.

Approximate spherical symmetry of the droplet flame was achieved in the experiments by eliminating the factors that would cause distortion of the flame. Effects of buoyancy were eliminated because the droplet was in free fall under the acceleration of gravity. The flow pipe drew air surrounding the falling droplets downward so that the air flow velocity roughly matched the velocity of the droplet at the instant the fluorescence image was acquired. Finally, droplets of diameters ranging from 100 to 400 μm were used because the small size tends to better exhibit spherical symmetry than larger droplets typically used in droplet experiments.

Being dark red, the droplets are the brightest objects in the average fluorescence images in Figures 5.1, 5.2, and 5.3. This is caused by some droplet-scattered laser light passing through the optical filter and being imaged by the ICCD camera. Note that the droplet image appears small and distinct in the OH PLIF images, but large and diffuse in the NO

PLIF images. The droplet sizes were comparable in the two cases, so it is not related to physical size of the droplet. Rather, the variation in droplet appearance is due to a difference in the degree of attenuation of the laser wavelength and transmission of fluorescence exhibited by the respective optical filters used for OH and NO PLIF. The filters used for OH PLIF do a better job of attenuating the laser wavelength to reduce the intensity of the droplet image but still transmit sufficient fluorescence to be imaged by the camera. In contrast, the filter used for NO PLIF did not attenuate the laser light very well, causing bleeding of the pixels on the ICCD camera that resulted in the blob-like appearance of the droplets in the NO PLIF images. Moreover, the NO PLIF filter transmitted only a fraction of the fluorescence light to the camera, resulting in a low signal-to-noise ratio.

As implied above, the signal-to-noise ratio was higher for OH than for NO PLIF. This is caused by a number of factors including transmission of fluorescence light by the optical filter as discussed already. Another major factor was the intensity of the laser beam. Due to unknown reasons, the doubling crystal in the dye laser that converted the fundamental beam to a ultra-violet one, did not function as efficiently as it did so when new. As such, the laser pulse energy was reduced to about one-third of the specified output of the laser. Instead of a 226.03 nm beam of 2 to 3 mJ per pulse, the measured pulse energy was only a few hundred microjoules per pulse. This reduction caused a corresponding reduction in fluorescence and signal-to-noise. Accordingly, high-quality fluorescence images for OH PLIF were obtained, but the NO PLIF images were less than satisfactory. All of the NO PLIF images failed to show a distinct region between the flame and the droplet in which fluorescence was absent. In some cases, the images showed only a very weak peak where the flame is located. These deficiencies were due to a signal-to-noise ratio that was simply too low.

All of the fluorescence images show a dark stripe in the fluorescence ring/cloud to the right side of the droplet. This is caused by the droplet blocking laser light, creating a fluorescence shadow. The laser sheet passes from left to right and when it strikes the droplet it is scattered away from the initial path. Therefore, the fluorescing species to the right of the droplet do not receive laser light, and therefore do not fluoresce.

A further observation worth mentioning is the asymmetry of the intensity of the fluorescence images. Figure 5.1E is a good example of this phenomenon because the peak intensity of the fluorescence ring is orange below the droplet, but green-blue above the droplet. The fluorescence is more intense below the droplet because the timing of the droplet was intentionally devised so that the most intense part of the laser sheet passed through the bottom half of the droplet flame. Details of this are found in Chapter 3. The passing of the most intense part of the laser sheet below the droplet also explains why some of the NO PLIF images appear flattened above the droplet. This is especially apparent in Figures 5.1F, 5.2D, and 5.3B.

Consider the average fluorescence images in Figures 5.1F and 5.2C, E. These three images show a peak fluorescence intensity that is offset to the lower left instead of immediately below the droplet. This is not caused by asymmetry in the distribution of the fluorescence species, nor some effect of the laser sheet. Instead, it is due to slight misalignment in the flow of air around the droplet relative to the droplet trajectory. As explained in the introduction, it was necessary to draw air downward through the flow pipe to mitigate the distorting affects of buoyancy on the flame. In the case of these three images, the pipe was positioned so that enough droplet flames were pulled to the lower left that the averaged image shows a bias in that direction. During experiments, effort was exerted to ensure that the flow pipe
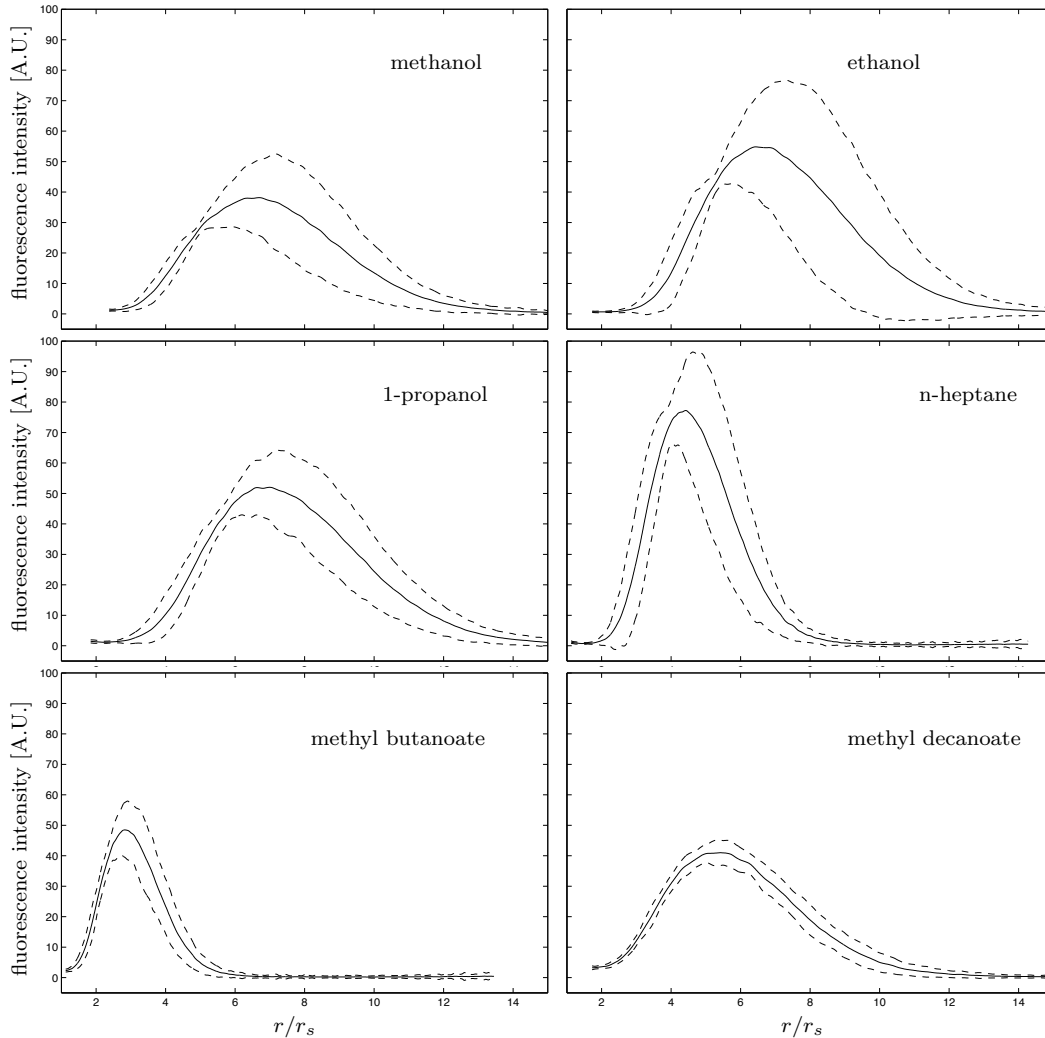
FIGURE 5.4. Profiles of hydroxyl radical (OH) in liquid droplet flames comprised of the indicated fuel approximately 16 ms after ignition are shown by solid curves. The 95% confidence contours are shown as dashed curves.

was positioned to minimize this effect. The bias shown here was, however, deemed to be acceptable when examined in context of the difficulty in obtaining the data to create them.

5.2.2. RADIAL OH PROFILES OF ISOLATED DROPLET FLAMES. The plots in Figure 5.4 show profiles of OH concentration in droplet flames approximately 16 ms after ignition for the fuels methanol, ethanol, 1-propanol, n-heptane, metyl butanoate, and methyl decanoate. These profiles were obtained by processing fluorescence images as described in Section 3.7. The vertical axis is intensity of the fluorescence signal with arbitrary units. Fluorescence

intensity is proportional to concentration of the fluorescing species. As such, the vertical axis can be thought of as concentration in arbitrary units. The the horizontal axis is radial distance r normalized by the time-dependent radius of the droplet surface $r_s = r_s(t)$. The solid contours represent fluorescence intensity (species concentration) of OH. The dashed contours above and below the solid contour are the 95% confidence interval

The six plots in Figure 5.4 corresponding to the six fuels tested all exhibit similar behavior. Near the droplet surface at $r/r_s = 1$, the OH concentration is near zero. The lack of OH near the droplet surface makes sense because OH is a combustion intermediate species formed in the hot, highly reactive flame region. Since the flame resides some finite distance away from the droplet surface, no OH is expected to be present near the droplet surface. Moreover, a lack of OH near $r/r_s = 1$ should be expected since the fluorescence images themselves showed no OH fluorescence between the flame and the droplet surface.

For $r/r_s > 1$, the OH concentration profiles in Figure 5.4 rise smoothly to a peak, then fall back to approximately zero. The flame can be assumed to be located at or very near to the peak OH concentration. The image processing conducted to obtain profiles of OH and NO concentration around the droplet flames was conducted in the same manner for all of the fuels examined in the experiments. Therefore, OH profiles can be compared among the six fuels. Likewise, NO profiles can be compared among the six fuels. (However, it is not meaningful to compare the intensity of OH with NO profiles since the two species are scaled differently by the inherent physics of the problem and the manner in which the image processing was carried out.) For example, in the methyl decanoate plot in Figure 5.4, the peak OH intensity is approximately 40 and approximately 80 for n-heptane. That means that approximately double the OH was observed in n-heptane compared to methyl

decanoate. The dashed curves above and below the concentration curves represent the 95% confidence intervals (i.e., plus or minus two standard deviations). The confidence intervals were determined based on the scatter in intensity of each point in the fluorescence image. The data acquired to produce the profiles were obtained approximately 16 ms after ignition of the droplet.

Since the OH profiles shown in Figure 5.4 correspond to 16 ms after ignition, the premixed fuel and air has been consumed and the droplet flames flames have most likely transitioned to a non-premixed flame. The OH profiles therefore represent the quasi-steady state configuration. The OH radical is a principle combustion intermediate, so the peak OH concentration is very close to, if not co-located with, the flame. The original intent of the experiments were to acquire fluorescence images during the premixed burn phase of the droplet combustion. However, the premixed burn phase for all of the fuels occurs very rapidly during which time, the droplet flame was obscured by the ignition coil. The fluorescence images presented here were acquired when the droplet flame was immediately below the ignition coil so that they represented the state of combustion at the earliest possible moment.

Figure 5.5 shows profiles of OH concentration obtained from planar laser-induced fluorescence spectroscopy for n-heptane droplets. The time indicated in each of the three plots represents the length of time since ignition. The trend from top to bottoms shows a declining magnitude in the concentration of OH. Also, the peak fluorescence intensity also appears to be moving inward toward the droplet surface.

5.2.3. RADIAL NO PROFILES OF ISOLATED DROPLET FLAMES. Figure 5.6 contains profiles of NO fluorescence obtained from planar laser-induced fluorescence spectroscopy of burning droplets of the indicated fuel approximately 16 ms after ignition. The solid line
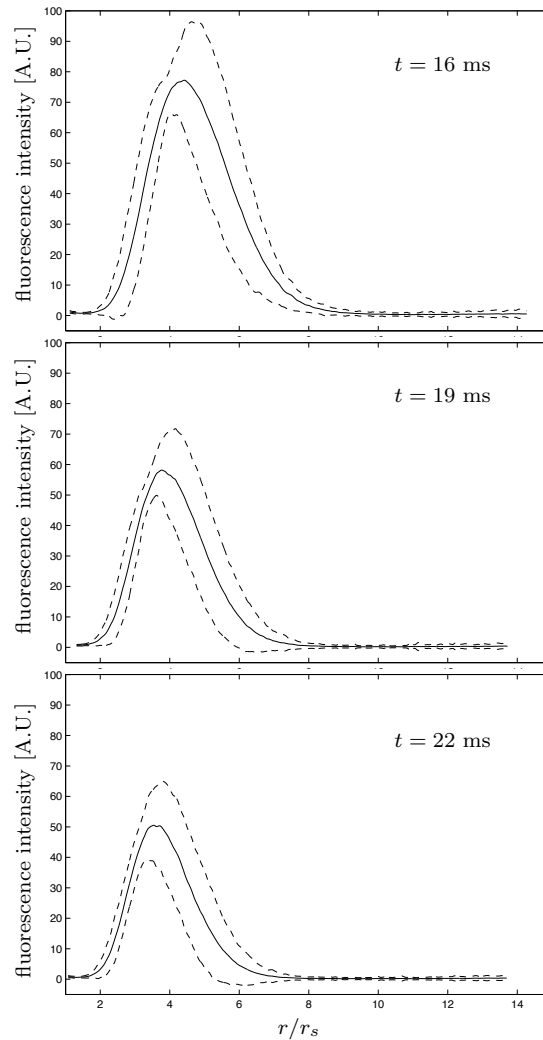
FIGURE 5.5. Profiles of hydroxyl radical (OH) in n-heptane droplet flames at indicated time after ignition are shown by solid curves. The 95% confidence contours are shown as dashed curves. The top plot is identical to the middle right plot in Figure 5.4.

represents the fluorescence intensity and therefore the NO concentration in the flame. The dashed contours above and below are the 95% confidence intervals.

Like the profiles of OH presented above, with increasing r/r_s the contours exhibit a local minima near the droplet surface, rise to a peak, then fall away toward zero. In the case of the NO profiles in Figure 5.7, however, the concentrations do not reach zero near the droplet surface. It is expected that concentration of NO at the droplet surface be very small, if not zero. This is made apparent by the results of the numerical modeling which showed that for

145
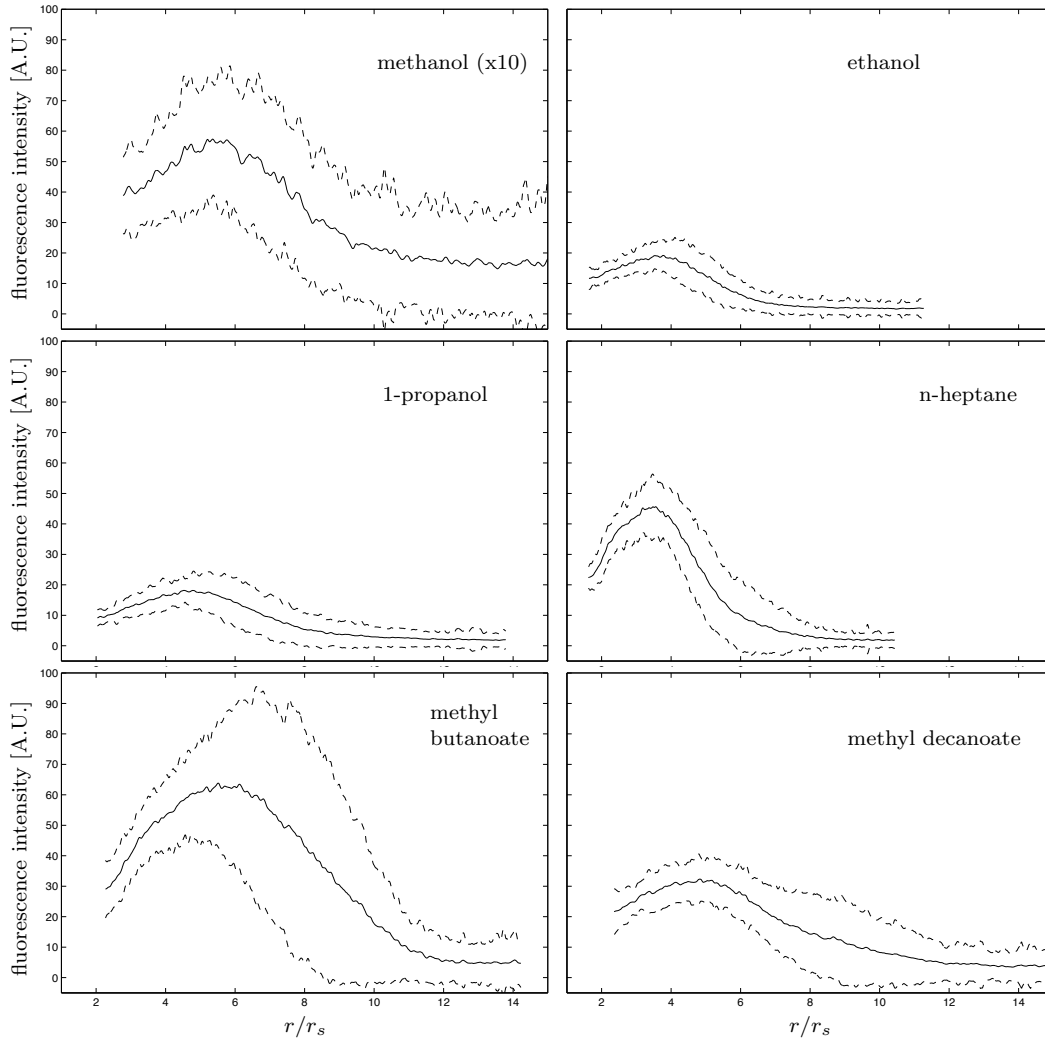
FIGURE 5.6. Experimentally-obtained profiles of nitric oxide (NO) in liquid droplet flames comprised of the indicated fuel approximately 16 ms after ignition are shown by solid curves. The 95% confidence contours are shown as dashed curves. Note that the top left curve for methanol is multiplied by a factor of ten.

methyl butanoate (Figure 4.2) and n-heptane (Figure 4.4), very little NO is present near the droplet surface: $r/r_s = 1$. The exception is methanol which shows a finite concentration of NO at $r/r_s = 1$. Although, note that the NO curve for methanol is multiplied by a factor of 100 instead of that for methyl butanoate and n-heptane for which the factor is ten.

The reason for the NO contours not reaching zero near the droplet surface is most likely due to experimental artifacts. Consider the NO fluorescence images in Figures 5.1 through
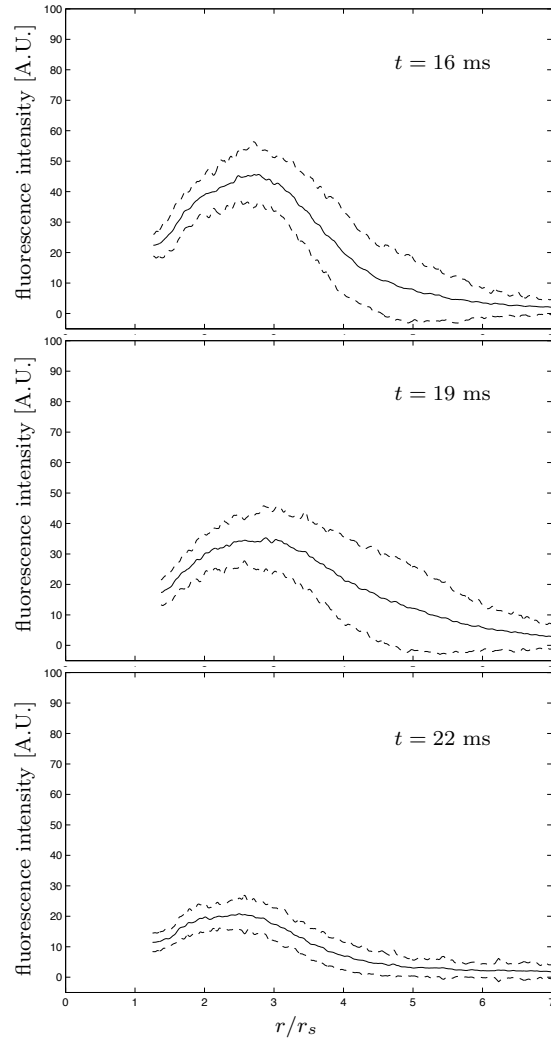
FIGURE 5.7. Experimentally-obtained profiles of nitric oxide (NO) in n-heptane droplet flames at indicated time after ignition are shown by solid curves. The 95% confidence contours are shown as dashed curves. The top plot is identical to the n-heptane plot in Figure 5.6.

5.3. As explained in the discussion associated with the figures, the large blurred droplet image is due to inadequate attenuation of laser light scattered by the droplet. When concentration profiles are created from those averaged fluorescence images for the respective fuels, the NO signal near the droplet surface appears to be large. However, the signal is almost certainly non-physical and probably caused by scattered laser light, not NO fluorescence.

Signal interference from scattered laser light is also the reason only the NO concentration plots for ethanol and n-heptane begin at $r/r_s = 1$, the droplet surface. The NO contours for

the remaining fuels are truncated so that data is shown only for approximately $r/r_s > 2$. The data that was truncated showed the NO contour rising rapidly near $r/r_s = 1$. A localized high concentration of NO at the droplet surface is non-physical and can be attributed to interference from droplet-scattered laser light. An example of a concentration contour that was not truncated is shown in Figure 3.11.

Despite NO fluorescence signal interference from scattered laser light for roughly $1 \leq r/r_s < 2$, useful data are present further from the droplet surface. It is interesting to note that methyl butanoate produced more NO than n-heptane when the adiabatic flame temperature of n-heptane is 35 K greater than that of methyl butanoate. Moreover, the result is also contrary to the simulations results, which show, for the corresponding time step, that n-heptane should produce more NO than methyl butanoate. This apparent contradiction is expanded upon in the following discussion section.

Figure 5.7 shows experimentally-obtained profiles of NO concentration (solid curve) as a function of normalized radius for approximately 16, 19, and 22 ms after ignition. The dashed contours are the 95% confidence intervals (i.e., two standard deviations). Like the corresponding OH fluorescence profiles (Figure 5.5), the trend with increasing time is a decline in the amount of NO and a slight movement of the peak toward the droplet surface. The 95% confidence intervals at t = 22 ms are particularly narrow, meaning that the NO fluorescence intensity of the single-shot images used to obtain the data were especially consistent.

5.3. Discussion

Figure 5.8 plots the peak NO signal (black circles) from the profiles in Figure 5.6 with respect to adiabatic flame temperature as found in Table 1.2. The error bars correspond to
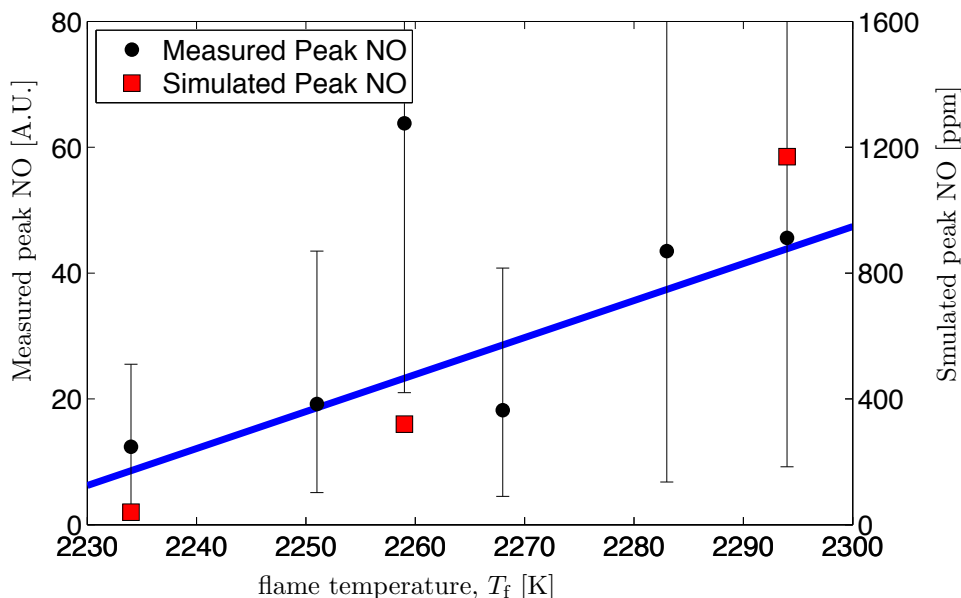
FIGURE 5.8. A plot showing how experimentally-measured NO in droplet flames with PLIF corresponds to the adiabatic flame temperature of the respective fuels.

the 95% confidence interval (plus or minus two standard deviations). For the most part, the peak NO correlates with adiabatic flame temperature of the respective fuel. The correlation is also seen in the peak NO values indicated by red squares obtained from the simulations at 16 ms after ignition for (left to right) methanol, methyl butanoate, and n-heptane.

This trend of increasing peak NO with increasing adiabatic flame temperature makes sense because as T_{f} increases, a corresponding increase in flame temperature would be expected as well, thereby enhancing Zel'dovich NO formation and NO_x formation chemistry overall. The exception to the trend of NO formation being proportional to adiabatic flame temperature in Figure 5.8 is the experimentally-measured peak NO of methyl butanoate at $T_{\mathrm{f}} = 2259$ K. The measured peak NO for methyl butanoate was in excess of even n-heptane.

There are a number of possible explanations for the relatively high NO measured for methyl butanoate. Perhaps methyl butanoate exhibits unique chemistry that results in a relative abundance of Fenimore NO_x precursors that leads to enhanced NO formation. Such

chemistry does not appear to be present in methyl decanoate since it appears to follow the correlations between adiabatic flame temperature and peak NO fairly well. Supposing the explanation is correct in which methyl butanoate exhibits unique chemistry for enhanced NO formation, then the chemical kinetic mechanism used for the methyl butanoate droplet ignition numerical modeling would have to be considered lacking because the enhanced NO formation was not apparent in the simulations.

A second explanation for relatively high peak NO for methyl butanoate seen in Figure 5.6 is experimental error. The challenging nature of the experiments makes such an explanation not unlikely. Regardless, further study of the matter is warranted. A colleague of the author is conducting PLIF and LIF spectroscopy on NO in steady, stoichiometrically-stratified flames of the same fuels studied here. The steady nature of the flames will permit a much improved signal-to-noise ratio for NO spectroscopy and will perhaps shed some light on the enhanced NO formation seen in the methyl butanoate experimental results.

A series of images are shown in Figure 5.9 which show how the experimentally-obtained average fluorescence image compares with the simulation result for n-heptane. The first row contains OH fluorescence data, with Figure 5.9A being the averaged fluorescence image for n-heptane that is identical to Figure 5.1E[1]. As explained in Section 3.7, the fluorescence field is angularly averaged to obtain a profile of the fluoresce intensity and therefore the concentration as a function of normalized radius. The profile thusly acquired is swept about the origin of a polar coordinate system to obtain Figure 5.9B. Figure 5.9C is created in the same way, but in this case the simulated NO profile from the numerical model 16 ms

---

[1]The false color levels have been slightly altered in the averaged fluorescence image to improve visibility of the fluorescence field and thereby facilitate comparison.

(A) OH Fluorescence (B) OH Angularly swept (C) OH Simulation

(D) NO Fluorescence (E) NO Angularly swept (F) NO Simulation
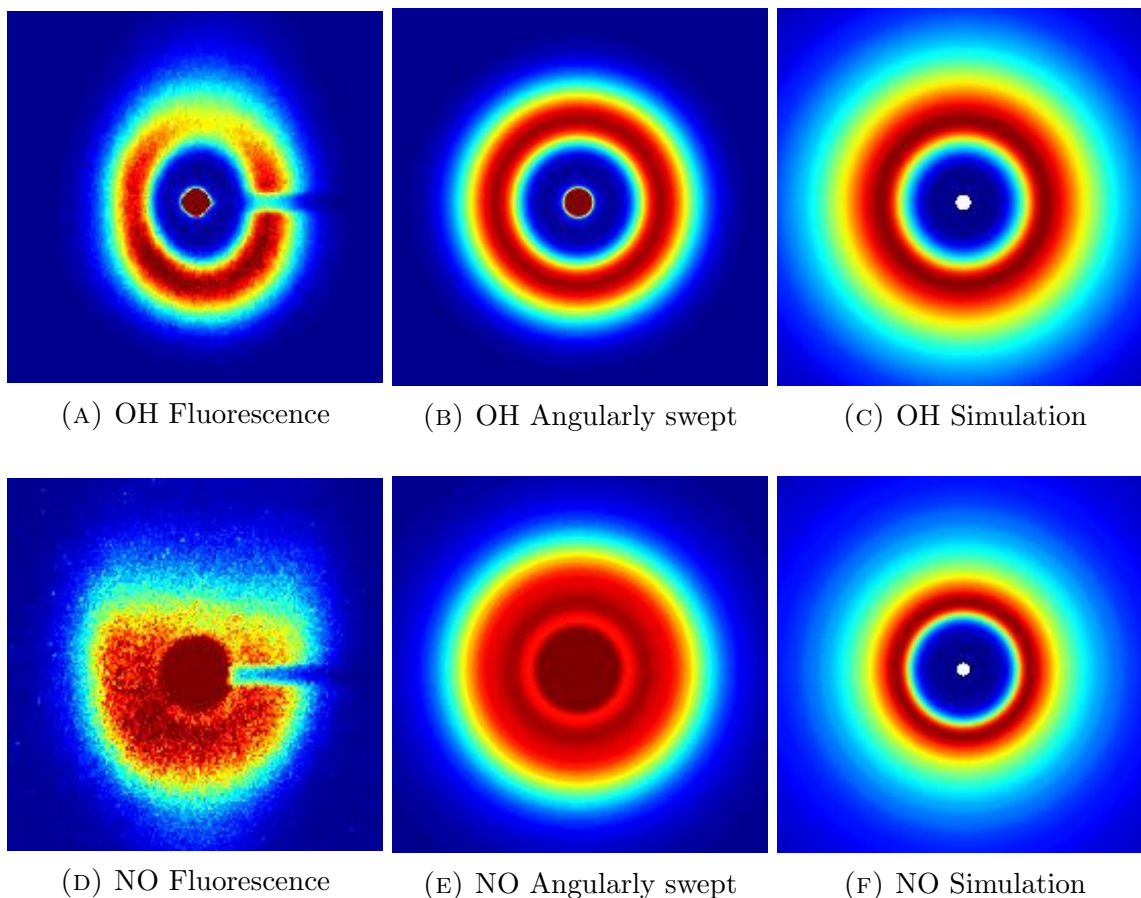
FIGURE 5.9. A comparison of OH and NO results for n-heptane 16 ms after ignition from planar laser-induced fluorescence spectroscopy experiments and transient, spherically-symmetric droplet autoignition and combustion simulations with detailed chemical kinetics, multi-component mass diffusion, and species-specific specific heat.

after ignition is swept about a polar origin. Figures 5.9D-F are the analogous images of experimental and numerical results for NO.

A striking feature of Figure 5.9 is the disparity in apparent droplet size between the angularly swept NO profile from the experiment and that of the numerical model. The droplet in the simulation images (Figures 5.9C,F) are indicated by the small white circle at the center and appears to be much smaller than that of the experiment (Figures 5.9B,E). The reason for the apparent contrast in droplet size is the laser light scattered by the droplet and imaged by the intensified CCD camera is sufficiently bright to cause bleeding of the pixels

on the camera sensor. The result is a droplet that appears much bigger than it actually is. The comparison between the two droplet images demonstrates how the droplet image that appears in all averaged fluorescence images in this work do not necessarily correlate with the actual droplet size.

Overall, Figure 5.9 shows a reasonable match between the experimental and numerical modeling results. With some refinement, it is not unreasonable to expect that planar laser-induced fluorescence spectroscopy of a falling droplet could be used to validate the droplet code and chemical kinetic mechanisms for liquid fuels.

In order to better compare the experimental and numerical simulation results, Figure 5.10 contains hydroxyl (OH) contours for methyl butanoate, n-heptane, and methanol. In all three plots, the horizontal axis is the radial coordinate normalized by the time-dependent radius of the liquid fuel droplet: $r/r_s(t)$. The red OH profiles were obtained experimentally from planar laser-induced fluorescence spectroscopy of freely-falling droplet flames and correspond to the left-hand vertical axis. The scale of the left-hand axis is identical to the vertical axis of the plots presented in Figure 5.4. The red experimental OH contours were shifted in r/r_s-space so that the peak OH concentration was coincident with that of the numerical modeling results. The vertical magnitude of the red experimental curves were not changed, but the extent of the vertical axis plotted was adjusted so that the peak of the experimental and numerical data was coincident in the vertical direction as well. The blue contours in Figure 5.10 represent the OH mass fraction obtained from numerical modeling of droplet flames of the respective fuels, and correspond to the right-hand axis.

An examination of the plots in Figure 5.10 show that for all three fuels, the simulation compares well with the experimental results from the droplet surface to the peak OH value.

152
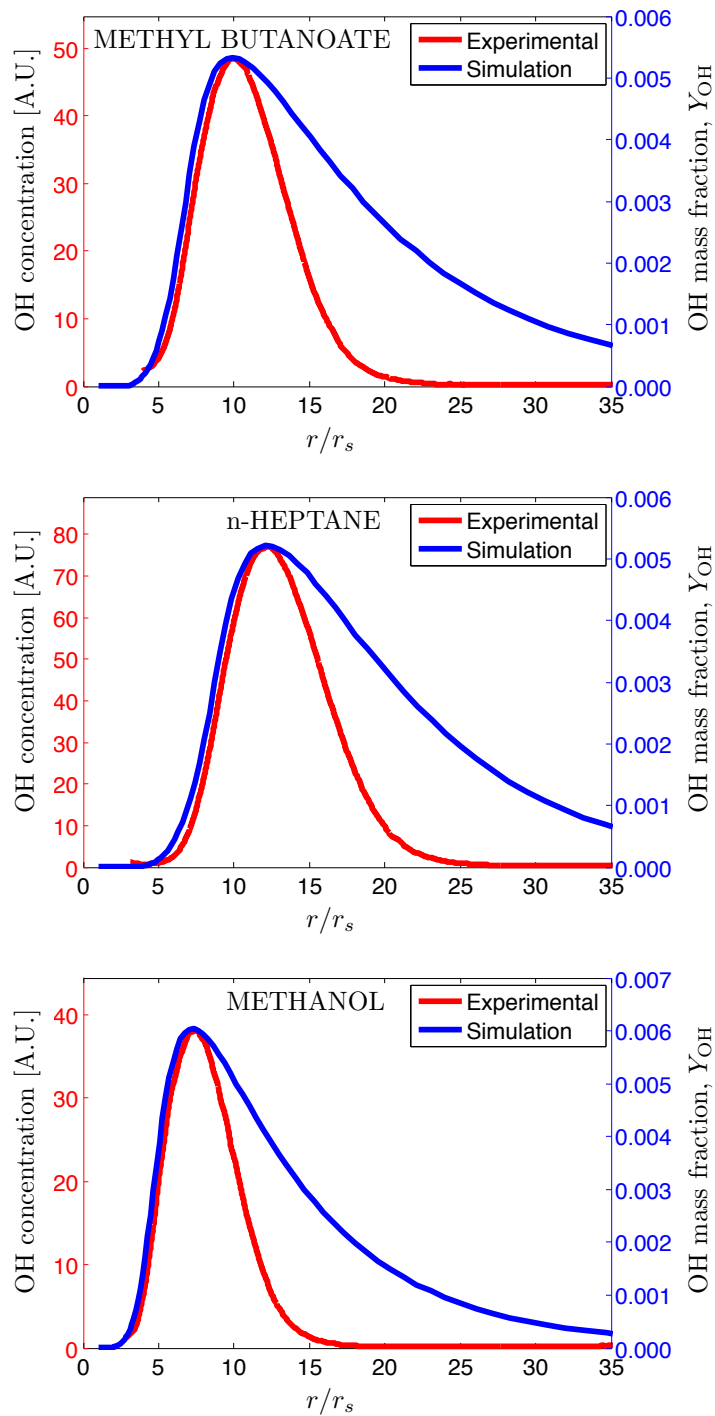
FIGURE 5.10. A comparison of OH concentration measurements from planar laser-induced fluorescence spectroscopy (red) and numerical modeling (blue) of a spherically-symmetric droplet flame with detailed chemical kinetics, multicomponent diffusion, and species-specific physical properties.

However, starting at the location of the peak OH value of the respective fuels, and for increasing r/r_s, the experimental and numerical results diverge somewhat. The experimental curve falls away faster than the numerical simulation results, so the experiment has a symmetric shape. The numerical simulation shows a long, gradual decrease with increasing r/r_s. The disparity of the OH concentration curve beyond the peak concentration between the experiment and simulation can probably be explained by the presence of convective transport in the experiment. One of the assumptions of the numerical simulations was that mass transport included diffusion, but not convection. In the experiment, efforts were made to minimize convective motion relative to the droplet, but some convective transport is inevitable. As such, some OH in the region beyond the peak OH location was transported away via convection, causing the OH concentration to be lower there. The reduction of OH caused the experimental OH curve to not exhibit the long tail like the numerical simulation results did.

CHAPTER 6

Isolated Droplet Autoignition and Combustion as a Physical Model for Diesel Sprays

One motivation to study isolated droplet autoignition and combustion is to determine if it can be considered a physical model to diesel sprays. The implication being results from droplet autoignition and combustion work can be applied to better understanding the same phenomena of a diesel spray in an engine. For example, droplet simulations or experimental results could be used to verify a chemical mechanism for a petroleum or biodiesel surrogate. Conceptually, the analogy makes sense: both combustion systems exhibit a cold liquid fuel in a hot ambient oxidizer, both have some finite induction time prior to ignition where fuel vapor diffuses into and mixes with the oxidizer ambient, both exhibit thermal autoignition behavior, and both have a premixed burn phase that transitions to a non-premixed, transport-controlled combustion regime. Despite these similarities, there exists a major difference in behavior between droplets and diesel sprays. Specifically, liquid fuel droplets always autoignite in very lean mixtures whereas diesel sprays do so in rich regions. The reason for the difference in ignition behavior is explained and implications explored in this chapter. The conclusion being that, at least as a physical analogy for understanding autoignition in diesel sprays, droplets are unsuitable.

6.1. Description of the Droplet Physical Model for Diesel Sprays

A detailed description of diesel spray autoignition and combustion in an engine is presented in Section 1.2 and that of isolated droplets in Section 1.3. In this section, the similarities in physical features between the two systems, and how this supports the concept of droplets as a physical model for diesel sprays, are discussed.

The fuel jet of a diesel engine is injected into a hot, high-pressure charge of air. The liquid fuel is much colder than the ambient, so the resulting thermal gradient causes energy to move into the liquid by way of diffusion. The enthalpy introduced to fuel from the ambient goes into raising the temperature of the liquid and enabling evaporation. The identical process occurs in a droplet of fuel that appears in a hot ambient. Heat moves from the hot ambient to the cold droplet, raising the temperature of the droplet and providing enthalpy for evaporation. Furthermore, in both cases, because the cold droplet is acting as an enthalpy sink, the temperature of the local gas phase is reduced. Moreover, the evaporating droplet is acting like a fuel vapor source. The combination of these factors makes for systems in which both temperature and stoichiometry are stratified. This is particularly important when examining the chemistry of ignition since chemical reaction rate is closely tied to stoichiometry and temperature.

The evaporation of fuel from sprays and droplets create a concentration gradient that drives the fuel vapor away from the liquid surface via mass diffusion. In droplet systems, diffusion is the sole mode of mass transport and it alone is responsible for fuel vapor moving away from the liquid and mixing with the ambient oxidizer. This is in contrast to a diesel fuel spray in which fuel vapor is transported and mixed via convective transport in addition to diffusion. Convective transport occurs when mass is moved about by bulk motion of the

fluid. This is exactly analogous to how one may detect the odor of perfume in the following two scenarios. First, even if a room is absolutely free of any air currents, one will eventually smell a perfume bottle after it is opened across the room because the molecules are brought to the nose by mass diffusion. On a breezy day, if a bottle is opened upwind the perfume will be promptly detectable because the bulk motion of the wind transports the molecules to your nose. (In the latter case, mass diffusion is undoubtedly occurring as well, however the mass flux of perfume will be due mostly to convection on a windy day.)

Certainly both modes of transport would become important if a droplet were to appear in a turbulent oxidizer. However, the quiescent state of the oxidizer ambient is a key attribute to the utility of droplet combustion as a simulated system. The quiescent ambient and diffusion as the principle mode of mass transport means that fluid momentum everywhere in the domain is sufficiently small as to be negligible. As such, there is no need to solve the momentum equation of fluid motion, thereby freeing computational resources. The computer power that might otherwise be occupied by solving the momentum equation can be put to use solving aspects of the simulation that make it more realistic like detailed chemistry and species-specific diffusion. Thus, it is essential that the droplet be assumed to experience a quiescent ambient, even at the expense of lacking the convective transport that is present in diesel sprays. As will be seen shortly, the presence of convective transport in diesel sprays is directly related to why droplet ignition and combustion is an unacceptable physical model for diesel sprays.

Diesel sprays and droplets both exhibit an induction period followed by autoignition. During the induction period, called the ignition delay and usually on the order of milliseconds, fuel is evaporated and the vapor transported into and mixed with the ambient oxidizer. This

constitutes a premixed fuel-air mixture because it is created prior to ignition. The actual ignition event is considered autoignition because in neither case is there an energy input sufficiently large to alone initiate thermal runaway of a fuel-air mixture. This is in contrast to a spark-ignited gasoline engine in which an electric arc provides the energy to trigger thermal runaway. In diesel engines and isolated droplets in a hot oxidizer, heat from the ambient enables the low-temperature exothermic and radical-producing chemical reactions that are the first steps in the chain reaction known as thermal runaway. While heat from the ambient provides the initial push, it is chemical heat release that provides the enthalpy required to exceed the activation energy, start thermal runaway, and ultimately achieve fully involved combustion. While both systems autoignite, they tend to do so at different stoichiometries. The reason for this is discussed at length later in this section.

As described above, fuel vapor produced by evaporation will be transported away from the liquid surface and mixed with the ambient oxidizer creating a fuel-air mixture. In a diesel spray, combustion of this mixture is called the premixed burn fraction and is responsible for the loud, clacking noise of less modern engines. The premixed burn fraction is also present in autoigniting droplets in a hot ambient. However, while the premixed burn fraction in diesel engines is rich, in droplet ignition, it is lean.

Just as both diesel sprays and droplets have a premixed burn fraction, they both also transition to a diffusion flame following consumption of the premixed fuel and air.

6.2. Advantages of a Physical Model for Diesel Spray

There are a number of advantages to using isolated droplet ignition and combustion as a physical model for diesel spray. Namely, experiments and computer simulations to study compression-ignition phenomena are made significantly easier. In this section, these

benefits are explained and explored. Conducting experiments on droplet flames is vastly easier and cheaper than analogous studies on engines. For example, this thesis reports on the implementation of OH and NO PLIF on burning droplets in free-fall. The experiments are sufficiently straight-forward that they could be implemented by most any dedicated research group able to acquire the capital for the required lasers, optics, and camera. This is in contrast to PLIF conducted on a research engine, which requires a heavily modified engine and associated support equipment, in addition to the laser diagnostic components. The difficulty and expense associated with engine diagnostics makes it infeasible for all but the most well-established groups.

Once a droplet combustion facility is set up and experiments become routine, only a tiny volume of fuel is required to acquire data. This is advantageous when one wishes to conduct experiments on a particularly expensive or rare substance. For example, the biodiesel surrogate, methyl decanoate, costs hundreds of dollars per liter. Furthermore, a fuel derived from some manner of microorganism may be in the early development stage with a laboratory production capacity of only a few tens of milliliters per week. The droplet generation apparatus used to conduct the experiments reported on by this thesis required only about 50 ml of fuel. In fact, it would be a simple matter to design and construct a similar device that would required even less fuel; even 20 ml is not unreasonable. This is in contrast to an engine test in which the required fuel is on the order of tens of liters. This factor of 1000 increase in fuel volume may make experiments with expensive or rare fuels impractical.

Presently, a spherical-symmetric domain is the sole geometry in which computational simulation of liquid fuel combustion is possible with detailed chemical kinetics [68]. The

reason this is the case is in part that a spherically-symmetric domain is described spatially by a single variable: radius. Therefore, it is necessary to solve equations only in terms of radius and time. Naturally, a single spatial variable will also adequately describe a one-dimensional flat flame. However, in the formulation of the boundary conditions, a spherically-symmetric domain possesses a key advantage over a one-dimensional rectilinear one. The far field boundary conditions for a sufficiently large spherically-symmetric domain are Dirichlet. This means that for a combustion simulation, gas composition and temperature are held constant at the outer boundary for all time. This is in contrast to a one-dimensional rectilinear domain in which the far field boundary conditions can vary in time. Clearly, constraining the far field boundary conditions to fixed values is much easier than devoting computational effort to determining them with each timestep.

6.3. Ignition in Turbulent Non-premixed Flames

The ignition of an isolated droplet of fuel in a hot ambient is similar to the ignition of a diesel spray in an engine because they both do so spontaneously as a result of heat released from exothermic low-temperature reactions. One of the principle areas of study of the research reported on in this thesis is to justify whether or not the ignition and combustion of an isolated fuel droplet could act as a physical model for ignition and combustion of a diesel spray. If the analogy were shown to be a strong one, it would be a boon for combustion researchers because simulation and experiments on isolated droplets are far easier and cheaper than attempting the same on a operating diesel engine.

In order to evaluate the viability of the analogy between ignition and combustion of an isolated fuel droplet and a diesel spray, it is necessary to delve into the theoretical treatment of non-premixed flames. First, we examine the flame structure based on a new variable

called mixture fraction. From this treatment, a quantity called mixture fraction appears that implicitly couples the chemistry of combustion and mixing due to diffusion and convection. With this framework in place, it is possible to understand how temperature, pressure, fuel and oxidizer chemistry, and mixing affect ignition processes in non-premixed flames. Ultimately, the stoichiometry of ignition in droplets is, in general, found to be different from that of diesel sprays. Therefore, it must be concluded that for ignition at least, isolated fuel droplets are an unsuitable physical model for diesel sprays.

6.3.1. MIXTURE FRACTION SPACE. A non-premixed flame is one in which the fuel and oxidizer streams are initially separate, but are later allowed to mix by diffusion and possibly convection. Moreover, in the case of diesel engine sprays and the droplets studied for this thesis, spontaneous ignition of the fuel and oxidizer mixture may occur. In this section, a simplified non-premixed flame is examined to develop theoretical concepts needed for discussion. In particular, two quantities are described that prove to be important parameters in turbulent combustion. These two parameters, mixture fraction and scalar dissipation, also enable the discussion of ignition of turbulent non-premixed flames, the subject of the following subsection.

In order to introduce the concept of mixture fraction, it is useful to consider a simplified non-premixed flame. The coupling functions are obtained, then used to derive mixture fraction[1]. The following assumptions are made in order to proceed:

(1) Single-step overall chemical reaction with N species.

(2) Pressure is constant for all time.

(3) Mach number is small everywhere for all time.

---

[1]Unless indicated otherwise, the derivation in this subsection largely follows Poinsot and Veynante [84].

(4) Diffusion is fixed at a single value for all species.

(5) Specific heat is fixed at a single value for all species and is invariant with tempera-

ture.

(6) Unity Lewis number: $Le = \lambda/(C_p \rho D) = 1$, which implies $\rho D = \lambda/C_p$.

(7) Quantities in the reaction zone are solely a function of time and mixture fraction.

Assumption (1) implies the chemical reaction can be written in the following way:

$$\sum_{i=1}^{N} \nu_i' M_i \rightarrow \sum_{i=1}^{N} \nu_i'' M_i, \tag{54}$$

where ν_i is the molar quantity of species i, which is a molecule (or atom) with symbol rep-

resented by M_i. The prime and double primes indicate reactants and products, respectively.

If the fuel is symbolized by F, oxidizer by O, and products by P, then one can write the

reaction this way:

$$\nu_F F + \nu_O O \rightarrow \nu_P P. \tag{55}$$

The species equation is written in terms of mass fraction thus:

$$\frac{\partial \rho Y_k}{\partial t} + \frac{\partial}{\partial x_i}(\rho u_i Y_k) - \frac{\partial}{\partial x_i}\left(\rho D \frac{\partial Y_k}{\partial x_i}\right) = w_k, \tag{56}$$

where $i = 1, 2, 3$ represent three mutually orthogonal spatial directions, $k = F, O, P$ are the

three species considered, and w_k is formation or consumption of species k due to chemical

reactions (combustion). Suppose the one-step overall chemical reaction rate is given by:

$$Q = \frac{w_k}{W_k \nu_k} \tag{57}$$

where W_k is the molar mass of species k. Then a simple rearrangement gives species-specifc reaction rate:

$$w_k = W_k \nu_k \mathcal{Q}. \tag{58}$$

The reaction rate of oxidizer is related to that of fuel via:

$$w_O = \sigma \, w_F, \tag{59}$$

where

$$\sigma = \frac{\nu_O W_O}{\nu_F W_F} \tag{60}$$

is a stoichiometric mass ratio of oxidizer with respect to fuel. The heat release rate per unit mass of fuel consumed is represented by the following:

$$q = \sum_{k=1}^{N} \left(h_{f,k}^{\circ} \frac{W_k \nu_k}{W_F \nu_F} \right), \tag{61}$$

where the term $h_{f,k}^{\circ}$ is the formation enthalpy for species k. Now it is possible to relate heat release rate to chemical reaction rate of fuel by way of:

$$w_T = -q \, w_F. \tag{62}$$

Equations for fuel, oxidizer, and energy can now be written by using the equations above:

$$\frac{\partial \rho Y_F}{\partial t} + \frac{\partial}{\partial x_i}(\rho u_i Y_F) - \frac{\partial}{\partial x_i}\left(\rho D \frac{\partial Y_F}{\partial x_i} \right) = w_F \tag{63}$$

$$\frac{\partial \rho Y_O}{\partial t} + \frac{\partial}{\partial x_i}(\rho u_i Y_O) - \frac{\partial}{\partial x_i}\left(\rho D \frac{\partial Y_O}{\partial x_i} \right) = \sigma w_F \tag{64}$$

$$\frac{\partial \rho T}{\partial t} + \frac{\partial}{\partial x_i}(\rho u_i T) - \frac{\partial}{\partial x_i}\left(\frac{\lambda}{C_p} \frac{\partial T}{\partial x_i} \right) = -\frac{q}{C_p} w_F. \tag{65}$$

As before, subscript $i = 1, 2, 3$ represents three mutually orthogonal spatial directions. With the three equations above, the three coupling functions can be derived. First, Equation (64) is multiplied by $1/\sigma$ and subtracted from Equation (63). This eliminates the chemical reaction term w_F and, when like terms are combined, demonstrates that the quantity $\beta_1 = \sigma Y_F - Y_O$ is a conserved scalar because it is described by the following conservation equation:

$$\frac{\partial \rho \beta_j}{\partial t} + \frac{\partial}{\partial x_i}(\rho u_i \beta_j) - \frac{\partial}{\partial x_i}\left(\rho D \frac{\partial \beta_j}{\partial x_i}\right) = 0, \tag{66}$$

where $j = 1$ in this case. Second, Equation (65) is multiplied by C_p/q and added to Equation (63) to yield the conserved scalar $\beta_2 = C_p T/q - Y_F$. Notice Assumption (6) was invoked to replace λ/C_p with ρD so that the diffusion terms could be combined. Finally, Equation (64) is multiplied by $1/\sigma$ and added to Equation (65) multiplied by C_p/q to arrive at $\beta_3 = \sigma C_p T/q + Y_O$. These three conserved scalars represent the three coupling functions for the system and are summarized here:

$$\beta_1 = \sigma Y_F - Y_O \tag{67}$$

$$\beta_2 = \frac{C_p T}{q} - Y_F \tag{68}$$

$$\beta_3 = \sigma \frac{C_p T}{q} + Y_O. \tag{69}$$

As noted above, the functions β_j, $j = 1, 2, 3$ are conserved insofar as they make Eqauation (66) true, but can vary due to diffusion and convection (but not reaction).

Non-premixed flames such as the one examined in this subsection have separate fuel and oxidizer inlet streams. (Or, for a closed chamber, initially separated fuel and oxidizer regions.) Suppose the location of the fuel and oxidizer inlets are symbolized by superscripts B^-

and B^+, respectively. It is possible to normalize the coupling functions by their (boundary) values at these locations using the following formula:

$$\xi_j = \frac{\beta_j - \beta_j^{B^+}}{\beta_j^{B^-} - \beta_j^{B^+}}. \tag{70}$$

Naturally, at the oxidizer inlet there is no fuel present ($Y_F^{B^+} = 0$) and at the fuel inlet no oxidizer is found ($Y_O^{B^-} = 0$). Moreover, let the temperature of the fuel and oxidizer streams at the respective inlets be $T_F^{B^-}$ and $T_O^{B^+}$. Similarly, let the mass fraction of the fuel and oxidizer at the respective inlets be $Y_F^{B^-}$ and $Y_O^{B^+}$. Then, using Equation (70) for $j = 1, 2, 3$, these equations are obtained:

$$\xi_1 = \frac{\sigma Y_F - Y_O + Y_O^{B^+}}{\sigma Y_F^{B^-} + Y_O^{B^+}} \tag{71}$$

$$\xi_2 = \frac{\frac{C_p}{q}\left(T - T_O^{B^+}\right) + Y_F}{\frac{C_p}{q}\left(T_F^{B^-} - T_O^{B^+}\right) + Y_F^{B^-}} \tag{72}$$

$$\xi_3 = \frac{\frac{\sigma C_p}{q}\left(T - T_O^{B^+}\right) + Y_O - Y_O^{B^+}}{\frac{\sigma C_p}{q}\left(T_F^{B^-} - T_O^{B^+}\right) - Y_O^{B^+}} \tag{73}$$

The above equations hold interesting properties. At the fuel inlet, all three equations are equal to unity: $\xi_1^{B^-} = \xi_2^{B^-} = \xi_3^{B^-} = 1$. On the other hand, all three equations are equal to zero at the oxidizer inlet: $\xi_1^{B^+} = \xi_2^{B^+} = \xi_3^{B^+} = 0$. In fact, at any point in the system, all three equations are equal to the same quantity because they are equivalent:

$$\xi = \xi_1 = \xi_2 = \xi_3. \tag{74}$$

The quantity ξ is called the mixture fraction and is an important tool for studying non-premixed ignition and combustion systems. In words, mixture fraction is the ratio of material

present that originated from the fuel stream to the total amount of material. Notice that neither the fuel nor oxidizer streams need be pure; either stream can contain any amount of diluent. As implied above, the following is true for mixture fraction:

$$\xi = 1 \quad \text{at the fuel inlet,}$$

$$\xi = 0 \quad \text{at the oxidizer inlet.}$$

Elsewhere in a non-premixed combustion system, mixture fraction takes on values between zero and one depending on the degree of mixing. In premixed combustion, where fuel and air are already homogenous, mixture fraction is a fixed quantity for all time, and so not very useful. It is worth emphasizing that it was necessary to assume unity Lewis number to arrive at a definition of mixture fraction.

When treated as an independent variable, mixture fraction becomes a useful platform for examining behavior of non-premixed flames. Its definition is rooted in the availability of reactants and so, when quantities are plotted with respect to mixture fraction, the influence of chemistry becomes evident [24]. For example, consider the plot in Figure 6.1, which is adapted from Figure 4 of Reference [85]. It contains contours of mass fraction of hydroxyl (OH) with respect to mixture fraction at three time steps. These data are results of a laminar ignition and combustion simulation with detailed hydrogen-air chemistry [85]. At initial time, diluted hydrogen and air are separated, then allowed to mix via diffusion and convection. At time $t = 0$, the chemistry is in a frozen state and no OH is present. This means there are no chemical reactions occurring, no radicals being produced, nor heat being released. However, hydrogen and air become mixed with increasing time, making chemical reactions possible. The use of detailed chemistry implies that the low-temperature chemistry
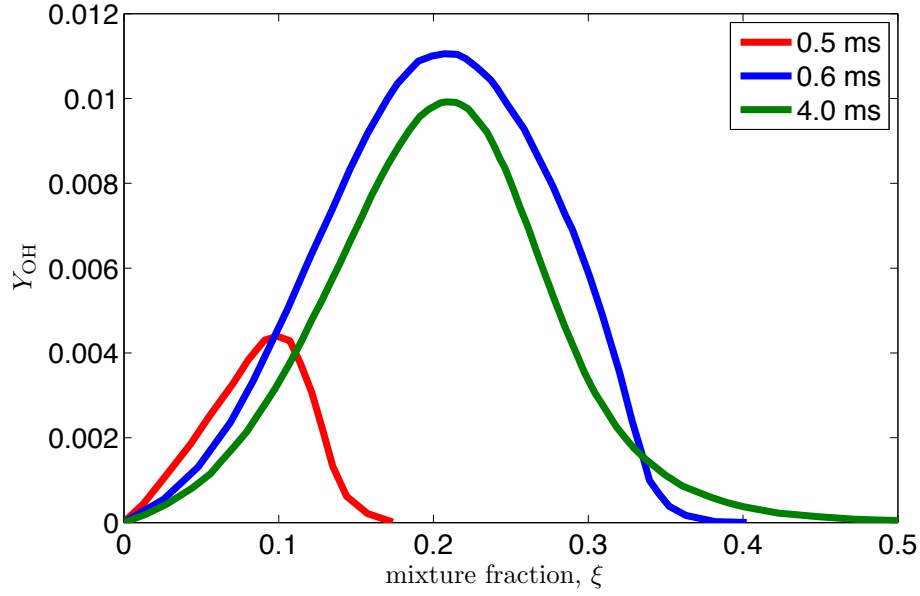
FIGURE 6.1. Plot adapted from Mastorakos, 2009 that shows profiles of OH mass fraction at the indicated times.

is included as part of the simulation. The low-temperature chemistry comprises the reactions that have a sufficiently low activation energy threshold that they will proceed even at low temperatures (albeit slowly). These reactions produce heat and radicals like OH that are important for starting the spontaneous ignition phase that leads to vigorous combustion. The formation of OH is demonstrated by the small peak at $t = 0.5$ ms, centered about a mixture fraction of $\xi = 0.1$. The fact that at later time, the contour of OH mass fraction is taller and broader suggests that the small peak at 0.1 ms captures the ignition phase of combustion. The low-temperature chemistry that is responsible for ignition has created a pool of OH radicals among regions where mixture fraction is around $Y_{OH} = 0.1$. At later time, vigorous combustion is generating OH at a fast rate, resulting in the tall, broad peaks for OH mass fraction at $t = 0.6$ ms and $t = 4.0$ ms.

A number of interesting features can be gleaned from the plot in Figure 6.1 by virtue of it having mixture fraction as its independent variable. First, notice that the mixture fraction

for peak OH mass fraction is about $\xi = 0.1$ at $t = 0.1$ ms as pointed out before, but around $\xi = 0.22$ for all later times. This suggests that the early exothermic chemical reactions responsible for ignition is more active at lower mixture fraction than that for chemistry of vigorous combustion. This sort of behavior is evident in fuels other than hydrogen as well. The mixture fraction for which ignition is most favorable for a given thermodynamic state (i.e., temperature and pressure of fuel and oxidizer) of a combustion system is called the *most reactive mixture fraction*, ξ_{MR} [85, 59]. A non-premixed flame undergoing vigorous combustion is expected to reside at the stoichiometric mixture fraction [24], which can be referred to as ξ_{st}. It was shown that $\xi_{MR} < \xi_{st}$ for the dilute hydrogen-air combustion simulation [85] discussed above, but it has also been shown to be true for methane [86] as well. However, ξ_{MR} can also be greater than ξ_{st}, as was shown for n-heptane [56]. So to summarize, it is the case that in general: $\xi_{MR} \neq \xi_{st}$. This may be surprising since the flame, where maximum radical production and heat release occurs, is located at ξ_{st} during vigorous combustion in a non-premixed flame.

Second, in the plot in Figure 6.1, notice there is a distinct range of mixture fraction over which OH is present. Some of this spread is the result of mass transport, but it also indicates that OH formation (and therefore combustion chemistry) is occurring over a distinct range of mixture fractions. Again consider the OH mass fraction curve at 0.5 ms. It is centered at small mixture fractions, meaning that the mixture does not ignite everywhere simultaneously, but only in regions that have low mixture fraction: from $\xi \approx 0$ to $\xi \approx .16$. The fact that the OH mass fraction curves are broader, and centered a higher mixture fraction for time $t > 0.5$ ms means that the flame has propagated into more rich regions following ignition. These observations show how useful it can be to examine a non-premixed combustion system in
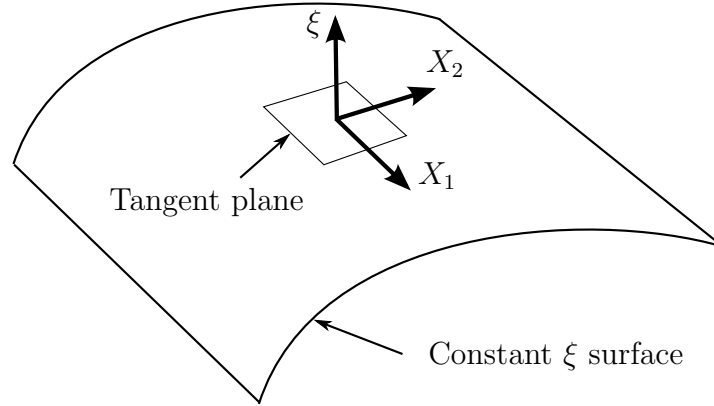
FIGURE 6.2. A surface of constant mixture fraction with a tangent plane in (X_1, X_2, ξ)-space. Coordinates X_1 and X_2 represent mutually orthogonal directions along the constant-ξ surface.

terms of mixture fraction. This will be exploited for the deeper discussion of non-premixed ignition below.

6.3.2. SCALAR DISSIPATION. It is often useful to rewrite conservation equations with mixture fraction as the independent variable. This has the effect of reducing the number of spatial variables, even in complex multi-dimensional combustion systems. The reason this is an acceptable practice is that the reaction zone in which the chemistry of combustion actually occurs is very thin. If its thickness is sufficiently small compared to flame curvature and wrinkling scales, one can treat the reaction zone as a series of small laminar flames embedded in the flowfield, even when significant turbulence is present. These embedded laminar flames are called flamelets and comprise a foundational principle on which turbulent combustion simulation is based [24, 84]. The reason they are considered laminar, even when the flowfield is turbulent, is that convective transport over the width of the reaction zone is negligibly small.

The simulations conducted for the research reported on in this thesis are not turbulent, but important insights can be had by following derivations of some of the equations used in

turbulent flow simulations. Recall Assumption (6) from the previous subsection that stated that quantities like temperature and mass fraction in the reaction zone vary only with time and mixture fraction. This is not an unreasonable assumption because gradients in mixture fraction space are much larger than those along spatial directions.

Consider the diagram in Figure 6.2 that depicts some arbitrary surface of constant-ξ in mixture fraction space. Since reaction zones (i.e., flames) conform to surfaces of constant mixture fraction, one could imagine a flame coinciding with the constant-ξ surface in the figure. Also shown is a plane that is tangent to the constant-ξ surface. The axes X_1 and X_2 lie in the tangent plane and are mutually orthogonal spatial directions along the surface of constant-ξ. The axis normal to the tangent plane (and the X_1 and X_2 directions) is the mixture fraction axis. It is easy to imagine that quantities change little along X_1 and X_2 because the character of the reaction zone will be similar for a fixed mixture fraction. However, since it lies normal to the reaction zone, change in quantities along the ξ-axis will be significant. For example, as one moves toward a flame from a short distance away along the ξ-axis, temperature and combustion intermediates like OH increases rapidly while fuel and oxidizer species drop to near zero. This justifies neglecting derivatives with respect to X_1 and X_2, but keeping those of ξ. Physically, this represents the idea that the flame structure is locally one-dimensional and need be described only by mixture fraction and time. Formally, this is written as:

$$T \;=\; T(\xi, t) \tag{75}$$

$$Y_k \;=\; Y_k(\xi, t), \tag{76}$$

for $k = 1, \cdots, N$ species [84].

The general species conservation equation in terms of mass fraction is given by Equation (56). By mapping from (t, x_1, x_2, x_3) to (t, X_1, X_2, ξ), a change of variable is accomplished, where the third spatial dimension is replaced by mixture fraction and the two remaining spatial variables become an orthogonal basis for surfaces of constant mixture fraction. The mapping is involved so is not presented here (but can be found in, e.g., Reference [24]). However, worth noting is that those terms are discarded that contain only derivatives of the spatial variables as was justified above. The end result is the species equation in terms of mixture fraction [24]:

$$\frac{\partial \rho Y_k}{\partial t} - \frac{1}{2} \rho \chi \frac{\partial^2 Y_k}{\partial \xi^2} = w_k, \tag{77}$$

where

$$\chi = 2D \left(\frac{\partial \xi}{\partial x_i} \right)^2, \tag{78}$$

is a new quantity called the scalar dissipation rate. The energy equation can be similarly mapped to obtain:

$$\rho \frac{\partial T}{\partial t} - \frac{1}{2} \rho \chi \frac{\partial^2 T}{\partial \xi^2} = w_T. \tag{79}$$

Equations (77) and (79) are referred to as the *flamelet equations* and are used to simulate the reaction zone in turbulent non-premixed ignition and combustion problems. Such simulations are not part of the work reported on in this thesis, but their derivation shows the origin of scalar dissipation rate, a quantity that is important to the discussion of ignition in turbulent non-premixed flames that appears shortly. Scalar dissipation rate has units of inverse time and can be considered a diffusivity in mixture fraction space [87]. This makes sense because it is a diffusivity coefficient multiplied by the square of mixture fraction gradient [see Equation (78)].
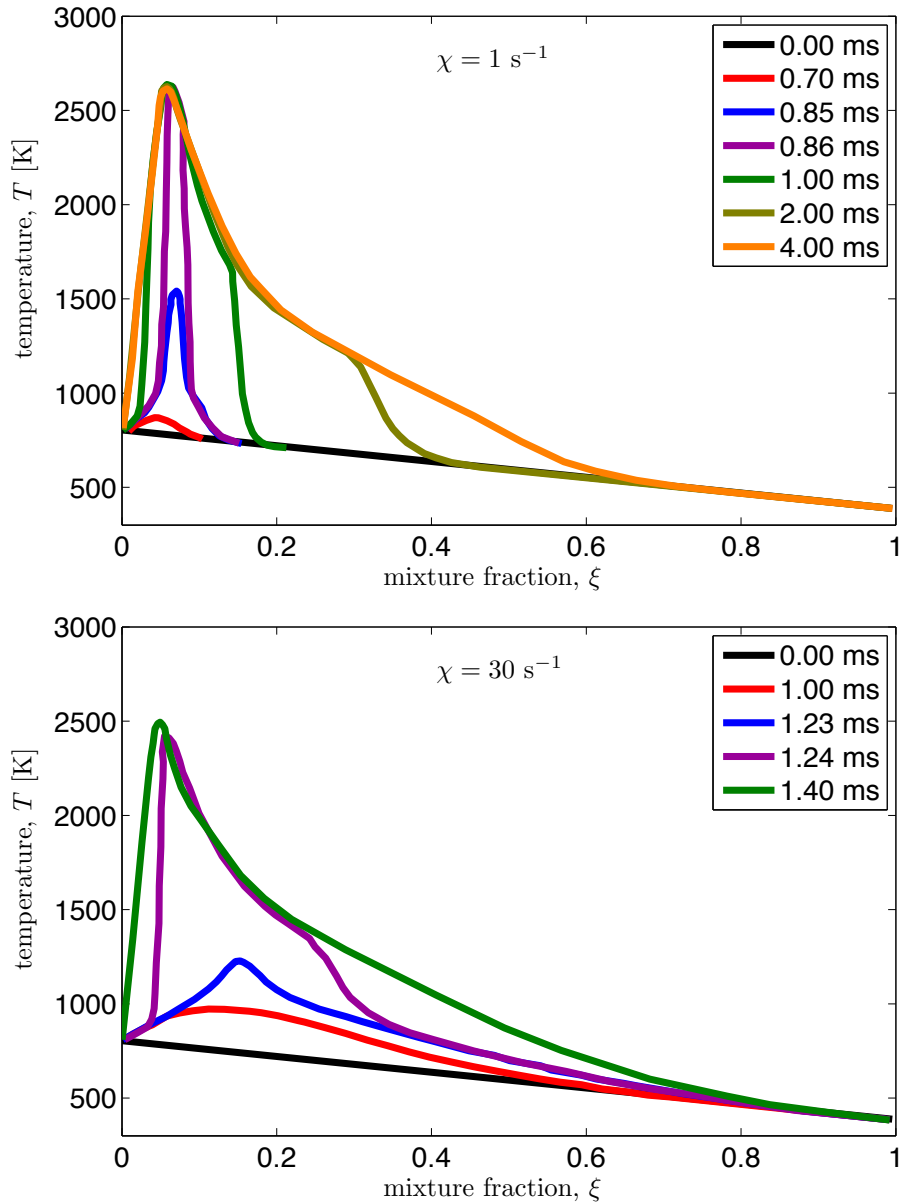
FIGURE 6.3. Temperature curves in mixture fraction space for a series of timesteps. Adapted from Pitch and Peters, 1998.

One of the advantages of using the flamelet equations for species and temperature is that they are de-coupled from the flow velocity field. Instead of an explicit convection term, the influence of convective transport is captured by scalar dissipation rate, χ [18]. The utility of this is the ability to parameterize the effect of the flow field on the chemistry of combustion, thereby facilitating the study of the influence of the former on the latter.

To better understand how scalar dissipation rate influences ignition phenomena, consider the plots in Figure 6.3, which were adapted from Reference [18]. They depict the time evolution of temperature distributions in mixture fraction space for non-premixed n-heptane and air simulations that are identical accept for the scalar dissipation rate. The top and bottom simulations in Figure 6.3 have $\chi = 1$ s^{-1} and $\chi = 30$ s^{-1}, respectively as indicated. The stoichiometric mixture fraction is $\xi_{\text{stoic}} = 0.062$. In the $\chi = 1$ s^{-1} case, the temperature rise at early time ($t = 0.70$ ms) is confined to a narrow region near the stoichiometric mixture fraction. The next two curves ($t = 0.85$ and 0.86 ms) show the temperature leaping up to the maximum value as the rate of reactions increases rapidly due to thermal runaway. The next three curves ($t = 1.0$, 2.0, and 4.0 ms) show the flame propagating left and right in mixture fraction space that is the same thing as saying the flame is propagating into lean and rich regions in cartesian space. However, note that the peak temperature remains at or very near the stoichiometric mixture fraction.

Now examine the bottom plot in Figure 6.3 in which the scalar dissipation rate is thirty times greater than that above. This means that the transport of heat by dissipation will be thirty times faster. This is apparent by looking at the temperature curve at $t = 1.0$ ms where it shows a very broad range of mixture fractions have increased in temperature since initial time. The most chemically reactive region is still restricted to a narrow region, but the high rate of scalar dissipation is causing heat to be distributed over a large range of mixtures [18]. At $t = 1.23$ ms, a narrow peak indicating thermal runaway is seen. The next time step, $t = 1.24$, shows the flame propagating into both lean and rich mixture fractions as in the previous case. Finally, the equilibrium position is achieved with a peak temperature at 2500 K.

The effect of increased scalar dissipation rate is clear when comparing the two simulation results in Figure 6.3. The case with the higher scalar dissipation rate showed evidence of enhanced heat transport by virtue of very broad temperature distributions prior to ignition. Ignition was delayed because it took longer for chemical heat release and scalar dissipation to become balanced. This was due to heat being transported away from the reaction zone at a higher rate due to higher scalar dissipation rate. The most reactive mixture fraction for the two cases were different. When scalar dissipation was $\chi = 1$ s^{-1}, the most reactive mixture fraction was $\xi_{\mathrm{MR}} \approx 0.05$. On the other hand, when $\chi = 30$ s^{-1}, $\xi_{\mathrm{MR}} \approx 0.11$. This is explained by recalling the most reactive mixture fraction is a competition between availability of reactants and the temperature-dependent reaction rate. For the $\chi = 1$ s^{-1} case, the low scalar dissipation rate meant there was only a very narrow range of mixture fractions at elevated temperature. In that case, high temperature won out over availability of reactants, causing ξ_{MR} to be lean. However, in the the $\chi = 30$ s^{-1} case, a high scalar dissipation rate mean there was a broad range of mixture fractions at elevated temperature. Therefore, a region with a favorable availability of reactants that also had a sufficiently high temperature exhibited the onset of thermal runaway; a region in which ξ_{MR} was rich. Although not related to ignition phenomena, also note that the peak temperature achieved is lower for the case with $\chi = 30$ s^{-1} because the rate of transport of heat away from the flame is much higher.

6.3.3. IGNITION OF TURBULENT NON-PREMIXED FLAMES. The purpose of the preceding discussion has been to explain the concept of the most reactive mixture fraction ξ_{MR} and scalar dissipation χ. These concepts are vital to understanding ignition phenomena in turbulent non-premixed combustion environments like diesel engine fuel sprays and why they

are different from that encountered in droplet autoignition. What follows is an explanation of how the concepts of most reactive mixture fraction ξ_{MR} and scalar dissipation χ can be used to understand autoignition phenomena in turbulent non-premixed flames.

First, a detailed phenomenological description of turbulent non-premixed ignition is warranted. As noted numerous times already, a non-premixed flame is one in which the fuel and oxidizer are separated at initial time. This can be further clarified by specifying that the fuel and air are not only separate at initial time, by there is no ignition source such as a spark or hot surface. As such, as time moves forward from initial time, the fuel and air are permitted to mix by diffusion and possibly convection. This mixing permits the low-temperature reactions between fuel and oxidizer to occur that are the first steps to thermal runaway, autoignition, and thence, vigorous combustion. Such a scheme is different from a system in which combustion has always been occurring (steady state combustion), or one in which ignition has happened some time ago and non-premixed combustion has reached some manner of steady state. In this latter type of system, the fuel and oxidizer still issue from distinct inlets, but they remain unmixed until they reach the reaction zone of the flame where they are consumed in the chemical reactions of combustion.

To further muddle the issue, a diesel spray after ignition is a *partially* non-premixed combustion system because the liquid jet entrains air near the injector exit [30]. A further technicality worth noting is that autoignition is not always the result of thermal runaway. In previous discussions of the low-temperature chemistry, the author was careful to state that local accumulation of either heat or chain-branching radicals were necessary for ignition to proceed. The latter requirement being the case for, e.g., hydrogen-air ignition at certain thermodynamic states. Ignition by chain-branching radicals is found as part of a
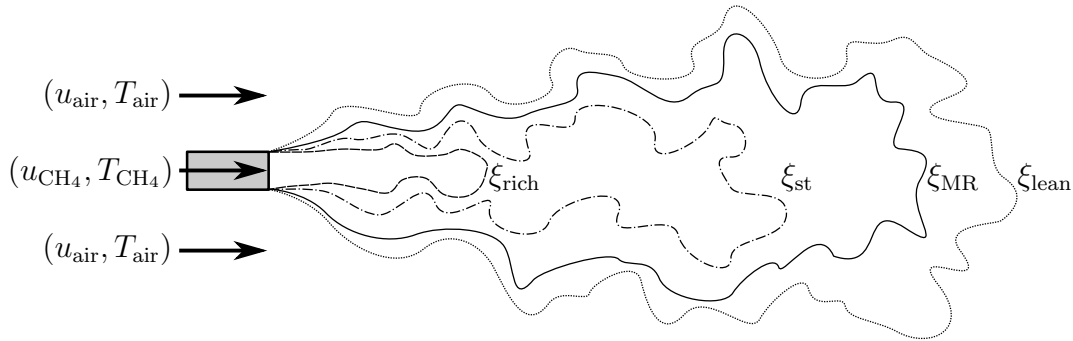
FIGURE 6.4. Diagram of a gaseous methane jet flowing into a hot air ambient with contours of rich, stoichiometric, most reactive, and lean mixture fractions. The diagram is adapted from Mastorakos, 2009.

larger discussion on hydrogen explosion limits in Law's text; see Reference [24]. While the forthcoming discussion is specifically on heat release and thermal transport in the context of ignition of turbulent mixtures, it should be understood that it extends to that of radicals as well since the modes of transport and formation are concomitant.

Consider a high speed jet of pure gaseous fuel (say, methane) injected into a hot, co-flowing air as depicted in Figure 6.4. Such a configuration is similar to the injection of a diesel spray into an engine, but here a gaseous fuel is used for the sake of explanation. The hot air ambient may or may not be already turbulent, but assume the fuel jet is sufficiently faster than the coflow that turbulent mixing is certain. In other words, Reynolds number is well above the transitional value, $Re > 1 \times 10^4$. Furthermore, assume the air is hot (1000 K) compared to the fuel (300 K).

Methane issuing from the jet exit mixes with the air by diffusion and convection, forming regions of fuel-air mixtures with a range of concentrations quantified by the mixture fraction field of the jet. Some iso-contours of mixture fraction are shown in Figure 6.4. The contours are drawn irregularly to represent the effect of turbulent transport. By definition, $\xi = 1$

at the jet exit since the gas is pure fuel. Well away from the jet $\xi = 0$ since only air is present. Mixture fraction takes on values between zero and one elsewhere depending on the degree of mixing between fuel and air. The rich and lean contours represent unspecified values of mixture fraction and merely demonstrate that fuel-air mixtures are expected to be rich near the jet exit and lean well downstream of the jet exit. The stoichiometric mixture fraction contour, labeled as ξ_{st}, indicates the location of mixtures that are in stoichiometric proportion. Were vigorous combustion ongoing, the flame would conform to the ξ_{st} contour. The most reactive mixture fraction (ξ_{MR}) contour will be explained presently.

Similarly to that of mass transport, heat from the ambient is mixed with the cold fuel stream by thermal diffusion and convection. Although not depicted in Figure 6.4, this creates a temperature field that ranges from T_{CH_4} at the jet exit to T_{air} far from the jet. But here is a key point: the resulting temperature of the local mixture is not necessarily species-specific. That is to say, not all rich regions are cold and not all lean regions hot. For any given mixture fraction, there will be mixtures that exhibit any temperature over the range T_{CH_4} to T_{air}. This means that the low-temperature[2] chemistry is able to "select" that combination of temperature and concentration that is most favorable to proceed for the given fuel and oxidizer. There is no feature of geometry or physics that would prevent the formation of any mixture fraction between zero and one with any temperature between T_{CH_4} to T_{air}. The reason this point is so strongly emphasized here is that this is *not* the case with autoigniting isolated droplets. As will be explained shortly, the physics of transport in isolated droplet ignition only permits certain combinations of mixture fraction and temperature.

---

[2]That is to say, low in comparison to the temperature of vigorous combustion which, for hydrocarbon fuels and air, is roughly 2000 K.

Returning to Figure 6.4 and examining the most reactive mixture fraction, it is apparent that ξ_{MR} is lean in this case. It has been shown that the most reactive mixture fraction can be lean for methane [86]. The ξ_{MR} contour indicates the physical location in the methane-air jet that exhibit mixture fraction and temperature for which the low-temperature chemical reactions are the most active. However, as implied previously, having a mixture for which $\xi = \xi_{\text{MR}}$ is not sufficient for ignition to occur. It is also necessary that scalar dissipation be sufficiently low that heat released by the low-temperature reactions occur at a rate faster than it be dissipated by turbulent transport and diffusion. This implies that there is a critical scalar dissipation χ_{crit} below which ignition is possible in finite time at locations where $\xi \approx \xi_{\text{MR}}$ [85]. Therefore, locations in which $\chi < \chi_{\text{crit}}$ and $\xi \approx \xi_{\text{MR}}$ will ignite spontaneously. This condition will be symbolized herein as: $(\chi < \chi_{\text{crit}}, \xi \approx \xi_{\text{MR}})$.

In locations where $(\chi < \chi_{\text{crit}}, \xi \approx \xi_{\text{MR}})$, heat released by low-temperature reactions will accumulate and locally raise the temperature of the mixture. The increase in temperature accelerates the rate of chemical reaction, which in turn releases still more heat, and so on. This self-perpetuating cycle is referred to as thermal runaway and it very quickly leads to vigorous combustion. The thermal runaway may be very localized, producing a small flame called a flame kernel. If there are many regions where $(\chi < \chi_{\text{crit}}, \xi \approx \xi_{\text{MR}})$, more than one kernel may form. Regardless, the kernel(s) move rapidly from the ξ_{MR} contour to the ξ_{st} contour. The flame will then split and propagate in opposite directions along the ξ_{st} contour consuming fuel and air that mixed prior to ignition [85]. After premixed fuel and air are exhausted, the combustion transitions to a non-premixed phase. This means that the pure fuel jet is enveloped by a flame, and oxidizer from the ambient does not meet fuel until they reach the flame reaction zone.

In the example described above, methane was selected as the fuel. As noted previously, for the given fuel and ambient temperatures, the most reactive mixture fraction ξ_{MR} happens to be lean for methane. As such, the flame kernel propagated *inward* towards the stoichiometric contour ξ_{MR}. For other fuels such as n-heptane, the most reactive mixture fraction may be rich, meaning that the flame kernel would have to propagate *outward* toward the stoichiometric mixture fraction contour.

The salient point of the autoigniting methane jet described above is the fact that ξ_{MR} is not restricted by the physics of the problem in any way. The value of ξ_{MR} was solely a function of the fuel and oxidizer chemistry and their respective initial temperatures. This is different from the case of isolated droplet ignition as will be shown in the next subsection.

In terms of ignition phenomena discussed above, a liquid fuel jet like that in a diesel engine is similar to the gaseous methane jet used in the example at the beginning of this section. Specifically, a liquid jet undergoing evaporation will act as a source of fuel vapor that will mix with the ambient oxidizer and, if the $(\chi < \chi_{crit}, \xi \approx \xi_{MR})$ requirements are met, ignition will occur. This will be followed by flame propagation to the stoichiometric contour and then transition to non-premixed combustion. An important difference with liquid fuel jets is that heat is required to raise the temperature of the liquid fuel to the boiling point and for the subsequent phase change. Prior to ignition, heat will be absorbed from the hot ambient then, once vigorous combustion is established, from the flame.

It has been shown that for ignition to occur in turbulent fuel jets (gaseous or liquid), the following condition must be met: $(\chi < \chi_{crit}, \xi \approx \xi_{MR})$. The scalar dissipation rate must be small enough that transport of heat is slower than its release by chemical reactions. This permits the formation of a localized pool of hot mixture in which thermal runaway will

occur. Moreover, the mixture fraction of the fuel-air mixture must be equal or similar to the most reactive mixture fraction. That is, the mixture fraction in which chemical reaction are the most active for a given mixture temperature and pressure. These same concepts can be applied to the ignition of liquid fuel droplets as well.

6.4. Ignition of Isolated Liquid Fuel Droplets

In this section, the discussion returns to isolated droplet to focus specifically on ignition and how it differs from that of diesel spray ignition. This provides the foundation on which to base the conclusion that isolated droplet ignition is an unsuitable physical model for diesel spray ignition.

Consider again Figure 1.5 in which generic profiles of mass fraction and temperature are depicted for isolated droplet ignition and combustion. The first plot (Figure 1.5a) shows a small dip in oxygen and a localized bump in temperature that are caused by low-temperature chemical reactions that are the precursors to ignition. It appears that the fuel mass fraction contour is nominally zero in that location, but it is known that a tiny amount of fuel is actually present [24]. Regardless, this means that the fuel-air mixture is very lean. In fact, the mixture in which ignition begins will always be lean, regardless of the fuel considered. The reason for this is due to the physics of the problem.

It is necessary that the ambient in which a droplet is located be quiescent so that the sole modes of transport of species is by diffusion and Stephan flow of the fuel. Convective (e.g., turbulent) flow is not permitted because it would necessitate solution of the momentum equation in simulations, thereby negating any benefit of studying the droplet geometry. By virtue of the spherical symmetry of the problem, the fuel mass fraction prior to ignition will always be maximum at the droplet surface and decline to nominally zero in the far

field. Likewise, prior to ignition, the temperature will be minimal at the droplet surface and reaching the maximum in the far field. These two facts mean that there is a limited range of mixture fraction for which the temperature is sufficiently high for the low-temperature reactions to proceed. In fact, that mixture fraction will always be quite lean. This is in contrast to ignition in turbulent non-premixed flames where turbulent mixing causes a large range of mixture fraction to be sufficiently warm for low-temperature chemistry to occur. The result is that isolated droplets will always ignite in the warm lean region far from the droplet surface. This will be the case even when using fuels (e.g., n-heptane, petroleum diesel) that would otherwise ignite in a rich zone in a turbulent spray. It is for this reason that isolated droplet ignition (in a quiescent ambient) is an unsuitable physical model for ignition in a

6.5. CONCLUSION

This chapter presented a discussion of the suitability of using isolated droplet ignition and combustion as a physical model for diesel spray ignition and combustion. There are a number of benefits to such a scheme such as the relative ease of conducting experiments on droplets compared to the interior of operating diesel engines. Moreover, the spherical symmetry of droplet ignition and combustion results in much reduced computational expense of simulations compared to other geometries, thereby permitting the use of detailed chemistry and distinct transport properties. Were isolated droplet ignition and combustion be a viable physical model for that of diesel sprays, it would represent a powerful tool for verification of chemical mechanisms for practical long-chain fuels like petroleum diesel and biodiesel, and their surrogates.

Fundamental theory of ignition of turbulent non-premixed flames was included to show the origin of the two key parameters of that phenomena: most reactive mixture fraction ξ_{MR} and critical scalar dissipation rate χ_{crit}. It was shown that in a turbulent non-premixed combustion system, a region will ignite spontaneously if both of the following requirements are met: (a) the mixture fraction is equal or similar to the most reactive mixture fraction ($\xi \approx \xi_{\mathrm{MR}}$); (b) the scalar dissipation rate is smaller than the critical scalar dissipation rate ($\chi < \chi_{\mathrm{crit}}$). Results from experiments and simulations were cited to show that ξ_{MR} could be rich or lean depending on the temperature of the respective fuel and oxidizer streams and the chemistry of the fuel.

Next, ignition in isolated droplets was revisited to show how the geometry of transport resulted in ignition starting in a lean region for all fuels, even those that ignite in a rich region in turbulent non-premixed combustion systems like diesel sprays. The conclusion was made that isolated droplet ignition was an *unsuitable* physical model for diesel sprays because it was not possible to mimic rich ignition that occurs in diesel sprays.

CHAPTER 7

Future Work and Conclusion

7.1. Future Work

A number of improvements of apparatus and procedures were conceived while conducting the present experiments and are summarized in this section. Also, a proposal for experiments in which a wire-stabilized droplet are ignited in a rapid compression machine are described.

7.1.1. Variable Geometry Combustion Duct with Vitiated Air. In the course of setting up and conducting the experiments conducted for this dissertation, an apparatus for a new set of experiments was conceived that would eliminate many of the difficulties and sources of error encountered. Such an apparatus would take the form of a variable geometry duct in which a lean flat-flame burner provides a hot oxidizer gas that flows downward through the duct. Droplets would be introduced into the top of the duct through a port and fall along the centerline of the duct. The cross-sectional area of the duct would constrict so that the flow velocity roughly matched that of the falling droplet. This would minimize distortion of the droplet flame by convective transport. Moreover, since the droplet is falling under the influence of gravity, distortion due to buoyancy would be reduced as well.

When product gasses of a lean flat flame burner are used as a hot oxidizing ambient, the gas is referred to as *vitiated air* [85]. Varying the proportion of oxygen, nitrogen, and fuel gas supplied to the flat flame burner would dictate the temperature the droplet experiences as it falls through the vitiated air. The height of the flat flame burner would be adjustable so that the time during which the droplet experiences the hot ambient could be changed as well.

Optical ports in the variable-geometry duct would permit the passage of a laser sheet and fluorescence emissions so PLIF images could be acquired. In contrast to the present system in which the coil blocked the laser sheet and fluorescence emissions, the moments leading up to and and during autoignition could be captured with fluorescence images. Indeed, the entire processes could be captured: autoignition, propagation of the reaction sheet through premixed fuel and air, transition to non-premixed combustion, and quasi-steady state non-premixed combustion. What is more, a second digital camera would be set up to capture silhouette images of the droplet to obtain the diameter for each individual droplet.

It is believed that the NO and OH fluorescence images obtained from such a system would be of sufficiently high quality that they could be compared to associated isolated spherically-symmetric droplet autoignition and combustion simulations. This would enable the tuning of parameters important for NO_x formation in the chemical mechanism of the associated liquid fuel.

7.1.2. IMPROVED DROPLET GENERATOR GEOMETRY. During experimentation, an inordinate amount of time was spent attempting to extract bubbles or struggling with inadequate seals. A new droplet generator design is proposed in which the extraction of bubbles is facilitated by a dedicated port at the top of the device from which they can be withdrawn. Moreover, the seals of the droplet generator would be implemented in such a way that the pressure they exert on the piezoelectric disk would be constant every time the device was assembled. In this way, the diameter of the droplets produced would be independent of how tightly the threaded fasteners were torqued. This is in contrast to the current setup in which the droplet diameter will change significantly with a small change in threaded faster tightness.

7.1.3. IMPROVED MANAGEMENT OF LIQUID FUEL TEMPERATURE. It was discovered that the temperature of the fuel in the droplet generator affected the quality and consistency of the droplet formed. This was due to the change is viscosity of the fuel with temperature, which is an important factor in the droplet formation processes at the tip of the glass nozzle. As described in Section 3.4, heating of the liquid fuel by the coil was mitigated by affixing a thick rubber insulator to the glass nozzle and installing a stainless steel heat shield. Even greater confidence in the temperature stability of the liquid fuel could be assured by installation of some manner of water cooling jacket to the nozzle and droplet generator body. Although, such active cooling may prove unnecessary if a duct such as that described in Section 7.1.1 is implemented. Lee discusses management of liquid fuel temperature in his dissertation on droplet flames [82].

7.1.4. ALTERNATIVE SCHEMES FOR PLIF OF DROPLET FLAMES. Significant difficulty in obtaining NO PLIF results for this thesis was encountered due to the proximity of the fluorescence bands to the pumping wavelength. The result was it being necessary to select a filter that had a relatively low transmissivity in the fluorescence bands in exchange for significant attenuation of the pump wavelength. The scheme used for NO PLIF was selected primarily because it was strongly touted in reference [77].

What was not apparent then and is now obvious, is the need for strong attenuation of the pump wavelength in combination with high transmissivity of the fluorescence band. This was achieved in [77] using expensive custom mirrors that were simply out of the question for this work. Should this path of inquiry be taken up again, a revisiting of references [78, 88, 89] would be in order to seek a fluorescence scheme that can be accomplished with less expensive stock filters. Schemes that were discarded in reference [77] as being unsuitable

185

in high pressure environments may very well be perfectly useful for these one-atmosphere droplet flames.

Another plausible scheme for PLIF of droplet flames is the two-photon technique [73, 20] in which transitions in the vacuum ultra-violet (200 - 220 nm) are accessed via two photon absorption. This would virtually eliminate the difficulty in attenuating laser light scattered by the droplet because the laser wavelength would be hundreds of nanometers longer than the fluorescence bands, making the filtering of them a trivial matter. This is in contrast to the present scheme in which the laser wavelength was roughly 10 to 20 nm shorter than the fluorescence bands. As might be expected, there is a tradeoff in implementing two-photon instead of one-photon PLIF, and that is the cross section for two photon absorption is much smaller than single photon PLIF like that used in these experiments. Therefore, the signal levels would be correspondingly lower [20]. However, two-photon PLIF still might provide superior signal because an optical filter with much higher transmissivity of the fluorescence bands could be used. Moreover, it would no longer be necessary to double the fundamental beam of the dye laser, thereby avoiding the attendant losses. A combination of significantly higher beam intensity and greater transmissivity of the optical filter might counter any deficiency due to smaller two-photon absorption cross section.

7.1.5. WIRE-STABILIZED DROPLET IN RCM WITH A LEAN METHANE MIXTURE. Interest in duel fuel compression ignition engines has grown recently [90]. A otherwise typical compression-ignition (diesel) engine has natural gas or some other gaseous fuel mixture introduced into the air intake stream. The liquid fuel is injected near the top of the piston stroke as usual and autoignites, initiating combustion of the liquid and gaseous fuel. The amount of liquid fuel injected into the cylinder is reduced in proportion to the heat released

by combustion of the gaseous fuel. For the purpose of better understanding the autoignition, combustion, and NO_x formation phenomena associated with combinations of liquid and gaseous fuels, a series of experiments are suggested using a rapid-compression machine (RCM), planar laser-induced fluorescence (PLIF) spectroscopy, and wire-stabilized droplet combustion. A custom chamber with optical access ports for a laser sheet and fluorescence emissions would be manufactured for the RCM. A thin wire would span the center of the chamber upon which a liquid fuel droplet would be introduced with a syringe. The RCM would be charged with a very lean methane-air mixture and engaged, causing a rapid increase in pressure and temperature in the chamber. The liquid fuel vapor would autoignite and consume the droplet and the methane in the chamber. A high-speed (kilohertz) PLIF system would acquire two-dimensional fluorescence images for OH and NO species of the combustion processes.

The OH fluorescence images would provide insight into how the autoignition event is different in an ambient comprised of a very lean methane-air mixture be depicting the location of the flame front in time. Variation in NO fluorescence with time would indicate the relative importance of Fenimore NO_x and Zel'dovich NO formation mechanisms. A parallel computational effort of droplet autoignition and combustion in a lean methane-air mixture could be conducted as well.

7.2. CONCLUSION

Transient simulation of spherically-symmetric autoignition and combustion of liquid droplets of methyl butanoate, methanol, and n-heptane was conducted. New detailed gas-phase chemical kinetic mechanisms were used that were created by combining established fuel mechanisms with oxides of nitrogen (NO_x) chemistry. The computer code used was

previously-developed and, in addition to detailed chemical kinetics, employed species-specific transport and radiative heat transfer to the ambient and droplet surface.

Simulation results presented show concentrations of fuel, oxidizer, major combustion products, important intermediate species, and oxides of nitrogen: NO, N_2O, and NO_2. The outcome of the simulations showed the expected sequence of events: chemically frozen induction time, localized gas phase heating due to low-temperature chemistry, reaction wave propagating through premixed fuel and air, reaching maximum temperature just prior to transition to non-premixed combustion, and establishing of quasi-steady state non-premixed combustion. Comparison of simulation cases with two levels of NO_x chemistry detail show that incorporating only Zel'dovich NO chemistry and neither Fenimore nor N_2O NO_x chemistry may lead to dramatic underprediction of NO_x formation. Total mass of NO formed by n-heptane droplet simulation was at least a factor of five greater than that formed by methyl butanoate or methanol.

Planar laser-induced fluorescence (PLIF) spectroscopy was conducted on spherically-symmetric droplet flames in free fall. A piezoelectric droplet generator created a monodisperse stream of droplets that were ignited by a resistive wire coil. The droplet flames fell through a laser sheet whose wavelength was tuned so as to induce fluorescence in hydroxyl (OH) and nitric oxide (NO) molecules in the flames. An intensified CCD camera captured fluorescence images that were later processed and averaged to created qualitative radial profiles of OH and NO concentration in the flame. OH and NO PLIF was conducted approximately 16 ms after ignition of droplets of these fuels: methyl decanoate, methyl butanoate, n-heptane, methanol, ethanol, and 1-propanol.

It has been surmised for decades that autoignition and combustion of spherically-symmetric isolated fuel droplets could act as a physical model for diesel spray ignition and combustion in compression ignition (diesel) engines. This appears to be a reasonable conjecture since both phenomena share important physics: chemically frozen induction time in which stoichiometric and thermal stratification occurs by diffusive transport, thermal autoignition of premixed fuel and air, propagation of premixed flame, and transition to quasi-steady non-premixed combustion near a cold liquid-phase fuel. Were the droplet physical model a viable concept, progress toward improving understanding of auto-ignition, combustion, and emissions formation phenomena in compression ignition engines would be made significantly easier (and therefore cheaper). Sophisticated diagnostics could be applied to droplet flames, avoiding the tremendous challenge of implementing them in an operating diesel engine. The experimental results could be used to validate detailed chemical mechanisms of practical, large-molecular-mass fuels with detailed NO_x chemistry that would otherwise not be possible because the spherical-symmetry of droplet flames requires only a single spatial variable, thereby freeing significant computational resources.

Given the tremendous possibilities of using autoignition and combustion of spherically-symmetric isolated fuel droplets as a physical model for diesel sprays, the suitability of the physical model was examined from a theoretical standpoint. While true that droplet and diesel spray share many physical characteristics, the stoichiometry of ignition in the two systems is different. In droplets, irrespective of the fuel used, autoignition alway initiates in the relatively hot lean region far from the droplet. In diesel sprays, depending on the thermodynamic conditions and fuel reactivity, ignition my occur in lean *or* rich regions by

virtue of turbulent transport of heat and mass. In large molecular weight fuels like n-heptane or petroleum diesel fuel, ignition always occurs in mixtures that are quite rich ($\phi \approx 3$).

Most reactive mixture fraction and critical scalar dissipation rate are derived as part of explaining how turbulent flames are different from quiescent droplet flames. It is shown that for a turbulent non-premixed flame to ignite, two requirements must be met: (1) the fuel and air mixture fraction be equal or similar to the most reactive mixture fraction, (2) the local scalar dissipation rate must be less than the critical scalar dissipation rate. Due to the effect of scalar dissipation rate on transport and mixing in turbulent, non-premixed flames, it is concluded that, at least as far as autoignition is concerned, autoignition and combustion of spherically-symmetric isolated fuel droplets is an unsuitable physical model for diesel sprays in engines.

Bibliography

[1] United States Energy Information Administration, "How much electricity does an american home use?," http://www.eia.gov/tools/faqs/faq.cfm?id=97&t=3, December 2013.

[2] United States Energy Information Administration, "International energy statistics," http://www.eia.gov/countries/data.cfm, May 2014.

[3] United States Energy Information Administration, "How much carbon dioxide is produced by burning gasoline and diesel fuel?," http://www.eia.gov/tools/faqs/faq.cfm?id=307&t=11, May 2014.

[4] N. Oreskes, "The scientific consensus on climate change," *Science*, vol. 306, no. 5702, p. 1686, 2004.

[5] "A comprehensive analysis of biodiesel impacts on exhaust emissions," Tech. Rep. EPA420-P-02-001, United States Environmental Protection Agency, 2002.

[6] C. T. Bowman, "Control of combustion-generated nitrogen oxide emissions: Technology driven by regulation," *Symposium (International) on Combustion*, vol. 24, no. 1, pp. 859 – 878, 1992.

[7] I. Glassman, *Combustion*. Acedemic Press, 3rd ed., 1996.

[8] K. Wark and C. F. Warner, *Air Pollution: Its Origin and Control*. Prentice Hall, 3rd ed., 1997.

[9] "A plain english guide to the clearn air act," Tech. Rep. EPA-456/K-07-001, United States Environmental Protection Agency.

[10] United States Environmental Protenction Agency, "National Summary of Nitrogen Oxides Emissions," http://www.epa.gov/cgi-bin/broker?_service=data&_debug=0&_program=dataprog.national_1.sas&polchoice=NOX,

accessed 1 June 2014.

[11] C. J. Mueller, A. L. Boehman, and G. C. Martin, "Investigation of the origin of increased NOx emissions in a heavy-duty compression-ignition engine fueled with soy biodiesel," *Abstracts of papers of the American Chemical Society*, vol. 238, August 2009.

[12] S. Garner, R. Sivaramakrishnan, and K. Brezinsky, "The high-pressure pyrolysis of saturated and unsaturated C-7 hydrocarbons," *Proceedings of the Combustion Institute*, vol. 32, no. 1, pp. 461–467, 2009.

[13] T. Grumstrup, A. J. Marchese, F. L. Dryer, and T. Farouk, "Contributions of thermal and prompt NO_x chemistry on NO_x formation near igniting oxygenated liquid fuel droplets," in *8 th U. S. National Combustion Meeting Organized by the Western States Section of the Combustion Institute*, no. 070HE-0123, 2013.

[14] A. A. Konnov, "Implementation of the NCN pathway of prompt-NO formation in the detailed reaction mechanism," *Combustion and Flame*, vol. 156, no. 11, pp. 2093 – 2105, 2009.

[15] N. Lamoureux, P. Desgroux, A. El Bakali, and J. F. Pauwels, "Experimental and numerical study of the role of NCN in prompt-NO formation in low-pressure CH4-O-2-N-2 and C2H2-O-2-N-2 flames," *COMBUSTION AND FLAME*, vol. 157, pp. 1929–1941, OCT 2010.

[16] N. Lamoureux, P. Desgroux, A. El Bakali, and J.-F. Pauwels, "Experimental and numerical study of the role of NCN in the prompt-NO formation in low pressure CH4/O-2/N-2 and C2H2/O-2/N-2 flames (vol 157, pg 1929, 2010)," *COMBUSTION AND FLAME*, vol. 160, pp. 745–746, MAR 2013.

[17] B. A. Williams and J. W. Fleming, "Experimental and modeling study of NO formation in 10 torr methane and propane flames: Evidence for additional prompt-NO precursors," *PROCEEDINGS OF THE COMBUSTION INSTITUTE*, vol. 31, no. 1, pp. 1109–1117, 2007.

[18] H. Pitsch and N. Peters, "Investigation of the ignition process of sprays under diesel engine conditions using reduced n-heptane chemistry," *SAE transactions*, vol. 107, no. 4, pp. 1029–1038, 1998.

[19] S. Vogel, C. Hasse, J. Gronki, S. Andersson, N. Peters, J. Wolfrum, and C. Schulz, "Numerical simulation and laser-based imaging of mixture formation, ignition, and soot formation in a diesel spray," *Proceedings of the Combustion Institute*, vol. 30, no. 2, pp. 2029–2036, 2005.

[20] G. Martin, C. Mueller, and C. Lee, "Two-photon nitric oxide laser-induced fluorescence measurements in a diesel engine," *APPLIED OPTICS*, vol. 45, pp. 2089–2100, MAR 20 2006.

[21] U. Niemann, R. Seiser, and K. Seshadri, "Ignition and extinction of low molecular weight esters in nonpremixed flows," *Combustion Theory and Modelling*, vol. 14, no. 6, pp. 875–891, 2010.

[22] J. Miller, M. Pilling, and E. Troe, "Unravelling combustion mechanisms through a quantitative understanding of elementary reactions," *Proceedings of the Combustion Institute*, vol. 30, no. 1, pp. 43–88, 2005.

[23] J. A. Miller and C. T. Bowman, "Mechanism and modeling of nitrogen chemistry in combustion," *Progress in Energy and Combustion Science*, vol. 15, no. 4, pp. 287 – 338, 1989.

[24] C. K. Law, *Combustion Physics*. Cambridge University Press, 2006.

[25] Y. B. Zeldovich *Acta Physicochim*, vol. 21, 1946.

[26] C. Bowman, "Gas-phase reaction mechanisms for nitrogen oxide formation and removal in combustion," in *POLLUTANTS FROM COMBUSTION - FORMATION AND IMPACT ON ATMOSPHERIC CHEMISTRY* (C. Vovelle, ed.), vol. 547, pp. 123–144, SPRINGER, 2000.

[27] S. R. Turns, "Understanding NO_x formation in nonpremixed flames: Experiments and modeling," *Progress in Energy and Combustion Science*, vol. 21, no. 5, pp. 361 – 385, 1995.

[28] C. P. Fenimore, "13th Symposium (International) of the Combustion Institute," (Pittsburgh), pp. 373–379, The Combustion Institute, 1971.

[29] L. Moskaleva and M. Lin, "The spin-conserved reaction $CH+N_2 \rightarrow H+NCN$: A major pathway to prompt NO studied by quantum/statistical theory calculations and kinetic modeling of rate constant," *Proceedings of the Combustion Institute*, vol. 28, no. 2, pp. 2393–2401, 2000.

[30] J. E. Dec, "Conceptual model of DI diesel combustion based on laser-sheet imaging," *SAE Transactions*, vol. 106, no. 3, pp. 1319–1348, 1997.

[31] V. Gopalakrishnan and J. Abraham, "An investigation of ignition behavior in diesel sprays," *Proceedings of the Combustion Institute*, vol. 29, no. 1, pp. 641–646, 2002.

[32] C. LAW, "Recent advances in droplet vaporization and combustion," *PROGRESS IN ENERGY AND COMBUSTION SCIENCE*, vol. 8, no. 3, pp. 171–201, 1982.

[33] D. B. Spalding, "The combustion of liquid fuels," in *Symposium (International) on Combustion*, vol. 4, pp. 847–864, 1953.

[34] G. A. E. Godsave, "Studies of the combustion of drops in a fuel spray—the burning of single drops of fuel," in *Symposium (International) on Combustion*, vol. 4, pp. 818–830, 1953.

[35] M. Goldsmith, "On the burning of single drops of fuel in an oxidizing atmosphere," *Journal of Jet Propulsion*, vol. 24, no. 4, pp. 245–251, 1954.

[36] H. Wise, J. Lorell, and B. J. Wood, "The effects of chemical and physical parameters on the burning rate of a liquid droplet," in *Symposium (International) on Combustion*, vol. 5, pp. 132–141, 1955.

[37] G. Faeth, "Current status of droplet and liquid combustion," *Progress in Energy and Combustion Science*, vol. 3, no. 4, pp. 191–224, 1977.

[38] W. A. Sirignano, *Fluid Dynamics and Transport of Droplets and Sprays*. Cambridge University Press, 2010.

[39] C. LAW, "ASYMPTOTIC THEORY FOR IGNITION AND EXTINCTION IN DROPLET BURNING," *COMBUSTION AND FLAME*, vol. 24, no. 1, pp. 89–98, 1975.

[40] A. Makino, "Ignition criteria for a fuel droplet expressed in explicit form," *Combustion science and technology*, vol. 80, no. 4-6, pp. 305–317, 1991.

[41] T. E. Daubert, R. P. Danner, H. Sibul, and C. Stebbins, *Physical and thermodynamic properties of pure chemicals: data compilation*. Hemisphere Publishing Corporation, 1989.

[42] B. E. Poling and J. P. Prausnitz, J. M.and O'Connell, *The properties of gases and liquids*. McGraw-Hill, 2001.

[43] M. J. Murphy, J. D. Taylor, and R. L. McCormick, "Compendium of experimental cetane number data," Subcontractor Report NREL/SR-540-36805, National Renewable

Energy Laboratory, 2004.

[44] C. V. Naik, C. K. Westbrook, O. Herbinet, W. J. Pitz, and M. Mehl, "Detailed chemical kinetic reaction mechanism for biodiesel components methyl stearate and methyl oleate," *PROCEEDINGS OF THE COMBUSTION INSTITUTE*, vol. 33, no. 1, pp. 383–389, 2011.

[45] T. Farouk and F. L. Dryer, "Tethered methanol droplet combustion in carbon-dioxide enriched environment under microgravity conditions," *Combustion and Flame*, vol. 159, no. 1, pp. 200 – 209, 2012.

[46] A. LEE and C. LAW, "AN EXPERIMENTAL INVESTIGATION ON THE VAPOR-IZATION AND COMBUSTION OF METHANOL AND ETHANOL DROPLETS," *COMBUSTION SCIENCE AND TECHNOLOGY*, vol. 86, no. 1-6, pp. 253–265, 1992.

[47] K. G. Kroenlein, *Numerical Simulation of Isolated Droplet Combustion Under Microgravity Conditions*. PhD thesis, Princeton University, 2007.

[48] M. C. Hicks, V. Nayagam, and F. A. Williams, "Methanol droplet extinction in carbon-dioxide-enriched environments in microgravity," *Combustion and Flame*, vol. 157, no. 8, pp. 1439 – 1445, 2010.

[49] A. Marchese and F. Dryer, "The effect of liquid mass transport on the combustion and extinction of bicomponent droplets of methanol and water," *Combustion and Flame*, vol. 105, no. 1-2, pp. 104–122, 1996.

[50] "Bioenergy conversion factors," https://bioenergy.ornl.gov/papers/misc/energy_conv.html, accessed 3 June 2014.

[51] A. Marchese, F. Dryer, and V. Nayagam, "Numerical modeling of isolated n-alkane droplet flames: Initial comparisons with ground and space-based microgravity experiments," *COMBUSTION AND FLAME*, vol. 116, pp. 432–459, FEB 1999.

[52] C. S. Cooper and N. M. Laurendeau, "Quantitative measurements of nitric oxide in high-pressure (2–5 atm), swirl-stabilized spray flames via laser-induced fluorescence," *Combustion and Flame*, vol. 123, no. 1–2, pp. 175 – 188, 2000.

[53] T. I. Farouk and F. L. Dryer, "Isolated n-heptane droplet combustion in microgravity: Cool flames–two-stage combustion," *Combustion and Flame*, vol. 161, no. 2, pp. 565–581, 2014.

[54] T. Held, A. Marchese, and F. Dryer, "A semi-empirical reaction mechanism for n-heptane oxidation and pyrolysis," *Combustion Science and Technology*, vol. 123, no. 1-6, pp. 107–146, 1997.

[55] M. Andac and F. Egolfopoulos, "Diffusion and kinetics effects on the ignition of premixed and non-premixed flames," *Proceedings of the Combustion Institute*, vol. 31, no. 1, pp. 1165 – 1172, 2007.

[56] V. Gopalakrishnan and J. Abraham, "Effects of multicomponent diffusion on predicted ignition characteristics of an n-heptane diffusion flame," *COMBUSTION AND FLAME*, vol. 136, no. 4, pp. 557–566, 2004.

[57] E. Ranzi, A. Frassoldati, R. Grana, A. Cuoci, T. Faravelli, A. Kelley, and C. K. Law, "Hierarchical and comparative kinetic modeling of laminar flame speeds of hydrocarbon and oxygenated fuels," *Progress in Energy and Combustion Science*, vol. 38, no. 4, pp. 468 – 501, 2012.

[58] Y. C. Liu and C. T. Avedisian, "A comparison of the spherical flame characteristics of sub-millimeter droplets of binary mixtures of n-heptane/iso-octane and n-heptane/toluene with a commercial unleaded gasoline," *Combustion and Flame*, vol. 159, no. 2, pp. 770 – 783, 2012.

[59] E. Mastorakos, T. Baritaud, and T. Poinsot, "Numerical simulations of autoignition in turbulent mixing flows," *Combustion and Flame*, vol. 109, no. 1-2, pp. 198–223, 1997.

[60] R. L. McCormick, M. S. Graboski, T. L. Alleman, A. M. Herring, and K. S. Tyson, "Impact of biodiesel source material and chemical structure on emissions of criteria pollutants from a heavy-duty engine," *Environmental Science & Technology*, vol. 35, no. 9, pp. 1742–1747, 2001.

[61] A. J. Marchese, T. L. Vaughn, K. Kroenlein, and F. L. Dryer, "Ignition delay of fatty acid methyl ester fuel droplets: Microgravity experiments and detailed numerical modeling," *Proceedings of the Combustion Institute*, vol. 33, no. 2, pp. 2021 – 2030, 2011.

[62] A. J. Marchese, T. Grumstrup, and T. L. Vaughn, "Examination of the Role of C_2O Radical in Methyl Ester NO_x Formation," in *Western States Meeting of the Combustion Institute*, (Boulder, Colorado), March 2010.

[63] S. Y. CHO, R. A. YETTER, and F. L. DRYER, "A computer-model for one-dimensional mass and energy-transport in and around chemically reacting particles, including complex gas-phase chemistry, multicomponent molecular-diffusion, surface evaporation, and heterogeneous reaction," *Journal of Computational Physics*, vol. 102, no. 1, pp. 160–179, 1992.

[64] A. J. Marchese and F. L. Dryer, "The effect of non-luminous thermal radiation in microgravity droplet combustion," *Combustion science and technology*, vol. 124, no. 1-6, pp. 371–402, 1997.

[65] T. Vaughn, M. Hammill, M. Harris, and A. Marchese, "Ignition delay of bio-ester fuel droplets," SAE Technical Paper 2006-01-3302, 2006.

[66] . T. Farouk and F. L. Dryer, "Microgravity droplet combustion: effect of tethering fiber on burning rate and flame structure," *Combustion Theory and Modelling*, vol. 15, no. 4, pp. 487–515, 2011.

[67] T. Farouk, Y. Liu, A. Savas, C. Avedisian, and F. Dryer, "Sub-millimeter sized methyl butanoate droplet combustion: Microgravity experiments and detailed numerical modeling," *Proceedings of the Combustion Institute*, 2012.

[68] Y. C. Liu, T. Farouk, A. J. Savas, F. L. Dryer, and C. T. Avedisian, "On the spherically symmetrical combustion of methyl decanoate droplets and comparisons with detailed numerical modeling," *Combustion and Flame*, vol. 160, no. 3, pp. 641–655, 2013.

[69] J. Li, Z. Zhao, A. Kazakov, M. Chaos, F. L. Dryer, and J. J. Scire, "A comprehensive kinetic mechanism for CO, CH_2O, and CH_3OH combustion," *International Journal of Chemical Kinetics*, vol. 39, no. 3, pp. 109–136, 2007.

[70] "CHEMKIN 10112, Reaction Design: San Diego, 2011."

[71] Reaction Design, *CHEMKIN Theory Manual*, December 2011.

[72] A. J. Marchese, *Single and Multicomponent Liquid Droplet Combustion: Detailed Kinetic Modeling and Microgravity Experiments*. PhD thesis, Princeton University, 1996.

[73] A. C. Eckbreth, *Laser diagnostics for combustion temperature and species*. Gordon and Breach Publishers, 1996.

[74] K. Kohse-Höinghaus and J. B. Jeffries, *Applied combustion diagnostics*. Taylor & Francis, 2002.

[75] J. Daily, "Laser induced fluorescence spectroscopy in flames," *Progress in energy and combustion science*, vol. 23, no. 2, pp. 133–199, 1997.

[76] K. C. Smyth and D. R. Crosley, "Detection of minor species with laser techniques," in *Applied Combustion Diagnostics* (K. Kohse-Höinghaus and J. B. Jeffries, eds.), ch. 2, pp. 9–68, Taylor & Francis, 2002.

[77] W. Bessler, C. Schulz, T. Lee, D. Shin, M. Hofmann, J. Jeffries, J. Wolfrum, and R. Hanson, "Quantitative NO-LIF imaging in high-pressure flames," *APPLIED PHYSICS B-LASERS AND OPTICS*, vol. 75, pp. 97–102, JUL 2002.

[78] W. G. Bessler, C. Schulz, T. Lee, J. B. Jeffries, and R. K. Hanson, "Strategies for laser-induced fluorescence detection of nitric oxide in high-pressure flames. I. A-X (0, 0) excitation," *Applied Optics*, vol. 41, no. 18, pp. 3547–3557, 2002.

[79] T. Vaughn, M. Wessel, A. Marchese, and M. Harris, "Microgravity ignition delay of bio-ester fuel droplets," in *45th AIAA Aerospace Sciences Meeting and Exhibit*, no. AIAA-2007-741, American Institute of Aeronautics and Astronautics, 2007.

[80] J. Yang, W. Chien, M. King, and W. Grosshandler, "A simple piezoelectric droplet generator," *Experiments in fluids*, vol. 23, no. 5, pp. 445–447, 1997.

[81] A. LOZANO, B. YIP, and R. HANSON, "Acetone - a tracer for concentration measurements in gaseous flows by planar laser-induced fluorescence," *Experiments in Fluids*, vol. 13, pp. 369–376, OCT 1992.

[82] A. Lee, *Droplet combustion and gasification mechanisms of multicomponent and reactive materials*. PhD thesis, University of California at Davis, 1990.

[83] S. R. Turns, *Introduction to Combustion*. McGraw-Hill, 2nd ed., 2000.

[84] T. Poinsot and D. Veynante, *Theoretical and Numerical Combustion*. Philadelphia, USA: R. T. Edwards, Inc., 2 ed., 2005.

[85] E. Mastorakos, "Ignition of turbulent non-premixed flames," *Progress in Energy and Combustion Science*, vol. 35, no. 1, pp. 57 – 97, 2009.

[86] S.-K. Kim, Y. Yu, J. Ahn, and Y.-M. Kim, "Numerical investigation of the autoignition of turbulent gaseous jets in a high-pressure environment using the multiple-RIF model," *Fuel*, vol. 83, no. 3, pp. 375 – 386, 2004.

[87] N. Peters, *Turbulent Combustion*. Cambridge University Press, 2000.

[88] W. Bessler, C. Schulz, T. Lee, J. Jeffries, and R. Hanson, "Strategies for laser-induced fluorescence detection of nitric oxide in high-pressure flames. II. A-X(0,1) excitation," *Applied Optics*, vol. 42, no. 12, pp. 2031–2042, 2003.

[89] W. Bessler, C. Schulz, T. Lee, J. Jeffries, and R. Hanson, "Strategies for laser-induced fluorescence detection of nitric oxide in high-pressure flames. III. Comparison of A-X excitation schemes," *Applied Optics*, vol. 42, no. 24, pp. 4922–4936, 2003.

[90] P. Samuel and G. Karim, "An analysis of fuel droplets ignition and combustion within homogeneous mixtures of fuel and air," SAE Technical Paper 940901, 1994.

[91] J. I. Steinfeld, *Molecules and Radiation: An Introduction to Modern Molecular Spectroscopy*. Dover Publications, 2nd ed., 2005.

Appendix A

Mapping of the Spherically-Symmetric Energy Equation to a Convection-Free Form

The convection-free formulation of the energy equation follows Law [24]. A convection-free formulation of the energy equation for a spherically symmetric domain is mathematically cumbersome. However, it is useful for the study of combustion physics because analogous results can be drawn from other geometries that are inherently convection free like ignition of a mixture by a hot surface and a chamber flame. Consider the conservation of energy equation for a one-step overall, second-order reaction:

$$\frac{\tilde{m}}{\tilde{r}^2}\frac{d\tilde{T}}{d\tilde{r}} - \frac{1}{\tilde{r}^2}\frac{d}{d\tilde{r}}\left(\tilde{r}^2\frac{d\tilde{T}}{d\tilde{r}}\right) = Da_c\,\tilde{Y}_O\tilde{Y}_F\,e^{-\tilde{T}_a/\tilde{T}}. \tag{80}$$

This equation can be mapped to a form that contains no convection term by a change of variable:

$$\xi \equiv 1 - e^{-\tilde{m}/\tilde{r}}. \tag{81}$$

The derivative of Equation (81) is:

$$\frac{d\xi}{d\tilde{r}} = -\frac{\tilde{m}}{\tilde{r}^2}e^{-\tilde{m}/\tilde{r}}. \tag{82}$$

In terms of the new variable ξ, Equation (82) is written as:

$$\frac{d\xi}{d\tilde{r}} = -\frac{\ln^2(1-\xi)}{\tilde{m}}(1-\xi). \tag{83}$$

Solve Equation (81) for $\tilde{r}$ to obtain:

$$\tilde{r} = -\frac{\tilde{m}}{\ln(1-\xi)}. \tag{84}$$

Apply the chain rule to the derivatives and substitute Equation (84) into (80) to obtain the following:

$$\frac{\ln^2(1-\xi)}{\tilde{m}}\frac{d\tilde{T}}{d\xi}\frac{d\xi}{d\tilde{r}} - \frac{\ln^2(1-\xi)}{\tilde{m}^2}\frac{d}{d\xi}\frac{d\xi}{d\tilde{r}}\left[\frac{\tilde{m}^2}{\ln^2(1-\xi)}\frac{d\tilde{T}}{d\xi}\frac{d\xi}{d\tilde{r}}\right] = Da_c\,\tilde{Y}_O\tilde{Y}_F\,e^{-\tilde{T}_a/\tilde{T}}. \tag{85}$$

Now substitute Equation (83) for the $d\xi/d\tilde{r}$ derivatives in Equation (85):

$$\frac{\ln^2(1-\xi)}{\tilde{m}}\left(\frac{\ln^2(1-\xi)}{\tilde{m}}\right)(1-\xi)\frac{d\tilde{T}}{d\xi}$$

$$-\frac{\ln^2(1-\xi)}{\tilde{m}^2}\left(\frac{\ln^2(1-\xi)}{\tilde{m}}\right)(1-\xi)\frac{d}{d\xi}\left[\frac{\tilde{m}^2}{\ln^2(1-\xi)}\left(\frac{\ln^2(1-\xi)}{\tilde{m}}\right)(1-\xi)\frac{d\tilde{T}}{d\xi}\right]$$

$$= Da_c\,\tilde{Y}_O\tilde{Y}_F\,e^{-\tilde{T}_a/\tilde{T}}. \tag{86}$$

Numerous cancellations and simplifications are possible, which result in this equation:

$$-\frac{(1-\xi)\ln^4(1-\xi)}{\tilde{m}^2}\left[\frac{d\tilde{T}}{d\xi} + \frac{d}{d\xi}\left((1-\xi)\frac{d\tilde{T}}{d\xi}\right)\right] = Da_c\,\tilde{Y}_O\tilde{Y}_F\,e^{-\tilde{T}_a/\tilde{T}}. \tag{87}$$

Both sides of the above equation can be divided by the first factor and the $d/d\xi$ derivative applied to the terms inside the curved brackets using the product rule to get:

$$\frac{d\tilde{T}}{d\xi} - \frac{d\tilde{T}}{d\xi} + (1-\xi)\frac{d^2\tilde{T}}{d\xi^2} = -Da_c\left[\frac{\tilde{m}^2}{(1-\xi)\ln^4(1-\xi)}\right]\tilde{Y}_O\tilde{Y}_F\,e^{-\tilde{T}_a/\tilde{T}}. \tag{88}$$

The first and second terms in the above equation cancel (thereby eliminating convection) and the $(1 - \xi)$ factor in the third term is moved to the right hand side to arrive at the final result:

$$\frac{d^2\tilde{T}}{d\xi^2} = -Da_c \left[\frac{\tilde{m}^2}{(1 - \xi)^2 \ln^4(1 - \xi)} \right] \tilde{Y}_O \tilde{Y}_F \ e^{-\tilde{T}_a/\tilde{T}}. \tag{89}$$

APPENDIX B

Derivation of the Structure Equation for the Temperature Perturbation

The derivation of the structure equation for the temperature perturbation follows Law [24]. The convection-free form of the spherically symmetric conservation of energy equation [Equation (36)] is:

$$\frac{d^2\tilde{T}}{d\xi^2} = -Da_c \left[\frac{\tilde{m}^2}{(1-\xi)^2 \ln^4(1-\xi)} \right] \tilde{Y}_O \tilde{Y}_F \, e^{-\tilde{T}_a/\tilde{T}}. \tag{90}$$

The associated coupling functions for oxidizer and fuel are, respectively:

$$\tilde{Y}_O = -\tilde{T} + \tilde{Y}_{O,\infty}(1-\xi) - \beta_v \xi + \tilde{T}_\infty \tag{91}$$

$$\tilde{Y}_F = -\tilde{T} + (1-\beta_v)\xi + \tilde{T}_\infty \tag{92}$$

where

$$\beta_v = (\tilde{T}_\infty - \tilde{T}_s) + \tilde{q}_v. \tag{93}$$

Recall $\tilde{r} = r/r_s$ so that at the droplet surface, $\tilde{r} = 1$. Noting the definition of ξ in Equation (35), ξ at the droplet surface is:

$$\xi_s = 1 - e^{-\tilde{m}} \tag{94}$$
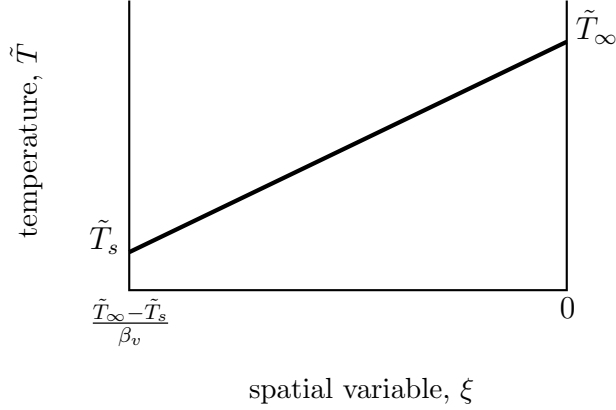
FIGURE B.1. Temperature profile for nearly-frozen regime.

In the nearly frozen regime, the rate of evaporation from the fuel droplet is given by the classical solution for the evaporation rate for an isolated non-reacting droplet.

$$\tilde{m}_v = \ln\left(\frac{\beta_v}{\tilde{q}_v}\right). \tag{95}$$

Substitute Equation (95) into (94) to obtain:

$$\xi_s = 1 - \frac{\tilde{q}_v}{\beta_v} \tag{96}$$

that can be rewritten as

$$\xi_s = \frac{\beta_v - \tilde{q}_v}{\beta_v}. \tag{97}$$

Now substitute the definition of β_v [Equation (93)] into the numerator of the above equation to get:

$$\xi_s = \frac{\tilde{T}_\infty - \tilde{T}_s}{\beta_v}. \tag{98}$$

The temperature profile for the nearly frozen regime is linear as shown in Figure (B.1). At the droplet surface, the spatial variable $\xi = (\tilde{T}_\infty - \tilde{T}_a)/\beta_v$ and nondimensional temperature $\tilde{T} = \tilde{T}_s$. In the far field, $\xi = 0$ and $\tilde{T} = \tilde{T}_\infty$. The equation for the temperature profile can

206

be written in point slope form:

$$\tilde{T} - \tilde{T}_\infty = \frac{\tilde{T}_\infty - \tilde{T}_s}{\left[-\frac{\tilde{T}_\infty - \tilde{T}_a}{\beta_v} \right]} \xi \tag{99}$$

that can be simplified thus:

$$\tilde{T} - \tilde{T}_\infty = -\beta_v \xi. \tag{100}$$

Recalling $\xi = \epsilon \chi$, the above can be written as:

$$\tilde{T} - \tilde{T}_\infty = -\beta_v \epsilon \chi. \tag{101}$$

Moving the $\tilde{T}_\infty$ term to the right hand side results in the equation for the temperature profile

for the nearly frozen (nf) regime that is the leading order solution to Equation (90):

$$\tilde{T}_{\mathrm{nf}} = \tilde{T}_\infty - \beta_v \epsilon \chi. \tag{102}$$

The perturbed inner solution is given by:

$$\tilde{T}_{\mathrm{in}} = \tilde{T}_{\mathrm{nf}} + \epsilon \theta(\chi) + \mathcal{O}(\epsilon^2). \tag{103}$$

Equation (102) is substituted into (103) to result in the following:

$$\tilde{T}_{\mathrm{in}} = \tilde{T}_\infty + \epsilon \left[\theta(\chi) - \beta_v \chi \right] + \mathcal{O}(\epsilon^2). \tag{104}$$

The above equation for the inner solution is substituted into the coupling equations [Equations (91) and (92)] for $\tilde{T}$ that results in the following forms for the oxidizer and fuel coupling

equations, respectively:

$$\tilde{Y}_O = \tilde{Y}_{O,\infty} \tag{105}$$

$$\tilde{Y}_F = \epsilon \left[\chi - \theta \right]. \tag{106}$$

Now we are ready to map the ODE in $\tilde{T}(\xi)$ [Equation (90)] to one in $\theta(\chi)$. First, the left hand side of the equation is expanded using the chain rule:

$$\frac{d}{d\chi} \frac{d\chi}{d\xi} \frac{d\tilde{T}}{d\chi} \frac{d\chi}{d\xi} = -Da_c \left[\frac{\tilde{m}^2}{(1-\xi)^2 \ln^4(1-\xi)} \right] \tilde{Y}_O \tilde{Y}_F \, e^{-\tilde{T}_a/\tilde{T}}. \tag{107}$$

Since the derivative $d\chi/d\xi = 1/\epsilon$, the left hand side becomes:

$$\frac{1}{\epsilon^2} \frac{d^2\tilde{T}}{d\chi^2} = -Da_c \left[\frac{\tilde{m}^2}{(1-\xi)^2 \ln^4(1-\xi)} \right] \tilde{Y}_O \tilde{Y}_F \, e^{-\tilde{T}_a/\tilde{T}}. \tag{108}$$

The second derivative of the inner solution, Equation (104), is:

$$\frac{d^2\tilde{T}_{\text{in}}}{d\chi^2} = \epsilon \frac{d^2\theta}{d\chi^2}. \tag{109}$$

Equation (109) is substituted into the left hand side of Equation (108) to obtain:

$$\frac{1}{\epsilon} \frac{d^2\theta}{d\chi^2} = -Da_c \left[\frac{\tilde{m}^2}{(1-\xi)^2 \ln^4(1-\xi)} \right] \tilde{Y}_O \tilde{Y}_F \, e^{-\tilde{T}_a/\tilde{T}}. \tag{110}$$

The fraction in the square brackets above can be approximated by a Taylor series expansion about $\xi = 0$:

$$\frac{\tilde{m}^2}{(1-\xi)^2 \ln^4(1-\xi)} \approx \tilde{m}^2 \left[\frac{1}{\xi^4} + \frac{1}{6\xi^2} + \frac{1}{6\xi} + \cdots \right]. \tag{111}$$

If we drop the $\mathcal{O}(\xi^{-2})$ and higher terms above and recall $\xi = \epsilon\chi$, we can write Equation (110) as:

$$\frac{d^2\theta}{d\chi^2} = -Da_c \frac{\tilde{m}^2}{\epsilon^3\chi^4} \tilde{Y}_O \tilde{Y}_F \; e^{-\tilde{T}_a/\tilde{T}}. \tag{112}$$

Now we can substitute Equations (105) and (106) for the nondimensional mass fractions for oxidizer and fuel to obtain:

$$\frac{d^2\theta}{d\chi^2} = -Da_c \frac{\tilde{m}^2(\chi - \theta)}{\epsilon^2\chi^4} \tilde{Y}_{O,\infty} \; e^{-\tilde{T}_a/\tilde{T}}. \tag{113}$$

All that remains now is to substitute the inner solution, Equation (104), for $\tilde{T}$ in the exponent of Euler's number:

$$\frac{d^2\theta}{d\chi^2} = -Da_c \frac{\tilde{m}^2(\chi - \theta)}{\epsilon^2\chi^4} \tilde{Y}_{O,\infty} \; e^{\char`\^\left[\dfrac{-\tilde{T}_a}{\tilde{T}_\infty + \epsilon(\theta - \beta_v\chi)}\right]}. \tag{114}$$

The exponent in the square brackets can be rewritten:

$$\frac{d^2\theta}{d\chi^2} = -Da_c \frac{\tilde{m}^2(\chi - \theta)}{\epsilon^2\chi^4} \tilde{Y}_{O,\infty} \; e^{\char`\^\left[\dfrac{-\tilde{T}_a}{\tilde{T}_\infty} \cdot \dfrac{1}{1 + \frac{\epsilon}{\tilde{T}_\infty}(\theta - \beta_v\chi)}\right]}. \tag{115}$$

The second factor in the exponent can be approximated with a Taylor series expansion about $\epsilon(\theta - \beta_v\chi)/\tilde{T}_\infty = 0$ as:

$$\frac{1}{1 + \frac{\epsilon}{\tilde{T}_\infty}(\theta - \beta_v\chi)} \approx 1 - \frac{\epsilon}{\tilde{T}_\infty}(\theta - \beta_v\chi) + \cdots, \tag{116}$$

so we can rewrite Equation (115) to obtain:

$$\frac{d^2\theta}{d\chi^2} = -Da_c \frac{\tilde{m}^2(\chi - \theta)}{\epsilon^2\chi^4} \tilde{Y}_{O,\infty} \; e^{\char`\^\left[\dfrac{-\tilde{T}_a}{\tilde{T}_\infty}\left(1 - \frac{\epsilon}{\tilde{T}_\infty}(\theta - \beta_v\chi)\right)\right]}. \tag{117}$$

The $-\tilde{T}_a/\tilde{T}_\infty$ factor in the exponent is distributed through to get:

$$\frac{d^2\theta}{d\chi^2} = -Da_c \frac{\tilde{m}^2(\chi - \theta)}{\epsilon^2 \chi^4} \tilde{Y}_{O,\infty} \, e^{\hat{}} \left[\frac{-\tilde{T}_a}{\tilde{T}_\infty} + \epsilon \frac{\tilde{T}_a}{\tilde{T}_\infty^2} (\theta - \beta_v \chi) \right]. \tag{118}$$

Since $\epsilon = \tilde{T}_\infty^2/\tilde{T}_a$, the exponent can be simplified resulting in the following:

$$\frac{d^2\theta}{d\chi^2} = -Da_c \frac{\tilde{m}^2(\chi - \theta)}{\epsilon^2 \chi^4} \tilde{Y}_{O,\infty} \, e^{\frac{-\tilde{T}_a}{\tilde{T}_\infty}} e^{(\theta - \beta_v \chi)}. \tag{119}$$

Finally, by defining a reduced Damköhler number

$$\Delta = \left(\frac{\tilde{m}_{v,0}}{\tilde{T}_\infty^2/\tilde{T}_a} \right)^2 Da_c \, \tilde{Y}_{O,\infty} \, e^{-\tilde{T}_a/\tilde{T}_\infty}, \tag{120}$$

we arrive at the objective of the derivation:

$$\boxed{\frac{d^2\theta}{d\chi^2} = \Delta \frac{(\chi - \theta)}{\chi^4} e^{(\theta - \beta_v \chi)}.} \tag{121}$$

APPENDIX C

Molecular Spectroscopy

The discussion appearing in this appendix largely follows Eckbreth [73]. The spectrum of a molecule is comprised of a series of discrete energy state transitions that span a combination of vibrational, rotational, and electronic excitation modes. These three modes can be, to a first-order approximation, decoupled and treated separately according to the Born-Oppenheimer approximation [73]. Here, only molecules containing two atoms are considered since this work is concerned only with spectroscopy of OH and NO.

C.1. Vibrational Modes

Vibrational modes of a diatomic molecule can be simplistically modeled as a harmonic oscillator in which permitted energy states are given by

$$E_v = h\nu \left(v + \frac{1}{2} \right), \quad \text{for } v = 0, 1, 2, 3, ... \tag{122}$$

Here, h is Planck's constant; ν is frequency, and v is the vibrational quantum number. In reality, diatomic molecules act like anharmonic oscillators wherein higher order terms are also permitted:

$$E_v = hc \left[w_e \left(v + \frac{1}{2} \right) - w_e x_e \left(v + \frac{1}{2} \right)^2 + w_e y_e \left(v + \frac{1}{2} \right)^3 - \cdots \right] \tag{123}$$

where $w_e = \nu/c$ is a wavenumber of units [cm^{-1}]; $x_e, y_e, ...$ are small parameters; and c is the speed of light.
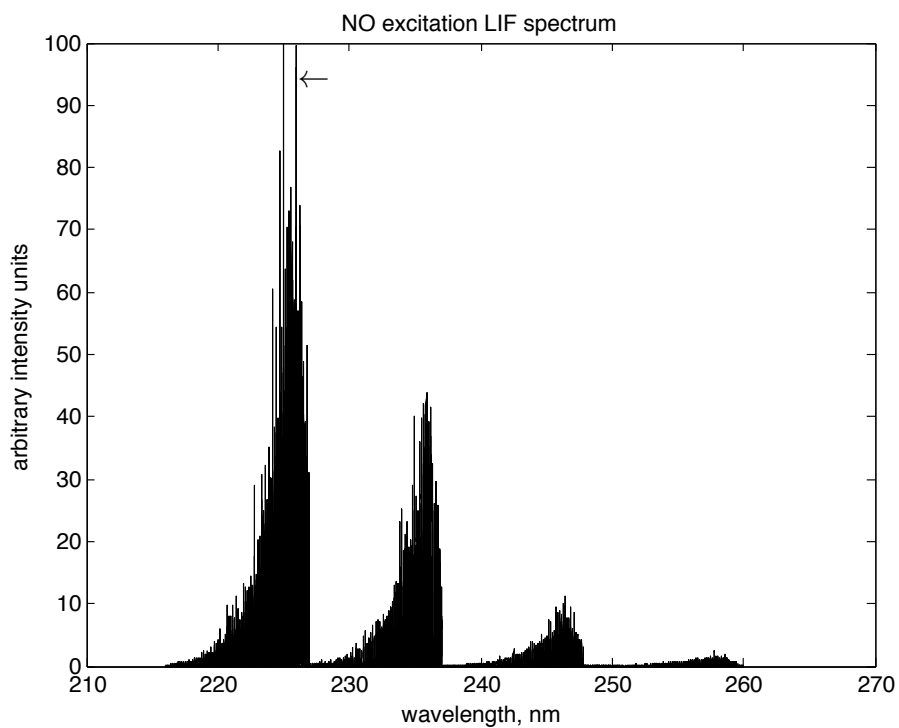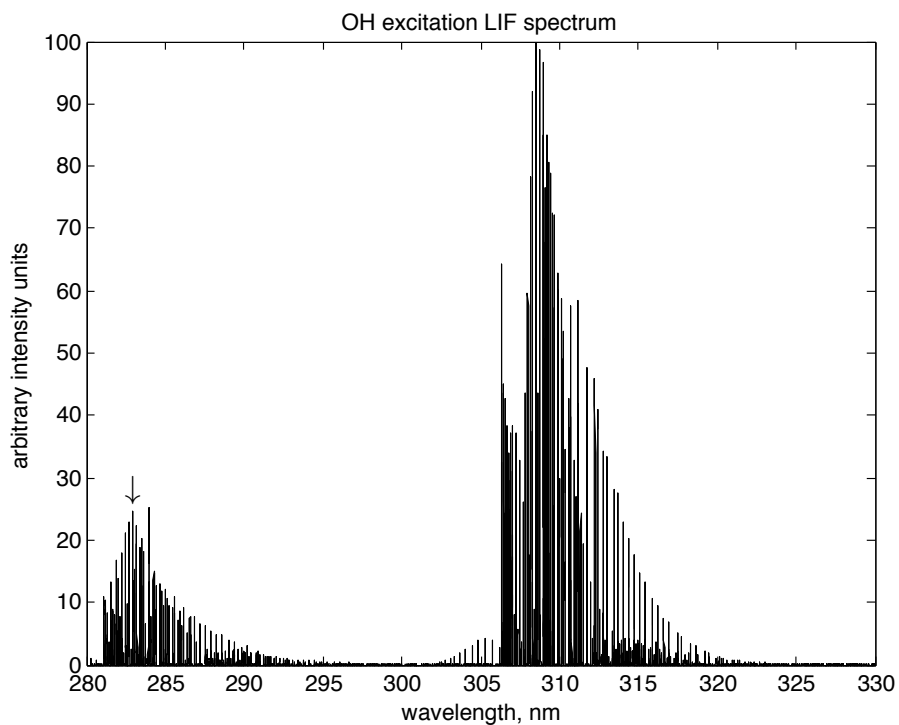
FIGURE C.1. Plots showing excitation spectra for hydroxyl radical (top) and nitric oxide (bottom). The arrows indicate the transition to which the pump laser was tuned to carry out LIF.

The rotational mode can initially be thought of in terms of a rigid rotator whose energy is described by

$$E_r = hcBJ(J+1) \tag{124}$$

where B the rotational constant, and J the rotational quantum number[1]. The rotational constant is as follows:

$$B = \frac{h}{8\pi^2 cI} \tag{125}$$

with I representing the molecular moment of inertia. In reality, molecules are not rigid and internuclear distance will vary with rotational energy, thereby causing the moment of inertia to change. This can be accounted for by a correction factor D, the centrifugal distortion constant, so that Equation (124) becomes

$$E_r = hc \left[BJ(J+1) - DJ^2(J+1)^2 \right]. \tag{126}$$

A further level of complexity is added to the rotational mode when one considers that vibration of the molecule will change its rotational moment of inertia. This is accounted for by new forms of the rotational constant and centrifugal distortion constant:

$$B_v = B_e - \alpha_e \left(v + \frac{1}{2} \right) \tag{127}$$

$$D_v = D_e + \beta_e \left(v + \frac{1}{2} \right), \tag{128}$$

---

[1]Here, B should not be confused with the Einsten coefficient for stimulated emission: B_{mn}. Nor should J be confused with the total electronic angular momentum number: $\vec{J} = \vec{L} + \vec{S}$. The notation is, unfortunately, standard.

where the quantities with a subscript e are indicative of those at the equilibrium position of the nuclei. Equation (126) then becomes:

$$E_r = hc \left[B_v J(J+1) - D_v J^2 (J+1)^2 \right].$$

(129)

C.3. Electronic Modes

Electronic spectroscopy of molecules is concerned with the principle quantum number n and electronic orbital angular momentum ℓ. The Bohr model of the atom indicates that only those electronic orbits are permitted for which:

$$\ell = n \frac{h}{2\pi}, \quad \text{for } n = 0, 1, 2, 3, \dots.$$

(130)

As in atomic spectroscopy, electrons with $\ell = 0, 1, 2, 3, \dots$ are referred to as $s, p, d, f, \dots$ electrons. The electronic orbital angular momentum $\vec{\ell}$ is spatially quantized such that its component along the internuclear axis m_ℓ takes on integer values: $m_\ell = \ell, \ell - 1, \dots, -\ell$. The permitted combinations of states n and ℓ are denoted by λ, the magnitude of which is $\lambda \equiv |m_\ell|$. Electrons for which $\lambda = 0, 1, 2, 3, \dots$ are described as $\sigma, \pi, \delta, \phi, \dots$ electrons. Notice that m_ℓ can be either positive or negative when $\lambda \neq 0$ because $\lambda \equiv |m_\ell|$. This means that those states for which $\lambda = 1, 2, 3, \dots$ are doubly degenerate, a condition referred to as lambda-doubling. With the above in mind, electrons are identified by writing: $n\ell\lambda$ [73]. For example, suppose an electron has a principle quantum number of three, orbital angular momentum number of two, and the magnitude of the component of $\vec{\ell}$ along the internuclear axis equal to one. This electron is described by $3d\pi$.

In multi-electron systems, the state of each individual electron can be considered inde-

pendently, then summed. For example, the ith electron has a state described by n_i, ℓ_i, and

λ_i. The states that arise from a system containing multiple electrons are described by the

total electronic orbital angular momentum quantum number $\vec{\Lambda}$ such that:

$$\vec{\Lambda} = \sum_i \vec{\lambda}_i. \tag{131}$$

Notice the use of $\vec{\lambda}_i$ as a vector quantity. This is different from the single-electron case in

which electrons exhibiting m_ℓ or $-m_\ell$ have the same energy. The reason for this is since we

are summing states of multiple electrons, we must now account for the sign of the component

of the electronic orbital angular momentum along the internuclear axis. This implies that

$$\vec{\Lambda} = \sum_i \vec{\lambda}_i = \sum_i m_{\ell i}. \tag{132}$$

The states for various integer values of $\vec{\Lambda}$ are named in a manner that is analogous to those

with single electrons: states exhibiting $\vec{\Lambda} = 0, 1, 2, 3, ...$ are named $\Sigma, \Pi, \Delta, \Phi$, etc. Since $\vec{\Lambda}$ is a

vector quantity and can point in opposite directions, states $\Pi, \Delta, \Phi, ...$ are doubly degenerate.

(State Σ is not degenerate since it corresponds to $\vec{\Lambda} = 0$, which is non-directional.) Finally,

spins of individual electrons s_i are summed to give total spin:

$$\vec{S} = \sum_i \vec{s}_i, \tag{133}$$

which is used to determine multiplicity, $2S + 1$, of a state. The numerical value of the mul-

tiplicity of a state appears as a superscript preceding the capital greek letter. For example,

an electronic state with $\Lambda = 1$ and multiplicity 2 appears as: $^2\Pi$.

C.4. Transition Wavelength

As noted previously, the energy of a transition and therefore the wavelength of the emitted photon is, roughly speaking, the sum of the energy potential from the electronic mode, vibrational mode, and rotational mode. This can be written as:

$$\lambda = \frac{hc}{(T_e' - T_e'') + (G_{v'} - G_{v''}) + (F_{v'} - F_{v''})} \tag{134}$$

where T, G, and F represent energy for electronic, vibrational, and rotational modes, respectively. The single prime indicates quantities corresponding to the upper level of the transition and those that are doubly primed are of the lower level of the transition. The variable λ is the wavelength of the emitted photon. Numerical values for the electronic states T_e are obtained from solutions to the Schrodinger wave equation. Vibrational modes G_v are obtained from Equation (123). [91]

The above discussion had the purpose of determining the wavelength of a given transition. The following will establish the intensity of a transition. Consider an absorption transition from lower level $mv''J''$ to upper level $nv'J'$. The transition probability (i.e., linestrength) is written as

$$B_{mn,v''v',J''J'} = \frac{2\pi^2}{3h^2\epsilon_0 g_m} |R_e^{nm}|^2 \left|R_{\text{vib}}^{v'v''}\right|^2 \frac{\left|R_{\text{rot}}^{J'J''}\right|^2}{2J'' + 1} \tag{135}$$

where ϵ_0 is the permittivity of free space and g_m is the degeneracy of the (lower) m level. The latter three factors in Equation (135) contain R's with subscripts e, vib, and rot that are the matrix elements for electronic, vibrational, and rotational transitions, respectively. The square of the determinant of these matrices are termed: electronic transition probability,

$|R_{\text{e}}^{nm}|^2$; Franck-Condon factor, $\left|R_{\text{vib}}^{v'v''}\right|^2$; and rotational linestrength, $\left|R_{\text{rot}}^{J'J''}\right|^2$. Recall that

$$g_m B_{mn} = g_n B_{nm} \tag{136}$$

and

$$\frac{A_{nm}}{B_{nm}} = \frac{8\pi h \nu^3}{c^3} = \frac{hw^3}{\pi^2 c^3} \tag{137}$$

where ν is the light frequency, c is the speed of light, and w is wavelength. One can manipulate Equation (135) using (136) and (137) to obtain the transition probability for spontaneous emission:

$$A_{nm,v'v'',J'J''} = \frac{2\omega^3}{3hc^3\epsilon_0 g_n} |R_{\text{e}}^{nm}|^2 \left|R_{\text{vib}}^{v'v''}\right|^2 \frac{\left|R_{\text{rot}}^{J'J''}\right|^2}{2J'+1}. \tag{138}$$

Now that transition probability for absorption and transition probability for spontaneous emission are known, an equation for laser-induced fluorescence signal power can be written:

$$F_{\text{fl}} = h\nu \frac{\Omega}{4\pi} \ell A N_1^0 \frac{B_{12}}{B_{12} + B_{21}} \frac{A_{21}}{1 + \frac{I_{\text{sat}}^\nu}{I_\nu}} \tag{139}$$

where Ω is the solid angle over which fluorescence is collected; ℓ, the length along the laser beam axis over which fluorescence is collected; A, the cross-sectional area of the laser beam; and N_1^0, initial ground state population. Variables ℓ and A describe the probe volume: the region from which fluorescence is collected and detected by the LIF system. These quantities, along with Ω are illustrated in Figure [C.2]. The area A is determined by the focusing of the probe beam and length ℓ by the aperture of the detector, or entrance slit width of the monochromator or spectrometer.
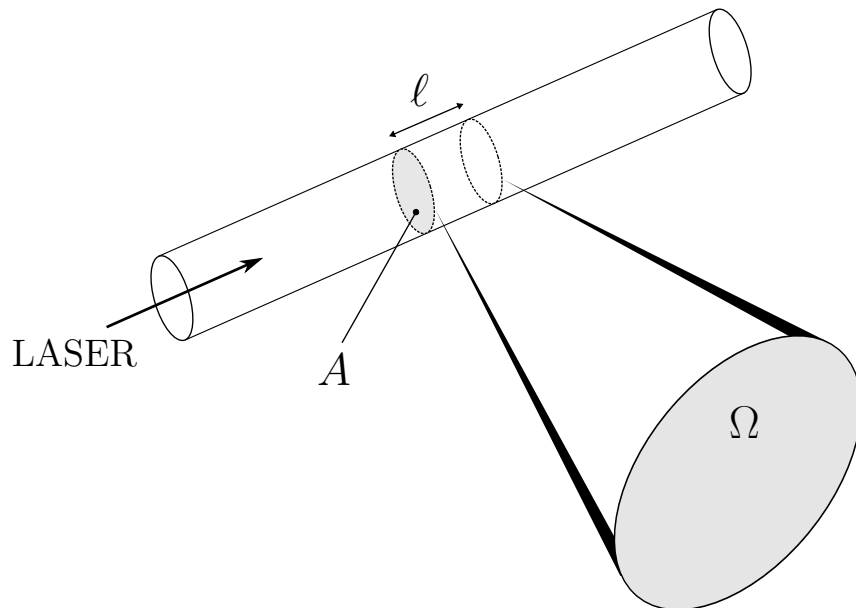
FIGURE C.2. A diagram illustrating the geometry of the LIF probe volume with cross-sectional area A and length ℓ.

APPENDIX D

Tips for Operations of the Sirah Cobra Stretch

Dye Laser

The dye laser used for this work was a Cobra Stretch by Sirah, which is a subsidiary of Spectra-Physics, which is itself a subsidiary of Newport. The device was found to be difficult to tune due to poor mechanical design and awkward layout. However, once accomplished the laser seemed to remain fairly consistent. A number of lessons were learned during the course of setup and experimentation for this thesis. These are recounted here since they do not appear in the manual or literature.

We struggled mightily to prevent the scorching of the quartz dye cells by the pump beam. It was thought at one time that the scorching was caused by accidentally applying the pump beam to the dye laser without the dye circulators operating. This resulted in the installation of an interlock that permitted the firing of the Nd:YAG pump laser only when the dye circulators were running. Nonetheless, scorching events continued to occur intermittently following implementation of the interlocks. Although they didn't solve the cell scorching problem, the interlocks are probably still a good idea since applying the pump laser without dye circulation is a bad practice.

When the dye laser was converted over to the wavelength necessary to conduct NO PLIF, coumarin dye was used, which has a lifetime of only a few hours. Since it was then necessary to mix fresh dye nearly every day, extreme care was taken to remove bubbles from the circulators when filled with fresh dye. The reason for this was that we suspected a bubble passing through the dye cell during a pump beam pulse might be the cause of the dye cell

scorching. Since the extra care was taken to remove bubbles from the dye circulators, no dye cell scorching has occurred. And, given the significant number of hours the dye laser has run in the intervening time, it seem likely that bubbles are the ultimate cause of dye cell scorching.

The removal of bubbles from the dye circulators is accomplished with a sequence of simple techniques. When filling the circulators with fresh dye, turn them on for about a minute to fill all of the plumbing with dye. Then shut off the circulators and observe the tube that carries dye from the reservoir to the pump inlet. Often, a bubble will appear from the pump head and rise into the reservoir. More bubbles from the pump head can be evacuated by picking up the dye circulator and tipping it backwards till the barb fitting is pointing straight up. Do this for both dye circulators, then run them for another thirty seconds. Following the tipping excercise, it is then necessary to cycle the circulators on and off in ten second intervals (on for ten seconds, off for ten seconds, etc.). This should be repeated until no bubbles are seen to flow out of the dye return tube into the reservoir when the circulator is running; sometimes this takes more than ten on-off cycles. It is a tedious process, but the repetative cycling seems to prevent cell scorching. Once no bubbles are seen flowing from the dye return line, the circulator is ready to run. Ensure the dye return tube is pushed well below the level of the dye in the reservoir to minimize entrainment of air bubbles that could get sucked into the pump and sent to the dye cell.

If scorching does occur, or if the housing for the dye cell is clipping the top of the beam, it is a simple matter to shim up the dye cell. Cut a square of sheet metal in a shape that is similar to the bottom of the dye cell housing. Fix it to the bottom of the dye cell housing

with a thin film of silicone. Multiple shims can be applied this way and easily removed by prying them off with a thin screwdriver or knife.

If scorching or some other optical damage occurs to the dye cell that shimming cannot alleviate, the cell can be removed from the housing, flipped around 180 degrees, and installed again. No chemical or mechanical method was found that successfully removed the scorching residue from the interior of a dye cell. No damage was ever observed on the capillary cell and there was never a reason to replace it.

The dye laser exhibited a tiny amount of drift in wavelength from day to day. It is necessary to conduct a daily LIF scan of a flame to check the wavelength and set it to the optimal position. This procedure is explained in the body of this document.

If the energy of the beam seems unusually low, first check the energy of the pump laser. If the pump beam seems normal, measure the fundamental beam of the dye laser before the BBO crystal, but after the amplifier. If the fundamental beam seems normal try fine-tuning the BBO crystal. However, be aware that changing the position of the doubling crystal may change the shape of the intensity profile of the laser sheet. If energy of the fundamental beam is lower than expected, try tweaking the three beam splitters in the dye laser housing. Note that the knob adjustment necessary is probably very small; so small as to be barely perceptible as motion by ones fingers. As such, it is necessary to proceed with caution to avoid de-tuning the dye laser.

Scattered and reflected laser light from the dye laser's fundamental beam (and presumably the second harmonic as well) escapes through gaps in the housing. Control these emissions with black felt or other opaque material.

Discussion of Optical Filter Selection for PLIF

systems

A few lessons regarding optical filters were learned during the course of setting up, debugging, and operating the PLIF system used for the research reported on by this thesis. As described in the body of this document, a two-filter scheme was used for OH PLIF: Schott glass filters UG-11 and WG-305. These filters were purchased from Andover corporation and were relatively inexpensive. They did a good job of attenuating scattered laser light, which was critical for these experiments since the droplets scattered a tremendous amount. Normally, there is a tradeoff between good attenuation of laser light and transmissivity of fluorescence wavelengths. However, with this scheme, the transmisivity of fluorescence wavelengths was quite high: some 40 to 80%. One of the fortuitous features of OH fluorescence is that the probing wavelength (~ 283 nm) is quite far from the fluorescence bands ($300 - 330$ nm). This means that laser light is less likely to be able to sneak under the wings of the bandpass of this filter combination. A second beneficial occurrence is that Schott happens to mass produces these particular filter materials, making it easy and cheap to obtain.

Selecting a filter for NO PLIF proved to be more of a challenge. As noted in the body of this thesis, the article by Bessler, et al. [77] was used as a guide in building the system. For spectral discrimination, they used a long-pass filter and a pair of high-reflectivity mirrors (237 ± 5 nm). With such a scheme, it is likely that both attenuation of laser light and transmissivity of fluorescence bands was excellent. Unfortunately, such a scheme is also quite expensive since such mirrors are custom and typically cost around $2000 each. This

method was out of reach for us due to cost. Instead we tried a number of stock bandpass filters.

Filters made from Schott glass UG-5 is often seen in the literature for NO PLIF. However, it was found to be unsuitable for our purposes because it did not attenuate laser light scattered by the droplet sufficiently. It was also tested on a purely gaseous bunsen flame and it was found to be adequate for that purpose. Before settling on the filter we ended up using, we tried another Andover filter with a larger bandpass: 254 ± 10. Like the UG-5, this filter proved to be inadequate in attenuating laser light. Also like the UG-5, it would probably be entirely suitable for NO PLIF in gaseous flames. We finally settled on the filter noted in the body of this thesis (248 ± 5) because it significantly attenuated the laser wavelength. However, fluorescence signal suffered and it was necessary to average a huge number of fluorescence images to obtain a useful result. This proved to be a tedious exercise.

One thing we failed to consider prior to disassembly of the experiment for moving, was trying to probe at a different wavelength. This might have allowed use of a filter with higher transmissivity of fluorescence. Bessler et al. [77] used the line at 226.0324 nm because there was a local minima in the absorptivity of oxygen there. However, interference from oxygen is only an issue at high pressures like they were working with. Since these experiments were atmospheric pressure, there may be some other scheme that is better suited. The Bessler paper [77] is a derivative of an extensive study on identifying the optimal LIF/PLIF scheme for NO. The results of that study are References [78, 88, 89].

To summarize, when selecting filters for NO PLIF (or any species for that matter), in the absence of interference concerns, one has the unenviable task of balancing high attenuation

of the probing laser wavelength, high transmissivity of the fluorescence bands of the species of interest, and cost of the filter.

Droplet Generator Operations and

Trouble-shooting

A strobe light is absolutely essential for diagnosing problems with a droplet generator because it permits you to see droplet that are otherwise too small and too fast to be visible. We were able to obtain the classic General Radio 1531 Strobotac from Ebay, but not after purchasing a lemon the first time (that we kept for parts). These are workhorses if you can find one in good shape; unfortunately, they haven't been manufactured for many decades. There must be modern devices that would be entirely suitable as well. Ensure the strobe rate is adjustable over a wide range (1 to 100s of Hertz) so you can observe the droplets at different points in the formation process. A strobe light will make multiple drops, satellite drops, and jittery drops visible and allow one to observe the effect of adjustments in real time (e.g., varying pulse voltage).

If the droplet generator is free of bubbles, the sound of the piezoelectric disk actuating should be fairly quiet, like the ticking of a clock. If the sound is loud and hollow, there is probably a bubble in the chamber. A simple test to check for bubbles, is to rock the droplet generator back and forth as the piezoelectric disk actuates. If a bubble is present, buoyancy will cause the bubble to move to the upper end of the tilted chamber. As it slides along the underside of the disk, the bubble causes the sound of disk actuation to modulate in a way that is obvious. If a bubble is detected, then it must be extracted with a syringe as described in the body of this thesis.

Sometimes a small bubble (2 to 3 mm) will adhere to the wall of the chamber even when tilted in a manner just described. In such cases, the body of the droplet generator should be struck quite firmly with (e.g.) the plastic handle of a screw driver to dislodge the bubble so it can be drawn out. There are a number of behaviors that would cause one to suspect a small bubble is present in the chamber. A small bubble will not necessarily preclude the formation of single bubbles like larger bubbles, but minor difficulties may occur such as the following:

- No voltage can be found that produces single droplets without satellites.
- Single droplets will form, but they jump about. Successive droplets do not arrive at the same location over a fixed interval.
- Single droplets form normally, but only for about a minute, then multiple droplets and satellites are produced.

If you are not able to produce droplets of any kind no matter what voltage you attempt, the nozzle may be clogged. This can be verified by examining the tip of the nozzle while backlighting it with a flashlight. Since the orifice is small, it may not take much debris to clog it. We did not filter our fuel, but we did take care to keep the droplet generator very clean. We had a clogged nozzle on only two occasions when seals incompatible with the methyl butanoate started to disintegrate. To clear the clog, empty the fuel out of the droplet generator and flow liquid (e.g., methanol) through the nozzle backwards with a syringe.

Hydrostatic pressure in the droplet generator can be varied by changing the elevation of the fuel reservoir relative to the nozzle. During normal operation, the liquid level in the reservoir should be about the same height as the end of the glass nozzle. Some fuels are more sensitive than others to hydrostatic pressure. For example, methyl butanoate proved

to be extremely sensitive, to the point where it was necessary to mount the fuel reservoir on a micrometer-actuated linear stage to make minute adjustments to the elevation of the fuel reservoir. Of course, the hydrostatic pressure can also be changed by adding fuel to the reservoir. It is a good habit to check the drops with the strobe after adding fuel to the reservoir to make sure they are still normal.

The piezoelectric disk is delicate and should be handled carefully. Tiny arcs seen on the ceramic are indicative of cracks and is cause for replacement. When soldering leads to the disk, it is best to keep the solder sites small. Use a soldering iron with a fairly hot setting and try to minimize residence time. Apply the tip of the iron, quickly dab with solder and pull away. The wires should be fine, multiple-filament conductors that are fairly flexible. Try to minimize loads applied to the disk by wires under tension. We hung the wires in a loose coil above the disk.

Image Processing Scripts

This appendix contains the MATLAB scrips used to conduct image processing on the fluorescence images of droplet flames. There are three scripts and were executed in the order in which they appear. The output of the first is the input of the second and the output of the second is the output of the third. The names of the files are:

- xcorr_drop_center_03.m

- avg_fluor_images_AU.m

- fluor_profile_NO_AE.m

```
%xcorr_drop_center_00.m
%Use two dimensional cross correlation to find the droplet in the image.
%Record the location of the droplet and the frame number.

%Torben Grumstrup
%13 Jan 2014

close all
clear all
format compact
clc

FileNameRoot = 'TG2014032015uu_export_';
FilePath = 'C:\PLIF_data\TG20140320\TG2014032015uu\';

%Coordinates of region to zoom in on to better see the droplet.
VertZoom = 212:512;
HorizZoom = 150:549;

%Threashold for peak of cross correlation.
CorrThresh = 9;

%Load image of canonical droplet.  Thsi is the image from frame 36 of
%of the TG20140113154x set.
load('TG2014031713xx_0290_drop');

FrameNum = 290;

%Initialize array to contain frame number and droplet coordinates.
DropCoords = NaN * ones(FrameNum,3);

cc = 1;
figure('Position',[20 200 600 400])
for aa = 1:FrameNum
    clc
    disp(aa)
    %Get droplet PLIF image

    FilePathName = [FilePath, FileNameRoot, num2str(aa, '%04.f'), '.tif'];
    %disp(FilePathName)

    %convert to type double
    framedata = double(imread(FilePathName));

    %flatten image
    imA = flipud(mean(framedata, 3));
```

```matlab
    clear framedata

    %Crop out region of image to examine for droplet location.
    imB = imA(VertZoom, HorizZoom);
    %clear imA

    if 0 %Show pcolor of image.
%        figure('Position',[20 700 600 400])
        h = pcolor(imB);
        set(h,'edgecolor','none')
        title([FileNameRoot(1:14) ': Frame ' num2str(cc)])
        xlabel('y-axis, pixels')
        ylabel('x-axis, pixels')
        pause(.1)
    end

    %Take two-dimensional cross correlation
    NCC = TG_normxcorr2(DropIm,imB);

    %Get index of maximum correlation.
    [max_NCC, imax] = max(abs(NCC(:)));

    %Convert index to coords.  Transpose to actual image.
    [VertPeakNCC, HorizPeakNCC] = ind2sub(size(NCC),imax(1));
    VertDrop = round(VertPeakNCC - 0.5 * size(DropIm, 1)) + VertZoom(1) -1;
    HorizDrop= round(HorizPeakNCC- 0.5 * size(DropIm, 2)) + HorizZoom(1) -
1;


    if 0
        figure('Position',[600 700 600 400])
        surf(NCC), shading flat
    end

    %Calculate a measure of SNR.
    SNR = max_NCC / mean(abs(NCC(:)));

    if SNR > CorrThresh
       DropCoords(cc,:) = [aa HorizDrop VertDrop];
       cc = cc+1;
       if 0 %Show pcolor of image.
           %figure('Position',[500 700 600 400])
           h = pcolor(imA);
           set(h,'edgecolor','none')
           title([FileNameRoot(1:14) ': Frame ' num2str(cc)])
           xlabel('y-axis, pixels')
```

```matlab
            ylabel('x-axis, pixels')
            text(HorizDrop, VertDrop,'+', 'Color', [1 1 1])
          pause(0.0001)
        end
    end
end
DropCoords = DropCoords(1:cc-1,:)

ImageSaveName = 'TG2014032015uu_DropCoords_AA.mat';

if 1
    save(ImageSaveName, 'DropCoords')
    fileattrib(ImageSaveName, '-w') %Clear write permission.
end
```

```matlab
close all
clear all
format compact
clc

%=================================================================
%==================    USER INPUT    =============================
%=================================================================
CropD = 300;    %Half dimension of cropped out image. Final image will
                %   be 2*CropD by 2*CropD.

PadSize = 250;  %Size of zero padding around image so that the crop
                %   doesn't exceed index dimensions.

VertBound = 100; %Boundary of vertical coord of center.  That is,
                %   the droplet has to be within mean of all vertical
                %   coordinates plus or minus VertBound.

SheetFlat = 0; %Variable to control the amount of normalization
                %   carried out by the laser sheet profile.  Zero
                %   corresponds to no change to sheet profile.

BGoffset = 4.62;    %Offset to accomodate bright backgrounds in movies made
                %   after cleaning of filter in DiCam Pro.

%Load doplet center coordinate array.
load('TG2014032015uu_DropCoords_AA.mat');

%Create vars containing path and file name root for fluorescence image.
FileNameRoot = 'TG2014032015uu_export_';
FilePath = 'C:\PLIF_data\TG20140320\TG2014032015uu\';

%Name for saving the averaged fluorescence image.
%SaveName = 'TG2014012715xx_fluor_AA.mat';

%Variables for normalization to laser power.  Units are nV*sec.
Pwr1 = 42.6;      %frames 1-290
Pwr2 = NaN;       %frames 291-580
Pwr3 = NaN;       %frames 581-870
Pwr4 = NaN;       %frames 871-1160

Pwr5 = NaN;         %frames 1161-1450
Pwr6 = NaN;         %frames 1451-1740
Pwr7 = NaN;         %frames 1741-2030
```

```matlab
Pwr8 = NaN;          %frames 2031-2320
%===============================================================
%===============================================================
%===============================================================
%Load background image.
load('TG2014031913vv_background_AA.mat')

%Load laser sheet profile image.
load('TG2014031913vv_profile_AA.mat');
SheetIm = (SheetIm + SheetFlat)/(SheetFlat+1);

if 0
    figure
    plot(SheetIm(:,1))
end



CenterCoords = DropCoords;

%Get length of above array.
Len = length(CenterCoords);

%Calc mean value of vertical coordinates of all droplets.
VertMean = round(mean(DropCoords(:,3)));

%Initialize array to contain summed fluorescence images.
SumIm = zeros(2*CropD+1);

AvgNum = 0;%Initilize variable to keep track of number of frames averaged.
FailNum = 0;%Record number of discarded images.
FailIndex = NaN * ones(Len,1);% Record index of discarded images.
BG_avg    = NaN * ones(Len,1);% Record mean background pixel value.

if 1 %View individual frame
    for cc = 1:Len
        clc
        disp(['Frame number examined:  ' num2str(CenterCoords(cc,1))])
        disp(['Number of frames averaged:  ' num2str(AvgNum)])
        FilePathName = [FilePath, FileNameRoot, num2str(CenterCoords(cc,1),
'%04.f'), '.tif'];
        %disp(FilePathName)

        if (CenterCoords(cc,3) < VertMean + VertBound) && (CenterCoords(cc,
3) > VertMean - VertBound)
            %convert to type double
```

```matlab
framedata = double(imread(FilePathName));

%flatten image by averaging the three color channels of image.
imA = flipud(mean(framedata, 3));
%imA = mean(framedata, 3);

%Subtract off background image from fluorescence image.
imAA = imA - BackgroundIm - BGoffset;

if 1    %Mask out droplet and fluorescence and get average
        %  background pixel count.
    imF = imAA;
    imF(find(imF>0)) = 0; %Set positive pixels to zero.
    ImAvg = mean(imF(:)); %Get mean value

    BG_avg(cc) = ImAvg; %Record mean value

    if 0 %Display masked image and average pixel value.
        h=pcolor(imF);
        set(h,'edgecolor','none')
        axis image
        disp(num2str(ImAvg))
        pause
    end
end

%Set negative pixels to zero.
imAAA= imAA;
imAAA(find(imAAA<0)) = 0;
%imD(find(imD>1.5)) =0
%     figure('Position',[20 700 600 400])
%     h=pcolor(imAA);
%     set(h,'edgecolor','none')
%     break

%Normalize image with laser sheet profile image.
imB = imAAA./ SheetIm;

%Normalize image with laser power for image set.
if CenterCoords(cc,1) < 291
    PNorm = Pwr1;
elseif CenterCoords(cc,1) < 581
    PNorm = Pwr2;
elseif CenterCoords(cc,1) < 871
    PNorm = Pwr3;
elseif CenterCoords(cc,1) < 1161
```

```matlab
                PNorm = Pwr4;
        elseif CenterCoords(cc,1) < 1451
                PNorm = Pwr5;
        elseif CenterCoords(cc,1) < 1741
                PNorm = Pwr6;
        elseif CenterCoords(cc,1) < 2031
                PNorm = Pwr7;
        elseif CenterCoords(cc,1) < 2321
                PNorm = Pwr8;
        else
                PNorm = NaN;
        end

        imC = imB/PNorm;


        %h=pcolor(imA);
        %set(h,'edgecolor','none')

        %Pad image with zeros.
        PadimA = TG_padarray(imC,[PadSize PadSize]);

        %Get coordinates of droplet center.
        DropHorz = round(CenterCoords(cc,2)) + PadSize;
        DropVert = round(CenterCoords(cc,3)) + PadSize;
        %break
        %Crop out part of image with drop at center.
            %when using indeces to crop an image, flip x and y
arguments.
        imE = PadimA(DropVert-CropD:DropVert+CropD, DropHorz-
CropD:DropHorz+CropD);
        %imB = imcrop(imA, [DropX-CropD, DropY-CropD, 2*CropD,
2*CropD]);

        if 0
            %figure('Position',[20 700 600 400])
            h=pcolor(imE);
            set(h,'edgecolor','none')
            pause
        end

        SumIm = SumIm + imE; %Add frame to sum stack.

        AvgNum = AvgNum + 1; %Increment number of frames to average

        BG_avg(AvgNum) = ImAvg; %Record mean value of background
```

```
        else
            FailNum = FailNum + 1;
            FailIndex(FailNum) = cc;
        end
    end
end

FailIndex = FailIndex(1:FailNum);
BG_avg = BG_avg(1:AvgNum);
BG_avg_avg = mean(BG_avg)

if 1 %Normalize summed image and shop bright pixels.
    NormIm = SumIm ./AvgNum;

    imC = NormIm - min(NormIm(:));
    imD = imC;
    pixchop = 1;
    imD(find(imD>pixchop)) = pixchop;
end

if 1 %Display pcolor plot of averaged fluorescence image.
    figure('Position',[20 600 600 400])
    %image(framedata)
    h=pcolor(imD)
    %h=pcolor(280:350,270:340,imA(280:350,270:340))
    set(h,'edgecolor','none')
    %shading interp
    axis image
    title([FileNameRoot(1:14) ': Frame ' num2str(cc)])
    xlabel('y-axis')
    ylabel('x-axis')
end

if 1 %Display autocorrelation of background average vector.
    figure('Position',[600 600 600 400])
    plot(TG_xcorr(BG_avg - mean(BG_avg)));
    title('Auto-correlation of background intensity')
end

ImageSaveName = 'TG2014032015uu_fluor_AA'

if 1 %Save average fluorescence image.
    save([ImageSaveName '.mat'], 'imD')
    fileattrib([ImageSaveName '.mat'], '-w') %Clear write permission.
```

```
    %Create a read only version of this script, recording the settings
    %which created the average fluorescence image saved above.
    ThisMFile = [mfilename]; %Obtains m file name and path
    ScriptBackupName = [ImageSaveName '_' ThisMFile '.dat']
    copyfile([ThisMFile '.m'], ScriptBackupName);
    fileattrib(ScriptBackupName, '-w') %Clear write permission.
end
```

```
%Version: AA
%    Finds the average profile by integrating azimuthally.
%
%Version: AB
%    the size of imX and imY are determined by finding the size of the input
%    image FluorIm.  In this way, they will always be the same.
%
%Version: AC
%    Changed radial distance from which pixel values are gathered.  Want to
%    be able to see more of the background region below fluorescence cloud.
%
%Version: AD
%    Cloned from AC.  In addition to the average contour, find the plus and
%    minus one standard deviation contours as well.  Save these contours.
%
%Version: AE
%    Cloned from AD.  Incorporate code so that the conversion from pixels to
%    microns can be entered.  Also, need to scale average fluorescence
%    contour with respect to radius.  Made 95% confidence contours dashed
%    lines.  Determine the confidence contours with respect to the radius-
%    scaled fluorescence intensity array.  Include code to indicate location
%    of droplet surface on plot.

close all
clear all
format compact
clc

%Indicate fuel of droplet.
%    1 = methanol
%    2 = ethanol
%    3 = 1-propanol
%    4 = n-heptane
%    5 = methyl butanoate
%    6 = methyl decanoate
Fuel = 3;

%Factor to scale data to look nice on plots.
PlotScale = 2.75;

%Load image of averaged fluorescence image.
    FluorFileName = 'TG2014032013uu_fluor_AA.mat';
    load(FluorFileName);
    FluorIm = imD;

    [imX imY] = meshgrid(1:length(FluorIm), 1:length(FluorIm));
```

```matlab
    SumIm = zeros(512,640);
    ctr = [round(.5*size(imD,1)) round(.5*size(imD,2))];

%Get XY-coordinates of each polar point.
    theta  = linspace(210,330,2000);
    radius = linspace(0,250,2000);

%Get radius vector in mm.  See p. 131 of brown lab book.
    radius_mm = radius * 32.6 / 1000;

    [T R] = meshgrid(theta, radius);

    X = ctr(1) + R .* cos(T * pi / 180);
    Y = ctr(2) + R .* sin(T * pi / 180);

%Get value of intensity at each polar point.
    %ZI = interp2(X,Y,Z,XI,YI)
    Z = interp2(imX, imY, FluorIm, X, Y);

%Get cartesian array of fluorescence intensity scaled by radial distance
%the droplet center.
    RScaledZ = Z .* R;

%Obtain the mean contour from cartesian plot.
    MeanC = mean(Z,2);

%Radius-scaled mean fluorescence contour.
    RScaledMeanC1 = mean(RScaledZ,2) * PlotScale;

%Obtain the standard deviation of each row of the stretched out plot.
    Cstd = std(RScaledZ,0,2);

%Obtain the curves for 95% confidence contours (i.e. two std devn.).
    SigmaPlus = RScaledMeanC1 + 2*Cstd;
    SigmaMinus= RScaledMeanC1 - 2*Cstd;

%Get fuel droplet diameter based on user provide fuel identity.  See p.131
%in brown lab book for numerical values.  Quantities are in millimeters.
    switch Fuel
        case 1
            DropDia = 0.584;
        case 2
            DropDia = 0.139;
        case 3
            DropDia = 0.286;
```

```
        case 4
            DropDia = 0.637;
        case 5
            DropDia = 0.593;
        case 6
            DropDia = 0.258;
        otherwise
            DropDia = NaN;
    end

%Determine the index of the vector containing the radial distance which is
%the nearest to or coincident with the droplet surface.
FirstInd = find(radius_mm >= DropDia, 1, 'first')

if 1
    figure('Position',[20 600 600 400])
    %image(framedata)
    pcolor(imX, imY, FluorIm)
    shading flat
    xlabel('y-axis, pixels')
    ylabel('x-axis, pixels')
    axis image
end

if 1 %Plot some representative profiles.
    figure('Position', [570 600 600 400]); hold on
    i1 = 1;
    i2 = 118;
    i3 = 251;
    i4 = 383;
    plot(R(:,i1)/1000,Z(:,i1), 'k')
    plot(R(:,i2)/1000,Z(:,i2), 'r')
    plot(R(:,i3)/1000,Z(:,i3), 'g')
    plot(R(:,i4)/1000,Z(:,i4), 'b')
    plot(R(:,1)/1000,mean(Z,2), 'm')
    hold off
    xlabel('radial distance')
    ylabel('pixel count intensity')
    title('Representative profiles for indicated angles')
    legend('10^o','90^o','180^o','270^o','mean')
    box on
end

if 1
        figure('Position', [20 120 600 400]); hold on
    plot(radius_mm(FirstInd:end), RScaledMeanC1(FirstInd:end), 'k')
```

```
    %plot(radius_mm(FirstInd:end), SigmaPlus(FirstInd:end), '--k')
    %plot(radius_mm(FirstInd:end), SigmaMinus(FirstInd:end), '--k')
    %title(FluorFileName, 'Interpreter', 'none')
    xlabel('radius, [mm]', 'FontName', 'Times')
    ylabel('fluorescence intensity, A.U.', 'FontName', 'Times')
    axis([0 8 -5 100])
end
```

Chemical Kinetic Mechanism: Methyl Butanoate with Full NO$_x$

The following contains the chemical kinetic mechanism for methyl butanoate with full NO$_x$ that was used for the spherically symmetric isolated droplet simulations. Note that the appended nitrogen chemistry begins with reaction 627. The C, C$_2$, and C$_2$O chemistry that was added appears on the last page of the file.

```
--------------------------------------------------------------------------------
                      C
                  P   H
                  H   A
                  A   R
SPECIES           S   G  MOLECULAR  TEMPERATURE  ELEMENT COUNT
CONSIDERED        E   E  WEIGHT     LOW   HIGH     C     H     N     O     AR
--------------------------------------------------------------------------------
  1. O2           G   0  3.1999E+01  300  5000     0     0     0     2     0
  2. CO           G   0  2.8011E+01  300  5000     1     0     0     1     0
  3. CO2          G   0  4.4010E+01  300  5000     1     0     0     2     0
  4. H2O          G   0  1.8015E+01  300  5000     0     2     0     1     0
  5. CH4          G   0  1.6043E+01  300  5000     1     4     0     0     0
  6. C2H4         G   0  2.8054E+01  300  5000     2     4     0     0     0
  7. C3H6         G   0  4.2081E+01  300  5000     3     6     0     0     0
  8. C4H8-1       G   0  5.6108E+01  300  5000     4     8     0     0     0
  9. CH2O         G   0  3.0026E+01  300  5000     1     2     0     1     0
 10. CH3CHO       G   0  4.4054E+01  300  5000     2     4     0     1     0
 11. C2H2         G   0  2.6038E+01  300  5000     2     2     0     0     0
 12. MP2D         G   0  8.6091E+01  300  5000     4     6     0     2     0
 13. MB3D         G   0  1.0012E+02  300  5000     5     8     0     2     0
 14. MB2D         G   0  1.0012E+02  300  5000     5     8     0     2     0
 15. C2H3CHO      G   0  5.6065E+01  300  5000     3     4     0     1     0
 16. C2H5CHO      G   0  5.8081E+01  300  5000     3     6     0     1     0
 17. H            G   0  1.0080E+00  300  5000     0     1     0     0     0
 18. H2           G   0  2.0159E+00  300  5000     0     2     0     0     0
 19. O            G   0  1.5999E+01  300  5000     0     0     0     1     0
 20. OH           G   0  1.7007E+01  300  5000     0     1     0     1     0
 21. N2           G   0  2.8013E+01  300  5000     0     0     2     0     0
 22. HO2          G   0  3.3007E+01  200  3500     0     1     0     2     0
 23. H2O2         G   0  3.4015E+01  300  5000     0     2     0     2     0
 24. AR           G   0  3.9948E+01  300  5000     0     0     0     0     1
 25. HCO          G   0  2.9019E+01  300  5000     1     1     0     1     0
 26. HOCHO        G   0  4.6026E+01  300  5000     1     2     0     2     0
 27. HOCH2O       G   0  4.7034E+01  300  5000     1     3     0     2     0
 28. CH3OH        G   0  3.2042E+01  300  5000     1     4     0     1     0
 29. CH2OH        G   0  3.1034E+01  300  5000     1     3     0     1     0
 30. CH3O         G   0  3.1034E+01  300  5000     1     3     0     1     0
 31. CH3O2H       G   0  4.8042E+01  300  5000     1     4     0     2     0
 32. CH3O2        G   0  4.7034E+01  300  5000     1     3     0     2     0
 33. CH3          G   0  1.5035E+01  300  5000     1     3     0     0     0
 34. CH2          G   0  1.4027E+01  250  4000     1     2     0     0     0
 35. CH2s         G   0  1.4027E+01  300  4000     1     2     0     0     0
 36. CH           G   0  1.3019E+01  300  5000     1     1     0     0     0
 37. C2H6         G   0  3.0070E+01  300  5000     2     6     0     0     0
 38. C2H5         G   0  2.9062E+01  300  5000     2     5     0     0     0
 39. C2H3         G   0  2.7046E+01  300  5000     2     3     0     0     0
 40. C2H          G   0  2.5030E+01  300  5000     2     1     0     0     0
 41. CH3CO        G   0  4.3046E+01  300  5000     2     3     0     1     0
 42. CH2CHO       G   0  4.3046E+01  300  5000     2     3     0     1     0
 43. CH2CO        G   0  4.2038E+01  300  5000     2     2     0     1     0
 44. HCCO         G   0  4.1030E+01  300  4000     2     1     0     1     0
 45. C2H5O        G   0  4.5062E+01  300  5000     2     5     0     1     0
 46. C2H5O2H      G   0  6.2069E+01  300  5000     2     6     0     2     0
 47. C2H5O2       G   0  6.1061E+01  300  5000     2     5     0     2     0
 48. C2H3O1-2     G   0  4.3046E+01  300  5000     2     3     0     1     0
 49. C2H3CO       G   0  5.5057E+01  300  5000     3     3     0     1     0
 50. C2H5CO       G   0  5.7073E+01  300  5000     3     5     0     1     0
 51. C3H8         G   0  4.4097E+01  300  5000     3     8     0     0     0
 52. IC3H7        G   0  4.3089E+01  300  5000     3     7     0     0     0
 53. NC3H7        G   0  4.3089E+01  300  5000     3     7     0     0     0
 54. C3H5-A       G   0  4.1073E+01  300  5000     3     5     0     0     0
 55. C3H5-T       G   0  4.1073E+01  300  5000     3     5     0     0     0
 56. C3H4-P       G   0  4.0065E+01  300  4000     3     4     0     0     0
 57. C3H4-A       G   0  4.0065E+01  300  4000     3     4     0     0     0
 58. C3H3         G   0  3.9057E+01  300  4000     3     3     0     0     0
 59. C3H2         G   0  3.8049E+01  150  4000     3     2     0     0     0
 60. C3H5O        G   0  5.7073E+01  300  5000     3     5     0     1     0
 61. C3H6OOH1-2   G   0  7.5088E+01  300  5000     3     7     0     2     0
 62. C3H6OOH1-3   G   0  7.5088E+01  300  5000     3     7     0     2     0
 63. C3H6OOH2-1   G   0  7.5088E+01  300  5000     3     7     0     2     0
 64. NC3H7O2      G   0  7.5088E+01  300  5000     3     7     0     2     0
 65. IC3H7O2      G   0  7.5088E+01  300  5000     3     7     0     2     0
 66. NC3H7O       G   0  5.9089E+01  300  5000     3     7     0     1     0
 67. C3H6O1-2     G   0  5.8081E+01  300  5000     3     6     0     1     0
 68. C3H6O1-3     G   0  5.8081E+01  300  5000     3     6     0     1     0
 69. CH3CHCO      G   0  5.6065E+01  300  5000     3     4     0     1     0
 70. SC4H9        G   0  5.7116E+01  300  5000     4     9     0     0     0
 71. C4H71-3      G   0  5.5100E+01  300  5000     4     7     0     0     0
 72. C4H6         G   0  5.4092E+01  300  5000     4     6     0     0     0
 73. NC3H7CO      G   0  7.1100E+01  300  5000     4     7     0     1     0
 74. MB           G   0  1.0213E+02  300  5000     5    10     0     2     0
 75. MB2J         G   0  1.0113E+02  300  5000     5     9     0     2     0
 76. MB3J         G   0  1.0113E+02  300  5000     5     9     0     2     0
 77. MB4J         G   0  1.0113E+02  300  5000     5     9     0     2     0
 78. MBMJ         G   0  1.0113E+02  300  5000     5     9     0     2     0
 79. C5H7O2       G   0  9.9110E+01  300  5000     5     7     0     2     0
 80. MB2O         G   0  1.1713E+02  300  5000     5     9     0     3     0
 81. MB3O         G   0  1.1713E+02  300  5000     5     9     0     3     0
```

243

82.	MBMOO	G	0	1.3313E+02	300	5000	5	9	0	4	0
83.	MB2OO	G	0	1.3313E+02	300	5000	5	9	0	4	0
84.	BAOJ	G	0	8.7099E+01	300	5000	4	7	0	2	0
85.	BA4J	G	0	8.7099E+01	300	5000	4	7	0	2	0
86.	MP3J	G	0	8.7099E+01	300	5000	4	7	0	2	0
87.	MP2D3J	G	0	8.5083E+01	300	5000	4	5	0	2	0
88.	MP2D2J	G	0	8.5083E+01	300	5000	4	5	0	2	0
89.	MP2DMJ	G	0	8.5083E+01	300	5000	4	5	0	2	0
90.	ME	G	0	7.4080E+01	300	5000	3	6	0	2	0
91.	ME2J	G	0	7.3072E+01	300	5000	3	5	0	2	0
92.	MEMJ	G	0	7.3072E+01	300	5000	3	5	0	2	0
93.	CH3OCO	G	0	5.9045E+01	300	5000	2	3	0	2	0
94.	CH2CHCHCO	G	0	6.8076E+01	300	5000	4	4	0	1	0
95.	CJHCHCHCO	G	0	6.7068E+01	300	5000	4	3	0	1	0
96.	CH3CHCHO	G	0	5.7073E+01	300	5000	3	5	0	1	0
97.	CH2COOH	G	0	5.9045E+01	300	5000	2	3	0	2	0
98.	C2H3CO2	G	0	7.1056E+01	300	5000	3	3	0	2	0
99.	CN	G	0	2.6018E+01	200	6000	1	0	1	0	0
100.	H2CN	G	0	2.8034E+01	200	6000	1	2	1	0	0
101.	N	G	0	1.4007E+01	200	6000	0	0	1	0	0
102.	NH	G	0	1.5015E+01	200	6000	0	1	1	0	0
103.	HCN	G	0	2.7026E+01	200	6000	1	1	1	0	0
104.	NO	G	0	3.0006E+01	200	6000	0	0	1	1	0
105.	HCNO	G	0	4.3025E+01	250	4000	1	1	1	1	0
106.	HOCN	G	0	4.3025E+01	300	4000	1	1	1	1	0
107.	HNCO	G	0	4.3025E+01	200	6000	1	1	1	1	0
108.	NCO	G	0	4.2017E+01	200	6000	1	0	1	1	0
109.	N2O	G	0	4.4013E+01	200	6000	0	0	2	1	0
110.	NH2	G	0	1.6023E+01	200	6000	0	2	1	0	0
111.	N2O3	G	0	7.6012E+01	200	6000	0	0	2	3	0
112.	HNO	G	0	3.1014E+01	200	6000	0	1	1	1	0
113.	NO2	G	0	4.6005E+01	200	6000	0	0	1	2	0
114.	C2N2	G	0	5.2036E+01	200	6000	2	0	2	0	0
115.	NNH	G	0	2.9021E+01	200	6000	0	1	2	0	0
116.	NH3	G	0	1.7031E+01	200	6000	0	3	1	0	0
117.	N2H2	G	0	3.0029E+01	200	6000	0	2	2	0	0
118.	HONO	G	0	4.7013E+01	200	6000	0	1	1	2	0
119.	NO3	G	0	6.2005E+01	200	6000	0	0	1	3	0
120.	HNO3	G	0	6.3013E+01	200	6000	0	1	1	3	0
121.	N2H3	G	0	3.1037E+01	200	6000	0	3	2	0	0
122.	N2H4	G	0	3.2045E+01	200	6000	0	4	2	0	0
123.	CNN	G	0	4.0025E+01	200	6000	1	0	2	0	0
124.	HCNN	G	0	4.1033E+01	300	5000	1	1	2	0	0
125.	N2O4	G	0	9.2011E+01	200	6000	0	0	2	4	0
126.	NH2OH	G	0	3.3030E+01	200	6000	0	3	1	1	0
127.	HNOH	G	0	3.2022E+01	300	4000	0	2	1	1	0
128.	H2NO	G	0	3.2022E+01	300	4000	0	2	1	1	0
129.	HNNO	G	0	4.5021E+01	300	4000	0	1	2	1	0
130.	HCNH	G	0	2.8034E+01	200	6000	1	2	1	0	0
131.	NCN	G	0	4.0025E+01	200	6000	1	0	2	0	0
132.	HNCN	G	0	4.1033E+01	300	4000	1	1	2	0	0
133.	H2CNO	G	0	4.4403E+01	200	6000	1	2	1	1	0
134.	CH3NO	G	0	4.5041E+01	200	6000	1	3	1	1	0
135.	C	G	0	1.2011E+01	300	5000	1	0	0	0	0
136.	C2O	G	0	4.0022E+01	300	4000	2	0	0	1	0
137.	C2	G	0	2.4022E+01	200	6000	2	0	0	0	0

		(k = A T**b exp(-E/RT))		
REACTIONS CONSIDERED		A	b	E
1. H+O2<=>O+OH		3.55E+15	-0.4	16600.0
Reverse Arrhenius coefficients:		1.03E+13	0.0	-133.0
2. O+H2<=>H+OH		5.08E+04	2.7	6292.0
Reverse Arrhenius coefficients:		2.64E+04	2.7	4880.0
3. OH+H2<=>H+H2O		2.16E+08	1.5	3430.0
Reverse Arrhenius coefficients:		2.29E+09	1.4	18320.0
4. O+H2O<=>OH+OH		2.97E+06	2.0	13400.0
Reverse Arrhenius coefficients:		1.45E+05	2.1	-2904.0
5. H2+M<=>H+H+M		4.58E+19	-1.4	104400.0
Reverse Arrhenius coefficients:		1.14E+20	-1.7	820.0

H2	Enhanced by	2.500E+00
H2O	Enhanced by	1.200E+01
CO	Enhanced by	1.900E+00
CO2	Enhanced by	3.800E+00

| 6. O2+M<=>O+O+M | | 4.42E+17 | -0.6 | 118900.0 |
| Reverse Arrhenius coefficients: | | 6.16E+15 | -0.5 | 0.0 |

H2	Enhanced by	2.500E+00
H2O	Enhanced by	1.200E+01
AR	Enhanced by	8.300E-01
CO	Enhanced by	1.900E+00
CO2	Enhanced by	3.800E+00
CH4	Enhanced by	2.000E+00
C2H6	Enhanced by	3.000E+00

| 7. OH+M<=>O+H+M | | 9.78E+17 | -0.7 | 102100.0 |
| Reverse Arrhenius coefficients: | | 4.71E+18 | -1.0 | 0.0 |

| H2 | Enhanced by | 2.500E+00 |

```
         H2O         Enhanced by    1.200E+01
         AR          Enhanced by    7.500E-01
         CO          Enhanced by    1.500E+00
         CO2         Enhanced by    2.000E+00
         CH4         Enhanced by    2.000E+00
         C2H6        Enhanced by    3.000E+00
  8. H2O+M<=>H+OH+M                                  1.91E+23   -1.8   118500.0
     Reverse Arrhenius coefficients:                4.50E+22   -2.0        0.0
         H2          Enhanced by    7.300E-01
         H2O         Enhanced by    1.200E+01
         AR          Enhanced by    3.800E-01
         CH4         Enhanced by    2.000E+00
         C2H6        Enhanced by    3.000E+00
  9. H+O2(+M)<=>HO2(+M)                              1.48E+12    0.6        0.0
     Low pressure limit:  0.34820E+17 -0.41100E+00 -0.11150E+04
     TROE centering:      0.50000E+00  0.10000E-29  0.10000E+31  0.10000E+11
         H2          Enhanced by    1.300E+00
         H2O         Enhanced by    1.400E+01
         AR          Enhanced by    6.700E-01
         CO          Enhanced by    1.900E+00
         CO2         Enhanced by    3.800E+00
         CH4         Enhanced by    2.000E+00
         C2H6        Enhanced by    3.000E+00
 10. HO2+H<=>H2+O2                                   1.66E+13    0.0      823.0
     Reverse Arrhenius coefficients:                3.17E+12    0.3    55510.0
 11. HO2+H<=>OH+OH                                   7.08E+13    0.0      295.0
     Reverse Arrhenius coefficients:                2.03E+10    0.7    36840.0
 12. HO2+O<=>OH+O2                                   3.25E+13    0.0        0.0
     Reverse Arrhenius coefficients:                3.22E+12    0.3    53280.0
 13. HO2+OH<=>H2O+O2                                 2.89E+13    0.0     -497.0
     Reverse Arrhenius coefficients:                5.84E+13    0.2    69080.0
 14. H2O2+O2<=>HO2+HO2                               1.14E+16   -0.3    49730.0
     Reverse Arrhenius coefficients:                1.03E+14    0.0    11040.0
     Declared duplicate reaction...
 15. H2O2+O2<=>HO2+HO2                               2.14E+13   -0.3    37280.0
     Reverse Arrhenius coefficients:                1.94E+11    0.0    -1409.0
     Declared duplicate reaction...
 16. H2O2(+M)<=>OH+OH(+M)                            2.95E+14    0.0    48430.0
     Low pressure limit:  0.12020E+18  0.00000E+00  0.45500E+05
     TROE centering:      0.50000E+00  0.10000E-29  0.10000E+31  0.10000E+11
         H2          Enhanced by    2.500E+00
         H2O         Enhanced by    1.200E+01
         AR          Enhanced by    6.400E-01
         CO          Enhanced by    1.900E+00
         CO2         Enhanced by    3.800E+00
         CH4         Enhanced by    2.000E+00
         C2H6        Enhanced by    3.000E+00
 17. H2O2+H<=>H2O+OH                                 2.41E+13    0.0     3970.0
     Reverse Arrhenius coefficients:                1.26E+08    1.3    71410.0
 18. H2O2+H<=>H2+HO2                                 2.15E+10    1.0     6000.0
     Reverse Arrhenius coefficients:                3.72E+07    1.7    22000.0
 19. H2O2+O<=>OH+HO2                                 9.55E+06    2.0     3970.0
     Reverse Arrhenius coefficients:                8.57E+03    2.7    18560.0
 20. H2O2+OH<=>H2O+HO2                               2.00E+12    0.0      427.2
     Reverse Arrhenius coefficients:                3.66E+10    0.6    31320.0
     Declared duplicate reaction...
 21. H2O2+OH<=>H2O+HO2                               1.70E+18    0.0    29410.0
     Reverse Arrhenius coefficients:                3.12E+16    0.6    60300.0
     Declared duplicate reaction...
 22. CO+O(+M)<=>CO2(+M)                              1.80E+10    0.0     2384.0
     Low pressure limit:  0.13500E+25 -0.27880E+01  0.41910E+04
         H2          Enhanced by    2.000E+00
         O2          Enhanced by    6.000E+00
         H2O         Enhanced by    6.000E+00
         AR          Enhanced by    5.000E-01
         CO          Enhanced by    1.500E+00
         CO2         Enhanced by    3.500E+00
         CH4         Enhanced by    2.000E+00
         C2H6        Enhanced by    3.000E+00
 23. CO+O2<=>CO2+O                                   1.05E+12    0.0    42540.0
     Reverse Arrhenius coefficients:                8.04E+15   -0.8    51230.0
 24. CO+OH<=>CO2+H                                   1.78E+05    1.9    -1158.0
     Reverse Arrhenius coefficients:                4.72E+11    0.7    24260.0
 25. CO+HO2<=>CO2+OH                                 1.57E+05    2.2    17940.0
     Reverse Arrhenius coefficients:                1.19E+08    1.7    79910.0
 26. HCO+M<=>H+CO+M                                  4.75E+11    0.7    14870.0
     Reverse Arrhenius coefficients:                3.58E+10    1.0     -457.3
         H2          Enhanced by    2.000E+00
         H2O         Enhanced by    1.200E+01
         CO          Enhanced by    1.500E+00
         CO2         Enhanced by    2.000E+00
         CH4         Enhanced by    2.000E+00
         C2H6        Enhanced by    3.000E+00
 27. HCO+O2<=>CO+HO2                                 7.58E+12    0.0      410.0
     Reverse Arrhenius coefficients:                1.20E+12    0.3    33950.0
 28. HCO+H<=>CO+H2                                   7.34E+13    0.0        0.0
     Reverse Arrhenius coefficients:                2.21E+12    0.7    88230.0
 29. HCO+O<=>CO+OH                                   3.02E+13    0.0        0.0
     Reverse Arrhenius coefficients:                4.72E+11    0.6    86820.0
```

```
30. HCO+O<=>CO2+H                                    3.00E+13    0.0        0.0
    Reverse Arrhenius coefficients:                  1.24E+18   -0.6   112200.0
31. HCO+OH<=>CO+H2O                                  1.02E+14    0.0        0.0
    Reverse Arrhenius coefficients:                  3.26E+13    0.6   103100.0
32. HCO+CH3<=>CH4+CO                                 2.65E+13    0.0        0.0
    Reverse Arrhenius coefficients:                  7.29E+14    0.2    89770.0
33. HCO+HO2<=>CH2O+O2                                2.50E+14   -0.1    13920.0
    Reverse Arrhenius coefficients:                  8.07E+15    0.0    53420.0
34. HCO+HO2<=>CO2+H+OH                               3.00E+13    0.0        0.0
    Warning...all REV parameters are zero... 0.000E+00 0.000 0.000E+00
            this reaction will be treated as irreversible
35. CH2O+CO<=>HCO+HCO                                9.19E+13    0.4    73040.0
    Reverse Arrhenius coefficients:                  1.80E+13    0.0        0.0
36. HCO+HCO<=>H2+CO+CO                               3.00E+12    0.0        0.0
    Warning...all REV parameters are zero... 0.000E+00 0.000 0.000E+00
            this reaction will be treated as irreversible
37. HCO+H(+M)<=>CH2O(+M)                             1.09E+12    0.5     -260.0
    Low pressure limit:  0.13500E+25 -0.25700E+01  0.14250E+04
    TROE centering:      0.78240E+00  0.27100E+03  0.27550E+04  0.65700E+04
    H2              Enhanced by    2.000E+00
    H2O             Enhanced by    6.000E+00
    AR              Enhanced by    7.000E-01
    CO              Enhanced by    1.500E+00
    CO2             Enhanced by    2.000E+00
    CH4             Enhanced by    2.000E+00
    C2H6            Enhanced by    3.000E+00
38. CO+H2(+M)<=>CH2O(+M)                             4.30E+07    1.5    79600.0
    Low pressure limit:  0.50700E+28 -0.34200E+01  0.84348E+05
    TROE centering:      0.93200E+00  0.19700E+03  0.15400E+04  0.10300E+05
    H2              Enhanced by    2.000E+00
    H2O             Enhanced by    6.000E+00
    AR              Enhanced by    7.000E-01
    CO              Enhanced by    1.500E+00
    CO2             Enhanced by    2.000E+00
    CH4             Enhanced by    2.000E+00
    C2H6            Enhanced by    3.000E+00
39. CH2O+OH<=>HCO+H2O                                7.82E+07    1.6    -1055.0
    Reverse Arrhenius coefficients:                  4.90E+06    1.8    29030.0
40. CH2O+H<=>HCO+H2                                  5.74E+07    1.9     2740.0
    Reverse Arrhenius coefficients:                  3.39E+05    2.2    17930.0
41. CH2O+O<=>HCO+OH                                  6.26E+09    1.1     2260.0
    Reverse Arrhenius coefficients:                  1.92E+07    1.4    16040.0
42. CH2O+CH3<=>HCO+CH4                               3.83E+01    3.4     4312.0
    Reverse Arrhenius coefficients:                  2.06E+02    3.2    21040.0
43. CH2O+HO2<=>HCO+H2O2                              7.10E-03    4.5     6580.0
    Reverse Arrhenius coefficients:                  2.43E-02    4.1     5769.0
44. CH3O(+M)<=>CH2O+H(+M)                            6.80E+13    0.0    26170.0
    Low pressure limit:  0.18670E+26 -0.30000E+01  0.24307E+05
    TROE centering:      0.90000E+00  0.25000E+04  0.13000E+04  0.10000E+100
    H2              Enhanced by    2.000E+00
    H2O             Enhanced by    6.000E+00
    CO              Enhanced by    1.500E+00
    CO2             Enhanced by    2.000E+00
    CH4             Enhanced by    2.000E+00
    C2H6            Enhanced by    3.000E+00
45. CH3O+O2<=>CH2O+HO2                               4.38E-19    9.5    -5501.0
    Reverse Arrhenius coefficients:                  1.42E-20    9.8    21080.0
46. CH2O+CH3O<=>CH3OH+HCO                            6.62E+11    0.0     2294.0
    Reverse Arrhenius coefficients:                  8.39E+10    0.1    17710.0
47. CH4+CH3O<=>CH3+CH3OH                             6.12E+02    2.9     8248.0
    Reverse Arrhenius coefficients:                  1.44E+01    3.1     6935.0
48. CH3O+CH3<=>CH2O+CH4                              1.20E+13    0.0        0.0
    Reverse Arrhenius coefficients:                  6.75E+13    0.2    82810.0
49. CH3O+H<=>CH2O+H2                                 2.00E+13    0.0        0.0
    Reverse Arrhenius coefficients:                  1.23E+11    0.7    81270.0
50. CH3O+HO2<=>CH2O+H2O2                             3.01E+11    0.0        0.0
    Reverse Arrhenius coefficients:                  1.07E+12    0.0    65270.0
51. CH2O+H(+M)<=>CH2OH(+M)                           5.40E+11    0.5     3600.0
    Low pressure limit:  0.12700E+33 -0.48200E+01  0.65300E+04
    TROE centering:      0.71870E+00  0.10300E+03  0.12910E+04  0.41600E+04
    H2              Enhanced by    2.000E+00
    H2O             Enhanced by    6.000E+00
    CO              Enhanced by    1.500E+00
    CO2             Enhanced by    2.000E+00
    CH4             Enhanced by    2.000E+00
    C2H6            Enhanced by    3.000E+00
52. CH2OH+O2<=>CH2O+HO2                              1.51E+15   -1.0        0.0
    Reverse Arrhenius coefficients:                  1.98E+14   -0.6    20060.0
    Declared duplicate reaction...
53. CH2OH+O2<=>CH2O+HO2                              2.41E+14    0.0     5017.0
    Reverse Arrhenius coefficients:                  3.15E+13    0.4    25080.0
    Declared duplicate reaction...
54. CH2OH+H<=>CH2O+H2                                6.00E+12    0.0        0.0
    Reverse Arrhenius coefficients:                  1.50E+11    0.8    74750.0
55. CH2OH+HO2<=>CH2O+H2O2                            1.20E+13    0.0        0.0
    Reverse Arrhenius coefficients:                  1.73E+14    0.1    58750.0
56. CH2OH+HCO<=>CH2O+CH2O                            1.80E+14    0.0        0.0
    Reverse Arrhenius coefficients:                  7.60E+14    0.5    59560.0
57. CH2OH+CH3O<=>CH2O+CH3OH                          2.40E+13    0.0        0.0
```

246

```
          Reverse Arrhenius coefficients:              1.28E+13    0.6    74980.0
58. OH+CH2OH<=>H2O+CH2O                                2.40E+13    0.0        0.0
          Reverse Arrhenius coefficients:              6.35E+12    0.7    89640.0
59. O+CH2OH<=>OH+CH2O                                  4.20E+13    0.0        0.0
          Reverse Arrhenius coefficients:              5.44E+11    0.7    73340.0
60. CH2O+CH3OH<=>CH2OH+CH2OH                           6.50E+12    0.7    68460.0
          Reverse Arrhenius coefficients:              3.00E+12    0.0        0.0
61. CH2OH+HO2<=>HOCH2O+OH                              1.00E+13    0.0        0.0
          Reverse Arrhenius coefficients:              8.17E+13    0.0    33470.0
62. CH3OH(+M)<=>CH3+OH(+M)                             1.90E+16    0.0    91730.0
     Low pressure limit:  0.29500E+45 -0.73500E+01  0.95460E+05
     TROE centering:      0.41400E+00  0.27900E+03  0.54590E+04  0.10000E+11
63. CH3OH(+M)<=>CH2OH+H(+M)                            2.69E+16   -0.1    98940.0
     Low pressure limit:  0.23400E+41 -0.63300E+01  0.10310E+06
     TROE centering:      0.77300E+00  0.69300E+03  0.53330E+04  0.10000E+11
64. CH3OH+H<=>CH3O+H2                                  3.60E+12    0.0     6095.0
          Reverse Arrhenius coefficients:              1.68E+11    0.2     5868.0
65. CH3OH+H<=>CH2OH+H2                                 1.20E+06    2.4     2583.0
          Reverse Arrhenius coefficients:              1.39E+04    2.5     8871.0
66. CH3OH+O<=>CH2OH+OH                                 3.88E+05    2.5     3080.0
          Reverse Arrhenius coefficients:              2.32E+03    2.6     7956.0
67. CH3OH+OH<=>CH3O+H2O                                5.13E+05    2.1     2450.0
          Reverse Arrhenius coefficients:              2.53E+05    2.2    17120.0
68. CH3OH+OH<=>CH2OH+H2O                               1.44E+06    2.0     -839.0
          Reverse Arrhenius coefficients:              1.76E+05    2.0    20340.0
69. CH3OH+O2<=>CH2OH+HO2                               2.05E+13    0.0    44900.0
          Reverse Arrhenius coefficients:              1.24E+12   -0.2    -3501.0
70. CH3OH+HO2<=>CH2OH+H2O2                             1.08E+04    2.5    10530.0
          Reverse Arrhenius coefficients:              7.20E+04    2.0      819.0
71. CH3OH+CH3<=>CH2OH+CH4                              3.19E+01    3.2     7172.0
          Reverse Arrhenius coefficients:              3.35E+02    2.8    15000.0
72. CH3O+CH3OH<=>CH2OH+CH3OH                           3.00E+11    0.0     4074.0
          Reverse Arrhenius coefficients:              7.42E+10   -0.1    10590.0
73. CH3OH+CH2O<=>CH3O+CH3O                             7.98E+12    0.5    81490.0
          Reverse Arrhenius coefficients:              6.03E+13    0.0        0.0
74. CH3+H(+M)<=>CH4(+M)                                1.27E+16   -0.6      383.0
     Low pressure limit:  0.19816E+34 -0.47600E+01  0.24440E+04
     TROE centering:      0.78300E+00  0.74000E+02  0.29400E+04  0.69600E+04
     H2           Enhanced by    2.000E+00
     H2O          Enhanced by    6.000E+00
     AR           Enhanced by    7.000E-01
     CO           Enhanced by    1.500E+00
     CO2          Enhanced by    2.000E+00
     CH4          Enhanced by    2.000E+00
     C2H6         Enhanced by    3.000E+00
75. CH4+H<=>CH3+H2                                     6.14E+05    2.5     9587.0
          Reverse Arrhenius coefficients:              6.73E+02    2.9     8047.0
76. CH4+OH<=>CH3+H2O                                   5.83E+04    2.6     2190.0
          Reverse Arrhenius coefficients:              6.78E+02    2.9    15540.0
77. CH4+O<=>CH3+OH                                     1.02E+09    1.5     8600.0
          Reverse Arrhenius coefficients:              5.80E+05    1.9     5648.0
78. CH4+HO2<=>CH3+H2O2                                 1.13E+01    3.7    21010.0
          Reverse Arrhenius coefficients:              7.17E+00    3.5     3468.0
79. CH4+CH2<=>CH3+CH3                                  2.46E+06    2.0     8270.0
          Reverse Arrhenius coefficients:              1.74E+06    1.9    12980.0
80. CH3+OH<=>CH2O+H2                                   8.00E+09    0.5    -1755.0
          Reverse Arrhenius coefficients:              1.07E+12    0.3    68210.0
81. CH3+OH<=>CH2s+H2O                                  4.51E+17   -1.3     1417.0
          Reverse Arrhenius coefficients:              1.65E+16   -0.9     1039.0
82. CH3+OH<=>CH3O+H                                    6.94E+07    1.3    11200.0
          Reverse Arrhenius coefficients:              1.50E+12    0.5     -110.0
83. CH3+OH<=>CH2OH+H                                   3.09E+07    1.6     4506.0
          Reverse Arrhenius coefficients:              1.65E+11    0.7     -284.0
84. CH3+OH<=>CH2+H2O                                   5.60E+07    1.6     5420.0
          Reverse Arrhenius coefficients:              9.22E+05    2.1    14060.0
85. CH3+HO2<=>CH3O+OH                                  1.00E+12    0.3     -687.5
          Reverse Arrhenius coefficients:              6.19E+12    0.1    24550.0
86. CH3+HO2<=>CH4+O2                                   1.16E+05    2.2    -3022.0
          Reverse Arrhenius coefficients:              2.02E+07    2.1    53210.0
87. CH3+O<=>CH2O+H                                     5.54E+13    0.1     -136.0
          Reverse Arrhenius coefficients:              3.83E+15   -0.1    68410.0
88. CH3+O2<=>CH3O+O                                    7.55E+12    0.0    28320.0
          Reverse Arrhenius coefficients:              4.72E+14   -0.5      288.0
89. CH3+O2<=>CH2O+OH                                   2.64E+00    3.3     8105.0
          Reverse Arrhenius coefficients:              5.28E-01    3.5    59920.0
90. CH3+O2(+M)<=>CH3O2(+M)                             7.81E+09    0.9        0.0
     Low pressure limit:  0.68500E+25 -0.30000E+01  0.00000E+00
     TROE centering:      0.60000E+00  0.10000E+04  0.70000E+02  0.17000E+04
91. CH3O2+CH2O<=>CH3O2H+HCO                            1.99E+12    0.0    11660.0
          Reverse Arrhenius coefficients:              1.32E+14   -0.9     9259.0
92. CH4+CH3O2<=>CH3+CH3O2H                             1.81E+11    0.0    18480.0
          Reverse Arrhenius coefficients:              2.23E+12   -0.7     -655.0
93. CH3OH+CH3O2<=>CH2OH+CH3O2H                         1.81E+12    0.0    13710.0
          Reverse Arrhenius coefficients:              2.35E+14   -1.0     2404.0
94. CH3O2+CH3<=>CH3O+CH3O                              5.08E+12    0.0    -1411.0
          Reverse Arrhenius coefficients:              1.97E+12    0.2    28070.0
95. CH3O2+HO2<=>CH3O2H+O2                              2.47E+11    0.0    -1570.0
          Reverse Arrhenius coefficients:              5.30E+14   -0.8    35520.0
96. CH3O2+CH3O2<=>CH2O+CH3OH+O2                        3.11E+14   -1.6    -1051.0
```

247

```
        Warning...all REV parameters are zero... 0.000E+00 0.000 0.000E+00
                this reaction will be treated as irreversible
  97. CH3O2+CH3O2<=>O2+CH3O+CH3O            1.40E+16  -1.6    1860.0
        Warning...all REV parameters are zero... 0.000E+00 0.000 0.000E+00
                this reaction will be treated as irreversible
  98. CH3O2+H<=>CH3O+OH                     9.60E+13   0.0       0.0
        Reverse Arrhenius coefficients:     1.72E+09   1.0   40780.0
  99. CH3O2+O<=>CH3O+O2                     3.60E+13   0.0       0.0
        Reverse Arrhenius coefficients:     2.23E+11   0.6   57520.0
 100. CH3O2+OH<=>CH3OH+O2                   6.00E+13   0.0       0.0
        Reverse Arrhenius coefficients:     1.54E+13   0.4   59160.0
 101. CH3O2H<=>CH3O+OH                      6.31E+14   0.0   42300.0
        Reverse Arrhenius coefficients:     2.51E+06   1.9   -2875.0
 102. H2+CH3O2<=>H+CH3O2H                   1.50E+14   0.0   26030.0
        Reverse Arrhenius coefficients:     1.69E+18  -1.1    8434.0
 103. CH2s<=>CH2                            1.00E+13   0.0       0.0
        Reverse Arrhenius coefficients:     4.49E+12   0.0    9020.0
 104. CH2s+CH4<=>CH3+CH3                    1.60E+13   0.0    -570.0
        Reverse Arrhenius coefficients:     5.07E+12  -0.1   13160.0
 105. CH2s+O2<=>CO+OH+H                     7.00E+13   0.0       0.0
        Warning...all REV parameters are zero... 0.000E+00 0.000 0.000E+00
                this reaction will be treated as irreversible
 106. CH2s+H2<=>CH3+H                       7.00E+13   0.0       0.0
        Reverse Arrhenius coefficients:     2.02E+16  -0.6   15270.0
 107. CH2s+H<=>CH2+H                        3.00E+13   0.0       0.0
        Reverse Arrhenius coefficients:     1.35E+13   0.0    9020.0
 108. CH2s+H<=>CH+H2                        3.00E+13   0.0       0.0
        Reverse Arrhenius coefficients:     6.95E+13  -0.3   12480.0
 109. CH2s+O<=>CO+H+H                       3.00E+13   0.0       0.0
        Warning...all REV parameters are zero... 0.000E+00 0.000 0.000E+00
                this reaction will be treated as irreversible
 110. CH2s+OH<=>CH2O+H                      3.00E+13   0.0       0.0
        Reverse Arrhenius coefficients:     1.15E+18  -0.8   85230.0
 111. CH2s+CO2<=>CH2O+CO                    3.00E+12   0.0       0.0
        Reverse Arrhenius coefficients:     4.37E+10   0.4   59810.0
 112. CH2+H(+M)<=>CH3(+M)                   2.50E+16  -0.8       0.0
        Low pressure limit:  0.32000E+28 -0.31400E+01  0.12300E+04
        TROE centering:      0.68000E+00  0.78000E+02  0.19950E+04  0.55900E+04
        H2              Enhanced by    2.000E+00
        H2O             Enhanced by    6.000E+00
        AR              Enhanced by    7.000E-01
        CO              Enhanced by    1.500E+00
        CO2             Enhanced by    2.000E+00
        CH4             Enhanced by    2.000E+00
        C2H6            Enhanced by    3.000E+00
 113. CH2+O2<=>CH2O+O                       2.40E+12   0.0    1500.0
        Reverse Arrhenius coefficients:     5.96E+14  -0.4   60980.0
 114. CH2+O2<=>CO2+H+H                      5.80E+12   0.0    1500.0
        Warning...all REV parameters are zero... 0.000E+00 0.000 0.000E+00
                this reaction will be treated as irreversible
 115. CH2+O2<=>CO+OH+H                      5.00E+12   0.0    1500.0
        Warning...all REV parameters are zero... 0.000E+00 0.000 0.000E+00
                this reaction will be treated as irreversible
 116. CH2+O<=>CO+H+H                        5.00E+13   0.0       0.0
        Warning...all REV parameters are zero... 0.000E+00 0.000 0.000E+00
                this reaction will be treated as irreversible
 117. CH2+H<=>CH+H2                         1.00E+18  -1.6       0.0
        Reverse Arrhenius coefficients:     5.16E+18  -1.8    3460.0
        Declared duplicate reaction...
 118. CH2+H<=>CH+H2                         2.70E+11   0.7   25700.0
        Reverse Arrhenius coefficients:     1.90E+11   0.7   28730.0
        Declared duplicate reaction...
 119. CH2+OH<=>CH+H2O                       1.13E+07   2.0    3000.0
        Reverse Arrhenius coefficients:     6.18E+08   1.7   21350.0
 120. CH+O2<=>HCO+O                         3.30E+13   0.0       0.0
        Reverse Arrhenius coefficients:     9.37E+12   0.2   71210.0
 121. CH+O<=>CO+H                           5.70E+13   0.0       0.0
        Reverse Arrhenius coefficients:     2.77E+15   0.0  176000.0
 122. CH+OH<=>HCO+H                         3.00E+13   0.0       0.0
        Reverse Arrhenius coefficients:     5.07E+14   0.0   88110.0
 123. CH+H2O<=>H+CH2O                       1.71E+13   0.0    -755.0
        Reverse Arrhenius coefficients:     8.37E+14   0.0   57520.0
 124. CH+CO2<=>HCO+CO                       1.70E+12   0.0     685.0
        Reverse Arrhenius coefficients:     2.56E+11   0.0   66460.0
 125. CH3+CH3(+M)<=>C2H6(+M)                9.21E+16  -1.2     635.8
        Low pressure limit:  0.11350E+37 -0.52460E+01  0.17050E+04
        TROE centering:      0.40500E+00  0.11200E+04  0.69600E+02  0.10000E+11
        H2              Enhanced by    2.000E+00
        H2O             Enhanced by    6.000E+00
        AR              Enhanced by    7.000E-01
        CO              Enhanced by    1.500E+00
        CO2             Enhanced by    2.000E+00
        CH4             Enhanced by    2.000E+00
        C2H6            Enhanced by    3.000E+00
 126. C2H5+H(+M)<=>C2H6(+M)                 5.21E+17  -1.0    1580.0
        Low pressure limit:  0.19900E+42 -0.70800E+01  0.66850E+04
        TROE centering:      0.84200E+00  0.12500E+03  0.22190E+04  0.68820E+04
        H2              Enhanced by    2.000E+00
        H2O             Enhanced by    6.000E+00
```

```
          AR              Enhanced by   7.000E-01
          CO              Enhanced by   1.500E+00
          CO2             Enhanced by   2.000E+00
          CH4             Enhanced by   2.000E+00
          C2H6            Enhanced by   3.000E+00
127. C2H6+H<=>C2H5+H2                          1.15E+08    1.9    7530.0
          Reverse Arrhenius coefficients:      1.06E+04    2.6    9760.0
128. C2H6+O<=>C2H5+OH                          3.55E+06    2.4    5830.0
          Reverse Arrhenius coefficients:      1.70E+02    3.1    6648.0
129. C2H6+OH<=>C2H5+H2O                        1.48E+07    1.9     950.0
          Reverse Arrhenius coefficients:      1.45E+04    2.5   18070.0
130. C2H6+O2<=>C2H5+HO2                        6.03E+13    0.0   51870.0
          Reverse Arrhenius coefficients:      2.92E+10    0.3    -593.0
131. C2H6+CH3<=>C2H5+CH4                       5.48E-01    4.0    8280.0
          Reverse Arrhenius coefficients:      4.62E-02    4.2   12050.0
132. C2H6+HO2<=>C2H5+H2O2                      6.92E+01    3.6   16920.0
          Reverse Arrhenius coefficients:      3.70E+00    3.6    3151.0
133. C2H6+CH3O2<=>C2H5+CH3O2H                  1.94E+01    3.6   17100.0
          Reverse Arrhenius coefficients:      2.02E+01    3.2    1734.0
134. C2H6+CH3O<=>C2H5+CH3OH                    2.41E+11    0.0    7090.0
          Reverse Arrhenius coefficients:      4.78E+08    0.5    9547.0
135. C2H6+CH<=>C2H5+CH2                        1.10E+14    0.0    -260.0
          Reverse Arrhenius coefficients:      1.97E+09    0.9   -1490.0
136. CH2s+C2H6<=>CH3+C2H5                      1.20E+14    0.0       0.0
          Reverse Arrhenius coefficients:      3.20E+12    0.1   17500.0
137. C2H4+H(+M)<=>C2H5(+M)                     1.08E+12    0.5    1822.0
          Low pressure limit:  0.12000E+43 -0.76200E+01  0.69700E+04
          TROE centering:       0.97500E+00  0.21000E+03  0.98400E+03  0.43740E+04
          H2              Enhanced by   2.000E+00
          H2O             Enhanced by   6.000E+00
          AR              Enhanced by   7.000E-01
          CO              Enhanced by   1.500E+00
          CO2             Enhanced by   2.000E+00
          CH4             Enhanced by   2.000E+00
          C2H6            Enhanced by   3.000E+00
138. C2H5+C2H3<=>C2H4+C2H4                     6.86E+11    0.1   -4300.0
          Reverse Arrhenius coefficients:      4.82E+14    0.0   71530.0
139. CH3+C2H5<=>CH4+C2H4                       1.18E+04    2.5   -2921.0
          Reverse Arrhenius coefficients:      2.39E+06    2.4   66690.0
140. C2H5+H<=>CH3+CH3                          9.69E+13    0.0     220.0
          Reverse Arrhenius coefficients:      2.03E+09    1.0   10510.0
141. C2H5+H<=>C2H4+H2                          2.00E+12    0.0       0.0
          Reverse Arrhenius coefficients:      4.44E+11    0.4   68070.0
142. C2H5+O<=>CH3CHO+H                         1.10E+14    0.0       0.0
          Reverse Arrhenius coefficients:      1.03E+17   -0.5   77420.0
143. C2H5+HO2<=>C2H5O+OH                       1.10E+13    0.0       0.0
          Reverse Arrhenius coefficients:      9.68E+15   -0.7   27650.0
144. CH3O2+C2H5<=>CH3O+C2H5O                   8.00E+12    0.0   -1000.0
          Reverse Arrhenius coefficients:      4.40E+14   -0.4   30890.0
145. C2H5O+O2<=>CH3CHO+HO2                     4.28E+10    0.0    1097.0
          Reverse Arrhenius coefficients:      1.32E+08    0.6   34130.0
146. C2H5+O2<=>C2H4+HO2                        3.78E+14   -1.0    4749.0
          Reverse Arrhenius coefficients:      4.40E+14   -1.0   18130.0
          Declared duplicate reaction...
147. C2H5+O2<=>C2H4+HO2                        4.00E-01    3.9   13620.0
          Reverse Arrhenius coefficients:      4.66E-01    3.9   27000.0
          Declared duplicate reaction...
148. C2H5+O2<=>CH3CHO+OH                       8.26E+02    2.4    5285.0
          Reverse Arrhenius coefficients:      2.25E+03    2.3   65970.0
149. C2H5O<=>CH3+CH2O                          1.32E+20   -2.0   20750.0
          Reverse Arrhenius coefficients:      3.00E+11    0.0    6336.0
150. C2H5O<=>CH3CHO+H                          5.43E+15   -0.7   22230.0
          Reverse Arrhenius coefficients:      8.00E+12    0.0    6400.0
151. H2+C2H5O2<=>H+C2H5O2H                     1.50E+14    0.0   26030.0
          Reverse Arrhenius coefficients:      1.69E+18   -1.1    8438.0
152. C2H5O2<=>C2H5+O2                          1.31E+62  -14.8   49180.0
          Reverse Arrhenius coefficients:      2.88E+56  -13.8   14620.0
153. C2H5O2+CH2O<=>C2H5O2H+HCO                 1.99E+12    0.0   11660.0
          Reverse Arrhenius coefficients:      1.32E+14   -0.9    9263.0
154. CH4+C2H5O2<=>CH3+C2H5O2H                  1.81E+11    0.0   18480.0
          Reverse Arrhenius coefficients:      2.24E+12   -0.7    -651.0
155. CH3OH+C2H5O2<=>CH2OH+C2H5O2H             1.81E+12    0.0   13710.0
          Reverse Arrhenius coefficients:      2.35E+14   -1.0    2408.0
156. C2H5O2+HO2<=>C2H5O2H+O2                   1.75E+10    0.0   -3275.0
          Reverse Arrhenius coefficients:      3.76E+13   -0.8   33820.0
157. C2H6+C2H5O2<=>C2H5+C2H5O2H                8.60E+00    3.8   17200.0
          Reverse Arrhenius coefficients:      8.96E+00    3.3    1838.0
158. C2H5O2H<=>C2H5O+OH                        6.31E+14    0.0   42300.0
          Reverse Arrhenius coefficients:      5.66E+08    1.0   -1705.0
159. C2H5O2<=>CH3CHO+OH                        2.52E+41  -10.2   43710.0
          Reverse Arrhenius coefficients:      1.50E+36   -9.3   69840.0
160. C2H5O2<=>C2H4+HO2                         1.82E+38   -8.4   37890.0
          Reverse Arrhenius coefficients:      4.63E+32   -7.4   16700.0
161. C2H3O1-2<=>CH3CO                          8.50E+14    0.0   14000.0
          Reverse Arrhenius coefficients:      1.00E+14    0.0   48710.0
162. C2H3O1-2<=>CH2CHO                         1.00E+14    0.0   14000.0
          Reverse Arrhenius coefficients:      1.24E+15   -0.4   44010.0
163. CH3CHO<=>CH3+HCO                          7.69E+20   -1.3   86950.0
          Reverse Arrhenius coefficients:      1.75E+13    0.0       0.0
```

```
164. CH3CHO+H<=>CH3CO+H2                           2.37E+13    0.0    3642.0
     Reverse Arrhenius coefficients:               1.64E+10    0.6   17600.0
165. CH3CHO+O<=>CH3CO+OH                           5.94E+12    0.0    1868.0
     Reverse Arrhenius coefficients:               2.13E+09    0.6   14410.0
166. CH3CHO+OH<=>CH3CO+H2O                         2.00E+06    1.8    1300.0
     Reverse Arrhenius coefficients:               1.35E+06    1.8   32850.0
167. CH3CHO+O2<=>CH3CO+HO2                         3.01E+13    0.0   39150.0
     Reverse Arrhenius coefficients:               1.09E+11    0.3   -1588.0
168. CH3CHO+CH3<=>CH3CO+CH4                        7.08E-04    4.6    1966.0
     Reverse Arrhenius coefficients:               4.47E-04    4.8   17460.0
169. CH3CHO+HO2<=>CH3CO+H2O2                       3.01E+12    0.0   11920.0
     Reverse Arrhenius coefficients:               1.20E+12   -0.1    9877.0
170. CH3O2+CH3CHO<=>CH3O2H+CH3CO                   3.01E+12    0.0   11920.0
     Reverse Arrhenius coefficients:               2.34E+13   -0.5    8282.0
171. CH3CHO+OH<=>CH3+HOCHO                         3.00E+15   -1.1       0.0
     Reverse Arrhenius coefficients:               5.35E+19   -1.7  119800.0
172. CH3CHO+OH<=>CH2CHO+H2O                        1.72E+05    2.4     815.0
     Reverse Arrhenius coefficients:               1.33E+05    2.5   24950.0
173. CH3CO(+M)<=>CH3+CO(+M)                        3.00E+12    0.0   16720.0
     Low pressure limit:  0.12000E+16  0.00000E+00  0.12518E+05
174. CH3CO+H<=>CH2CO+H2                            2.00E+13    0.0       0.0
     Reverse Arrhenius coefficients:               1.04E+13    0.2   60560.0
175. CH3CO+O<=>CH2CO+OH                            2.00E+13    0.0       0.0
     Reverse Arrhenius coefficients:               5.38E+12    0.2   59140.0
176. CH3CO+CH3<=>CH2CO+CH4                         5.00E+13    0.0       0.0
     Reverse Arrhenius coefficients:               2.36E+16   -0.2   62100.0
177. CH2CHO<=>CH2CO+H                              4.07E+15   -0.3   50600.0
     Reverse Arrhenius coefficients:               5.00E+13    0.0   12300.0
178. CH2CHO+O2<=>CH2O+CO+OH                        8.95E+13   -0.6   10120.0
     Warning...all REV parameters are zero... 0.000E+00 0.000 0.000E+00
             this reaction will be treated as irreversible
179. CH2+CO(+M)<=>CH2CO(+M)                        8.10E+11    0.0       0.0
     Low pressure limit:  0.26900E+34 -0.51100E+01  0.70950E+04
     TROE centering:      0.59070E+00  0.27500E+03  0.12260E+04  0.51850E+04
     H2                Enhanced by    2.000E+00
     H2O               Enhanced by    6.000E+00
     AR                Enhanced by    7.000E-01
     CO                Enhanced by    1.500E+00
     CO2               Enhanced by    2.000E+00
     CH4               Enhanced by    2.000E+00
     C2H6              Enhanced by    3.000E+00
180. CH2CO+H<=>CH3+CO                              1.10E+13    0.0    3400.0
     Reverse Arrhenius coefficients:               2.40E+12    0.0   40200.0
181. CH2CO+H<=>HCCO+H2                             2.00E+14    0.0    8000.0
     Reverse Arrhenius coefficients:               1.43E+11    0.5    4520.0
182. CH2CO+O<=>CH2+CO2                             1.75E+12    0.0    1350.0
     Reverse Arrhenius coefficients:               2.85E+09    0.8   49440.0
183. CH2CO+O<=>HCCO+OH                             1.00E+13    0.0    8000.0
     Reverse Arrhenius coefficients:               3.72E+09    0.5    3108.0
184. CH2CO+OH<=>HCCO+H2O                           1.00E+13    0.0    2000.0
     Reverse Arrhenius coefficients:               7.60E+10    0.4   13410.0
185. CH2CO+OH<=>CH2OH+CO                           2.00E+12    0.0   -1010.0
     Reverse Arrhenius coefficients:               8.17E+09    0.5   24530.0
186. CH2s+CH2CO<=>C2H4+CO                          1.60E+14    0.0       0.0
     Reverse Arrhenius coefficients:               3.75E+14    0.2  103400.0
187. CH+CH2O<=>H+CH2CO                             9.46E+13    0.0    -515.0
     Reverse Arrhenius coefficients:               1.62E+15    0.0   69060.0
188. CH+HCCO<=>CO+C2H2                             5.00E+13    0.0       0.0
     Reverse Arrhenius coefficients:               1.72E+17    0.0  164600.0
189. HCCO+OH<=>H2+CO+CO                            1.00E+14    0.0       0.0
     Warning...all REV parameters are zero... 0.000E+00 0.000 0.000E+00
             this reaction will be treated as irreversible
190. H+HCCO<=>CH2s+CO                              1.10E+13    0.0       0.0
     Reverse Arrhenius coefficients:               4.06E+07    1.6   18540.0
191. HCCO+O<=>H+CO+CO                              8.00E+13    0.0       0.0
     Warning...all REV parameters are zero... 0.000E+00 0.000 0.000E+00
             this reaction will be treated as irreversible
192. HCCO+O2<=>OH+CO+CO                            4.20E+10    0.0     850.0
     Warning...all REV parameters are zero... 0.000E+00 0.000 0.000E+00
             this reaction will be treated as irreversible
193. HCCO+M<=>CH+CO+M                              6.50E+15    0.0   58820.0
     Reverse Arrhenius coefficients:               1.39E+11    1.0  -13720.0
194. C2H3+H(+M)<=>C2H4(+M)                         6.08E+12    0.3     280.0
     Low pressure limit:  0.14000E+31 -0.38600E+01  0.33200E+04
     TROE centering:      0.78200E+00  0.20750E+03  0.26630E+04  0.60950E+04
     H2                Enhanced by    2.000E+00
     H2O               Enhanced by    6.000E+00
     AR                Enhanced by    7.000E-01
     CO                Enhanced by    1.500E+00
     CO2               Enhanced by    2.000E+00
     CH4               Enhanced by    2.000E+00
     C2H6              Enhanced by    3.000E+00
195. C2H4(+M)<=>C2H2+H2(+M)                        8.00E+12    0.4   88770.0
     Low pressure limit:  0.70000E+51 -0.93100E+01  0.99860E+05
     TROE centering:      0.73450E+00  0.18000E+03  0.10350E+04  0.54170E+04
     H2                Enhanced by    2.000E+00
     H2O               Enhanced by    6.000E+00
     AR                Enhanced by    7.000E-01
     CO                Enhanced by    1.500E+00
```

```
            CO2              Enhanced by    2.000E+00
            CH4              Enhanced by    2.000E+00
            C2H6             Enhanced by    3.000E+00
196. C2H4+H<=>C2H3+H2                          5.07E+07   1.9   12950.0
     Reverse Arrhenius coefficients:          1.60E+04   2.4    5190.0
197. C2H4+O<=>CH3+HCO                          8.56E+06   1.9     183.0
     Reverse Arrhenius coefficients:          3.30E+02   2.6   26140.0
198. C2H4+O<=>CH2CHO+H                         4.99E+06   1.9     183.0
     Reverse Arrhenius coefficients:          1.54E+09   1.2   18780.0
199. C2H4+OH<=>C2H3+H2O                        1.80E+06   2.0    2500.0
     Reverse Arrhenius coefficients:          6.03E+03   2.4    9632.0
200. C2H4+CH3<=>C2H3+CH4                       6.62E+00   3.7    9500.0
     Reverse Arrhenius coefficients:          1.91E+00   3.8    3280.0
201. C2H4+O2<=>C2H3+HO2                        4.00E+13   0.0   58200.0
     Reverse Arrhenius coefficients:          6.63E+10   0.2   -4249.0
202. C2H4+CH3O<=>C2H3+CH3OH                    1.20E+11   0.0    6750.0
     Reverse Arrhenius coefficients:          8.14E+08   0.3    -783.0
203. C2H4+CH3O2<=>C2H3+CH3O2H                  2.23E+12   0.0   17190.0
     Reverse Arrhenius coefficients:          7.93E+12  -0.6   -8167.0
204. C2H4+C2H5O2<=>C2H3+C2H5O2H                2.23E+12   0.0   17190.0
     Reverse Arrhenius coefficients:          7.94E+12  -0.6   -8163.0
205. CH+CH4<=>C2H4+H                           6.00E+13   0.0       0.0
     Reverse Arrhenius coefficients:          3.57E+14   0.0   55480.0
206. CH2s+CH3<=>C2H4+H                         2.00E+13   0.0       0.0
     Reverse Arrhenius coefficients:          6.13E+19  -1.2   73050.0
207. C2H2+H(+M)<=>C2H3(+M)                     3.11E+11   0.6    2589.0
     Low pressure limit:  0.22540E+41 -0.72690E+01  0.65770E+04
     TROE centering:      0.10000E+01  0.10000E-14  0.67500E+03  0.10000E+16
            H2               Enhanced by    2.000E+00
            H2O              Enhanced by    5.000E+00
            CO               Enhanced by    2.000E+00
            CO2              Enhanced by    3.000E+00
208. C2H3+O2<=>C2H2+HO2                        1.34E+06   1.6    -384.0
209. C2H3+O2<=>CH2O+HCO                        4.58E+16  -1.4    1015.0
210. C2H3+O2<=>CH2CHO+O                        1.00E+11   0.3      11.0
211. CH3+C2H3<=>CH4+C2H2                       3.92E+11   0.0       0.0
     Reverse Arrhenius coefficients:          3.50E+14  -0.2   70780.0
212. C2H3+H<=>C2H2+H2                          9.64E+13   0.0       0.0
     Reverse Arrhenius coefficients:          9.43E+13   0.3   69240.0
213. C2H3+OH<=>C2H2+H2O                        3.01E+13   0.0       0.0
     Reverse Arrhenius coefficients:          3.12E+14   0.1   84130.0
214. C2H+H(+M)<=>C2H2(+M)                      1.00E+17   0.0       0.0
     Low pressure limit:  0.37500E+34 -0.48000E+01  0.19000E+04
     TROE centering:      0.64600E+00  0.13200E+03  0.13150E+04  0.55660E+04
            H2               Enhanced by    2.000E+00
            H2O              Enhanced by    6.000E+00
            AR               Enhanced by    7.000E-01
            CO               Enhanced by    1.500E+00
            CO2              Enhanced by    2.000E+00
            CH4              Enhanced by    2.000E+00
            C2H6             Enhanced by    3.000E+00
215. C2H2+O2<=>HCCO+OH                         2.00E+08   1.5   30100.0
     Reverse Arrhenius coefficients:          2.23E+05   1.5   25400.0
216. O+C2H2<=>C2H+OH                           4.60E+19  -1.4   28950.0
     Reverse Arrhenius coefficients:          3.02E+15  -0.6   -1782.0
217. C2H2+O<=>CH2+CO                           6.12E+06   2.0    1900.0
     Reverse Arrhenius coefficients:          1.15E+06   2.0   52570.0
218. C2H2+O<=>HCCO+H                           1.43E+07   2.0    1900.0
     Reverse Arrhenius coefficients:          2.02E+05   2.0   13310.0
219. C2H2+OH<=>C2H+H2O                         3.37E+07   2.0   14000.0
     Reverse Arrhenius coefficients:          4.52E+04   2.7    -428.0
220. C2H2+OH<=>CH2CO+H                         2.19E-04   4.5   -1000.0
     Reverse Arrhenius coefficients:          2.16E-03   4.5   19670.0
221. C2H2+OH<=>CH3+CO                          4.83E-04   4.0   -2000.0
     Reverse Arrhenius coefficients:          3.49E-06   4.6   52120.0
222. C2H3CHO<=>C2H3+HCO                        2.00E+24  -2.1  103400.0
     Reverse Arrhenius coefficients:          1.81E+13   0.0       0.0
223. C2H3CHO+H<=>C2H3CO+H2                     1.34E+13   0.0    3300.0
     Reverse Arrhenius coefficients:          3.31E+10   0.6   22680.0
224. C2H3CHO+O<=>C2H3CO+OH                     5.94E+12   0.0    1868.0
     Reverse Arrhenius coefficients:          7.62E+09   0.6   19840.0
225. C2H3CHO+OH<=>C2H3CO+H2O                   9.24E+06   1.5    -962.0
     Reverse Arrhenius coefficients:          2.42E+05   2.0   33310.0
226. C2H3CHO+O2<=>C2H3CO+HO2                   1.00E+13   0.0   40700.0
     Reverse Arrhenius coefficients:          1.30E+11   0.3    5391.0
227. C2H3CHO+HO2<=>C2H3CO+H2O2                 3.01E+12   0.0   11920.0
     Reverse Arrhenius coefficients:          4.30E+12  -0.1   15300.0
228. C2H3CHO+CH3<=>C2H3CO+CH4                  2.61E+06   1.8    5911.0
     Reverse Arrhenius coefficients:          5.88E+06   1.9   26830.0
229. C2H3CHO+C2H3<=>C2H3CO+C2H4               1.74E+12   0.0    8440.0
     Reverse Arrhenius coefficients:          1.00E+13   0.0   28000.0
230. C2H3CHO+CH3O<=>C2H3CO+CH3OH              1.00E+12   0.0    3300.0
     Reverse Arrhenius coefficients:          5.30E+10   0.4   22910.0
231. C2H3CHO+CH3O2<=>C2H3CO+CH3O2H           3.01E+12   0.0   11920.0
     Reverse Arrhenius coefficients:          8.37E+13  -0.5   13710.0
232. C2H3CO<=>C2H3+CO                          1.37E+21  -2.2   39410.0
     Reverse Arrhenius coefficients:          1.51E+11   0.0    4810.0
233. C2H5CHO<=>C2H5+HCO                        1.50E+27  -3.2   87040.0
     Reverse Arrhenius coefficients:          1.81E+13   0.0       0.0
```

251

```
234. C2H5CHO+H<=>C2H5CO+H2                          4.00E+13    0.0     4200.0
     Reverse Arrhenius coefficients:               2.38E+10    0.7    18130.0
235. C2H5CHO+O<=>C2H5CO+OH                          5.00E+12    0.0     1790.0
     Reverse Arrhenius coefficients:               1.54E+09    0.6    14310.0
236. C2H5CHO+OH<=>C2H5CO+H2O                        2.69E+10    0.8     -340.0
     Reverse Arrhenius coefficients:               1.70E+08    1.3    28480.0
237. C2H5CHO+CH3<=>C2H5CO+CH4                       2.61E+06    1.8     5911.0
     Reverse Arrhenius coefficients:               1.41E+06    2.0    21380.0
238. C2H5CHO+HO2<=>C2H5CO+H2O2                      2.80E+12    0.0    13600.0
     Reverse Arrhenius coefficients:               9.63E+11    0.0    11530.0
239. C2H5CHO+CH3O<=>C2H5CO+CH3OH                    1.00E+12    0.0     3300.0
     Reverse Arrhenius coefficients:               1.28E+10    0.4    17460.0
240. C2H5CHO+CH3O2<=>C2H5CO+CH3O2H                  3.01E+12    0.0    11920.0
     Reverse Arrhenius coefficients:               2.01E+13   -0.5     8260.0
241. C2H5CHO+C2H5<=>C2H5CO+C2H6                     1.00E+12    0.0     8000.0
     Reverse Arrhenius coefficients:               6.43E+12    0.0    19700.0
242. C2H5CHO+C2H5O2<=>C2H5CO+C2H5O2H                3.01E+12    0.0    11920.0
     Reverse Arrhenius coefficients:               2.02E+13   -0.5     8264.0
243. C2H5CHO+O2<=>C2H5CO+HO2                        1.00E+13    0.0    40700.0
     Reverse Arrhenius coefficients:               3.13E+10    0.3      -58.0
244. C2H5CHO+C2H3<=>C2H5CO+C2H4                     1.70E+12    0.0     8440.0
     Reverse Arrhenius coefficients:               3.20E+12    0.1    30130.0
245. C2H5CO<=>C2H5+CO                               2.46E+23   -3.2    17550.0
     Reverse Arrhenius coefficients:               1.51E+11    0.0     4810.0
246. HOCH2O<=>CH2O+OH                               2.06E+21   -2.3    25730.0
     Reverse Arrhenius coefficients:               4.50E+15   -1.1        0.0
247. HOCH2O<=>HOCHO+H                               1.00E+14    0.0    14900.0
     Reverse Arrhenius coefficients:               1.12E+15   -0.3    11500.0
248. HOCHO<=>CO+H2O                                 2.45E+12    0.0    60470.0
     Reverse Arrhenius coefficients:               2.26E+03    2.1    52890.0
249. HOCHO<=>CO2+H2                                 2.95E+09    0.0    48520.0
     Reverse Arrhenius coefficients:               6.77E+05    1.0    51470.0
250. HOCHO<=>HCO+OH                                 3.47E+22   -1.5   110700.0
     Reverse Arrhenius coefficients:               1.00E+14    0.0        0.0
251. HOCHO+OH<=>H2O+CO2+H                           2.62E+06    2.1      916.0
     Warning...all REV parameters are zero... 0.000E+00 0.000 0.0
             this reaction will be treated as irreversible
252. HOCHO+OH<=>H2O+CO+OH                           1.85E+07    1.5     -962.0
     Warning...all REV parameters are zero... 0.000E+00 0.000 0.0
             this reaction will be treated as irreversible
253. HOCHO+H<=>H2+CO2+H                             4.24E+06    2.1     4868.0
     Warning...all REV parameters are zero... 0.000E+00 0.000 0.0
             this reaction will be treated as irreversible
254. HOCHO+H<=>H2+CO+OH                             6.03E+13   -0.3     2988.0
     Warning...all REV parameters are zero... 0.000E+00 0.000 0.0
             this reaction will be treated as irreversible
255. HOCHO+CH3<=>CH4+CO+OH                          3.90E-07    5.8     2200.0
     Warning...all REV parameters are zero... 0.000E+00 0.000 0.0
             this reaction will be treated as irreversible
256. HOCHO+HO2<=>H2O2+CO+OH                         1.00E+12    0.0    11920.0
     Warning...all REV parameters are zero... 0.000E+00 0.000 0.0
             this reaction will be treated as irreversible
257. HOCHO+O<=>CO+OH+OH                             1.77E+18   -1.9     2975.0
     Warning...all REV parameters are zero... 0.000E+00 0.000 0.0
             this reaction will be treated as irreversible
258. CH3+CO2<=>CH3OCO                               4.76E+07    1.5    34700.0
259. CH3O+CO<=>CH3OCO                               1.55E+06    2.0     5730.0
260. C3H8(+M)<=>CH3+C2H5(+M)                        1.29E+37   -5.8    97380.0
     Low pressure limit:  0.56400E+75 -0.15740E+02  0.98714E+05
     TROE centering:      0.31000E+00  0.50000E+02  0.30000E+04  0.90000E+04
     H2              Enhanced by    2.000E+00
     H2O             Enhanced by    6.000E+00
     AR              Enhanced by    7.000E-01
     CO              Enhanced by    1.500E+00
     CO2             Enhanced by    2.000E+00
     CH4             Enhanced by    2.000E+00
     C2H6            Enhanced by    3.000E+00
261. C3H8<=>NC3H7+H                                 3.75E+17   -0.4   101200.0
     Reverse Arrhenius coefficients:               1.00E+14    0.0        0.0
262. C3H8<=>IC3H7+H                                 2.38E+18   -0.7    98680.0
     Reverse Arrhenius coefficients:               1.00E+14    0.0        0.0
263. C3H8+O2<=>IC3H7+HO2                            2.00E+13    0.0    49640.0
     Reverse Arrhenius coefficients:               1.76E+09    0.6     -169.0
264. C3H8+O2<=>NC3H7+HO2                            6.00E+13    0.0    52290.0
     Reverse Arrhenius coefficients:               3.35E+10    0.3      -59.0
265. H+C3H8<=>H2+IC3H7                              1.30E+06    2.4     4471.0
     Reverse Arrhenius coefficients:               2.19E+01    3.3     9351.0
266. H+C3H8<=>H2+NC3H7                              3.49E+05    2.7     6450.0
     Reverse Arrhenius coefficients:               3.72E+01    3.3     8790.0
267. C3H8+O<=>IC3H7+OH                              5.49E+05    2.5     3140.0
     Reverse Arrhenius coefficients:               4.79E+00    3.4     6608.0
268. C3H8+O<=>NC3H7+OH                              3.71E+06    2.4     5505.0
     Reverse Arrhenius coefficients:               2.05E+02    3.0     6433.0
269. C3H8+OH<=>NC3H7+H2O                            1.05E+10    1.0     1586.0
     Reverse Arrhenius coefficients:               1.19E+07    1.5    18820.0
270. C3H8+OH<=>IC3H7+H2O                            4.67E+07    1.6      -35.0
     Reverse Arrhenius coefficients:               8.33E+03    2.5    19740.0
271. C3H8+HO2<=>IC3H7+H2O2                          6.32E+01    3.4    13720.0
     Reverse Arrhenius coefficients:               6.15E-01    3.6     2598.0
```

```
272. C3H8+HO2<=>NC3H7+H2O2                           4.08E+01    3.6    17160.0
     Reverse Arrhenius coefficients:                 2.52E+00    3.5     3500.0
273. CH3+C3H8<=>CH4+IC3H7                            6.40E+04    2.2     7520.0
     Reverse Arrhenius coefficients:                 9.82E+02    2.7    13940.0
274. CH3+C3H8<=>CH4+NC3H7                            9.04E-01    3.6     7154.0
     Reverse Arrhenius coefficients:                 8.79E-02    3.8    11030.0
275. IC3H7+C3H8<=>NC3H7+C3H8                         3.00E+10    0.0    12900.0
     Reverse Arrhenius coefficients:                 3.00E+10    0.0    12900.0
276. C2H3+C3H8<=>C2H4+IC3H7                          1.00E+11    0.0    10400.0
     Reverse Arrhenius coefficients:                 1.31E+11    0.0    17800.0
277. C2H3+C3H8<=>C2H4+NC3H7                          1.00E+11    0.0    10400.0
     Reverse Arrhenius coefficients:                 1.31E+11    0.0    17800.0
278. C2H5+C3H8<=>C2H6+IC3H7                          1.00E+11    0.0    10400.0
     Reverse Arrhenius coefficients:                 3.63E+10    0.0     9934.0
279. C2H5+C3H8<=>C2H6+NC3H7                          1.00E+11    0.0    10400.0
     Reverse Arrhenius coefficients:                 3.63E+10    0.0     9934.0
280. C3H8+C3H5-A<=>NC3H7+C3H6                        7.94E+11    0.0    20500.0
     Reverse Arrhenius coefficients:                 5.37E+16   -1.3    13400.0
281. C3H8+C3H5-A<=>IC3H7+C3H6                        7.94E+11    0.0    16200.0
     Reverse Arrhenius coefficients:                 5.37E+16   -1.3     9095.0
282. C3H8+CH3O<=>NC3H7+CH3OH                         3.00E+11    0.0     7000.0
     Reverse Arrhenius coefficients:                 1.22E+10    0.0     9182.0
283. C3H8+CH3O<=>IC3H7+CH3OH                         3.00E+11    0.0     7000.0
     Reverse Arrhenius coefficients:                 1.22E+10    0.0     9182.0
284. CH3O2+C3H8<=>CH3O2H+NC3H7                       1.39E+00    4.0    18280.0
     Reverse Arrhenius coefficients:                 1.66E+00    3.5     3024.0
285. CH3O2+C3H8<=>CH3O2H+IC3H7                       1.02E+01    3.6    14810.0
     Reverse Arrhenius coefficients:                 1.93E+00    3.4     2090.0
286. C2H5O2+C3H8<=>C2H5O2H+NC3H7                     1.39E+00    4.0    18280.0
     Reverse Arrhenius coefficients:                 1.67E+00    3.5     3028.0
287. C2H5O2+C3H8<=>C2H5O2H+IC3H7                     1.02E+01    3.6    14810.0
     Reverse Arrhenius coefficients:                 1.93E+00    3.4     2094.0
288. IC3H7<=>H+C3H6                                  6.92E+13    0.0    37690.0
     Reverse Arrhenius coefficients:                 2.64E+13    0.0     2160.0
289. IC3H7+H<=>C2H5+CH3                              2.00E+13    0.0        0.0
     Reverse Arrhenius coefficients:                 4.34E+07    1.2     8620.0
290. IC3H7+O2<=>C3H6+HO2                             4.50E-19    0.0     5020.0
     Reverse Arrhenius coefficients:                 2.00E-19    0.0    17500.0
291. IC3H7+OH<=>C3H6+H2O                             2.41E+13    0.0        0.0
     Reverse Arrhenius coefficients:                 2.98E+12    0.6    83820.0
292. IC3H7+O<=>CH3CHO+CH3                            4.82E+13    0.0        0.0
     Reverse Arrhenius coefficients:                 1.28E+11    0.8    86480.0
293. IC3H7+C2H5CHO<=>C2H5CO+C3H8                     1.70E+12    0.0     8440.0
     Reverse Arrhenius coefficients:                 1.90E+14    0.0    18790.0
294. NC3H7<=>CH3+C2H4                                9.97E+40   -8.6    41430.0
     Reverse Arrhenius coefficients:                 1.90E+34   -7.0    17100.0
295. NC3H7<=>H+C3H6                                  8.78E+39   -8.1    46580.0
     Reverse Arrhenius coefficients:                 2.07E+37   -7.4    12020.0
296. NC3H7+O2<=>C3H6+HO2                             3.00E-19    0.0     3000.0
     Reverse Arrhenius coefficients:                 2.00E-19    0.0    17500.0
297. C2H5CHO+NC3H7<=>C2H5CO+C3H8                     1.70E+12    0.0     8440.0
     Reverse Arrhenius coefficients:                 1.90E+14    0.0    18790.0
298. C2H5CHO+C3H5-A<=>C2H5CO+C3H6                    1.70E+12    0.0     8440.0
     Reverse Arrhenius coefficients:                 1.00E+13    0.0    28000.0
299. C2H3+CH3(+M)<=>C3H6(+M)                         2.50E+13    0.0        0.0
     Low pressure limit:  0.42700E+59 -0.11940E+02  0.97698E+04
     TROE centering:      0.17500E+00  0.13406E+04  0.60000E+05  0.10140E+05
300. C3H6<=>C3H5-A+H                                 2.01E+61  -13.3   118500.0
     Reverse Arrhenius coefficients:                 2.04E+61  -13.5    30610.0
301. C3H6<=>C3H5-T+H                                 5.62E+71  -16.6   139300.0
     Reverse Arrhenius coefficients:                 4.26E+68  -16.2    30080.0
302. C3H6+O<=>C2H5+HCO                               1.58E+07    1.8    -1216.0
     Reverse Arrhenius coefficients:                 9.19E+01    2.7    23110.0
303. C3H6+O<=>CH2CO+CH3+H                            2.50E+07    1.8       76.0
     Warning...all REV parameters are zero... 0.000E+00 0.000 0.000E+00
              this reaction will be treated as irreversible
304. C3H6+O<=>CH3CHCO+H+H                            2.50E+07    1.8       76.0
     Warning...all REV parameters are zero... 0.000E+00 0.000 0.000E+00
              this reaction will be treated as irreversible
305. C3H6+O<=>C3H5-A+OH                              5.24E+11    0.7     5884.0
     Reverse Arrhenius coefficients:                 1.10E+11    0.7    20150.0
306. C3H6+O<=>C3H5-T+OH                              6.03E+10    0.7     7632.0
     Reverse Arrhenius coefficients:                 9.48E+06    1.4      576.0
307. C3H6+OH<=>C3H5-A+H2O                            3.12E+06    2.0     -298.0
     Reverse Arrhenius coefficients:                 1.34E+07    1.9    30270.0
308. C3H6+OH<=>C3H5-T+H2O                            1.11E+06    2.0     1451.0
     Reverse Arrhenius coefficients:                 3.56E+03    2.6    10700.0
309. C3H6+HO2<=>C3H5-A+H2O2                          2.70E+04    2.5    12340.0
     Reverse Arrhenius coefficients:                 6.34E+06    1.8    12010.0
310. C3H6+HO2<=>C3H5-T+H2O2                          9.00E+03    2.5    23590.0
     Reverse Arrhenius coefficients:                 1.58E+03    2.5     1941.0
311. C3H6+H<=>C3H5-A+H2                              1.73E+05    2.5     2492.0
     Reverse Arrhenius coefficients:                 7.02E+04    2.5    18170.0
312. C3H6+H<=>C3H5-T+H2                              4.05E+05    2.5     9794.0
     Reverse Arrhenius coefficients:                 1.23E+02    3.2     4150.0
313. C3H6+H<=>C2H4+CH3                               2.30E+13    0.0     2547.0
     Reverse Arrhenius coefficients:                 7.27E+07    1.3    11200.0
314. C3H6+O2<=>C3H5-A+HO2                            4.00E+12    0.0    39900.0
     Reverse Arrhenius coefficients:                 8.51E+12   -0.3      887.0
```

253

```
315. C3H6+O2<=>C3H5-T+HO2                     1.40E+12    0.0   60700.0
     Reverse Arrhenius coefficients:          2.22E+09    0.3     369.0
316. C3H6+CH3<=>C3H5-A+CH4                     2.21E+00    3.5    5675.0
     Reverse Arrhenius coefficients:          8.18E+02    3.1   22890.0
317. C3H6+CH3<=>C3H5-T+CH4                     8.40E-01    3.5   11660.0
     Reverse Arrhenius coefficients:          2.32E-01    3.7    7552.0
318. C3H6+C2H5<=>C3H5-A+C2H6                   1.00E+11    0.0    9800.0
     Reverse Arrhenius coefficients:          5.37E+05    1.3   16440.0
319. C3H6+CH3O2<=>C3H5-A+CH3O2H               3.24E+11    0.0   14900.0
     Reverse Arrhenius coefficients:          2.00E+10    0.0   15000.0
320. C3H6+HO2<=>C3H6O1-2+OH                    1.29E+12    0.0   14900.0
     Reverse Arrhenius coefficients:          1.00E-10    0.0       0.0
321. C3H6+C2H5O2<=>C3H5-A+C2H5O2H             3.24E+11    0.0   14900.0
     Reverse Arrhenius coefficients:          2.00E+10    0.0   15000.0
322. C3H5-A<=>C2H2+CH3                         2.40E+48   -9.9   82080.0
     Reverse Arrhenius coefficients:          2.61E+46   -9.8   36950.0
323. C3H5-A<=>C3H4-A+H                         4.19E+13    0.2   61930.0
     Reverse Arrhenius coefficients:          2.40E+11    0.7    3007.0
324. C3H5-A+HO2<=>C3H5O+OH                     7.00E+12    0.0   -1000.0
     Reverse Arrhenius coefficients:          1.60E+12    0.1   11660.0
325. C3H5-A+CH3O2<=>C3H5O+CH3O                7.00E+12    0.0   -1000.0
     Reverse Arrhenius coefficients:          1.99E+15   -0.7   17020.0
326. C3H5-A+H<=>C3H4-A+H2                      1.23E+03    3.0    2582.0
     Reverse Arrhenius coefficients:          2.82E+00    3.8   47220.0
327. C3H5-A+CH3<=>C3H4-A+CH4                   1.00E+11    0.0       0.0
     Reverse Arrhenius coefficients:          4.92E+12    0.1   47780.0
328. C3H5-A+C2H5<=>C2H6+C3H4-A                 4.00E+11    0.0       0.0
     Reverse Arrhenius coefficients:          1.80E+12    0.1   40330.0
329. C3H5-A+C2H3<=>C2H4+C3H4-A                 1.00E+12    0.0       0.0
     Reverse Arrhenius coefficients:          1.62E+13    0.1   48190.0
330. C3H5-A+O2<=>C3H4-A+HO2                    2.18E+21   -2.9   30760.0
     Reverse Arrhenius coefficients:          2.61E+19   -2.4   20710.0
331. C3H4-A+C3H6<=>C3H5-A+C3H5-A               4.75E+08    0.7   28700.0
     Reverse Arrhenius coefficients:          8.43E+10    0.0    -262.0
332. C3H5-A+C2H5<=>C2H4+C3H6                   4.00E+11    0.0       0.0
     Reverse Arrhenius coefficients:          6.94E+16   -1.3   52800.0
333. C3H5-A+O2<=>CH2CHO+CH2O                   7.14E+15   -1.2   21050.0
     Reverse Arrhenius coefficients:          4.94E+16   -1.4   88620.0
334. C3H5-A+O2<=>C2H3CHO+OH                    2.47E+13   -0.4   23020.0
     Reverse Arrhenius coefficients:          1.99E+13   -0.6   75140.0
335. C3H5-A+O2<=>C2H2+CH2O+OH                  9.72E+29   -5.7   21450.0
     Warning...all REV parameters are zero... 0.000E+00 0.000 0.000E+00
             this reaction will be treated as irreversible
336. C3H5-T<=>C2H2+CH3                         2.16E+40   -8.3   45110.0
     Reverse Arrhenius coefficients:          1.61E+40   -8.6   20330.0
337. C3H5-T<=>C3H4-A+H                         3.51E+14   -0.4   40890.0
     Reverse Arrhenius coefficients:          8.50E+12    0.0    2000.0
338. C3H5-T<=>C3H4-P+H                         1.08E+15   -0.6   38490.0
     Reverse Arrhenius coefficients:          6.50E+12    0.0    2000.0
339. C3H5-T+O2<=>C3H4-A+HO2                    1.89E+30   -5.6   15540.0
     Reverse Arrhenius coefficients:          3.04E+31   -5.9   26810.0
340. C3H5-T+O2<=>CH2O+CH3CO                    3.71E+25   -4.0    7043.0
     Reverse Arrhenius coefficients:          1.87E+27   -4.4  101200.0
341. C3H5-T+H<=>C3H4-P+H2                      3.33E+12    0.0       0.0
     Reverse Arrhenius coefficients:          2.14E+16   -0.9   71050.0
342. C3H5-T+CH3<=>C3H4-P+CH4                   1.00E+11    0.0       0.0
     Reverse Arrhenius coefficients:          1.68E+16   -0.9   71530.0
343. C3H4-A+M<=>C3H3+H+M                       1.14E+17    0.0   70000.0
     Reverse Arrhenius coefficients:          1.80E+15   -0.4   10610.0
344. C3H4-A<=>C3H4-P                           1.20E+15    0.0   92400.0
     Reverse Arrhenius coefficients:          3.22E+18   -1.0   96590.0
345. C3H4-A+O2<=>C3H3+HO2                      4.00E+13    0.0   39160.0
     Reverse Arrhenius coefficients:          3.17E+11   -0.1     311.0
346. C3H4-A+HO2<=>CH2CO+CH2+OH                 4.00E+12    0.0   19000.0
     Reverse Arrhenius coefficients:          1.00E+00    0.0       0.0
347. C3H4-A+OH<=>CH2CO+CH3                     3.12E+12    0.0    -397.0
     Reverse Arrhenius coefficients:          1.81E+17   -1.4   36070.0
348. C3H4-A+OH<=>C3H3+H2O                      1.00E+07    2.0    1000.0
     Reverse Arrhenius coefficients:          1.60E+05    2.2   31730.0
349. C3H4-A+O<=>C2H4+CO                        7.80E+12    0.0    1600.0
     Reverse Arrhenius coefficients:          3.27E+08    1.3  121900.0
350. C3H4-A+O<=>C2H2+CH2O                      3.00E-03    4.6   -4243.0
     Reverse Arrhenius coefficients:          2.32E+02    3.2   81190.0
351. C3H4-A+H<=>C3H3+H2                        2.00E+07    2.0    5000.0
     Reverse Arrhenius coefficients:          3.02E+04    2.3   20840.0
352. C3H4-A+CH3<=>C3H3+CH4                     3.67E-02    4.0    6830.0
     Reverse Arrhenius coefficients:          5.06E-02    3.8   24210.0
353. C3H4-A+C3H5-A<=>C3H3+C3H6                 2.00E+11    0.0    7700.0
     Reverse Arrhenius coefficients:          2.64E+19   -2.7   42140.0
354. C3H4-A+C2H<=>C3H3+C2H2                    1.00E+13    0.0       0.0
     Reverse Arrhenius coefficients:          1.42E+16   -1.4   53820.0
355. C3H4-A+HO2<=>C2H4+CO+OH                   1.00E+12    0.0   14000.0
     Reverse Arrhenius coefficients:          1.00E+00    0.0       0.0
356. C3H4-A+HO2<=>C3H3+H2O2                    3.00E+13    0.0   14000.0
     Reverse Arrhenius coefficients:          1.55E+16   -1.4   44000.0
357. C2H2+CH3<=>C3H4-A+H                       6.74E+19   -2.1   31590.0
     Reverse Arrhenius coefficients:          6.41E+25   -3.3   21770.0
358. C3H4-P+M<=>C3H3+H+M                       1.14E+17    0.0   70000.0
     Reverse Arrhenius coefficients:          6.71E+11    0.6    6420.0
```

254

```
359. C3H4-P<=>C2H+CH3                              4.20E+16    0.0   100000.0
     Reverse Arrhenius coefficients:              1.02E+12    0.6    -1600.0
360. C3H4-P+O2<=>HCCO+OH+CH2                       1.00E+07    1.5    30100.0
     Reverse Arrhenius coefficients:              1.00E+00    0.0        0.0
361. C3H4-P+O2<=>C3H3+HO2                          2.00E+13    0.0    41600.0
     Reverse Arrhenius coefficients:              6.37E+11   -0.2     1021.0
362. C3H4-P+HO2<=>C2H4+CO+OH                       3.00E+12    0.0    19000.0
     Reverse Arrhenius coefficients:              1.00E+00    0.0        0.0
363. C3H4-P+OH<=>C3H3+H2O                          1.00E+07    2.0     1000.0
     Reverse Arrhenius coefficients:              6.44E+05    2.0    30000.0
364. C3H4-P+OH<=>CH2CO+CH3                         5.00E-04    4.5    -1000.0
     Reverse Arrhenius coefficients:              1.08E-02    4.1    31280.0
365. C3H4-P+O<=>C2H3+HCO                           3.20E+12    0.0     2010.0
     Reverse Arrhenius coefficients:              2.55E+12   -0.4    32350.0
366. C3H4-P+O<=>HCCO+CH3                           9.60E+08    1.0        0.0
     Reverse Arrhenius coefficients:              1.43E+04    1.8    26990.0
367. C3H4-P+O<=>HCCO+CH2+H                         3.20E-19    0.0     2010.0
     Reverse Arrhenius coefficients:              1.00E-30    0.0        0.0
368. C3H4-P+O<=>C3H3+OH                            7.65E+08    1.5     8600.0
     Reverse Arrhenius coefficients:              2.18E+08    1.3    22470.0
369. C3H4-P+H<=>C3H3+H2                            2.00E+07    2.0     5000.0
     Reverse Arrhenius coefficients:              1.22E+05    2.1    19110.0
370. C3H4-P+CH3<=>C3H3+CH4                         1.50E+00    3.5     5600.0
     Reverse Arrhenius coefficients:              8.31E+00    3.2    21250.0
371. C3H4-P+C2H<=>C3H3+C2H2                        1.00E+12    0.0        0.0
     Reverse Arrhenius coefficients:              5.30E+11   -0.4    49630.0
372. C3H4-P+C2H3<=>C3H3+C2H4                       1.00E+12    0.0     7700.0
     Reverse Arrhenius coefficients:              9.54E+11   -0.4    52450.0
373. C3H4-P+C3H5-A<=>C3H3+C3H6                     1.00E+12    0.0     7700.0
     Reverse Arrhenius coefficients:              4.93E+16   -1.7    37950.0
374. C2H2+CH3<=>C3H4-P+H                           4.23E+08    1.1    12090.0
     Reverse Arrhenius coefficients:              1.00E+14    0.0     4000.0
375. C3H3+O<=>CH2O+C2H                             1.00E+13    0.0        0.0
     Reverse Arrhenius coefficients:              5.45E+14    0.0    31610.0
376. C3H3+OH<=>C3H2+H2O                            1.00E+13    0.0        0.0
     Reverse Arrhenius coefficients:              1.34E+15    0.0    15680.0
377. C3H3+O2<=>CH2CO+HCO                           3.01E+10    0.0     2870.0
     Reverse Arrhenius coefficients:              4.88E+11    0.0    59470.0
378. C3H3+CH3<=>C2H5+C2H                           4.30E+15   -0.8    45630.0
     Reverse Arrhenius coefficients:              1.81E+13    0.0        0.0
379. C3H2+O2<=>HCO+HCCO                            5.00E+13    0.0        0.0
     Reverse Arrhenius coefficients:              2.33E+14   -0.2    77190.0
380. C3H3+H<=>C3H2+H2                              5.00E+13    0.0        0.0
     Reverse Arrhenius coefficients:              6.00E+07    1.4     4110.0
381. C3H2+OH<=>C2H2+HCO                            5.00E+13    0.0        0.0
     Reverse Arrhenius coefficients:              2.28E+16   -0.3    75020.0
382. C3H2+O2<=>HCCO+CO+H                           5.00E+13    0.0        0.0
     Warning...all REV parameters are zero... 0.000E+00 0.000 0.000E+00
             this reaction will be treated as irreversible
383. CH3CHCO+OH<=>C2H5+CO2                         1.73E+12    0.0    -1010.0
     Warning...all REV parameters are zero... 0.000E+00 0.000 0.000E+00
             this reaction will be treated as irreversible
384. CH3CHCO+H<=>C2H5+CO                           4.40E+12    0.0     1459.0
     Warning...all REV parameters are zero... 0.000E+00 0.000 0.000E+00
             this reaction will be treated as irreversible
385. CH3CHCO+O<=>CH3CHO+CO                         3.20E+12    0.0     -437.0
     Warning...all REV parameters are zero... 0.000E+00 0.000 0.000E+00
             this reaction will be treated as irreversible
386. NC3H7+HO2<=>NC3H7O+OH                         7.00E+12    0.0    -1000.0
     Reverse Arrhenius coefficients:              6.22E+15   -0.7    25310.0
387. CH3O2+NC3H7<=>CH3O+NC3H7O                     7.00E+12    0.0    -1000.0
     Reverse Arrhenius coefficients:              3.89E+14   -0.4    29550.0
388. NC3H7O<=>C2H5+CH2O                            2.72E+21   -2.4    15700.0
     Reverse Arrhenius coefficients:              1.00E+11    0.0     3496.0
389. NC3H7O<=>C2H5CHO+H                            8.90E+10    0.7    19800.0
     Reverse Arrhenius coefficients:              4.00E+12    0.0     6260.0
390. NC3H7O2<=>NC3H7+O2                            2.40E+20   -1.6    35960.0
     Reverse Arrhenius coefficients:              4.52E+12    0.0        0.0
391. IC3H7O2<=>IC3H7+O2                            3.13E+22   -2.2    38160.0
     Reverse Arrhenius coefficients:              7.54E+12    0.0        0.0
392. NC3H7O2+CH3O2<=>NC3H7O+CH3O+O2                1.40E+16   -1.6     1860.0
     Warning...all REV parameters are zero... 0.000E+00 0.000 0.000E+00
             this reaction will be treated as irreversible
393. NC3H7O2+C2H5O2<=>NC3H7O+C2H5O+O2              1.40E+16   -1.6     1860.0
     Warning...all REV parameters are zero... 0.000E+00 0.000 0.000E+00
             this reaction will be treated as irreversible
394. NC3H7O2+NC3H7O2<=>O2+NC3H7O+NC3H7O            1.40E+16   -1.6     1860.0
     Warning...all REV parameters are zero... 0.000E+00 0.000 0.000E+00
             this reaction will be treated as irreversible
395. NC3H7O2+CH3<=>NC3H7O+CH3O                     7.00E+12    0.0    -1000.0
     Reverse Arrhenius coefficients:              5.30E+12    0.0    26920.0
396. NC3H7O2+C2H5<=>NC3H7O+C2H5O                   7.00E+12    0.0    -1000.0
     Reverse Arrhenius coefficients:              7.54E+14   -0.6    29330.0
397. NC3H7O2+NC3H7<=>NC3H7O+NC3H7O                 7.00E+12    0.0    -1000.0
     Reverse Arrhenius coefficients:              7.61E+14   -0.6    28000.0
398. NC3H7O2+C3H5-A<=>NC3H7O+C3H5O                 7.00E+12    0.0    -1000.0
     Reverse Arrhenius coefficients:              1.96E+11    0.2    14340.0
399. IC3H7O2<=>C3H6+HO2                            1.20E+43   -9.4    41530.0
     Reverse Arrhenius coefficients:              2.30E+33   -7.3    16710.0
```

```
400. NC3H7O2<=>C3H6+HO2                            4.31E+36   -7.5   39510.0
     Reverse Arrhenius coefficients:               1.02E+28   -5.6   19440.0
401. NC3H7O2<=>C3H6OOH1-2                          6.00E+11    0.0   26850.0
     Reverse Arrhenius coefficients:               1.12E+08    0.6   11720.0
402. NC3H7O2<=>C3H6OOH1-3                          1.12E+11    0.0   24400.0
     Reverse Arrhenius coefficients:               2.72E+11   -0.5    8936.0
403. IC3H7O2<=>C3H6OOH2-1                          1.80E+12    0.0   29400.0
     Reverse Arrhenius coefficients:               1.12E+10    0.1   11810.0
404. C3H6OOH1-2<=>C3H6O1-2+OH                      6.00E+11    0.0   22000.0
     Reverse Arrhenius coefficients:               1.15E+11    0.5   38370.0
405. C3H6OOH1-3<=>C3H6O1-3+OH                      7.50E+10    0.0   15250.0
     Reverse Arrhenius coefficients:               1.19E+06    1.8   28710.0
406. C3H6OOH2-1<=>C3H6O1-2+OH                      6.00E+11    0.0   22000.0
     Reverse Arrhenius coefficients:               2.78E+08    1.2   36090.0
407. C3H6OOH1-2<=>C3H6+HO2                         7.83E+15   -1.3   15950.0
     Reverse Arrhenius coefficients:               1.00E+11    0.0   11000.0
408. C3H6OOH2-1<=>C3H6+HO2                         3.24E+18   -2.0   18970.0
     Reverse Arrhenius coefficients:               1.00E+11    0.0   11750.0
409. C3H6OOH1-3<=>OH+CH2O+C2H4                     3.04E+15   -0.8   27400.0
     Warning...all REV parameters are zero... 0.000E+00 0.000 0.000E+00
             this reaction will be treated as irreversible
410. C3H6OOH1-2<=>C2H4+CH2O+OH                     1.31E+33   -7.0   48120.0
     Warning...all REV parameters are zero... 0.000E+00 0.000 0.000E+00
             this reaction will be treated as irreversible
411. C3H5O<=>C2H3CHO+H                             1.00E+14    0.0   29100.0
     Reverse Arrhenius coefficients:               1.68E+14   -0.2   19690.0
412. C3H5O<=>C2H3+CH2O                             1.46E+20   -2.0   35090.0
     Reverse Arrhenius coefficients:               1.50E+11    0.0   10600.0
413. C3H5O+O2<=>C2H3CHO+HO2                        1.00E+12    0.0    6000.0
     Reverse Arrhenius coefficients:               1.29E+11    0.0   32000.0
414. C3H6O1-2<=>C2H4+CH2O                          6.00E+14    0.0   60000.0
     Reverse Arrhenius coefficients:               2.97E+11    1.0   31080.0
415. C3H6O1-2+OH<=>CH2O+C2H3+H2O                   5.00E+12    0.0       0.0
     Warning...all REV parameters are zero... 0.000E+00 0.000 0.000E+00
             this reaction will be treated as irreversible
416. C3H6O1-2+H<=>CH2O+C2H3+H2                     2.63E+07    2.0    5000.0
     Warning...all REV parameters are zero... 0.000E+00 0.000 0.000E+00
             this reaction will be treated as irreversible
417. C3H6O1-2+O<=>CH2O+C2H3+OH                     8.43E+13    0.0    5200.0
     Warning...all REV parameters are zero... 0.000E+00 0.000 0.000E+00
             this reaction will be treated as irreversible
418. C3H6O1-2+HO2<=>CH2O+C2H3+H2O2                 1.00E+13    0.0   15000.0
     Warning...all REV parameters are zero... 0.000E+00 0.000 0.000E+00
             this reaction will be treated as irreversible
419. C3H6O1-2+CH3O2<=>CH2O+C2H3+CH3O2H            1.00E+13    0.0   19000.0
     Warning...all REV parameters are zero... 0.000E+00 0.000 0.000E+00
             this reaction will be treated as irreversible
420. C3H6O1-2+CH3<=>CH2O+C2H3+CH4                  2.00E+11    0.0   10000.0
     Warning...all REV parameters are zero... 0.000E+00 0.000 0.000E+00
             this reaction will be treated as irreversible
421. C3H6O1-3<=>C2H4+CH2O                          6.00E+14    0.0   60000.0
     Reverse Arrhenius coefficients:               2.97E+11    0.0   31080.0
422. C3H6O1-3+OH<=>CH2O+C2H3+H2O                   5.00E+12    0.0       0.0
     Warning...all REV parameters are zero... 0.000E+00 0.000 0.000E+00
             this reaction will be treated as irreversible
423. C3H6O1-3+O<=>CH2O+C2H3+OH                     8.43E+13    0.0    5200.0
     Warning...all REV parameters are zero... 0.000E+00 0.000 0.000E+00
             this reaction will be treated as irreversible
424. C3H6O1-3+H<=>CH2O+C2H3+H2                     2.63E+07    2.0    5000.0
     Warning...all REV parameters are zero... 0.000E+00 0.000 0.000E+00
             this reaction will be treated as irreversible
425. C3H6O1-3+CH3O2<=>CH2O+C2H3+CH3O2H            1.00E+13    0.0   19000.0
     Warning...all REV parameters are zero... 0.000E+00 0.000 0.000E+00
             this reaction will be treated as irreversible
426. C3H6O1-3+HO2<=>CH2O+C2H3+H2O2                 1.00E+13    0.0   15000.0
     Warning...all REV parameters are zero... 0.000E+00 0.000 0.000E+00
             this reaction will be treated as irreversible
427. C3H6O1-3+CH3<=>CH2O+C2H3+CH4                  2.00E+11    0.0   10000.0
     Warning...all REV parameters are zero... 0.000E+00 0.000 0.000E+00
             this reaction will be treated as irreversible
428. SC4H9<=>C3H6+CH3                              4.80E+10    1.0   30350.0
     Reverse Arrhenius coefficients:               1.76E+04    2.5    6130.0
429. SC4H9<=>C4H8-1+H                              3.03E+11    0.6   36820.0
     Reverse Arrhenius coefficients:               4.24E+11    0.5    1230.0
430. SC4H9+O2<=>C4H8-1+HO2                         5.35E-01    3.7    9322.0
     Reverse Arrhenius coefficients:               1.57E+00    3.6   22600.0
431. C4H8-1<=>C3H5-A+CH3                           5.08E+19   -1.3   76510.0
     Reverse Arrhenius coefficients:               1.35E+13    0.0       0.0
432. C4H8-1<=>C2H3+C2H5                            2.88E+23   -2.0  101600.0
     Reverse Arrhenius coefficients:               9.00E+12    0.0       0.0
433. C4H8-1<=>H+C4H71-3                            3.72E+14   -0.1   85200.0
     Reverse Arrhenius coefficients:               5.00E+13    0.0       0.0
434. C4H8-1+O2<=>C4H71-3+HO2                       2.00E+13    0.0   37190.0
     Reverse Arrhenius coefficients:               4.65E+12    0.1    -168.0
435. C4H8-1+O<=>C4H71-3+OH                         1.75E+11    0.7    5884.0
     Reverse Arrhenius coefficients:               4.88E+09    1.1   22840.0
436. C4H8-1+H<=>C4H71-3+H2                         1.73E+05    2.5    2492.0
     Reverse Arrhenius coefficients:               9.28E+03    2.9   20860.0
437. C4H8-1+OH<=>C4H71-3+H2O                       3.12E+06    2.0    -298.0
```

```
      Reverse Arrhenius coefficients:             1.78E+06    2.3    32960.0
438. C4H8-1+CH3<=>C4H71-3+CH4                      2.21E+00    3.5     5675.0
      Reverse Arrhenius coefficients:             1.08E+02    3.4    25580.0
439. C4H8-1+HO2<=>C4H71-3+H2O2                     2.70E+04    0.7     5884.0
      Reverse Arrhenius coefficients:             8.38E+05    0.4     8246.0
440. C4H8-1+CH3O2<=>C4H71-3+CH3O2H                 2.70E+04    0.7     5884.0
      Reverse Arrhenius coefficients:             1.63E+07   -0.1     6651.0
441. C4H8-1+CH3O<=>C4H71-3+CH3OH                   4.00E+01    2.9     8609.0
      Reverse Arrhenius coefficients:             2.47E+02    2.7    27000.0
442. C4H8-1+C3H5-A<=>C4H71-3+C3H6                  7.90E+10    0.0    12400.0
      Reverse Arrhenius coefficients:             1.00E+11    0.0    17500.0
443. C4H8-1+C4H6<=>C4H71-3+C4H71-3                 2.35E+12    0.0    46720.0
      Reverse Arrhenius coefficients:             1.60E+12    0.0        0.0
444. C4H8-1+C2H5O2<=>C4H71-3+C2H5O2H               1.40E+12    0.0    14900.0
      Reverse Arrhenius coefficients:             3.16E+11    0.0    13000.0
445. C4H71-3<=>C4H6+H                              1.20E+14    0.0    49300.0
      Reverse Arrhenius coefficients:             4.00E+13    0.0     1300.0
446. C4H71-3+C2H5<=>C4H8-1+C2H4                    2.59E+12    0.0     -131.0
      Reverse Arrhenius coefficients:             1.15E+13    0.1    49440.0
447. C4H71-3+CH3O<=>C4H8-1+CH2O                    2.41E+13    0.0        0.0
      Reverse Arrhenius coefficients:             2.48E+12    0.3    66330.0
448. C4H71-3+O<=>C2H3CHO+CH3                       6.03E+13    0.0        0.0
      Reverse Arrhenius coefficients:             3.38E+15   -0.8    81630.0
449. C3H5-A+C4H71-3<=>C3H6+C4H6                    6.31E+12    0.0        0.0
      Reverse Arrhenius coefficients:             1.00E+10    0.0    50000.0
450. C4H71-3+O2<=>C4H6+HO2                         1.00E+09    0.0        0.0
      Reverse Arrhenius coefficients:             1.00E+11    0.0    17000.0
451. H+C4H71-3<=>C4H6+H2                           3.16E+13    0.0        0.0
      Reverse Arrhenius coefficients:             1.07E+13    0.0    56810.0
452. C2H5+C4H71-3<=>C4H6+C2H6                      3.98E+12    0.0        0.0
      Reverse Arrhenius coefficients:             3.21E+12    0.0    49840.0
453. C2H3+C4H71-3<=>C2H4+C4H6                      3.98E+12    0.0        0.0
      Reverse Arrhenius coefficients:             1.16E+13    0.0    57710.0
454. C4H6<=>C2H3+C2H3                              4.03E+19   -1.0    98150.0
      Reverse Arrhenius coefficients:             1.26E+13    0.0        0.0
455. C4H6+OH<=>C2H5+CH2CO                          1.00E+12    0.0        0.0
      Reverse Arrhenius coefficients:             3.73E+12    0.0    30020.0
456. C4H6+OH<=>CH2O+C3H5-A                         1.00E+12    0.0        0.0
      Reverse Arrhenius coefficients:             3.50E+06    0.0    71060.0
457. C4H6+OH<=>C2H3+CH3CHO                         1.00E+12    0.0        0.0
      Reverse Arrhenius coefficients:             5.44E+11    0.0    18550.0
458. C4H6+O<=>C2H4+CH2CO                           1.00E+12    0.0        0.0
      Reverse Arrhenius coefficients:             6.38E+11    0.0    94340.0
459. C4H6+O<=>CH2O+C3H4-A                          1.00E+12    0.0        0.0
      Reverse Arrhenius coefficients:             1.08E+12    0.0    79050.0
460. C2H3+C2H4<=>C4H6+H                            5.00E+11    0.0     7300.0
      Reverse Arrhenius coefficients:             1.00E+13    0.0     4700.0
461. NC3H7CO<=>NC3H7+CO                            1.00E+11    0.0     9600.0
      Reverse Arrhenius coefficients:             2.19E+03    1.8    -1100.0
462. MB<=>MB4J+H                                   1.86E+17   -0.3   101200.0
      Reverse Arrhenius coefficients:             1.00E+14    0.0        0.0
463. MB<=>MB3J+H                                   4.34E+18   -0.7    98760.0
      Reverse Arrhenius coefficients:             1.00E+14    0.0        0.0
464. MB<=>MB2J+H                                   5.97E+14    0.2    93380.0
      Reverse Arrhenius coefficients:             1.00E+14    0.0        0.0
465. MB<=>MBMJ+H                                   1.68E+17   -0.4   100500.0
      Reverse Arrhenius coefficients:             1.00E+14    0.0        0.0
466. MB(+M)<=>ME+C2H4(+M)                          4.00E+12    0.0    68000.0
      Low pressure limit:  0.44440E+78 -0.17910E+02  0.61350E+05
      TROE centering:      0.96370E+00  0.99990E+10  0.19700E+03  0.17860E+10
467. MB(+M)<=>MP3J+CH3(+M)                         7.21E+18   -0.9    87210.0
      Low pressure limit:  0.13080E+71 -0.15160E+02  0.84910E+05
      TROE centering:      0.15409E+00  0.33770E+02  0.56730E+10  0.67100E+10
468. MB(+M)<=>BAOJ+CH3(+M)                         1.28E+23   -2.0    88100.0
      Low pressure limit:  0.17440E+74 -0.15960E+02  0.85320E+05
      TROE centering:      0.21857E+00  0.10000E+01  0.63755E+04  0.82130E+10
469. MB(+M)<=>ME2J+C2H5(+M)                        2.70E+22   -1.9    85680.0
      Low pressure limit:  0.39100E+75 -0.16420E+02  0.83700E+05
      TROE centering:      0.86980E+00  0.74990E+10  0.16303E+01  0.75960E+08
470. MB(+M)<=>CH3OCO+NC3H7(+M)                     2.05E+24   -2.2    93020.0
      Low pressure limit:  0.10180E+69 -0.14470E+02  0.87650E+05
      TROE centering:      0.80130E+00  0.99580E+10  0.33530E+03  0.32890E+10
471. MB(+M)<=>NC3H7CO+CH3O(+M)                     3.71E+21   -1.4    98900.0
      Low pressure limit:  0.18070E+59 -0.11700E+02  0.91270E+05
      TROE centering:      0.25187E+00  0.37280E+03  0.94883E+10  0.50000E+10
472. MB+C2H3<=>C2H4+MB4J                           5.01E+11    0.0    18000.0
      Reverse Arrhenius coefficients:             3.41E+11    0.1    28120.0
473. MB+C2H5<=>C2H6+MB4J                           5.01E+10    0.0    13400.0
      Reverse Arrhenius coefficients:             1.16E+11   -0.1    13530.0
474. MB+CH3<=>CH4+MB4J                             4.53E-01    3.6     7154.0
      Reverse Arrhenius coefficients:             8.88E-02    3.8    11050.0
475. MB+CH3O<=>CH3OH+MB4J                          2.17E+11    0.0     6458.0
      Reverse Arrhenius coefficients:             1.00E+09    0.4     9045.0
476. MB+CH3O2<=>CH3O2H+MB4J                        2.02E+04    2.5    16490.0
      Reverse Arrhenius coefficients:             4.89E+04    2.0     1254.0
477. MB+H<=>H2+MB4J                                6.66E+05    2.5     6756.0
      Reverse Arrhenius coefficients:             1.43E+02    3.2     9116.0
478. MB+HO2<=>H2O2+MB4J                            2.02E+04    2.5    16490.0
      Reverse Arrhenius coefficients:             2.51E+03    2.5     2849.0
```

```
479. MB+O<=>OH+MB4J                              9.81E+05    2.4     4750.0
     Reverse Arrhenius coefficients:            1.11E+02    3.0     5698.0
480. MB+O2<=>HO2+MB4J                            3.00E+13    0.0    52290.0
     Reverse Arrhenius coefficients:            3.38E+10    0.3      -39.0
481. MB+OH<=>H2O+MB4J                            5.28E+09    1.0     1586.0
     Reverse Arrhenius coefficients:            1.21E+07    1.5    18840.0
482. MB+C2H3<=>C2H4+MB3J                         4.00E+11    0.0    16800.0
     Reverse Arrhenius coefficients:            1.17E+10    0.5    29360.0
483. MB+C2H5<=>C2H6+MB3J                         5.00E+10    0.0    10400.0
     Reverse Arrhenius coefficients:            4.99E+09    0.3    12970.0
484. MB+CH3<=>CH4+MB3J                           1.51E+00    3.5     5481.0
     Reverse Arrhenius coefficients:            1.27E-02    4.0    11820.0
485. MB+CH3O<=>CH3OH+MB3J                        1.45E+11    0.0     4571.0
     Reverse Arrhenius coefficients:            2.87E+07    0.8     9598.0
486. MB+CH3O2<=>CH3O2H+MB3J                      8.19E+03    2.6    13910.0
     Reverse Arrhenius coefficients:            8.50E+02    2.5     1114.0
487. MB+H<=>H2+MB3J                              1.30E+06    2.4     4471.0
     Reverse Arrhenius coefficients:            1.20E+01    3.4     9271.0
488. MB+HO2<=>H2O2+MB3J                          8.19E+03    2.6    13910.0
     Reverse Arrhenius coefficients:            4.37E+01    2.9     2709.0
489. MB+O<=>OH+MB3J                              5.52E+05    2.5     2830.0
     Reverse Arrhenius coefficients:            2.67E+00    3.5     6218.0
490. MB+O2<=>HO2+MB3J                            2.00E+13    0.0    49640.0
     Reverse Arrhenius coefficients:            9.66E+08    0.7     -249.0
491. MB+OH<=>H2O+MB3J                            4.68E+07    1.6      -35.0
     Reverse Arrhenius coefficients:            4.59E+03    2.5    19660.0
492. MB+C2H3<=>C2H4+MB2J                         4.00E+11    0.0    14300.0
     Reverse Arrhenius coefficients:            8.47E+13   -0.5    32240.0
493. MB+C2H5<=>C2H6+MB2J                         2.00E+11    0.0     7900.0
     Reverse Arrhenius coefficients:            1.45E+14   -0.7    15850.0
494. MB+CH3<=>CH4+MB2J                           1.20E-09    6.4      893.0
     Reverse Arrhenius coefficients:            7.34E-08    6.0    12610.0
495. MB+CH3O<=>CH3OH+MB2J                        4.58E+10    0.0     2873.0
     Reverse Arrhenius coefficients:            6.58E+10   -0.2    13280.0
496. MB+CH3O2<=>CH3O2H+MB2J                      6.14E+03    2.5    10530.0
     Reverse Arrhenius coefficients:            4.62E+06    1.4     3114.0
497. MB+H<=>H2+MB2J                              1.20E+06    2.4     2583.0
     Reverse Arrhenius coefficients:            8.04E+04    2.4    12760.0
498. MB+HO2<=>H2O2+MB2J                          6.14E+03    2.5    10530.0
     Reverse Arrhenius coefficients:            2.38E+05    1.9     4709.0
499. MB+O<=>OH+MB2J                              7.66E+05    2.4     1140.0
     Reverse Arrhenius coefficients:            2.69E+04    2.4     9908.0
500. MB+O2<=>HO2+MB2J                            2.00E+13    0.0    48200.0
     Reverse Arrhenius coefficients:            7.02E+12   -0.3     3691.0
501. MB+OH<=>H2O+MB2J                            1.15E+11    0.5       63.0
     Reverse Arrhenius coefficients:            8.15E+10    0.4    25140.0
502. MB+C2H3<=>C2H4+MBMJ                         5.01E+11    0.0    18000.0
     Reverse Arrhenius coefficients:            3.78E+11    0.1    28790.0
503. MB+C2H5<=>C2H6+MBMJ                         5.01E+10    0.0    13400.0
     Reverse Arrhenius coefficients:            1.29E+11    0.0    14200.0
504. MB+CH3<=>CH4+MBMJ                           2.27E+00    3.5     5481.0
     Reverse Arrhenius coefficients:            4.92E-01    3.7    10050.0
505. MB+CH3O<=>CH3OH+MBMJ                        2.18E+11    0.0     4571.0
     Reverse Arrhenius coefficients:            1.11E+09    0.4     7828.0
506. MB+CH3O2<=>CH3O2H+MBMJ                      1.23E+04    2.6    13910.0
     Reverse Arrhenius coefficients:            3.30E+04    2.1     -656.0
507. MB+H<=>H2+MBMJ                              1.95E+06    2.4     4471.0
     Reverse Arrhenius coefficients:            4.64E+02    3.1     7501.0
508. MB+HO2<=>H2O2+MBMJ                          1.23E+04    2.6    13910.0
     Reverse Arrhenius coefficients:            1.70E+03    2.6      939.0
509. MB+O<=>OH+MBMJ                              8.28E+05    2.5     2830.0
     Reverse Arrhenius coefficients:            1.04E+02    3.1     4448.0
510. MB+O2<=>HO2+MBMJ                            3.00E+13    0.0    49640.0
     Reverse Arrhenius coefficients:            3.75E+10    0.3    -2019.0
511. MB+OH<=>H2O+MBMJ                            7.02E+07    1.6      -35.0
     Reverse Arrhenius coefficients:            1.78E+05    2.2    17890.0
512. BAOJ<=>CO2+NC3H7                            4.05E+18   -1.8    25170.0
     Reverse Arrhenius coefficients:            1.00E+11    0.0    39360.0
513. MB2J<=>MP2D+CH3                             6.12E+22   -2.1    42390.0
     Reverse Arrhenius coefficients:            1.00E+13    0.0    14000.0
514. MB3J<=>C3H6+CH3OCO                          8.14E+12    0.3    33590.0
     Reverse Arrhenius coefficients:            8.80E+03    2.5     6130.0
515. MB4J<=>C2H4+ME2J                            2.63E+10    0.8    26100.0
     Reverse Arrhenius coefficients:            1.00E+04    2.5     6130.0
516. MB2J<=>MB2D+H                               9.73E+14   -0.3    39400.0
     Reverse Arrhenius coefficients:            2.50E+11    0.5     2620.0
517. MB3J<=>MB2D+H                               1.34E+11    0.7    34020.0
     Reverse Arrhenius coefficients:            2.50E+11    0.5     2620.0
518. MB3J<=>MB3D+H                               1.11E+11    0.7    37910.0
     Reverse Arrhenius coefficients:            4.24E+11    0.5     1230.0
519. MB4J<=>MB3D+H                               1.53E+12    0.3    36860.0
     Reverse Arrhenius coefficients:            2.50E+11    0.5     2620.0
520. MBMJ<=>NC3H7CO+CH2O                         1.64E+22   -2.3    32850.0
     Reverse Arrhenius coefficients:            3.89E+11    0.0    10900.0
521. MB4J<=>MB2J                                 1.79E+09    0.8    31740.0
     Reverse Arrhenius coefficients:            5.56E+11    0.2    39560.0
522. MB4J<=>MB3J                                 1.65E+10    0.9    39330.0
     Reverse Arrhenius coefficients:            7.09E+08    1.3    41770.0
523. MB4J<=>MBMJ                                 4.55E+09   -0.5    18820.0
```

```
        Reverse Arrhenius coefficients:        5.04E+09   -0.5   19490.0
524. MB3J<=>MBMJ                               9.26E+10   -0.7   13900.0
        Reverse Arrhenius coefficients:        2.39E+12   -1.0   12130.0
525. MB3J<=>MB2J                               1.41E+10    0.9   39470.0
        Reverse Arrhenius coefficients:        1.03E+14   -0.1   44850.0
526. MB2J<=>MBMJ                               2.81E+11   -0.6   26150.0
        Reverse Arrhenius coefficients:        1.00E+09    0.0   19000.0
527. MB2D+CH3<=>C5H7O2+CH4                     4.53E-01    3.6    7154.0
        Reverse Arrhenius coefficients:        2.53E+01    3.7   21490.0
528. MB3D+CH3<=>C5H7O2+CH4                     1.51E+00    3.5    5481.0
        Reverse Arrhenius coefficients:        4.12E+01    3.5   25100.0
529. MB2D+H<=>C5H7O2+H2                        6.66E+05    2.5    6756.0
        Reverse Arrhenius coefficients:        4.07E+04    3.0   19560.0
530. MB3D+H<=>C5H7O2+H2                        1.30E+06    2.4    4471.0
        Reverse Arrhenius coefficients:        3.89E+04    2.9   22550.0
531. MB2D+OH<=>C5H7O2+H2O                      5.28E+09    1.0    1586.0
        Reverse Arrhenius coefficients:        3.44E+09    1.4   29280.0
532. MB3D+OH<=>C5H7O2+H2O                      4.68E+07    1.6     -35.0
        Reverse Arrhenius coefficients:        1.49E+07    2.0   32940.0
533. MB2D+HO2<=>C5H7O2+H2O2                    2.38E+04    2.5   16490.0
        Reverse Arrhenius coefficients:        8.42E+05    2.4   13290.0
534. MB3D+HO2<=>C5H7O2+H2O2                    9.64E+04    2.6   13910.0
        Reverse Arrhenius coefficients:        1.67E+06    2.4   15990.0
535. C5H7O2+OH<=>MB2D+O                        3.15E+04    2.9   16140.0
        Reverse Arrhenius coefficients:        9.81E+05    2.4    4750.0
536. C5H7O2+OH<=>MB3D+O                        8.67E+03    2.9   19500.0
        Reverse Arrhenius coefficients:        5.52E+05    2.5    2830.0
537. C5H7O2<=>CH2CHCHCO+CH3O                   2.50E+13    0.0   45000.0
        Reverse Arrhenius coefficients:        3.64E+08    0.5   -3137.0
538. MB3D+O<=>MP3J+HCO                         1.58E+07    1.8   -1216.0
        Reverse Arrhenius coefficients:        2.19E+05    1.8   27760.0
539. MB2D+O<=>ME2J+CH3CO                       1.58E+07    1.8   -1216.0
        Reverse Arrhenius coefficients:        1.25E+04    2.5   31340.0
540. MP2D+O<=>ME2J+HCO                         1.58E+07    1.8   -1216.0
        Reverse Arrhenius coefficients:        3.13E+07    1.6   28710.0
541. MB3D+O<=>ME2J+CH2CHO                      2.50E+07    1.8      76.0
        Reverse Arrhenius coefficients:        8.94E+05    2.0   32680.0
542. MB2D+O<=>CH3OCO+CH3CHCHO                  5.01E+07    1.8      76.0
        Reverse Arrhenius coefficients:        7.81E+02    3.0   22500.0
543. MB2D<=>CH3+MP2D3J                         3.22E+20   -1.5   90070.0
        Reverse Arrhenius coefficients:        1.00E+13    0.0       0.0
544. MB3D<=>C2H3+ME2J                          2.18E+17   -0.5   90050.0
        Reverse Arrhenius coefficients:        1.00E+13    0.0       0.0
545. NC3H7CO<=>CH2CO+C2H5                      2.74E+09    1.4   35830.0
        Reverse Arrhenius coefficients:        1.00E+04    2.5    6130.0
546. CH2CHCHCO+H<=>CJHCHCHCO+H2               4.21E-03    4.6    2583.0
        Reverse Arrhenius coefficients:        2.43E-03    4.4   -3170.0
547. CH2CHCHCO+OH<=>CJHCHCHCO+H2O             1.01E+13    0.0    5955.0
        Reverse Arrhenius coefficients:        2.53E+13   -0.2   15360.0
548. CH2CHCHCO+CH3<=>CJHCHCHCO+CH4            3.31E+00    3.7    9500.0
        Reverse Arrhenius coefficients:        5.00E+01    3.5    4227.0
549. CH2CHCHCO+O<=>CJHCHCHCO+OH               1.20E+11    0.7    8959.0
        Reverse Arrhenius coefficients:        3.05E+10    0.5    1111.0
550. CH2CHCHCO+HO2<=>CJHCHCHCO+H2O2           8.50E+13    0.0   30430.0
        Reverse Arrhenius coefficients:        1.26E+15   -0.6    8369.0
551. CJHCHCHCO<=>C2H2+HCCO                     7.62E+46   -9.6   61020.0
        Reverse Arrhenius coefficients:        1.61E+40   -8.6   20330.0
552. CH2CHCHCO<=>C2H3+HCCO                     1.90E+20   -0.8  112000.0
        Reverse Arrhenius coefficients:        8.00E+12    0.0       0.0
553. CH2CHCHCO+H<=>CO+C3H5-A                   1.10E+13    0.0    3400.0
        Reverse Arrhenius coefficients:        8.13E+09    0.7   46050.0
554. CH2CHCHCO+H<=>C2H4+HCCO                   1.10E+13    0.0    3400.0
        Reverse Arrhenius coefficients:        1.29E+08    0.7   -1823.0
555. CH2CHCHCO+OH<=>HCCO+CH3CHO               3.73E+12    0.0   -1013.0
        Reverse Arrhenius coefficients:        1.93E+07    1.0     559.0
556. CH2CHCHCO+OH<=>CH3CHCHO+CO               3.73E+12    0.0   -1013.0
        Reverse Arrhenius coefficients:        1.76E+10    0.9   42420.0
557. MB2J+HO2<=>OH+MB2O                        2.00E+13    0.0   -1000.0
        Reverse Arrhenius coefficients:        8.91E+14   -0.4   21290.0
558. MB3J+HO2<=>OH+MB3O                        2.00E+13    0.0   -1000.0
        Reverse Arrhenius coefficients:        1.26E+18   -1.2   27810.0
559. MB2J+CH3O2<=>CH3O+MB2O                    2.00E+13    0.0   -1000.0
        Reverse Arrhenius coefficients:        5.58E+13   -0.1   25530.0
560. MB3J+CH3O2<=>CH3O+MB3O                    2.00E+13    0.0   -1000.0
        Reverse Arrhenius coefficients:        7.86E+16   -0.9   32050.0
561. MB2J+C2H5O2<=>C2H5O+MB2O                  7.00E+12    0.0   -1000.0
        Reverse Arrhenius coefficients:        4.40E+15   -0.9   26700.0
562. MB3J+C2H5O2<=>C2H5O+MB3O                  7.00E+12    0.0   -1000.0
        Reverse Arrhenius coefficients:        6.20E+18   -1.7   33220.0
563. MB2J+NC3H7O2<=>NC3H7O+MB2O               7.00E+12    0.0   -1000.0
        Reverse Arrhenius coefficients:        3.83E+13   -0.2   25230.0
564. MB3J+NC3H7O2<=>NC3H7O+MB3O               7.00E+12    0.0   -1000.0
        Reverse Arrhenius coefficients:        5.39E+16   -1.1   31750.0
565. MB3O<=>CH3CHO+ME2J                        2.83E+20   -2.3    7853.0
        Reverse Arrhenius coefficients:        9.33E+10    0.0    3943.0
566. MB2O<=>C2H5CHO+CH3CO                      4.20E+19   -1.7   13290.0
        Reverse Arrhenius coefficients:        9.33E+10    0.0    3943.0
567. BA0J<=>BA4J                               2.00E+11    0.0   16500.0
        Reverse Arrhenius coefficients:        4.66E+10    0.0   25290.0
```

```
568. BA4J<=>C2H4+CH2COOH                          5.97E+08    1.5   26590.0
     Reverse Arrhenius coefficients:             8.80E+03    2.5    6130.0
569. MBMOO<=>MBMJ+O2                              4.09E+20   -1.8   41050.0
     Reverse Arrhenius coefficients:             7.54E+12    0.0       0.0
570. MB2OO<=>MB2J+O2                              1.82E+20   -1.5   28910.0
     Reverse Arrhenius coefficients:             1.41E+13    0.0       0.0
571. CH3CHCHO<=>C2H3CHO+H                         3.52E+15   -0.5   41060.0
     Reverse Arrhenius coefficients:             6.50E+12    0.0    2900.0
572. CH3CHCHO<=>CH3CHCO+H                         1.14E+16   -0.7   40310.0
     Reverse Arrhenius coefficients:             5.00E+12    0.0    1200.0
573. CH3CHCHO+H2<=>C2H5CHO+H                      2.16E+05    2.4   18990.0
     Reverse Arrhenius coefficients:             4.31E+04    2.6    5265.0
574. CH3CHCHO+O2<=>CH3CHCO+HO2                    1.81E+11    0.0    1840.0
     Reverse Arrhenius coefficients:             2.73E+10    0.0   12690.0
575. CH3CHCHO+O2<=>C2H3CHO+HO2                    2.72E+11    0.0    7240.0
     Reverse Arrhenius coefficients:             1.73E+11   -0.2   19040.0
576. CH3CHCHO+O2<=>CH3CHO+CO+OH                   3.62E+10    0.0       0.0
     Warning...all REV parameters are zero... 0.000E+00 0.00 0.000E+00
              this reaction will be treated as irreversible
577. CH3CHCHO+HO2<=>C2H5CHO+O2                    7.35E+12    0.0    1310.0
     Reverse Arrhenius coefficients:             8.07E+13   -0.1   45070.0
578. CH2COOH<=>CH2CO+OH                           1.69E+18   -1.2   53720.0
     Reverse Arrhenius coefficients:             2.60E+12    0.0    -614.0
579. ME<=>CH3+CH3OCO                              3.57E+23   -2.1   94030.0
     Reverse Arrhenius coefficients:             1.81E+13    0.0       0.0
580. ME<=>CH3CO+CH3O                              1.20E+25   -2.3   99020.0
     Reverse Arrhenius coefficients:             3.00E+13    0.0       0.0
581. ME+H<=>ME2J+H2                               1.95E+06    2.4    4471.0
     Reverse Arrhenius coefficients:             1.03E+05    2.7   10380.0
582. ME+OH<=>ME2J+H2O                             7.02E+07    1.6     -35.0
     Reverse Arrhenius coefficients:             3.93E+07    1.8   20770.0
583. ME+CH3<=>ME2J+CH4                            2.27E+00    3.5    5481.0
     Reverse Arrhenius coefficients:             1.09E+02    3.3   12930.0
584. ME+HO2<=>ME2J+H2O2                           1.45E+04    2.6   13910.0
     Reverse Arrhenius coefficients:             4.41E+05    2.2    3819.0
585. ME+O<=>ME2J+OH                               8.28E+05    2.5    2830.0
     Reverse Arrhenius coefficients:             2.29E+04    2.7    7328.0
586. ME+CH3O2<=>ME2J+CH3O2H                       1.45E+04    2.6   13910.0
     Reverse Arrhenius coefficients:             8.57E+06    1.7    2224.0
587. ME+H<=>MEMJ+H2                               1.95E+06    2.4    4471.0
     Reverse Arrhenius coefficients:             1.96E+05    2.2    8041.0
588. ME+OH<=>MEMJ+H2O                             7.02E+07    1.6     -35.0
     Reverse Arrhenius coefficients:             7.51E+07    1.3   18430.0
589. ME+CH3<=>MEMJ+CH4                            2.27E+00    3.5    5481.0
     Reverse Arrhenius coefficients:             2.08E+02    2.8   10590.0
590. ME+HO2<=>MEMJ+H2O2                           1.45E+04    2.6   13910.0
     Reverse Arrhenius coefficients:             8.42E+05    1.7    1479.0
591. ME+O<=>MEMJ+OH                               8.28E+05    2.5    2830.0
     Reverse Arrhenius coefficients:             4.37E+04    2.2    4988.0
592. ME+CH3O2<=>MEMJ+CH3O2H                       1.45E+04    2.6   13910.0
     Reverse Arrhenius coefficients:             1.64E+07    1.2    -116.0
593. ME2J<=>CH2CO+CH3O                            5.49E+19   -1.5   43210.0
     Reverse Arrhenius coefficients:             5.00E+11    0.0   -1000.0
594. MEMJ<=>CH3CO+CH2O                            2.55E+24   -3.2   32230.0
     Reverse Arrhenius coefficients:             3.89E+11    0.0   10900.0
595. ME2J<=>MEMJ                                  5.23E+08    0.5   21340.0
     Reverse Arrhenius coefficients:             1.00E+09    0.0   19000.0
596. MP3J<=>C2H4+CH3OCO                           2.91E+13    0.2   33670.0
     Reverse Arrhenius coefficients:             1.32E+04    2.5    6130.0
597. MP3J<=>MP2D+H                                1.58E+12    0.5   34380.0
     Reverse Arrhenius coefficients:             2.50E+11    0.5    2620.0
598. MP2D+O<=>CH3OCO+CH2CHO                       5.01E+07    1.8      76.0
     Reverse Arrhenius coefficients:             2.21E+03    2.9   22630.0
599. MP2D<=>C2H3+CH3OCO                           7.96E+24   -2.5  107100.0
     Reverse Arrhenius coefficients:             1.81E+13    0.0       0.0
600. MP2D+H<=>MP2D3J+H2                           1.30E+06    2.4    4471.0
     Reverse Arrhenius coefficients:             2.53E+04    2.9    9571.0
601. MP2D+OH<=>MP2D3J+H2O                         4.68E+07    1.6     -35.0
     Reverse Arrhenius coefficients:             9.71E+06    2.0   19960.0
602. MP2D+CH3<=>MP2D3J+CH4                        1.51E+00    3.5    5481.0
     Reverse Arrhenius coefficients:             2.69E+01    3.5   12120.0
603. MP2D+HO2<=>MP2D3J+H2O2                       9.64E+03    2.6   13910.0
     Reverse Arrhenius coefficients:             1.09E+05    2.4    3009.0
604. MP2D+O<=>MP2D3J+OH                           5.52E+05    2.5    2830.0
     Reverse Arrhenius coefficients:             5.65E+03    2.9    6518.0
605. MP2D+CH3O2<=>MP2D3J+CH3O2H                   9.64E+03    2.6   13910.0
     Reverse Arrhenius coefficients:             2.12E+06    1.9    1414.0
606. MP2D+H<=>MP2D2J+H2                           6.02E+05    2.4    2583.0
     Reverse Arrhenius coefficients:             1.87E+06    2.3   12870.0
607. MP2D+OH<=>MP2D2J+H2O                         5.73E+10    0.5      63.0
     Reverse Arrhenius coefficients:             1.90E+12    0.3   25240.0
608. MP2D+CH3<=>MP2D2J+CH4                        6.01E-10    6.4     893.0
     Reverse Arrhenius coefficients:             1.71E-06    5.8   12720.0
609. MP2D+HO2<=>MP2D2J+H2O2                       3.61E+03    2.5   10530.0
     Reverse Arrhenius coefficients:             6.50E+06    1.8    4821.0
610. MP2D+O<=>MP2D2J+OH                           3.83E+05    2.4    1140.0
     Reverse Arrhenius coefficients:             6.26E+05    2.3   10020.0
611. MP2D+CH3O2<=>MP2D2J+CH3O2H                   3.61E+03    2.5   10530.0
     Reverse Arrhenius coefficients:             1.26E+08    1.4    3226.0
```

```
612. MP2D+H<=>MP2DMJ+H2                            1.96E+06    2.4    4471.0
     Reverse Arrhenius coefficients:             1.80E+07    2.2    8211.0
613. MP2D+OH<=>MP2DMJ+H2O                          7.02E+07    1.6     -35.0
     Reverse Arrhenius coefficients:             6.85E+09    1.3   18600.0
614. MP2D+CH3<=>MP2DMJ+CH4                         2.27E+00    3.5    5481.0
     Reverse Arrhenius coefficients:             1.90E+04    2.8   10760.0
615. MP2D+HO2<=>MP2DMJ+H2O2                        1.45E+04    2.6   13910.0
     Reverse Arrhenius coefficients:             7.68E+07    1.7    1649.0
616. MP2D+O<=>MP2DMJ+OH                            8.28E+05    2.5    2830.0
     Reverse Arrhenius coefficients:             3.98E+06    2.2    5158.0
617. MP2D+CH3O2<=>MP2DMJ+CH3O2H                    1.45E+04    2.6   13910.0
     Reverse Arrhenius coefficients:             1.49E+09    1.2      54.0
618. MP2D<=>C2H3CO+CH3O                            2.98E+22   -1.9   90170.0
     Reverse Arrhenius coefficients:             3.00E+13    0.0       0.0
619. MP2D<=>C2H3CO2+CH3                            3.84E+22   -2.0   88030.0
     Reverse Arrhenius coefficients:             3.00E+13    0.0       0.0
620. MP2D3J<=>C2H2+CH3OCO                          7.68E+19   -1.5   47410.0
     Reverse Arrhenius coefficients:             8.76E+09    0.8    4450.0
621. MP2D2J<=>C2H2+CH3OCO                          6.30E+24   -2.9   56150.0
     Reverse Arrhenius coefficients:             4.50E+12    0.0    8000.0
622. MP2DMJ<=>C2H3CO+CH2O                          5.75E+23   -2.8   23540.0
     Reverse Arrhenius coefficients:             3.89E+11    0.0   10900.0
623. MP2DMJ<=>MP2D3J                               4.35E+13   -1.4   12540.0
     Reverse Arrhenius coefficients:             9.26E+10   -0.7   13900.0
624. MP2DMJ<=>MP2D2J                               4.99E+09   -0.2   17160.0
     Reverse Arrhenius coefficients:             1.69E+09   -0.1   23710.0
625. MP2D2J<=>MP2D3J                               3.12E+13    0.2   42140.0
     Reverse Arrhenius coefficients:             1.96E+11    0.8   36950.0
626. C2H3CO2<=>C2H3+CO2                            8.64E+18   -1.7   35210.0
     Reverse Arrhenius coefficients:             1.50E+11    0.0   35200.0
627. CH+N2=NCN+H                                   3.00E+12    0.0   22155.0
628. CN+N2O=NCN+NO                                 6.00E+13    0.0   15360.0
     Declared duplicate reaction...
629. CN+N2O=NCN+NO                                 1.80E+10    0.0    1450.0
     Declared duplicate reaction...
630. CN+NCO=NCN+CO                                 1.80E+13    0.0       0.0
631. C2O+N2=NCN+CO                                 7.00E+11    0.0   17000.0
632. CH+N2=HNCN                                    1.65E+21   -3.6   14196.0
633. HNCN+M=>H+NCN+M                               1.79E+28   -3.4   64502.0
634. HNCN+O=NO+HCN                                 1.22E+14    0.1      73.5
635. HNCN+O=NH+NCO                                 5.60E+13    0.1      73.5
636. HNCN+O=CN+HNO                                 9.36E+12    0.1      73.5
637. HNCN+OH=NCN+H2O                               8.28E+03    2.8    3135.0
638. HNCN+O2=HO2+NCN                               1.26E+08    1.3   24240.0
639. NCN=N+CN                                      2.95E+30   -5.3  117090.0
640. NCN=C+N2                                      2.66E+28   -5.3   83110.0
641. NCN=CNN                                       3.69E+29   -5.8   78410.0
642. NCN+H=HCN+N                                   1.89E+14    0.0    8425.0
643. NCN+O=CN+NO                                   2.54E+13    0.1     -34.0
644. NCN+O=CO+N2                                   2.42E+02    2.3   -1135.0
645. NCN+O=N+NCO                                   2.20E+09    0.4    -157.0
646. NCN+N=N2+CN                                   1.00E+13    0.0       0.0
647. NCN+C=CN+CN                                   1.00E+13    0.0       0.0
648. NCN+OH=HCN+NO                                 3.32E+10   -1.0    7290.0
     Declared duplicate reaction...
649. NCN+OH=HCN+NO                                 4.69E+10    0.4    4000.0
     Declared duplicate reaction...
650. NCN+O2=NO+NCO                                 3.80E+09    0.5   24590.0
651. NCN+CH=HCN+CN                                 3.21E+13    0.0    -860.0
652. NCN+CN=C2N2+N                                 1.25E+14    0.0    8020.0
653. NCN+CH2=H2CN+CN                               7.99E+13    0.0    4630.0
654. H+H+N2=H2+N2                                  5.40E+18   -1.3       0.0
655. N2+O=NO+N                                     1.80E+14    0.0   76100.0
656. N+O2=NO+O                                     9.00E+09    1.0    6500.0
657. NO+M=N+O+M                                    9.64E+14    0.0  148300.0
     N2            Enhanced by    1.500E+00
     NO            Enhanced by    3.000E+00
     CO2           Enhanced by    2.500E+00
658. NO+NO=N2+O2                                   3.00E+11    0.0   65000.0
659. N2O(+M)=N2+O(+M)                              1.26E+12    0.0   62620.0
     Low pressure limit:  0.40000E+15  0.00000E+00  0.56640E+05
     O2            Enhanced by    1.400E+00
     N2            Enhanced by    1.700E+00
     H2O           Enhanced by    1.200E+01
     NO            Enhanced by    3.000E+00
     N2O           Enhanced by    3.500E+00
660. N2O+O=N2+O2                                   1.00E+14    0.0   28200.0
661. N2O+O=NO+NO                                   6.92E+13    0.0   26630.0
662. N2O+N=N2+NO                                   1.00E+13    0.0   20000.0
663. N2O+NO=N2+NO2                                 2.75E+14    0.0   50000.0
664. NO+O(+M)=NO2(+M)                              1.30E+15   -0.8       0.0
     Low pressure limit:  0.47200E+25 -0.28700E+01  0.15510E+04
     TROE centering:      0.96200E+00  0.10000E+02  0.79620E+04
     AR            Enhanced by    6.000E-01
     NO2           Enhanced by    6.200E+00
     NO            Enhanced by    1.800E+00
     O2            Enhanced by    8.000E-01
     N2O           Enhanced by    4.400E+00
     CO2           Enhanced by    0.000E+00
```

```
              H2O           Enhanced by    1.000E+01
665. NO+O(+CO2)=NO2(+CO2)                    1.30E+15   -0.8       0.0
     Low pressure limit:  0.40000E+23 -0.21600E+01  0.10510E+04
     TROE centering:       0.96200E+00  0.10000E+02  0.79620E+04
666. NO2+O=NO+O2                             3.91E+12    0.0    -238.0
667. NO2+N=N2O+O                             8.40E+11    0.0       0.0
668. NO2+N=NO+NO                             1.00E+12    0.0       0.0
669. NO2+NO=N2O+O2                           1.00E+12    0.0   60000.0
670. NO2+NO2=NO+NO+O2                        3.95E+12    0.0   27590.0
671. NO2+NO2=NO3+NO                          1.13E+04    2.6   22720.0
672. NO2+O(+M)=NO3(+M)                       1.33E+13    0.0       0.0
     Low pressure limit:  0.14900E+29 -0.40800E+01  0.24670E+04
     TROE centering:       0.86000E+00  0.10000E+02  0.28000E+04
              H2O           Enhanced by    1.000E+01
              O2            Enhanced by    8.000E-01
              H2            Enhanced by    2.000E+00
              CO2           Enhanced by    0.000E+00
673. NO2+O(+CO2)=NO3(+CO2)                   1.33E+13    0.0       0.0
     Low pressure limit:  0.13400E+29 -0.39400E+01  0.22770E+04
     TROE centering:       0.86000E+00  0.10000E+02  0.28000E+04
674. NO3=NO+O2                               2.50E+06    0.0   12120.0
675. NO3+NO2=NO+NO2+O2                       1.20E+11    0.0    3200.0
676. NO3+O=NO2+O2                            1.02E+13    0.0       0.0
677. NO3+NO3=NO2+NO2+O2                      5.12E+11    0.0    4870.0
678. N2O4(+M)=NO2+NO2(+M)                    4.05E+18   -1.1   12840.0
     Low pressure limit:  0.19600E+29 -0.38000E+01  0.12840E+05
              AR            Enhanced by    8.000E-01
              N2O4          Enhanced by    2.000E+00
              NO2           Enhanced by    2.000E+00
679. N2O4+O=N2O3+O2                          1.21E+12    0.0       0.0
680. NO2+NO(+M)=N2O3(+M)                     1.60E+09    1.4       0.0
     Low pressure limit:  0.10000E+34 -0.77000E+01  0.00000E+00
              N2            Enhanced by    1.360E+00
681. N2O3+O=NO2+NO2                          2.71E+11    0.0       0.0
682. N2+M=N+N+M                              1.00E+28   -3.3  225000.0
              N             Enhanced by    5.000E+00
              O             Enhanced by    2.200E+00
683. NH+M=N+H+M                              2.65E+14    0.0   75500.0
684. NH+H=N+H2                               3.20E+13    0.0     325.0
685. NH+N=N2+H                               9.00E+11    0.5       0.0
686. NH+NH=NNH+H                             5.10E+13    0.0       0.0
687. NH+NH=NH2+N                             5.95E+02    2.9   -2030.0
688. NH+NH=N2+H2                             1.00E+08    1.0       0.0
689. NH2+M=NH+H+M                            3.16E+23   -2.0   91400.0
690. NH+H2=NH2+H                             1.00E+14    0.0   20070.0
691. NH2+N=N2+H+H                            6.90E+13    0.0       0.0
692. NH2+NH=N2H2+H                           1.50E+15   -0.5       0.0
693. NH2+NH=NH3+N                            1.00E+13    0.0    2000.0
694. NH3+NH=NH2+NH2                          3.16E+14    0.0   26770.0
695. NH2+NH2=N2H2+H2                         1.00E+13    0.0    1500.0
696. N2H3+H=NH2+NH2                          5.00E+13    0.0    2000.0
697. NH3+M=NH2+H+M                           2.20E+16    0.0   93470.0
698. NH3+M=NH+H2+M                           6.30E+14    0.0   93390.0
699. NH3+H=NH2+H2                            5.42E+05    2.4    9920.0
700. NH3+NH2=N2H3+H2                         1.00E+11    0.5   21600.0
701. NNH=N2+H                                3.00E+08    0.0       0.0
702. NNH+M=N2+H+M                            1.00E+13    0.5    3060.0
703. NNH+H=N2+H2                             1.00E+14    0.0       0.0
704. NNH+N=NH+N2                             3.00E+13    0.0    2000.0
705. NNH+NH=N2+NH2                           2.00E+11    0.5    2000.0
706. NNH+NH2=N2+NH3                          1.00E+13    0.0       0.0
707. NNH+NNH=N2H2+N2                         1.00E+13    0.0    4000.0
708. N2H2+M=NNH+H+M                          5.00E+16    0.0   50000.0
              H2O           Enhanced by    1.500E+01
              O2            Enhanced by    2.000E+00
              N2            Enhanced by    2.000E+00
              H2            Enhanced by    2.000E+00
709. N2H2+M=NH+NH+M                          3.16E+16    0.0   99400.0
              H2O           Enhanced by    1.500E+01
              O2            Enhanced by    2.000E+00
              N2            Enhanced by    2.000E+00
              H2            Enhanced by    2.000E+00
710. N2H2+H=NNH+H2                           8.50E+04    2.6    -230.0
711. N2H2+N=NNH+NH                           1.00E+06    2.0       0.0
712. N2H2+NH=NNH+NH2                         1.00E+13    0.0    6000.0
713. N2H2+NH2=NH3+NNH                        8.80E-02    4.0   -1610.0
714. N2H3+NH=N2H2+NH2                        2.00E+13    0.0       0.0
715. N2H3+NNH=N2H2+N2H2                      1.00E+13    0.0    4000.0
716. N2H3+M=NH2+NH+M                         5.00E+16    0.0   60000.0
717. N2H3+M=N2H2+H+M                         1.00E+16    0.0   37000.0
718. N2H3+H=N2H2+H2                          1.00E+13    0.0       0.0
719. N2H3+H=NH+NH3                           1.00E+11    0.0       0.0
720. N2H3+N=N2H2+NH                          1.00E+06    2.0       0.0
721. N2H3+NH2=NH3+N2H2                       1.00E+11    0.5       0.0
722. N2H3+N2H2=N2H4+NNH                      1.00E+13    0.0    6000.0
723. N2H3+N2H3=NH3+NH3+N2                    3.00E+12    0.0       0.0
724. N2H3+N2H3=N2H4+N2H2                     1.20E+13    0.0       0.0
725. N2H4(+M)=NH2+NH2(+M)                    5.00E+14    0.0   60000.0
     Low pressure limit:  0.15000E+16  0.00000E+00  0.39000E+05
```

262

```
        N2              Enhanced by    2.400E+00
        NH3             Enhanced by    3.000E+00
        N2H4            Enhanced by    4.000E+00
726. N2H4+M=N2H3+H+M                            1.00E+15    0.0   63600.0
        N2              Enhanced by    2.400E+00
        NH3             Enhanced by    3.000E+00
        N2H4            Enhanced by    4.000E+00
727. N2H4+H=N2H3+H2                             7.00E+12    0.0    2500.0
728. N2H4+H=NH2+NH3                             2.40E+09    0.0    3100.0
729. N2H4+N=N2H3+NH                             1.00E+10    1.0    2000.0
730. N2H4+NH=NH2+N2H3                           1.00E+09    1.5    2000.0
731. N2H4+NH2=N2H3+NH3                          1.80E+06    1.7   -1380.0
732. N+OH=NO+H                                  2.80E+13    0.0       0.0
733. N2O+H=N2+OH                                2.20E+14    0.0   16750.0
734. N2O+H=NH+NO                                6.70E+22   -2.2   37155.0
735. N2O+H=NNH+O                                5.50E+18   -1.1   47290.0
736. N2O+H=HNNO                                 8.00E+24   -4.4   10530.0
737. N2O+OH=N2+HO2                              1.00E+14    0.0   30000.0
738. HNO+NO=N2O+OH                              8.50E+12    0.0   29580.0
739. HNO+NO+NO=HNNO+NO2                         1.60E+11    0.0    2090.0
740. NH+NO+M=HNNO+M                             1.63E+23   -2.6    1820.0
741. HNNO+H=N2O+H2                              2.00E+13    0.0       0.0
742. HNNO+H=NH2+NO                              1.00E+12    0.0       0.0
743. HNNO+O=N2O+OH                              2.00E+13    0.0       0.0
744. HNNO+OH=H2O+N2O                            2.00E+13    0.0       0.0
745. HNNO+OH=HNOH+NO                            1.00E+12    0.0       0.0
746. HNNO+NO=N2+HONO                            2.60E+11    0.0    1610.0
747. HNNO+NO=NNH+NO2                            3.20E+12    0.0     540.0
748. HNNO+NO=N2O+HNO                            1.00E+12    0.0       0.0
749. HNNO+NO2=N2O+HONO                          1.00E+12    0.0       0.0
750. HNNO+NO2=NNH+NO3                           1.00E+13    0.0   17000.0
751. NO2+H=NO+OH                                1.32E+14    0.0     362.0
752. NO2+OH=HO2+NO                              1.81E+13    0.0    6676.0
753. NO2+HO2=HONO+O2                            4.64E+11    0.0    -479.0
754. NO2+H2=HONO+H                              7.33E+11    0.0   28800.0
755. NO2+NH=N2O+OH                              8.65E+10    0.0   -2270.0
756. NO2+NH=NO+HNO                              1.24E+11    0.0   -2270.0
757. NO3+H=NO2+OH                               6.62E+13    0.0       0.0
758. NO3+OH=NO2+HO2                             1.21E+13    0.0       0.0
759. NO3+HO2=HNO3+O2                            5.55E+11    0.0       0.0
760. NO3+HO2=NO2+OH+O2                          1.51E+12    0.0       0.0
761. N2O4+H2O=HONO+HNO3                         2.52E+14    0.0   11590.0
762. N2O3+H2O=HONO+HONO                         3.79E+13    0.0    8880.0
763. H+NO(+M)=HNO(+M)                           1.52E+15   -0.4       0.0
      Low pressure limit:  0.40000E+21 -0.17500E+01  0.00000E+00
        H2O             Enhanced by    1.000E+01
        O2              Enhanced by    1.500E+00
        AR              Enhanced by    7.500E-01
        H2              Enhanced by    2.000E+00
        CO2             Enhanced by    3.000E+00
764. HNO+H=NO+H2                                4.46E+11    0.7     655.0
765. HNO+OH=NO+H2O                              1.30E+07    1.9    -956.0
766. HNO+O=OH+NO                                5.00E+11    0.5    2000.0
767. HNO+O=NO2+H                                5.00E+10    0.0    2000.0
768. HNO+O2=NO+HO2                              2.20E+10    0.0    9140.0
769. HNO+N=NO+NH                                1.00E+11    0.5    2000.0
770. HNO+N=H+N2O                                5.00E+10    0.5    3000.0
771. HNO+NH=NH2+NO                              5.00E+11    0.5       0.0
772. HNO+NH2=NH3+NO                             2.00E+13    0.0    1000.0
773. HNO+HNO=N2O+H2O                            3.63E-03    4.0    1190.0
774. HNO+HNO=HNOH+NO                            2.00E+08    0.0    4170.0
775. HNO+NO2=HONO+NO                            6.02E+11    0.0    2000.0
776. NO+OH(+M)=HONO(+M)                         2.00E+12   -0.1    -721.0
      Low pressure limit:  0.50800E+24 -0.25100E+01 -0.67600E+02
      TROE centering:      0.62000E+00  0.10000E+02  0.10000E+06
        H2O             Enhanced by    1.000E+01
        O2              Enhanced by    2.000E+00
        AR              Enhanced by    7.500E-01
        H2              Enhanced by    2.000E+00
        CO2             Enhanced by    0.000E+00
777. NO+OH(+CO2)=HONO(+CO2)                     2.00E+12   -0.1    -721.0
      Low pressure limit:  0.17000E+24 -0.23000E+01 -0.24600E+02
      TROE centering:      0.62000E+00  0.10000E+02  0.10000E+06
778. NO2+H+M=HONO+M                             1.40E+18   -1.5     900.0
779. HONO+H=HNO+OH                              5.64E+10    0.9    4970.0
780. HONO+H=NO+H2O                              8.12E+06    1.9    3840.0
781. HONO+O=OH+NO2                              1.20E+13    0.0    5960.0
782. HONO+OH=H2O+NO2                            1.69E+12    0.0    -517.0
783. HONO+NH=NH2+NO2                            1.00E+13    0.0       0.0
784. HONO+HONO=H2O+NO2+NO                       1.00E+13    0.0    8540.0
785. HONO+NH2=NO2+NH3                           5.00E+12    0.0       0.0
786. NO2+OH(+M)=HNO3(+M)                        2.41E+13    0.0       0.0
      Low pressure limit:  0.64200E+33 -0.54900E+01  0.23500E+04
      TROE centering:      0.10000E+01  0.10000E+02  0.11680E+04
        H2O             Enhanced by    1.000E+01
        O2              Enhanced by    2.000E+00
        AR              Enhanced by    7.500E-01
        H2              Enhanced by    2.000E+00
        CO2             Enhanced by    0.000E+00
```

```
787. NO2+OH(+CO2)=HNO3(+CO2)                      2.41E+13     0.0      0.0
     Low pressure limit:  0.58000E+33 -0.54000E+01 0.21860E+04
     TROE centering:      0.10000E+01  0.10000E+02 0.11680E+04
788. NO+HO2+M=HNO3+M                              1.50E+24    -3.5   2200.0
789. HNO3+H=H2+NO3                                5.56E+08     1.5  16400.0
790. HNO3+H=H2O+NO2                               6.08E+01     3.3   6290.0
791. HNO3+H=OH+HONO                               3.82E+05     2.3   6980.0
792. HNO3+OH=NO3+H2O                              1.03E+10     0.0  -1240.0
793. NH3+O=NH2+OH                                 1.10E+06     2.1   5210.0
794. NH3+OH=NH2+H2O                               5.00E+07     1.6    950.0
795. NH3+HO2=NH2+H2O2                             3.00E+11     0.0  22000.0
796. NH2+HO2=NH3+O2                               1.65E+04     1.6   2027.0
797. NH2+O=H2+NO                                  5.00E+12     0.0      0.0
798. NH2+O=HNO+H                                  4.50E+13     0.0      0.0
799. NH2+O=NH+OH                                  7.00E+12     0.0      0.0
800. NH2+OH=NH+H2O                                9.00E+07     1.5   -460.0
801. NH2+OH=NH2OH                                 1.79E+13     0.2      0.0
802. NH2+HO2=HNO+H2O                              5.68E+15    -1.1    707.0
803. NH2+HO2=H2NO+OH                              2.91E+17    -1.3   1248.0
804. NH2+O2=HNO+OH                                1.00E+13     0.0  26290.0
805. NH2+O2=H2NO+O                                6.00E+13     0.0  29880.0
806. NH2+NO=NNH+OH                                2.29E+10     0.4   -814.0
807. NH2+NO=N2+H2O                                2.77E+20    -2.6   1258.0
808. NH2+NO=H2+N2O                                1.00E+13     0.0  33700.0
809. NH2+NO2=N2O+H2O                              1.62E+16    -1.4    270.0
810. NH2+NO2=H2NO+NO                              6.48E+16    -1.4    270.0
811. NH+O=NO+H                                    7.00E+13     0.0      0.0
812. NH+O=N+OH                                    7.00E+12     0.0      0.0
813. NH+OH=HNO+H                                  2.00E+13     0.0      0.0
814. NH+OH=N+H2O                                  2.00E+09     1.2      0.0
815. NH+OH=NO+H2                                  2.00E+13     0.0      0.0
816. NH+HO2=HNO+OH                                1.00E+13     0.0   2000.0
817. NH+O2=HNO+O                                  4.00E+13     0.0  17880.0
818. NH+O2=NO+OH                                  4.50E+08     0.8   1190.0
819. NH+H2O=HNO+H2                                2.00E+13     0.0  13850.0
820. NH+N2O=N2+HNO                                2.00E+12     0.0   6000.0
821. NNH+O=NH+NO                                  2.00E+14     0.0   4000.0
822. NH+NO=N2+OH                                  6.10E+13    -0.5    120.0
823. N2H4+O=N2H2+H2O                              8.50E+13     0.0   1200.0
824. N2H4+O=N2H3+OH                               2.50E+12     0.0   1200.0
825. N2H4+OH=N2H3+H2O                             3.00E+10     0.7   1290.0
826. N2H4+OH=NH3+H2NO                             3.67E+13     0.0      0.0
827. N2H4+HO2=N2H3+H2O2                           4.00E+13     0.0   2000.0
828. N2H3+O=N2H2+OH                               2.00E+13     0.0   1000.0
829. N2H3+O=NNH+H2O                               3.16E+11     0.5      0.0
830. N2H3+O=NH2+HNO                               1.00E+13     0.0      0.0
831. N2H3+OH=N2H2+H2O                             3.00E+10     0.7   1290.0
832. N2H3+OH=NH3+HNO                              1.00E+12     0.0  15000.0
833. N2H3+O2=N2H2+HO2                             3.00E+12     0.0      0.0
834. N2H3+HO2=N2H2+H2O2                           1.00E+13     0.0   2000.0
835. N2H3+HO2=N2H4+O2                             8.00E+12     0.0      0.0
836. N2H3+NO=HNO+N2H2                             1.00E+12     0.0      0.0
837. N2H2+O=NH2+NO                                1.00E+13     0.0      0.0
838. N2H2+O=NNH+OH                                2.00E+13     0.0   1000.0
839. N2H2+OH=NNH+H2O                              5.92E+01     3.4  -1360.0
840. N2H2+HO2=NNH+H2O2                            1.00E+13     0.0   2000.0
841. N2H2+NO=N2O+NH2                              3.00E+10     0.0      0.0
842. NNH+O=N2+OH                                  1.70E+16    -1.2    500.0
843. NNH+OH=N2+H2O                                2.40E+22    -2.9   2444.0
844. NNH+O2=N2+HO2                                1.20E+12    -0.3    150.0
845. NNH+O2=N2O+OH                                2.90E+11    -0.3    150.0
846. NNH+HO2=N2+H2O2                              1.00E+13     0.0   2000.0
847. NNH+NO=N2+HNO                                5.00E+13     0.0      0.0
848. NH2OH+OH=HNOH+H2O                            2.50E+13     0.0   4250.0
849. H2NO+M=H2+NO+M                               7.83E+27    -4.3  60300.0
     H2O              Enhanced by    1.000E+01
850. H2NO+M=HNO+H+M                               2.80E+24    -2.8  64915.0
     H2O              Enhanced by    1.000E+01
851. H2NO+M=HNOH+M                                1.10E+29    -4.0  43980.0
     H2O              Enhanced by    1.000E+01
852. H2NO+H=HNO+H2                                3.00E+07     2.0   2000.0
853. H2NO+H=NH2+OH                                5.00E+13     0.0      0.0
854. H2NO+O=HNO+OH                                3.00E+07     2.0   2000.0
855. H2NO+OH=HNO+H2O                              2.00E+07     2.0   1000.0
856. H2NO+HO2=HNO+H2O2                            2.90E+04     2.7  -1600.0
857. H2NO+NH2=HNO+NH3                             3.00E+12     0.0   1000.0
858. H2NO+O2=HNO+HO2                              3.00E+12     0.0  25000.0
859. H2NO+NO=HNO+HNO                              2.00E+07     2.0  13000.0
860. H2NO+NO2=HONO+HNO                            6.00E+11     0.0   2000.0
861. HNOH+M=HNO+H+M                               2.00E+24    -2.8  58935.0
     H2O              Enhanced by    1.000E+01
862. HNOH+H=HNO+H2                                4.80E+08     1.5    380.0
863. HNOH+H=NH2+OH                                4.00E+13     0.0      0.0
864. HNOH+O=HNO+OH                                7.00E+13     0.0      0.0
     Declared duplicate reaction...
865. HNOH+O=HNO+OH                                3.30E+08     1.5   -360.0
     Declared duplicate reaction...
866. HNOH+OH=HNO+H2O                              2.40E+06     2.0  -1190.0
867. HNOH+HO2=HNO+H2O2                            2.90E+04     2.7  -1600.0
```

```
868. HNOH+NH2=HNO+NH3                                    1.80E+06    1.9    -1150.0
869. HNOH+NO2=HONO+HNO                                   6.00E+11    0.0     2000.0
870. HNOH+O2=HNO+HO2                                     3.00E+12    0.0    25000.0
871. HNOH+HNO=NH2OH+NO                                   1.00E+12    0.0     3000.0
872. C+N2+M=CNN+M                                        1.12E+15    0.0        0.0
873. C2H+NO=HCN+CO                                       6.00E+13    0.0      570.0
874. C2H+HCN=CN+C2H2                                     3.20E+12    0.0     1530.0
875. CH2+NO=HCN+OH                                       5.00E+11    0.0     2870.0
876. HCN+M=H+CN+M                                        3.57E+26   -2.6   124900.0
877. C2N2+M=>CN+CN+M                                     3.20E+16    0.0    94400.0
878. CH+N2(+M)=HCNN(+M)                                  3.10E+12    0.1        0.0
     Low pressure limit:  0.13000E+26 -0.31600E+01  0.74000E+03
     TROE centering:       0.66700E+00  0.23500E+03  0.21170E+04  0.45360E+04
     H2O          Enhanced by     1.000E+01
     O2           Enhanced by     2.000E+00
     AR           Enhanced by     7.500E-01
     H2           Enhanced by     2.000E+00
879. HCNN+H=H2+CNN                                       5.00E+13    0.0        0.0
880. HCNN+H=>CH2+N2                                      2.00E+13    0.0     3000.0
881. HCNN+O=OH+CNN                                       2.00E+13    0.0    20000.0
882. HCNN+O=CO+H+N2                                      5.00E+13    0.0    15000.0
883. HCNN+O=HCN+NO                                       5.00E+13    0.0    15000.0
884. HCNN+OH=H2O+CNN                                     1.00E+13    0.0     8000.0
885. HCNN+OH=H+HCO+N2                                    1.00E+13    0.0    16000.0
886. HCNN+O2=HO2+CNN                                     1.00E+12    0.0     4000.0
887. HCNN+O2=>H+CO2+N2                                   4.00E+12    0.0        0.0
888. HCNN+O2=HCO+N2O                                     4.00E+12    0.0        0.0
889. CNN+O=CO+N2                                         1.00E+13    0.0        0.0
890. CNN+O=CN+NO                                         1.00E+14    0.0    20000.0
891. CNN+OH=H+CO+N2                                      1.00E+13    0.0     1000.0
892. CNN+H=NH+CN                                         5.00E+14    0.0    40000.0
893. CNN+OH=HCN+NO                                       1.00E+12    0.0     1000.0
894. CNN+H=HCN+N                                         5.00E+13    0.0    25000.0
895. CNN+O2=NO+NCO                                       1.00E+13    0.0     5000.0
896. HNO+CH3=NO+CH4                                      8.20E+05    1.9      954.0
897. HONO+CH3=NO2+CH4                                    8.10E+05    1.9     5504.0
898. H2NO+CH3=CH3O+NH2                                   2.00E+13    0.0        0.0
899. H2NO+CH3=HNO+CH4                                    1.60E+06    1.9     2960.0
900. HNOH+CH3=HNO+CH4                                    1.60E+06    1.9     2096.0
901. NH2OH+CH3=HNOH+CH4                                  1.60E+06    1.9     6350.0
902. NH2OH+CH3=H2NO+CH4                                  8.20E+05    1.9     5500.0
903. N2H2+CH3=NNH+CH4                                    1.60E+06    1.9     2970.0
904. N2H3+CH3=N2H2+CH4                                   8.20E+05    1.9     1818.0
905. N2H4+CH3=N2H3+CH4                                   3.30E+06    1.9     5325.0
906. CH4+NH=CH3+NH2                                      9.00E+13    0.0    20080.0
907. CH4+NH2=CH3+NH3                                     1.20E+13    0.0    15150.0
908. CH3+NH2=CH2+NH3                                     1.60E+06    1.9     7570.0
909. C2H6+NH=C2H5+NH2                                    7.00E+13    0.0    16700.0
910. C2H6+NH2=C2H5+NH3                                   9.70E+12    0.0    11470.0
911. C3H8+NH2=NC3H7+NH3                                  1.70E+13    0.0    10660.0
912. C3H8+NH2=IC3H7+NH3                                  4.50E+11    0.0     6150.0
913. CH3+NO(+M)=CH3NO(+M)                                1.00E+13    0.0        0.0
     Low pressure limit:  0.19000E+19  0.00000E+00  0.00000E+00
     SRI centering:        0.30000E-01 -0.79000E+03  0.10000E+01
914. CH3NO+H=H2CNO+H2                                    4.40E+08    1.5      377.0
915. CH3NO+H=CH3+HNO                                     1.80E+13    0.0     2800.0
916. CH3NO+O=H2CNO+OH                                    3.30E+08    1.5     3615.0
917. CH3NO+O=CH3+NO2                                     1.70E+06    2.1        0.0
918. CH3NO+OH=H2CNO+H2O                                  3.60E+06    2.0    -1192.0
919. CH3NO+OH=CH3+HONO                                   2.50E+12    0.0     1000.0
920. CH3NO+CH3=H2CNO+CH4                                 7.90E+05    1.9     5415.0
921. CH3NO+NH2=H2CNO+NH3                                 2.80E+06    1.9     1073.0
922. H2CNO=HNCO+H                                        2.30E+42   -9.1    53840.0
923. H2CNO+O2=CH2O+NO2                                   2.90E+12   -0.3    17700.0
924. H2CNO+H=CH3+NO                                      4.00E+13    0.0        0.0
925. H2CNO+H=HCNO+H2                                     4.80E+08    1.5     -894.0
926. H2CNO+O=HCNO+OH                                     3.30E+08    1.5     -894.0
927. H2CNO+O=CH2O+NO                                     7.00E+13    0.0        0.0
928. H2CNO+OH=CH2OH+NO                                   4.00E+13    0.0        0.0
929. H2CNO+OH=HCNO+H2O                                   2.40E+06    2.0    -1192.0
930. H2CNO+CH3=C2H5+NO                                   3.00E+13    0.0        0.0
931. H2CNO+CH3=HCNO+CH4                                  1.60E+06    1.9    -1113.0
932. H2CNO+NH2=HCNO+NH3                                  1.80E+06    1.9    -1152.0
933. CH3+NO2=CH3O+NO                                     1.40E+13    0.0        0.0
934. CH+NO2=HCO+NO                                       1.20E+14    0.0        0.0
935. CH2+NO2=CH2O+NO                                     4.20E+13    0.0        0.0
936. CN+NO=N2+CO                                         1.00E+11    0.0        0.0
937. HNCO+M=H+NCO+M                                      5.00E+15    0.0   120000.0
938. HNCO+N=NH+NCO                                       4.00E+13    0.0    36000.0
939. CH3O+HNO=CH3OH+NO                                   3.16E+13    0.0        0.0
940. NCO+HO2=HNCO+O2                                     2.00E+13    0.0        0.0
941. N2O+CO=CO2+N2                                       2.51E+14    0.0    46000.0
942. N2O+CH2=CH2O+N2                                     1.00E+12    0.0        0.0
943. N2O+CH3=CH3O+N2                                     9.00E+09    0.0        0.0
944. N2O+HCO=CO2+H+N2                                    1.70E+14    0.0    20000.0
945. N2O+HCCO=CO+HCO+N2                                  1.70E+14    0.0    25500.0
946. N2O+C2H2=HCCO+H+N2                                  6.59E+16    0.0    61200.0
947. N2O+C2H3=CH2CHO+N2                                  1.00E+11    0.0        0.0
948. HOCN+O=NCO+OH                                       1.50E+04    2.6     4000.0
```

265

```
 949. HOCN+H=NCO+H2                                          2.00E+07   2.0    2000.0
 950. HOCN+H=NH2+CO                                          1.20E+08   0.6    2080.0
 951. HOCN+OH=NCO+H2O                                        6.38E+05   2.0    2560.0
 952. HOCN+CH3=NCO+CH4                                       8.20E+05   1.9    6620.0
 953. HOCN+NH2=NCO+NH3                                       9.20E+05   1.9    3645.0
 954. CN+NO2=CO+N2O                                          4.93E+14  -0.8     344.0
 955. CN+NO2=CO2+N2                                          3.70E+14  -0.8     344.0
 956. CN+CO2=NCO+CO                                          3.67E+06   2.2   26900.0
 957. CN+NH3=HCN+NH2                                         9.20E+12   0.0    -357.0
 958. HNCO+CN=HCN+NCO                                        1.50E+13   0.0       0.0
 959. HONO+NCO=HNCO+NO2                                      3.60E+12   0.0       0.0
 960. NCO+CH2O=HNCO+HCO                                      6.00E+12   0.0       0.0
 961. NH2+C=CH+NH                                            5.80E+11   0.7   20900.0
 962. C+N2=CN+N                                              5.20E+13   0.0   44700.0
 963. CH2+N2=HCN+NH                                          4.80E+12   0.0   35850.0
 964. C2+N2=CN+CN                                            1.50E+13   0.0   41700.0
 965. H2CN+N=N2+CH2                                          6.00E+13   0.0     400.0
 966. H2CN+H=HCN+H2                                          2.40E+08   1.5    -894.0
 967. H2CN+O=HCN+OH                                          1.70E+08   1.5    -894.0
 968. H2CN+O=HNCO+H                                          6.00E+13   0.0       0.0
 969. H2CN+O=HCNO+H                                          2.00E+13   0.0       0.0
 970. H2CN+M=HCN+H+M                                         3.00E+14   0.0   22000.0
 971. H2CN+HO2=HCN+H2O2                                      1.40E+04   2.7   -1610.0
 972. H2CN+O2=CH2O+NO                                        3.00E+12   0.0    6000.0
 973. H2CN+CH3=HCN+CH4                                       8.10E+05   1.9   -1113.0
 974. H2CN+OH=HCN+H2O                                        1.20E+06   2.0   -1192.0
 975. H2CN+NH2=HCN+NH3                                       9.20E+05   1.9   -1152.0
 976. C+NO=CN+O                                              2.00E+13   0.0       0.0
 977. CH+NO=HCN+O                                            8.69E+13   0.0       0.0
 978. CH+NO=CN+OH                                            1.68E+12   0.0       0.0
 979. CH+NO=CO+NH                                            9.84E+12   0.0       0.0
 980. CH+NO=NCO+H                                            1.67E+13   0.0       0.0
 981. CH2+NO=HNCO+H                                          2.50E+12   0.0    5970.0
 982. CH2+NO=HCNO+H                                          3.80E+13  -0.4     576.0
 983. CH2+NO=NH2+CO                                          2.30E+16  -1.4    1331.0
 984. CH2+NO=H2CN+O                                          8.10E+07   1.4    4110.0
 985. CH3+NO=HCN+H2O                                         2.40E+12   0.0   15700.0
 986. CH3+NO=H2CN+OH                                         5.20E+12   0.0   24240.0
 987. HCCO+NO=HCNO+CO                                        4.64E+13   0.0     700.0
 988. HCCO+NO=HCN+CO2                                        1.39E+13   0.0     700.0
 989. CH2s+NO=HCN+OH                                         1.00E+14   0.0       0.0
 990. HCNO=HCN+O                                             4.20E+31  -6.1   61210.0
 991. HCNO+H=HCN+OH                                          1.00E+14   0.0   12000.0
 992. HCNO+H=HNCO+H                                          2.10E+15  -0.7    2850.0
 993. HCNO+H=HOCN+H                                          1.40E+11  -0.2    2484.0
 994. HCNO+H=NH2+CO                                          1.70E+14  -0.8    2890.0
 995. HCNO+O=HCO+NO                                          7.00E+13   0.0       0.0
 996. CH2+N=HCN+H                                            5.00E+13   0.0       0.0
 997. CH2+N=NH+CH                                            6.00E+11   0.7   40500.0
 998. CH+N=CN+H                                              1.67E+14  -0.1       0.0
 999. CH+N=C+NH                                              4.50E+11   0.7    2400.0
1000. N+CO2=NO+CO                                            1.90E+11   0.0    3400.0
1001. N+HCCO=HCN+CO                                          5.00E+13   0.0       0.0
1002. CH3+N=H2CN+H                                           7.10E+13   0.0       0.0
1003. CH3+N=HCNH+H                                           1.20E+11   0.5     367.6
1004. HCNH=HCN+H                                             6.10E+28  -5.7   24270.0
1005. HCNH+H=H2CN+H                                          2.00E+13   0.0       0.0
1006. HCNH+H=HCN+H2                                          2.40E+08   1.5    -894.0
1007. HCNH+O=HNCO+H                                          7.00E+13   0.0       0.0
1008. HCNH+O=HCN+OH                                          1.70E+08   1.5    -894.0
1009. HCNH+OH=HCN+H2O                                        1.20E+06   2.0   -1192.0
1010. HCNH+CH3=HCN+CH4                                       8.20E+05   1.9   -1113.0
1011. C2H3+N=HCN+CH2                                         2.00E+13   0.0       0.0
1012. CN+H2O=HCN+OH                                          4.00E+12   0.0    7400.0
1013. CN+H2O=HOCN+H                                          4.00E+12   0.0    7400.0
1014. OH+HCN=HOCN+H                                          3.20E+04   2.5   12120.0
1015. OH+HCN=HNCO+H                                          5.60E-06   4.7    -490.0
1016. OH+HCN=NH2+CO                                          6.44E+10   0.0   11700.0
1017. HOCN+H=HNCO+H                                          1.00E+13   0.0       0.0
1018. HCN+O=NCO+H                                            1.38E+04   2.6    4980.0
1019. HCN+O=NH+CO                                            3.45E+03   2.6    4980.0
1020. HCN+O=CN+OH                                            2.70E+09   1.6   26600.0
1021. CN+H2=HCN+H                                            2.00E+04   2.9    1600.0
1022. CN+O=CO+N                                              1.90E+12   0.5     720.0
1023. CN+O2=NCO+O                                            7.20E+12   0.0    -400.0
1024. CN+OH=NCO+H                                            4.00E+13   0.0       0.0
1025. CN+HCN=C2N2+H                                          1.51E+07   1.7    1530.0
1026. CN+NO2=NCO+NO                                          5.32E+15  -0.8     344.0
1027. CN+N2O=NCO+N2                                          6.00E+12   0.0   15360.0
1028. C2N2+O=NCO+CN                                          4.57E+12   0.0    8880.0
1029. C2N2+OH=HNCO+CN                                        1.86E+11   0.0    2900.0
1030. C2N2+OH=HOCN+CN                                        2.00E+12   0.0   19000.0
1031. HNCO+H=H2+NCO                                          1.76E+05   2.4   12300.0
1032. HNCO+H=NH2+CO                                          3.60E+04   2.5    2340.0
1033. HNCO+M=NH+CO+M                                         1.10E+16   0.0   86000.0
      N2           Enhanced by   1.500E+00
      O2           Enhanced by   1.500E+00
      H2O          Enhanced by   1.860E+01
1034. HNCO+O=NCO+OH                                          2.20E+06   2.1   11430.0
```

266

```
1035. HNCO+O=NH+CO2                        9.80E+07    1.4     8530.0
1036. HNCO+O=HNO+CO                        1.50E+08    1.6    44012.0
1037. HNCO+OH=NCO+H2O                      3.45E+07    1.5     3600.0
1038. HNCO+OH=NH2+CO2                      6.30E+10   -0.1    11645.0
1039. HNCO+HO2=NCO+H2O2                    3.00E+11    0.0    29000.0
1040. HNCO+O2=HNO+CO2                      1.00E+12    0.0    35000.0
1041. HNCO+NH2=NCO+NH3                     5.00E+12    0.0     6200.0
1042. HNCO+NH=NCO+NH2                      1.04E+15    0.0    39390.0
1043. NCO+H=NH+CO                          5.36E+13    0.0        0.0
1044. NCO+O=NO+CO                          4.20E+13    0.0        0.0
1045. NCO+O=N+CO2                          8.00E+12    0.0     2500.0
1046. NCO+N=N2+CO                          2.00E+13    0.0        0.0
1047. NCO+OH=NO+HCO                        5.00E+12    0.0    15000.0
1048. NCO+M=N+CO+M                         2.20E+14    0.0    54050.0
1049. NCO+NO=N2O+CO                        4.60E+18   -2.0      934.0
1050. NCO+NO=N2+CO2                        5.80E+18   -2.0      934.0
1051. NCO+O2=NO+CO2                        2.00E+12    0.0    20000.0
1052. NCO+HCO=HNCO+CO                      3.60E+13    0.0        0.0
1053. NCO+NO2=CO+NO+NO                     2.83E+13   -0.6     -326.0
1054. NCO+NO2=CO2+N2O                      3.57E+14   -0.6     -326.0
1055. NCO+HNO=HNCO+NO                      1.80E+13    0.0        0.0
1056. NCO+NCO=CO+CO+N2                     3.00E+12    0.0        0.0
1057. NO+HCO=CO+HNO                        7.24E+13   -0.4        0.0
1058. NO2+CO=CO2+NO                        9.00E+13    0.0    33800.0
1059. NO2+HCO=H+CO2+NO                     8.40E+15   -0.8     1930.0
1060. CH3O+NO2=HONO+CH2O                   3.00E+12    0.0        0.0
1061. CH3O+NO=CH2O+HNO                     1.30E+14   -0.7        0.0
1062. NO2+CH2O=HONO+HCO                    1.00E+10    0.0    15100.0
1063. NO+CH2O=HNO+HCO                      1.00E+13    0.0    40820.0
1064. NO2+HCO=HONO+CO                      1.00E+13    0.0        0.0
1065. NO2+HCO=OH+NO+CO                     1.00E+14    0.0        0.0
1066. NCO+N=NO+CN                          2.70E+18   -1.0    17200.0
1067. CN+CH4=HCN+CH3                       9.00E+04    2.6     -300.0
1068. C+NO=CO+N                            2.80E+13    0.0        0.0
1069. NH+CO2=HNO+CO                        1.00E+13    0.0    14350.0
1070. NCO+CH4=HNCO+CH3                     1.00E+13    0.0     8130.0
1071. C+N2O=CN+NO                          4.80E+12    0.0        0.0
1072. CH+NH2=HCN+H+H                       3.00E+13    0.0        0.0
1073. CH+NH=HCN+H                          5.00E+13    0.0        0.0
1074. CH2+NH=HCN+H+H                       3.00E+13    0.0        0.0
1075. CH3+N=HCN+H+H                        2.00E+11    0.0        0.0
1076. CH3+N=HCN+H2                         7.10E+12    0.0        0.0
1077. CH4+N=NH+CH3                         1.00E+13    0.0    24000.0
1078. C3H3+N=HCN+C2H2                      1.00E+13    0.0        0.0
1079. CH+N2O=HCN+NO                        1.34E+13    0.0     -510.0
1080. CH+N2O=CO+H+N2                       5.20E+12    0.0     -510.0
1081. C2O+N2=>NCO+CN                       7.00E+11    0.0    17000.0
1082. CH2+C=CH+CH                          1.62E+12    0.7    46800.0
1083. CH2+M=C+H2+M                         1.60E+14    0.0    64000.0
1084. CH+O=C+OH                            1.52E+13    0.0     4730.0
1085. H2O+C=CH+OH                          7.80E+11    0.7    39300.0
1086. CH+H=C+H2                            7.90E+13    0.0      160.0
1087. C+OH=CO+H                            5.00E+13    0.0        0.0
1088. C+O2=CO+O                            1.20E+14    0.0     4000.0
1089. C+CH3=C2H2+H                         5.00E+13    0.0        0.0
1090. C+CH2=C2H+H                          5.00E+13    0.0        0.0
1091. C2+O=C+CO                            3.60E+14    0.0        0.0
1092. HCCO+OH=C2O+H2O                      3.00E+13    0.0        0.0
1093. C2O+H=CH+CO                          1.32E+13    0.0        0.0
1094. C2O+O=CO+CO                          5.20E+13    0.0        0.0
1095. C2O+OH=CO+CO+H                       2.00E+13    0.0        0.0
1096. C2O+O2=CO+CO+O                       2.00E+13    0.0        0.0
1097. C2O+O2=CO+CO2                        2.00E+13    0.0        0.0
1098. C2+OH=C2O+H                          5.00E+13    0.0        0.0
1099. C2H+OH=C2+H2O                        4.00E+07    2.0     8000.0
1100. C2+H2=C2H+H                          6.60E+13    0.0     7950.0
1101. C2+O2=CO+CO                          9.00E+12    0.0      980.0
```

UNITS for the preceding reactions (unless otherwise noted):
    A units mole-cm-sec-K, E units cal/mole